FACULTÉ DES ÉTUDES SUPÉRIEURES ET POSTDOCTORALES

uOttawa

L'Université canadienne
Canada's university

FACULTY OF GRADUATE AND POSTDOCTORAL STUDIES

Charbel Siklawi

AUTEUR DE LA THÈSE / AUTHOR OF THESIS

M.A.Sc. (Mechanical Engineering)

GRADE / DEGREE

Department of Mechanical Engineering

FACULTÉ, ÉCOLE, DÉPARTEMENT / FACULTY, SCHOOL, DEPARTMENT

Large Eddy Simulation(2D) Using Vortex-in-Cell and Filtered Density Function for Isothermally Reacting and Thermally Stratified Mixing Layers

TITRE DE LA THÈSE / TITLE OF THESIS

R. Milane

DIRECTEUR (DIRECTRICE) DE LA THÈSE / THESIS SUPERVISOR

CO-DIRECTEUR (CO-DIRECTRICE) DE LA THÈSE / THESIS CO-SUPERVISOR

EXAMINATEURS (EXAMINATRICES) DE LA THÈSE / THESIS EXAMINERS

M. Johnson

C. Mavriplis

Gary W. Slater

Le Doyen de la Faculté des études supérieures et postdoctorales / Dean of the Faculty of Graduate and Postdoctoral Studies

LARGE EDDY SIMULATION (2D) USING VORTEX-IN-CELL AND FILTERED DENSITY FUNCTION FOR ISOTHERMALLY REACTING AND THERMALLY STRATIFIED MIXING LAYERS

Charbel Siklawi

A thesis submitted to the Faculty of Graduate and Postdoctoral Studies
in partial fulfillment of the requirements for the degree of

MASTER OF APPLIED SCIENCE
in Mechanical Engineering

Ottawa-Carleton Institute for Mechanical and Aerospace Engineering

University of Ottawa

Ottawa, Canada

January 2009

Library and Archives Canada

Published Heritage Branch

395 Wellington Street
Ottawa ON K1A 0N4
Canada

Bibliothèque et Archives Canada

Direction du Patrimoine de l'édition

395, rue Wellington
Ottawa ON K1A 0N4
Canada

Your file Votre référence
ISBN: 978-0-494-58186-5
Our file Notre référence
ISBN: 978-0-494-58186-5

NOTICE:

The author has granted a non-exclusive license allowing Library and Archives Canada to reproduce, publish, archive, preserve, conserve, communicate to the public by telecommunication or on the Internet, loan, distribute and sell theses worldwide, for commercial or non-commercial purposes, in microform, paper, electronic and/or any other formats.

The author retains copyright ownership and moral rights in this thesis. Neither the thesis nor substantial extracts from it may be printed or otherwise reproduced without the author's permission.

AVIS:

L'auteur a accordé une licence non exclusive permettant à la Bibliothèque et Archives Canada de reproduire, publier, archiver, sauvegarder, conserver, transmettre au public par télécommunication ou par l'Internet, prêter, distribuer et vendre des thèses partout dans le monde, à des fins commerciales ou autres, sur support microforme, papier, électronique et/ou autres formats.

L'auteur conserve la propriété du droit d'auteur et des droits moraux qui protège cette thèse. Ni la thèse ni des extraits substantiels de celle-ci ne doivent être imprimés ou autrement reproduits sans son autorisation.

In compliance with the Canadian Privacy Act some supporting forms may have been removed from this thesis.

While these forms may be included in the document page count, their removal does not represent any loss of content from the thesis.

Conformément à la loi canadienne sur la protection de la vie privée, quelques formulaires secondaires ont été enlevés de cette thèse.

Bien que ces formulaires aient inclus dans la pagination, il n'y aura aucun contenu manquant.

Canada

ABSTRACT

A large eddy simulation based on the filtered vorticity transport equation has been coupled with the filtered mass weighted density function transport equation. The filtered vorticity transport has been formulated using the diffusion-velocity method and then solved using the vortex-in-cell scheme in conjunction with both Smagorinsky and dynamic eddy viscosity subgrid scale models for an anisotropic flow. The transport equation for filtered mass weighted density function is solved using the Lagrangian Monte-Carlo method. The methodology has been tested on both chemically reacting with no heat release and thermally stratified spatially growing mixing layers. It is shown that mixing has a greater effect on scalar field within the vortex structure as compared to the braid regions. Also for high Damköhler number (Da), the reaction zones are mainly limited to the thin reacting interfacial zones, i.e. the contact zone between the reactants, whereas for low Da, the reacting zones are spread as reacting pockets within the vortex structure. The effect of vorticity-temperature interaction, i.e., the volumetric expansion and baroclinic vorticity generation, on the flow field is also investigated by mixing a cold and a hot stream with temperature differences of 0, 5, 10, 30 and 50°K. The mixing layer is destabilized earlier and the pairing of vortical structures is reduced as temperature difference is increased. The characteristics of the flow field, i.e. the vorticity contours, the mean velocity, root-mean-square velocity fluctuations and negative cross-stream correlations are discussed. Also, the characteristics of the scalar field, i.e. the mean scalar profiles, root-mean-square scalar fluctuations profiles and filtered probability density function are presented.

ACKNOWLEDGEMENTS

My deepest gratitude is due firstly to my supervisor, Dr. Roger Milane. Throughout my years of study and research at the University of Ottawa, he provided encouragement and valuable technical knowledge and helped me maintain my focus on the research. I appreciate the technical suggestions he has constantly offered and thank him for being patient with me during these last few years.

My parents have given me infinite support and have kept their faith in me during these grueling graduate school years. I thank them for always being there to listen, for all the advice they gave me from time to time and for praying for me constantly.

TABLE OF CONTENTS

CHAPTER 3 FORMULATION FOR COMPRESSIBLE NON-REACTIVE FLOW AND SCALAR FIELDS 22

CHAPTER 4 FORMULATION FOR INCOMPRESSIBLE REACTIVE FLOW AND SCALAR FIELDS 54

LIST OF FIGURES

NOMENCLATURE

Roman Characters

a_{xy}	Mesh aspect ratio
C_{ϕ}	Mixing frequency constant
d	Distance between point vortices
Da	Damköhler number
H_x, H_y	Computational domain length and height
k	Chemical reaction rate
$\mathrm{N_v}$	Number of vortex particles
$\mathrm{N_x}, \mathrm{N_y}$	Number of grids in x- and y- directions
Pr	Prandtl number
Pr_t	Turbulent Prandtl number
r	Velocity ratio
Re	Reynolds number
Sc	Schmidt number
Sc_t	Turbulent Schmidt number
t	Time
t_{res}	Residence time
$\mathbf{u}$	Velocity vector
u, v	Cartesian velocity components
$\bar{U}$	Time averaged velocity

U_h, U_l	Upper and lower free stream velocities
U_H, U_C	Hot and cold free stream velocities
U_{avg}, U_c	Arithmetic average of the free stream velocities
$\mathbf{x}$	Position vector
x, y	Cartesian coordinates
x_v, x_c, x_T	Virtual origins for velocity, concentration and temperature
x_n, y_n	Coordinates of the vortex particles
y_{ov}, y_{oc}, y_{oT}	Lateral position of the velocity, concentration and temperature centerlines

Greek Symbols

Γ_i	Initial circulation of vortex particles
Γ_n	Circulation of the vortex element number n
Δt	Time step
$\Delta x, \Delta y$	Grid sizes in x-and y- directions
Δ_x, Δ_y	Filter sizes in x- and y- directions
η_v, η_c, η_T	Velocity, concentration and temperature similarity variables
ν	Kinematic viscosity
ν_t	Eddy viscosity
ξ	Concentration
ρ	Density
φ	Potential function
ϕ	Scalar variable

ψ	Stream function
ω	Vorticity
ω_f	Mixing frequency

Superscripts and Mathematical Symbols

$\tilde{\square}$	Favre filtered quantity
$\bar{\square}$	Filtered quantity
$\square'$	Fluctuation quantity

Subscripts

i, j	Indices
$\square_{rms}$	Root mean squared quantity
$\square_t$	Turbulent quantity

Acronyms

DNS	Direct numerical simulation
FDF	Filtered density function
FMDF	Filtered mass weighted density function
LES	Large eddy simulation
PDF	Probability density function
RANS	Reynolds averaged Navier-Stokes simulation
VIC	Vortex-In-Cell

Chapter 1

INTRODUCTION

1.1 Background Information

Most power generation and transportation systems currently in use rely on combustion processes for energy production. As a direct consequence, combustion related pollution emissions and global warming have become critical issues in today's scenario. In most practical applications, the flow field in which chemical reaction and heat release take place is turbulent, with the inherent advantage that turbulence greatly enhances mixing of chemical reactants, momentum and heat. A clear and detailed understanding of the factors governing turbulent combustion, therefore, is essential to efforts aimed at improving operational efficiency of these devices and reducing emissions.

The plane mixing layer is one of the simplest conceivable free shear flows to maintain turbulence. Turbulent mixing layers are commonly observed in various engineering applications such as combustion, propulsion and environmental flows. They involve complex flow phenomena such as the instability of flow, evolution and interactions of vortices. Due to their apparent simplicity and their richness in flow physics, mixing layers have attracted numerous computational and experimental studies to understand the fundamental mechanism of turbulent combustion.

Experiments and numerical simulations are both used, in a complementary fashion, to enhance our understanding of turbulent combustion. A number of review articles detail the progress made in each type of investigation. However, there is a general agreement that experiments involve more time and effort, and are also more expensive to conduct. Particularly, with the latest advancement in computing technology, simulations are now truly on par with experiments as a research tool.

1.1.1 Mixing Layer

A mixing layer is formed by the interaction of two parallel streams of fluid with different velocities. Mixing layers occur in many engineering problems of great importance. The boundary region of a jet, the slip-stream behind a wing, and the interface between a recirculation region and a free-stream are just a few examples. A typical geometry for a mixing layer is shown in Figure 1.1. The early observations by Brown and Roshko (1974) of large two-dimensional rollers in the low speed mixing layer led to a strong interest in the dynamics and evolution of these, so-called, coherent structures. Because of their importance in engineering applications, a great deal of effort has gone into experimentally and numerically studying turbulent mixing layers. Konrad (1976) found experimentally that the amount of mixing at the molecular scale was very small until a critical Reynolds number was reached, at which point the molecular mixing was enhanced; this phenomenon characterizes the transitional mixing layers.

1.1.2 Turbulence Modeling

A broad spectrum of length and time scales characterizes turbulent flow and combustion chemistry. Unfortunately, analytical solutions to even the simplest turbulent flows do not exist. As a result, various approaches are available for modeling turbulence. Based on the resolution of turbulence and on the simplifying assumptions invoked, turbulent flow simulations can be classified as Direct Numerical Simulations (DNS), Large-Eddy Simulations (LES) or Reynolds Averaged Navier-Stokes (RANS) simulations.

1.1.2.1 Direct Numerical Simulations (DNS)

In direct numerical simulations, all the spatial and temporal scales of the flow are resolved down to the Kolmogorov scales. No models are required, other than the conservation equations governing the flow and suitable boundary conditions for the configuration being studied. The advantage of DNS lies in the extremely detailed information about the flow that they provide: this is very difficult if not nearly impossible to measure in experiments. The fine resolution required by DNS places an immense requirement on computing resources and memory. In homogeneous turbulence, the computer requirements increase rapidly with increasing Reynolds number (Re) because the ratio of a solution domain to a computational grid is proportional to $Re^{3/4}$ and the computational cost increases approximately to Re^3. It is noted that with the improvement in computing abilities and numerical methods over the years, the complexity of flows computed by DNS has increased, but their Reynolds numbers are still low. In addition, very precise initial and boundary conditions must be used with high-order, low dissipation numerical methods. However, the importance of DNS as a research tool is emphasized, given that data from DNS can be used to validate turbulence models. DNS of turbulent reacting flows also requires solution of scalar fields, increasing computational cost and complexity considerably. In addition to resolving all scales of the flow, the scales of chemical reaction must be resolved.

1.1.2.2 Reynolds Averaged Navier-Stokes (RANS) Simulations

RANS modeling is the classical approach to treating turbulent flows. Unlike DNS, where every small motion of the flow is captured, in RANS methods, the governing equations are averaged to describe only the mean field. Local fluctuations and turbulent structures are integrated in the mean quantities and do not have to be described in the simulation. The main advantage of RANS methods is the low computational expense that is needed. As a consequence, complicated engineering and industrial flows are analyzed using RANS-based models, and these models are built into most commercial CFD software packages. Sufficient success has been achieved with these methods. This technique, however, fails to directly capture the dynamics of the large, mixing-controlling eddies. RANS turbulence models also rely heavily on empirically adjusted constants.

1.1.2.3 Large-Eddy Simulations (LES)

Intermediate in computational expense between DNS and RANS methods, LES can be defined as the simulation of a turbulent flow in which the unsteady large-scale motions are resolved explicitly while smaller scales are filtered using a spatial filtering operation applied to the instantaneous turbulent fields. The effect of the smaller, unresolved or sub-grid scales is modeled. LES capture most of the energy of the flow, and accounts for unsteadiness and complicated flow patterns, which cannot be captured in a RANS simulation. Modeling is restricted only to smaller scales which are universal in nature and unaffected by boundary conditions of the flow. In addition to the numerical grid size, the filter size is also a parameter in LES. Nevertheless, LES of turbulent combustion is a rapidly advancing field of research, a review of which is provided by Pitsch (2006). LES being the approach used in the current work is described in more detail in Chapters 3 and 4.

1.1.3 Vortex Methods

In the Navier-Stokes formulation, the pressure term must be solved by a separate elliptic equation, and the convection term often imposes severe time step limits in order to maintain stability. An alternative approach is to consider the problem in the vorticity field. Vortex methods are based on the discretization of the vorticity field into a finite number of vortex points or blobs which are tagged and traced at each time (Lagrangian approach).

Two of the benefits of the vortex methods are the absence of the pressure term and the automatic satisfaction of the continuity equation. The equations are now only dependent on vorticity and velocity. This greatly simplifies some numerical methods designed to solve the Navier-Stokes equations. A vortex method, then, is characterized by both the use of the Navier-Stokes (or Euler) equations in vorticity-velocity form, and by a Lagrangian discretization of the vorticity.

In flows with minimal viscous diffusion, another advantage of the vorticity formulation manifests itself. In these flows, the volume of fluid with significant vorticity magnitude is typically a small fraction of the total flow volume. This means that the flow can be represented in a more compact form by vorticity than is possible with velocity. This fact lends support to computational methods using vorticity.

Comparisons with Eulerian finite-difference schemes has shown that vortex methods can be faster by up to an order of magnitude, even when the volume is completely filled with vorticity (Ould-Salihi et al., 2000); most of the benefit being due to longer time steps allowed by the increased stability of the vortex method.

Direct numerical simulations (DNS) using vortex methods can be found in Leonard (1980), Inoue and Leonard (1987). Reynolds Averaged Navier-Stokes (RANS) simulations with vortex methods can be found in Baig and Milane (2004). Examples of Large Eddy simulation (LES) using vortex methods are found in Lin and Pratt (1987), Mansfield et al. (1998), Milane and Nourazar (1995, 1997) and Wang and Milane (2006).

1.1.3.1 Vortex-In-Cell

A vortex-in-cell scheme can be used to determine the velocity field, instead of the individual element velocities, as direct integration of the vorticity in Lagrangian scheme would produce. VIC is a pure PM (particle-mesh) algorithm, and is an extension of the Cloud-in-cell (CIC) algorithm. Birdsall and Fuss (1969) introduced the Cloud-in-cell method for plasma particle flows. The governing equations for these flows are very similar to those of the stream function equations, as both rely heavily on potential theory. The first particle-in-cell method (Harlow, 1956) was for hydrodynamic problems: it used a zero-size particle and nearest-grid-point method and did not use a Poisson equation. First, the elements' vorticities are placed onto a temporary grid. From this vorticity field, the velocity field is solved using either the vorticity-stream function formulation or the vorticity-velocity formulation, The vorticity-stream function formulation requires one solution to the Poisson equation for the 2D case, and three for the 3D case, whereas, the vorticity-velocity formulation requires two solutions of Poisson's equation for two-dimensional flow and three for three-dimensional flow. Christiansen (1973) first applied the VIC method to fluid flow problems, using a code developed for the simulation of the Kelvin-Helmholtz instability in two dimensions. He used the streamfunction approach. Wang and Milane (2006) have used VIC method for their Large Eddy Simulation of the planar mixing layer.

1.1.4 Turbulent Combustion

Combustion may occur in single-phase (gaseous fuel), two phases (liquid fuel) or three (solid fuel). This introduces additional phenomena such as breakdown of the liquid sheets, vaporization and droplet combustion. Based on the physical configuration, single-phase gaseous combustion can be broadly classified as premixed, non-premixed, and partially premixed. Only non-premixed single-phase gaseous combustion will be described, since that is the only concern in this thesis. Molecular level mixing of the fuel and oxidizer is essential to combustion in non-premixed systems. Turbulent mixing increases the scalar variance but only molecular diffusion enables formation of a combustible mixture where the chemical reactions occur. Chemical and fluid mechanical time scales play a crucial role in turbulent combustion. The ratio of a characteristic mixing time scale to a characteristic chemical time scale defines a Damköhler number. Different combustion regimes can be classified based on this non-dimensional parameter. For large Da, the chemical time scales are very small, causing reaction to occur in infinitely thin sheets. Turbulence causes wrinkling or distortion of these flame sheets. For small values of Da, the reaction zones will be spread throughout the domain.

Turbulent combustion involves a wide range of strongly coupled physical phenomena: heat releasing chemical reactions, molecular level diffusion of heat and species, turbulent convection, and thermodynamics. In general, equations for mass and momentum conservation, species and energy conservation equations, and an equation of state constitute governing equations for any combustion problem. These are a set of nonlinear, coupled partial differential equations that must be solved simultaneously, with appropriate initial and boundary conditions. The fluid mechanical properties must be well known to accurately describe mixing between reactants and in general, all transport phenomena occurring in turbulent flames. Detailed chemical reaction schemes are necessary to estimate fuel consumption rate, product and pollutant formation. Turbulence contains a wide range of space and time scales. Convection, diffusion and reaction processes interact on all these scales, which makes their exact treatment in a numerical simulation practically impossible. Simplifying assumptions are typically made based on the practical situation being modeled and on the relevant quantities and processes of importance.

1.2 Objectives

This thesis is part of ongoing research aimed at applying the VIC to the simulation of reacting mixing layer to study the effect of heat release on flame propagation and turbulence. The main objective of this thesis is twofold: first, to extend the code used by Wang (2005) to account for the isothermal reacting mixing layer flow, and second, to adjust and validate the same code for a low Mach number thermal mixing layer. The simulation of the reacting mixing layer with heat release will be left to future work.

From this main objective, a number of sub-objectives have been derived:

1- The Large Eddy Simulation (LES) scheme for the mixing layer developed by Wang (2005) based on the filtered vorticity transport equation formulated using the diffusion-velocity method in conjunction with FDF transport equation for passive scalar is extended to simulate the isothermal reacting mixing layer and to predict the flow field and the reactive scalar field. Results of the reacting mixing layer are compared with the experimental data of Masutani and Bowmann (1986) and with the LES results of Zhou and Pereira (2000).

2- Both the Smagorinsky and Dynamic Eddy Viscosity SGS models are used to model the effects of subgrid scale fluctuations. The effect of SGS models on the statistical results will be investigated.

3- The effect of Damköhler number on the isothermal reacting mixing layer will be studied by comparing results of different simulations with different mixture fraction.

4- For the thermal mixing layer, a low Mach number Large Eddy Simulation (LES) scheme is devised based on the filtered mass weighted vorticity transport equation formulated using the diffusion-velocity method in conjunction with FMDF transport equation for active scalar to predict the velocity and scalar fields. The Smagorinsky SGS model is used to model the effects of subgrid scales fluctuations. Results of the thermal mixing layer are compared with the experimental data of Mizuno et al. (2005).

5- The effect of enthalpy difference between the two free-steams on the flow field will be investigated.

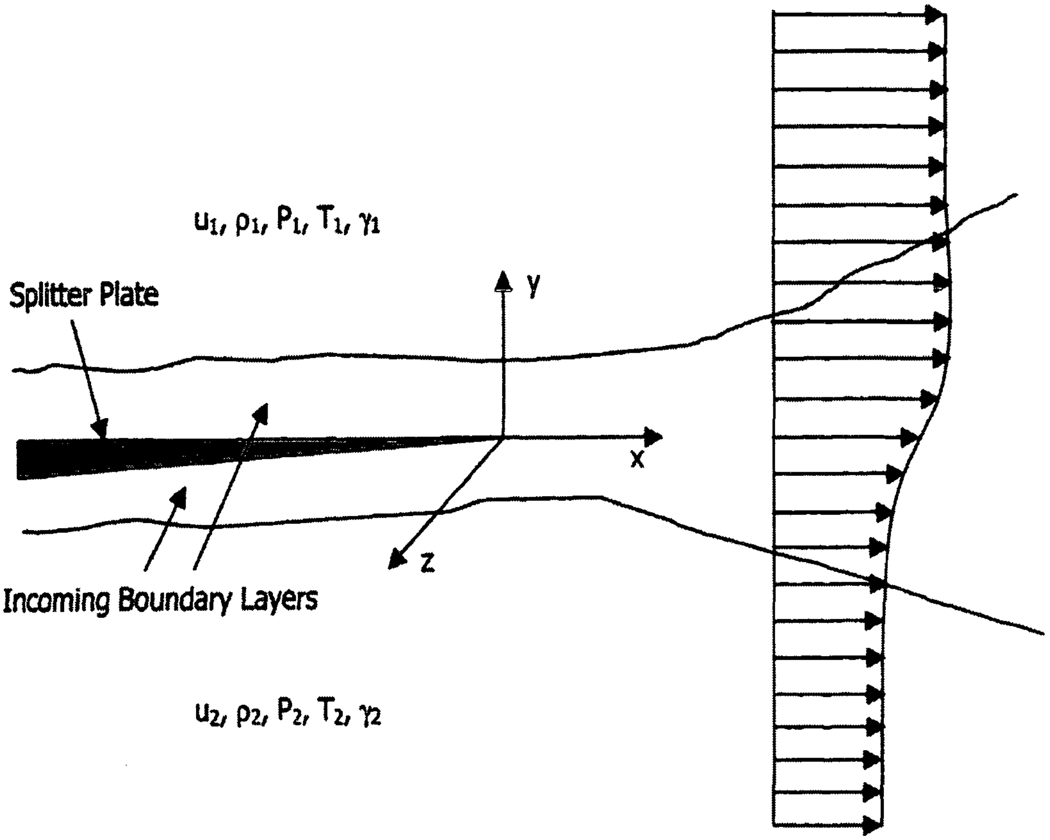

Figure 1-1: Schematic of a mixing layer.

Chapter 2

LITERATURE SURVEY

In this chapter, the relevant literature on experiments and numerical simulation of non-reacting and reacting flows, with and without heat release, related to the present study will be reviewed. The studies that apply LES to vortex methods simulation are introduced in Section 2.1. Also, the diffusion velocity method is reviewed in Section 2.2. The governing vorticity equation includes a baroclinic generation source term; related works are reviewed in Section 2.3. Relevant closure models used to solve for the chemically reacting flows are discussed in Section 2.4. Those include the probability density function which is implemented in the present study and hence is reviewed in Section 2.5. Previous contributions studying the thermal effects on the turbulence structure in mixing layers are summarized in Section 2.6.

Also the terminologies encountered in the literature and in the present study used to describe the interaction between the scalar and the flow fields are clarified. Scalar fields that do not affect pressure, density or velocity fields will be termed passive, while those that do will be called active. Scalar fields having a chemical source term of finite or infinite rate will be termed reactive.

2.1 Large Eddy Simulation in Vortex Methods

Large Eddy Simulation in vortex methods based on a Lagrangian approach (particle representation) was developed by (Mansfield et al., 1998). The authors filtered the vorticity transport equation and modeled the subgrid scale (SGS) velocity and vorticity fluctuations using the dynamic eddy viscosity model. The method was validated using a forced homogeneous, isotropic turbulence flow.

Previously, Milane and Nourazar (1995, 1997) used the core spreading technique to simulate the diffusion equation in the context of LES where the eddy viscosity SGS vorticity model (Mansour et al., 1979) and the SGS turbulent kinetic energy model (Bardina et al., 1980) were tested, respectively. The core spreading technique is valid in the limit of small viscosity (Greengard et al., 1985; Cottet and Koumoutsakos, 2000). Cottet (1996) developed a subgrid scale model based on an analysis of the truncation error of the filtered vorticity equation by removing all the backscatters produced by the flow strain. The author used the particle strength exchange (PSE) method to model subgrid scales. The method was validated using a two dimensional decaying turbulence. It is noted that the PSE method was developed by Degond and Mas-Gallic (1989) to simulate the diffusion term. The method consists of modifying the strength of the particles (Lagrangian scheme) using the integral approximation for the solution of the diffusion equation. In another development, Wang and Milane (2006) used the diffusion velocity method to solve for the diffusion term and to model the eddy viscosity subgrid scale. The method was validated using a two dimensional mixing layer. Results are in agreement with previous numerical simulation. A review of the method is presented in the next section.

2.2 Diffusion Velocity Method

The diffusion velocity method is an alternative way for simulating the diffusion equation. In this method, the viscous diffusion is produced by the vortices' movement induced by the diffusion velocities at which the vortices are carried following the procedure of vortex method. Originally, Ogami and Akamatsu (1991) introduced the method as an alternative to the random walk solution of the diffusion equation in order to solve flows with low Reynolds number values. The authors showed that the diffusion-velocity method can solve problems such as separation and reattachment of the boundary layer without use of the boundary layer theory. Lacombe and Mas-Gallic (1999) proved the existence and uniqueness result of the diffusion velocity method by solving the one-dimensional, two-dimensional and three-dimensional Navier-Stokes equations. Beaudoin et al. (2003) used the diffusion velocity method as an alternative to PSE method and concluded that for anisotropic diffusion problems the method is easier to implement than the PSE method. Recently, Milane (2004) showed that the diffusion velocity method can be extended to an Eddy-viscosity-based LES formulation and can simulate the dissipative effect of the subgrid scale model.

2.3 Baroclinic Generation of Vorticity

In general, the evolution of vorticity can be broken into contributions from advection (as vortex tubes move with the flow), stretching and twisting (as vortex tubes are pulled or twisted by the flow), and baroclinic vorticity generation which occurs whenever surfaces of constant density (isopycnic surfaces) and surfaces of constant pressure (isobaric surfaces) are not aligned, i.e. when there is a density gradient along surfaces of constant pressure. If a vortex sheet exhibits no surface tension or baroclinic source terms its vortex sheet strength remains constant over its entire surface. That restriction is broken for baroclinic flows in which the vortex sheet strength will vary with the amount of vorticity generated or destroyed.

Baroclinic flows are common in multi-fluid research. Esmaeeli and Tryggvason (2004) demonstrated a 3D front-tracking method of multi-fluid flow with phase change applied to film boiling simulations on a horizontal cylinder and multiple cylinders. Wang and Khoo (2004) used a boundary element method to determine the motion of a multi-fluid interface for simulations of bubbles underwater. De Sousa et al (2004) used an Eulerian Navier-Stokes with a front-tracking method to compute multi-fluid flows in three-dimensional simulation of static and rising bubbles. Baker and Beale (2004) computed the two-dimensional motion of an interface separating two incompressible and inviscid fluids using a vortex method.

Knio and Ghoneim (1992) simulated a three-dimensional mixing layer with density ratio of 2 using the vortex method together with the transport element method to follow the density stratification. The fluid acceleration was much higher than gravitational acceleration; hence the baroclinic source term did not contain the gravity term and as such was written in terms of the fluid acceleration only. A two-dimensional vortex sheet method was used by Reinaud et al. (1999) to simulate a variable-density mixing layer. Gravity was also neglected and baroclinic effects were produced by the local acceleration.

Chang et al. (1996) used a level set two-dimensional vorticity-based method to compute the motion of interfaces tracking large density jumps. The method was validated for the merging of two bubbles with same and different densities. Zhang and Ghoneim (1996) used a transport element method to compute the spread and dispersion of an axisymmetric dense gas cloud following its sudden release. Baroclinic vorticity generation is encountered in flows with temperature variations and also in chemically reactive flows with heat release; related works will be reviewed in Section (2.6).

2.4 Chemical Reaction Closure Models

In simulating combustion, simplifications can be made in certain cases by assuming separation between turbulence time scales and chemical time scales. To that purpose, the Damköhler number (Da) defined as the ratio of a characteristic mixing time to a characteristic chemical time is used to characterize combustion. For very large values of Da, when chemical reactions can be considered infinitely fast, reactants are assumed to be in chemical equilibrium. This leads to the conserved scalar formalism (Bilger, 1980) in non-premixed combustion, which reduces a reacting flow situation to a mixing problem. For large Da number, i.e. when the chemistry is not infinitely fast but still fast compared to turbulent mixing, reactions occur in a thin sheet near the stoichiometric surface. The turbulent flame, in such cases, is viewed as an ensemble of laminar flame elements called flamelets. A simple reactive-diffusive balance, in terms of the conserved scalar, parameterized by the scalar dissipation rate describes each flamelet accurately. The flamelet concept has been reviewed by Peters (1984) and Peters (1986). Another approach called Conditional Moment Closure (CMC) was provided independently by Klimenko (1990) and Bilger (1993). They suggested that instead of considering conventional averages, the reactive scalars should be conditioned on mixture fraction for non-premixed combustion.

Knio and Ghoniem (1990) extended the transport element method to treat chemically reactive flow using a single-step reaction mechanism in conjunction with the vortex method. The method was validated for a two-dimensional mixing layer with a wide range of Da. In a subsequent work, Knio and Ghoniem (1992) extended the method to a three-dimensional mixing layer flow under the limitation of infinite-rate kinetics and infinitely-small heat release. Recently, Lakkis and Ghoniem (2003) developed a method based on the vortex method in conjunction with a conserved scalar equation, i.e. the Schvab-Zeldovich formulation for high Da number to model combustion. The method was validated for an axisymmetric vortex ring.

For intermediate range of Da number, turbulence-chemistry interactions are important. Therefore it becomes necessary to model turbulence-chemistry interactions with reasonable details. The flamelet (Sanders et al., 1997), CMC (Barlow et al., 1999), transport element method and the Schvab-Zeldovich formulation have been used to model combustion, however the probability density function method (PDF) (Pope, 2000) is another approach to deal with situations involving finite rate chemistry.

2.5 Probability Density Function (PDF)

One method used to solve the problem of turbulent reacting flows is the probability density function method (PDF) which has been widely used for many years (Pope, 2000). The inherent advantage of the PDF method is that any complex chemistry can be treated exactly. Furthermore from the numerical stand point, the transported PDF methods pose high dimensionality. Hence, conventional finite volume or finite difference methods are not computationally viable. The PDF transport equations are therefore solved in a Lagrangian frame-work using Monte-Carlo methods (Pope, 1985). The PDF is represented in discrete form by a large number of stochastic particles. Particle properties evolve in time such that their distribution is equivalent to the PDF at all times (Pope, 1994). The advantage of Monte-Carlo simulations is that their memory requirements depend linearly on the dimensionality of the problem. Whereas, their efficiency, as any statistical model, scales with the square-root of the number of PDF particles considered. Therefore to double the accuracy, the number of particles must be increased fourfold. In the context of LES with isothermal, constant density reacting flow, Colucci et al. (1998) developed the method using the momentum equation and the filtered density function (FDF). The method was validated for two-dimensional reacting jet flow and two-dimensional and three-dimensional mixing layers. Later on, the method was extended to a low Mach number, variable density reacting flows by (Jaberi et al., 1999) using the Filtered Mass Density Function (FMDF). The method was validated for two-dimensional reacting jet flow and two-dimensional and three-dimensional mixing layers. Zhou and Pereira (2000) implemented the FDF developed by Colucci et al. (1998) to investigate the two-dimensional, gas-phase, spatially developing, reacting and non-reacting, constant-density, plane mixing layer in a flow regime prior to the mixing transition similar to the experiment of Masutani and Bowmann (1986). The FDF results showed satisfactory agreement with experimental measurements.

2.6 Thermal Effect on Reactive and Non-Reactive Mixing Layers

Numerous studies have examined aspects of the organized structure in the mixing layer, and from these the mixing layer has gained popularity as a canonical turbulent free shear flow. Those aspects of mixing layers having received significant attention include effects of the free-stream densities on the growth rate of incompressible non-reacting turbulent mixing layers. Brown (1974) used similarity variables to derive an expression for the effect of the free-stream density ratio ρ_2/ρ_1 and free-stream velocity ratio U_2/U_1 on the growth rate of temporally developing mixing layers. Dimotakis (1986) obtained a similar expression for the growth rate in spatially developing turbulent mixing layers. The latter showed good agreement with experimentally measured growth rates in isothermal mixing layers over a wide range of density ratios and speed ratios (e.g. Brown and Roshko 1974; Dimotakis 1991) and with numerical simulations of non-reacting turbulent mixing layers (e.g. Soteriou and Ghoneim, 1995).

The presence of such density effects even in isothermal mixing layers strongly suggests that density changes due to heat release will also affect the flow. The density changes that occur in exothermic reacting turbulent mixing layers produce local baroclinic generation of vorticity, as well as dilatation, which together lead to the overall heat release effects. The strong heat release typical in turbulent combustion affects the turbulent flow field mainly by reducing the density, increasing the kinematic viscosity and, secondarily, by altering the local pressure gradient. Exactly how these influences occur, however, is not well understood and it is not immediately obvious if the effect of heat release should be to increase or decrease the growth rate of the flow. The dilatation due to exothermicity might suggest an increase in the growth rate with increasing heat release. However, experiments by Wallace (1981) at relatively low levels of heat release, producing adiabatic temperature rises of less than 400 °K, suggested a slight decrease in the layer growth rate with increasing heat release. Hermanson and Dimotakis (1989) subsequently used a hydrogen–fluorine mixing layer to produce adiabatic flame temperatures rises up to 940 °K. Even with this larger heat release, they found that the growth rate of the layer decreased slightly with increasing heat release, up to 15% at their highest flame temperatures.

Several numerical studies have examined the effects of various mechanisms that occur due to heat release, such a baroclinic generation and dilatation, on the detailed fluid dynamics within exothermic reacting turbulent mixing layers. Ghoniem, et al. (1988) have used a transport element method to investigate reacting mixing layers, and McMurtry, et al. (1989) used direct numerical simulations (DNS) of a temporally developing turbulent mixing layer to investigate effects of heat release. Their results also confirmed the decrease in layer growth rate and entrainment ratio with heat release. Sekar and Mukunda (1990) conducted a DNS study of compressible reacting turbulent mixing layers with heat release, and also observed similar reductions in growth rate and entrainment rate due to heat release. Dahm (2005) showed that the reduced growth rate and entrainment properties noted above, which result from density variations within the mixing layer produced by the temperature rise due to exothermic reaction, are quantitatively consistent with changes due to the free-stream density ratio in non-reacting mixing layers. Tacina and Dahm (2000) suggested the "equivalence principle" stating that density changes due to exothermic reaction can be related to an equivalent non-reacting mixing layer, in which the temperature of one of the free-stream fluids is raised to an effective value determined by the peak temperature and the overall stoichiometry.

In a recent experiment, Mizuno et al. (2005) developed a measurement procedure using a two-component LDV combined with a fine cold-wire thermometer to investigate the measurement of the turbulent heat flux in thermal mixing layer, with the aim of simulating the thermal mixing in HVAC unit, where hot air heated by a heater-core and cold air cooled by an evaporator is mixed to control the air temperature blown into the compartment. Their results indicated that self similar profiles for the mean velocity and the root-mean-square velocity fluctuations are not reached within the length of their measurement domain.

It is noted that a considerable amount of work has been performed to understand the flow evolution and mixing of scalars in uniformly sheared flow with small temperature difference as done by La Rue et al. (1981), Ma and Warhaft (1986) and Ferchichi and Tavoularis (1992). These works provide important information on statistics of mixture fraction and temperature dissipation for passive scalars.

2.7 Outline of This Document

The thesis is organized as follows. In Chapter 3, the low Mach number governing equations, boundary conditions and methodologies used to simulate the thermal mixing layer are developed. The governing equations, boundary conditions and methodologies used to solve the incompressible isothermal reacting flow are presented in Chapter 4. Finally, results from the isothermal reacting mixing layer and the thermal mixing layer simulations are presented and validated in Chapters 5 and 6 respectively. Conclusions are summarized in Chapter 7, together with directions for future work.

Chapter 3

FORMULATION FOR COMPRESSIBLE NON-REACTIVE FLOW AND SCALAR FIELDS

In this chapter, the formulations of the fully compressible vorticity and energy equations are derived along with the compressible filtering, the associated SGS and mixing models. For flows with considerable temperature and density variations, the full compressible formulations have to be used even for low Mach number regimes, e.g. low subsonic thermal mixing layer. The flow field governing equations and modeling are presented in Section 3.1. The scalar field governing equations and modeling are discussed in Section 3.2. The initial and boundary conditions for the thermal mixing layer under study are presented in Section 3.3. Solution algorithms for the flow and scalar field are stated in Section 3.4.

3.1 Flow Field

The continuity equation for the variable density flow is

$$\frac{\partial \rho}{\partial t} + \frac{\partial \rho \boldsymbol{u}_i}{\partial \boldsymbol{x}_i} = 0 \tag{3.1}$$

where ρ is the density and $\boldsymbol{u}_i$ is the velocity vector. By developing the terms another form for the continuity equation is obtained as

$$\frac{D\rho}{Dt} + \rho \frac{\partial \boldsymbol{u}_i}{\partial \boldsymbol{x}_i} = 0 \tag{3.2}$$

The vorticity equation (Green, 1995) is

$$\frac{D\vec{\boldsymbol{\omega}}}{Dt} = -\vec{\boldsymbol{\omega}}(\nabla.\vec{\boldsymbol{u}}) + (\vec{\boldsymbol{\omega}}.\nabla)\vec{\boldsymbol{u}} + \frac{1}{\rho}\nabla\rho \times \left(\vec{g} - \frac{D\vec{\boldsymbol{u}}}{Dt}\right) + \nu\nabla^2\vec{\boldsymbol{\omega}} + \nabla \times \vec{g} \tag{3.3}$$

where, in Eq. 3.3, the first term on the left hand side (LHS) is the time rate of change of vorticity following a vortex element, the first term on the right hand side (RHS) represents the change of vorticity arising from fluid expansion, the second term on the RHS is the vortex stretching term and is equal to zero for the two dimensional flow, the third term on the RHS is the combination of the baroclinic term, which causes the reduction/generation of vorticity due to misalignment of density gradient and pressure gradient lines, and the shear stress variations in a density gradient flow, the fourth term on the RHS represents the diffusion of vorticity due to the action of viscosity, and the last term represents the gravity effect, where the gravity field $\vec{\mathrm{g}}$ is a potential field and hence its curl $\nabla \times \vec{\mathrm{g}}$ is equal to zero by definition. For a two-dimensional flow with negligible gravity field, the vorticity equation becomes

$$\frac{D\omega}{Dt} = -\omega(\nabla.\vec{\mathbf{u}}) - \frac{1}{\rho}\nabla\rho \times \left(\frac{\mathrm{D}\vec{\mathbf{u}}}{\mathrm{Dt}}\right) + \nu\nabla^2\omega \tag{3.4}$$

Furthermore, assuming the kinematic viscosity ν = constant and developing the terms in Eq. 3.4 to obtain

$$\frac{\partial\omega}{\partial t} + \boldsymbol{u}_j\frac{\partial\omega}{\partial\boldsymbol{x}_j} = -\omega\frac{\partial\boldsymbol{u}_i}{\partial\boldsymbol{x}_i} - \frac{1}{\rho}\nabla\rho \times \left(\frac{\partial\boldsymbol{u}_i}{\partial t} + \boldsymbol{u}_j\frac{\partial\boldsymbol{u}_i}{\partial\boldsymbol{x}_j}\right) + \nu\nabla^2\omega \tag{3.5}$$

Multiplying by ρ, the equation becomes

$$\rho\frac{\partial\omega}{\partial t} + \rho\boldsymbol{u}_j\frac{\partial\omega}{\partial\boldsymbol{x}_j} = -\rho\omega\frac{\partial\boldsymbol{u}_i}{\partial\boldsymbol{x}_i} - \nabla\rho \times \left(\frac{\partial\boldsymbol{u}_i}{\partial t} + \boldsymbol{u}_j\frac{\partial\boldsymbol{u}_i}{\partial\boldsymbol{x}_j}\right) + \rho\nu\nabla^2\omega \tag{3.6}$$

Introducing ρ in the derivatives on the right hand side of the equation, the vorticity equation is

$$\begin{aligned}\frac{\partial\rho\omega}{\partial t} + \frac{\partial\rho\boldsymbol{u}_j\omega}{\partial\boldsymbol{x}_j} - \omega\left(\frac{\partial\rho}{\partial t} + \boldsymbol{u}_j\frac{\partial\rho}{\partial\boldsymbol{x}_j} + \rho\frac{\partial\boldsymbol{u}_j}{\partial\boldsymbol{x}_j}\right) \\ = -\rho\omega\frac{\partial\boldsymbol{u}_i}{\partial\boldsymbol{x}_i} - \nabla\rho \times \left(\frac{\partial\boldsymbol{u}_i}{\partial t} + \boldsymbol{u}_j\frac{\partial\boldsymbol{u}_i}{\partial\boldsymbol{x}_j}\right) + \mu\nabla^2\omega\end{aligned} \tag{3.7}$$

Using the continuity equation, the third group of terms on LHS is nil and the vorticity equations becomes

$$\frac{\partial\rho\omega}{\partial t} + \frac{\partial\rho\boldsymbol{u}_j\omega}{\partial\boldsymbol{x}_j} = -\rho\omega\frac{\partial\boldsymbol{u}_i}{\partial\boldsymbol{x}_i} - \nabla\rho \times \left(\frac{\partial\boldsymbol{u}_i}{\partial t} + \boldsymbol{u}_j\frac{\partial\boldsymbol{u}_i}{\partial\boldsymbol{x}_j}\right) + \mu\nabla^2\omega \tag{3.8}$$

3.1.1 The Filtered Vorticity Equation

The LES equations are obtained by applying a low-pass spatial filter G of width Δ to the vorticity transport equation. This eliminates scales smaller than Δ. Mathematically, the filtered field for any quantity $\phi(x, y, t)$, is given by

$$\bar{\phi} = \iint \phi(\zeta,\eta,t)\, G(x-\zeta, y-\eta)\, d\zeta\, d\eta \tag{3.9}$$

Such a filter will be called a "bar-filter." Scales of motion are then decomposed into a gridscale $\bar{\phi}$ and subgrid-scale part ϕ'.

3.1.1.1 Favre Filtering

If the basic bar-filter is applied to the compressible continuity equation, the term $\overline{\rho \boldsymbol{u}_j}$ appears, hence the necessity to introduce a corresponding subgrid term $\left(\overline{\rho \boldsymbol{u}_j} - \bar{\rho}\bar{\boldsymbol{u}}_j\right)$ in the continuity equation, that require its own modeling. It is, however, possible and also more common to formally avoid the occurrence of a subgrid term in the continuity equation by selecting a "mass-weighted" filter, called Favre filter, and defined as

$$\tilde{\phi}(x,y,t) = \frac{\iint \rho(\zeta,\eta,t)\, \phi(\zeta,\eta,t)\, G(x-\zeta, y-\eta)\, d\zeta\, d\eta}{\iint \rho(\zeta,\eta,t)\, G(x-\zeta, y-\eta)\, d\zeta\, d\eta} \tag{3.10}$$

where G(x,y) is the spatial filter shape. For a two dimensional flow, the velocity and vorticity fields are decomposed in the filtered field (over-line for the bar-filtering and over-tilde for the Favre filtered quantities), and the subgrid scale field (superscript ′ for bar-filtering and superscript ″ for Favre-filtered quantities). While the use of Favre filtering simplifies the form of the filtered equations, it introduces ambiguities, because an exact relationship between the $\tilde{\phi}$ and $\bar{\phi}$ is difficult to obtain, and approximations have to be made. Consequently, the flow statistics may be hard to compare with the experimental ones unless the subgrid scale terms are small. The Favre-filtered velocity is defined as

$$\tilde{\mathbf{u}} = \frac{\overline{\rho \mathbf{u}}}{\bar{\rho}}$$

along with the fluctuation defined as $\mathbf{u}'' = \mathbf{u} - \tilde{\mathbf{u}}$. Therefore, the flux vector in the compressible continuity equation is expressed as $\overline{\rho \boldsymbol{u}} = \bar{\rho}\tilde{\boldsymbol{u}}$. For the case where compressibility effects are small, i.e. the density shows negligible variations, $\tilde{u} \rightarrow \bar{u}$. Overall, any flow variable ϕ can be decomposed in two ways as

$$\phi = \bar{\phi} + \phi' = \tilde{\phi} + \phi''$$

where $\bar{\phi}$ and ϕ' are the bar filtered large scale and subgrid scale variables, and $\tilde{\phi}$ and ϕ'' are the Favre filtered large scale and subgrid scale variables, respectively.

3.1.1.2 Favre Filtered Governing Equations

Filtering the continuity equation (Eq.3.1)

$$\overline{\frac{\partial \rho}{\partial t} + \frac{\partial \rho \boldsymbol{u}_i}{\partial \boldsymbol{x}_i}} = 0 \tag{3.11}$$

Using the filter linearity property, $\overline{\varphi + \psi} = \bar{\varphi} + \bar{\psi}$, the continuity is written as

$$\overline{\frac{\partial \rho}{\partial t}} + \overline{\frac{\partial \rho \boldsymbol{u}_i}{\partial \boldsymbol{x}_i}} = 0 \tag{3.12}$$

Employing the commutation with derivation, $\overline{\frac{\partial \varphi}{\partial x}} = \frac{\partial \bar{\varphi}}{\partial x}$ to get

$$\frac{\partial \bar{\rho}}{\partial t} + \frac{\partial \overline{\rho \boldsymbol{u}_i}}{\partial \boldsymbol{x}_i} = 0 \tag{3.13}$$

Using the Favre filtering, i.e. $\overline{\rho u_i} = \bar{\rho}\tilde{u}_i$, the final form of the continuity equation is

$$\frac{\partial \bar{\rho}}{\partial t} + \frac{\partial}{\partial \boldsymbol{x}_i}(\bar{\rho}\tilde{\boldsymbol{u}}_i) = 0 \tag{3.14}$$

Furthermore filtering the vorticity transport equation (Eq. 3.8)

$$\overline{\frac{\partial \rho\omega}{\partial t} + \frac{\partial \rho \boldsymbol{u}_j \omega}{\partial \boldsymbol{x}_j} = -\rho\omega\frac{\partial \boldsymbol{u}_i}{\partial \boldsymbol{x}_i} - \nabla p \times \left(\frac{\partial \boldsymbol{u}_i}{\partial t} + \boldsymbol{u}_j\frac{\partial \boldsymbol{u}_i}{\partial \boldsymbol{x}_j}\right) + \mu\nabla^2\omega} \tag{3.15}$$

Using the filter linearity property, Eq. 3.15 is written as

$$\frac{\partial \overline{\rho\omega}}{\partial t} + \frac{\partial \overline{\rho \boldsymbol{u}_j \omega}}{\partial \boldsymbol{x}_j} = -\overline{\rho\omega \frac{\partial \boldsymbol{u}_i}{\partial \boldsymbol{x}_i}} - \overline{\nabla\rho \times \left(\frac{\partial \boldsymbol{u}_i}{\partial t} + \boldsymbol{u}_j \frac{\partial \boldsymbol{u}_i}{\partial \boldsymbol{x}_j}\right)} + \overline{\mu\nabla^2\omega} \tag{3.16}$$

Using the decomposition $\overline{\rho \mathbf{u}_j \omega} = \bar{\rho}\tilde{\mathbf{u}}_j\tilde{\omega} + (\overline{\rho \mathbf{u}_j \omega} - \bar{\rho}\tilde{\mathbf{u}}_j\tilde{\omega})$, where the first term is the LES grid-resolved convective flux of $\mathbf{x}_i$-momentum and the second term is the corresponding SGS contribution (Sagaut, 2002). Also, using the decomposition for the dilatation, the baroclinic generation and the diffusion term, Eq. 3.16 is written as

$$\begin{aligned}\frac{\partial \bar{\rho}\tilde{\omega}}{\partial t} + \frac{\partial \bar{\rho}\tilde{\boldsymbol{u}}_j\tilde{\omega}}{\partial \boldsymbol{x}_j} + \frac{\partial \bar{\rho}\widetilde{\boldsymbol{u}_j\omega}}{\partial \boldsymbol{x}_j} - \frac{\partial \bar{\rho}\tilde{\boldsymbol{u}}_j\tilde{\omega}}{\partial \boldsymbol{x}_j}&\\ = -\bar{\rho}\tilde{\omega}\frac{\partial \tilde{\boldsymbol{u}}_i}{\partial \boldsymbol{x}_i} - \nabla\bar{\rho} \times \left(\frac{\partial \tilde{\boldsymbol{u}}_i}{\partial t} + \tilde{\boldsymbol{u}}_j \frac{\partial \tilde{\boldsymbol{u}}_i}{\partial \boldsymbol{x}_j}\right) + \mu\nabla^2\tilde{\omega}&\\ + \left(-\overline{\rho\omega\frac{\partial \boldsymbol{u}_i}{\partial \boldsymbol{x}_i}} + \bar{\rho}\tilde{\omega}\frac{\partial \tilde{\boldsymbol{u}}_i}{\partial \boldsymbol{x}_i}\right)&\\ + \left(-\overline{\nabla\rho \times \left(\frac{D\boldsymbol{u}}{Dt}\right)} + \nabla\bar{\rho} \times \left(\frac{\partial \tilde{\boldsymbol{u}}_i}{\partial t} + \tilde{\boldsymbol{u}}_j \frac{\partial \tilde{\boldsymbol{u}}_i}{\partial \boldsymbol{x}_j}\right)\right) + \left(\overline{\mu\nabla^2\omega} - \mu\nabla^2\tilde{\omega}\right)&\end{aligned} \tag{3.17}$$

Using continuity, the final form of the Favre-filtered vorticity equation is

$$\begin{aligned}\frac{\partial \tilde{\omega}}{\partial t} + \tilde{\boldsymbol{u}}_j \frac{\partial \tilde{\omega}}{\partial x_j} = -\tilde{\omega}\frac{\partial \tilde{\boldsymbol{u}}_i}{\partial \boldsymbol{x}_i} - \frac{1}{\bar{\rho}}\nabla\bar{\rho} \times \left(\frac{\partial \tilde{\boldsymbol{u}}_i}{\partial t} + \tilde{\boldsymbol{u}}_j \frac{\partial \tilde{\boldsymbol{u}}_i}{\partial \boldsymbol{x}_j}\right) + \nu\frac{\partial^2\tilde{\omega}}{\partial x_i}&\\ - R_{ij} - B_{ij} - D_{ij} + V&\end{aligned} \tag{3.18}$$

where R_{ij} is the subgrid scale vorticity stress which accounts for the effects of the unresolved velocity and vorticity fluctuations.

$$R_{ij} = \frac{\delta}{\delta x_j}\left(\widetilde{\boldsymbol{u}_j\omega} - \tilde{\boldsymbol{u}}_j\tilde{\omega}\right) \tag{3.19}$$

B_{ij} is the baroclinic subgrid scale term written as,

$$B_{ij} = \frac{1}{\bar{\rho}}\overline{\nabla\rho \times \left(\frac{D\boldsymbol{u}}{Dt}\right)} - \frac{1}{\bar{\rho}}\overline{\nabla\rho} \times \left(\frac{\partial \tilde{\boldsymbol{u}}_j}{\partial t} + \tilde{\boldsymbol{u}}_j \frac{\partial \tilde{\boldsymbol{u}}_i}{\partial \boldsymbol{x}_j}\right) \tag{3.20}$$

D_{ij} is the dilatation subgrid scale term given by,

$$D_{ij} = \frac{1}{\bar{\rho}}\overline{\rho\omega\frac{\partial \boldsymbol{u}_i}{\partial \boldsymbol{x}_i}} - \tilde{\omega}\frac{\partial \tilde{\boldsymbol{u}}_i}{\partial \boldsymbol{x}_i} \tag{3.21}$$

and the viscous subgrid scale term is,

$$V = \overline{\nu\nabla^2\omega} - \nu\nabla^2\tilde{\omega} \tag{3.22}$$

The terms R_{ij}, B_{ij},, D_{ij} and V are modeled as in the next section.

3.1.2 SGS Modeling

The function of subgrid-scale models has been explained by Piomelli (2001): "*In large-eddy simulations, the dissipative scales of motion are resolved poorly, or not at all. The main role of the subgrid scale model must be, therefore, to remove energy from the resolved scales, mimicking the drain that is usually associated with the energy cascade. Thus, it is not necessary for a model to represent the "exact" SGS stresses accurately at each point in space and time, but only to account for their global effect.*"

As suggested in the above quotation (Piomelli 2001), all the subgrid scale terms are modeled using the eddy viscosity model as,

$$R_{ij} + B_{ij} + D_{ij} + V = -\frac{\partial}{\partial \boldsymbol{x}_j}\left(\boldsymbol{\nu}_{t_j}\frac{\partial \tilde{\omega}}{\partial \boldsymbol{x}_j}\right) \tag{3.23}$$

Substituting Eq. 3.23 into Eq. 3.18, the filtered vorticity equation becomes

$$\begin{aligned}\frac{\partial \tilde{\omega}}{\partial t} + \tilde{\boldsymbol{u}}_j\frac{\partial \tilde{\omega}}{\partial \boldsymbol{x}_j} = -\tilde{\omega}\frac{\partial \tilde{\boldsymbol{u}}_i}{\partial \boldsymbol{x}_i} - \frac{1}{\bar{\rho}}\nabla\bar{\rho} \times \left(\frac{\partial \tilde{\boldsymbol{u}}_i}{\partial t} + \tilde{\boldsymbol{u}}_j\frac{\partial \tilde{\boldsymbol{u}}_i}{\partial \boldsymbol{x}_j}\right) + \frac{\partial}{\partial \boldsymbol{x}_j}\left(\nu\frac{\partial \tilde{\omega}}{\partial \boldsymbol{x}_j}\right) \\ + \frac{\partial}{\partial \boldsymbol{x}_j}\left(\boldsymbol{\nu}_{t_j}\frac{\partial \tilde{\omega}}{\partial \boldsymbol{x}_j}\right)\end{aligned} \tag{3.24}$$

3.1.2.1 Subgrid Scale Models

Studying the effect of variable density on the flow field due to dilatation and baroclinic generation of vorticity is the main objective of this study rather than investigating various subgrid models. The SGS terms can be either modeled (Moin et al., 1991) or simply neglected (Erlebacher et al., 1990). In the present work, the SGS terms are modeled using the Smagorinsky eddy-viscosity model used by Wang and Milane (2006).

In this model, the effect of the subgrid scales is modeled purely as an enhanced diffusivity for the large-scale flow. The eddy viscosities ($\nu_{t,j}$) for the Smagorinsky SGS model, in Eq. 3.24 are expressed for an anisotropic flow following Sagaut (2002) as

$$\nu_{t_x} = C_r^2 (\Delta^3)^{\frac{2}{9}} \Delta_x^{\frac{4}{3}} (2S_{ij}S_{ij})^{\frac{1}{2}}$$

$$and \tag{3.25}$$

$$\nu_{t_y} = C_r^2 (\Delta^3)^{\frac{2}{9}} \Delta_y^{\frac{4}{3}} (2S_{ij}S_{ij})^{\frac{1}{2}}$$

Eq. 3.25 has been extended to anisotropic flow by simply using different filter sizes Δ_x and Δ_y in x- and y-directions, respectively, $\Delta = (\Delta_x \Delta_y)^{1/2}$ or $\Delta = \max(\Delta_x, \Delta_y)$, and the modulus of strain rate for 2D flow $|\bar{S}| = (2S_{ij}S_{ij})^{\frac{1}{2}}$ has been calculated by (Wang , 2005) as

$$\begin{aligned} (2S_{ij}S_{ij})^{\frac{1}{2}} &= \left[2\left(\frac{\partial \bar{U}}{\partial y}\right)^2 + \frac{1}{2}\left(\frac{\partial \bar{U}}{\partial y} + \frac{\partial \bar{V}}{\partial x}\right)^2\right]^{\frac{1}{2}} \\ &= \left[2\left(\frac{\partial \bar{V}}{\partial x}\right)^2 + \frac{1}{2}\left(\frac{\partial \bar{U}}{\partial y} + \frac{\partial \bar{V}}{\partial x}\right)^2\right]^{\frac{1}{2}} \end{aligned} \tag{3.26}$$

The SGS model constant depends on the type of the governing equations (vorticity or momentum) and on the type of the SGS model used. In the current study, the constant for the Smagorinsky SGS model has been chosen following the work of (Mansfield, Knio and Meneveau 1998) where the constant $C_r = 0.12$, has been obtained by balancing enstrophy production and dissipation for homogenous and isotropic flow.

3.1.3 Fractional Step

In this work, the method of fractional steps is used to solve the vorticity equation (Eq. 3.24). This method is helpful because it usually reduces the dimensions and order of the equations to a series of substeps (Cottet and Koumoutsakos, 2000). Each substep describes a physical phenomenon in the vorticity equation. In the vortex method, Eq. 3.24 is split into three fractional steps:

$$\frac{\partial \widetilde{\omega}}{\partial t} + \widetilde{\boldsymbol{u}}_j \frac{\partial \widetilde{\omega}}{\partial \boldsymbol{x}_j} = -\widetilde{\omega} \frac{\partial \widetilde{\boldsymbol{u}}_i}{\partial \boldsymbol{x}_i} \tag{3.27}$$

$$\frac{\partial \widetilde{\omega}}{\partial t} = -\frac{1}{\bar{\rho}} \nabla \bar{\rho} \times \left(\frac{\partial \widetilde{u}_i}{\partial t} + \widetilde{\boldsymbol{u}}_j \frac{\partial \widetilde{\boldsymbol{u}}_i}{\partial \boldsymbol{x}_j} \right) \tag{3.28}$$

$$\frac{\partial \widetilde{\omega}}{\partial t} = \frac{\partial}{\partial \boldsymbol{x}_j} \left(\nu \frac{\partial \widetilde{\omega}}{\partial \boldsymbol{x}_j} \right) + \frac{\partial}{\partial \boldsymbol{x}_j} \left(\boldsymbol{\nu}_{t_j} \frac{\partial \widetilde{\omega}}{\partial \boldsymbol{x}_j} \right) \tag{3.29}$$

In the first substep the transport of vorticity due to convection and volumetric expansion (dilatation), is obtained from the solution of Eq. 3.27. In the second substep, the generation of baroclinic vorticity due to pressure-density interactions is obtained by solving Eq. 3.28. In the third substep, diffusion and SGS terms effects are simulated using the diffusion velocity method for Eq. 3.29. The essence of applying the fractional step in vorticity transport equation is that, in the first substep the flow is considered as non-viscous, so that the theorem of conservation of vorticity and circulation could be applied.

3.1.3.1 First Substep

Eq. 3.27 is written for a two-dimensional motion of an incompressible, inviscid and barotropic flow. This equation governs the evolution of vorticity transported by the convection and dilatation of the flow. Eq. 3.27 is satisfied by solving for the velocity using Helmholtz decomposition for a vector field, in which the velocity can be split into two components

$$\tilde{\boldsymbol{u}} = \tilde{\boldsymbol{u}}_{\omega} + \tilde{\boldsymbol{u}}_{D}$$

where the solution for the decomposed velocity is described as follows:

- $\tilde{\boldsymbol{u}}_{w}$ is a solenoidal field i.e.$\nabla.\tilde{\boldsymbol{u}}_{\omega} = 0$, therefore a stream function ψ is defined such that

  $$\tilde{\boldsymbol{u}}_{\omega} = \nabla \times \psi$$

  $$\tilde{u}_{\omega} = \frac{\partial\psi}{\partial y} \; and \; \tilde{v}_{\omega} = -\frac{\partial\psi}{\partial x} \tag{3.30}$$

  With $\tilde{u}_{w}, \tilde{v}_{w}$ are the components of the solenoidal velocity $\tilde{\boldsymbol{u}}_{w}$. For a two-dimensional flow, the vorticity vector reduces to one component in the z-direction perpendicular to the xy-plane (the plane of motion)

  $$\tilde{\omega} = \frac{\partial\tilde{v}}{\partial y} - \frac{\partial\tilde{u}}{\partial x} \tag{3.31}$$

  Combining Eq. 3.30and 3.31, the following Poisson equation is obtained

  $$\nabla^{2}\psi = -\tilde{\omega} \tag{3.32}$$

- $\tilde{\boldsymbol{u}}_D = \nabla\varphi$ is the velocity potential produced by the volumetric expansion of the flow due to the temperature variations and φ is a potential function,

$$\tilde{u}_D = \frac{\partial\varphi}{\partial x} \text{ and } \tilde{v}_D = \frac{\partial\varphi}{\partial y} \tag{3.33}$$

By replacing the velocity decomposition into the continuity (Eq. 3.14) having $\nabla.\tilde{\boldsymbol{u}}_w = 0$ then $\tilde{\boldsymbol{u}}_D$ is obtained by solving the resulting Poisson equation.

$$\nabla^2\varphi = -\frac{1}{\bar{\rho}}\frac{D\bar{\rho}}{Dt} \tag{3.34}$$

3.1.3.2 Second Substep

For barotropic flows, the second substep reduces to $\frac{\partial\tilde{\omega}}{\partial t} = 0$, thus the circulation is constant along a particle path (Kelvin theorem) and the evolution of vorticity and velocity fields are computed using the first and third sub-steps. But for a baroclinic flow where the second sub-step is non-zero, the circulation of each vortex element must be updated each time step. To this end, the rate of change of circulation ($\Gamma = \int_A \omega\, dA$) is obtained from Eq.3.28 as

$$\frac{\partial\tilde{\Gamma}}{\partial t} = \int\limits_A \frac{\partial\tilde{\omega}}{\partial t} dA = -\int\limits_A \left[\frac{1}{\bar{\rho}}\nabla\bar{\rho} \times \left(\frac{\partial\tilde{\boldsymbol{u}}_i}{\partial t} + \tilde{\boldsymbol{u}}_j\frac{\partial\tilde{\boldsymbol{u}}_i}{\partial \boldsymbol{x}_j}\right)\right] dA \tag{3.35}$$

where A is the area. Moreover, according to the low Mach number approximation the density variation is only affected by temperature variation, therefore the equation of state is written as

$$\frac{\nabla\bar{\rho}}{\bar{\rho}} = -\frac{\nabla\tilde{T}}{\tilde{T}}$$

Substituting into Eq. 3.35, to get

$$\frac{\partial \tilde{\Gamma}}{\partial t} = \int_A \left[\frac{\nabla \tilde{T}}{\tilde{T}} \times \left(\frac{\partial \tilde{\boldsymbol{u}}_i}{\partial t} + \tilde{\boldsymbol{u}}_j \frac{\partial \tilde{\boldsymbol{u}}_i}{\partial \boldsymbol{x}_j} \right) \right] dA \tag{3.36}$$

Eq. 3.36 shows the direct relation between the change in temperature and the change of the vortices circulations.

3.1.3.3 Third Substep

Eq. 3.29 governs the effect of diffusion on the transport of vorticity, it can be written after rearranging as

$$\frac{\partial \tilde{\omega}}{\partial t} + \frac{\partial}{\partial \boldsymbol{x}_j} \left[\left(- \frac{\left(\nu + \boldsymbol{\nu}_{t_j} \right)}{\tilde{\omega}} \frac{\partial \tilde{\omega}}{\partial \boldsymbol{x}_j} \right) \tilde{\omega} \right] = 0$$

The term $\left(- \frac{\left(\nu + \nu_{t_j} \right)}{\tilde{\omega}} \frac{\partial \tilde{\omega}}{\partial x_j} \right)$ behaves as a convective velocity

$$\tilde{\boldsymbol{u}}_{diff} = - \frac{\left(\nu + \boldsymbol{\nu}_{tj} \right)}{\tilde{\omega}} \frac{\partial \tilde{\omega}}{\partial \boldsymbol{x}_j} \tag{3.37}$$

where $\tilde{\boldsymbol{u}}_{diff}$ is called the diffusion velocity and is solved following Ogami et al. (1991). The third substep equation is solved using the diffusion velocity method reviewed in Section 2.2.

3.1.4 Discretization of the Equations

The numerical solution of the vorticity transport equation requires obtaining the velocity components at each node. The velocity field is obtained by solving for the two Poisson's equations (Eq. 3.32 and Eq. 3.34). Using a rectangular computational domain with a uniform grid in each coordinate with Δx and Δy being the grid sizes in the x- and y-directions, respectively. Eq. 3.32 is discretized using the extrapolated Liebmann's method with central difference approximation for the spatial derivatives as shown in Abdolhosseini (2000)

$$\psi^{n+1}_{(i,j)} = \frac{1}{2(1+\beta^2)}\left[\psi^{n}_{(i-1,j)} + \psi^{n}_{(i+1,j)} + \beta^2\left(\psi^{n}_{(i,j-1)} + \psi^{n}_{(i,j+1)}\right)\right] + \Delta x^2 \tilde{\omega}_{(i,j)}$$

Similarly, Eq. 3.34 is

$$\nabla^2 \varphi = \frac{1}{\tilde{T}}\frac{D\tilde{T}}{Dt}$$

When expanded it becomes

$$\frac{\partial^2 \varphi}{\partial x^2} + \frac{\partial^2 \varphi}{\partial y^2} = \frac{1}{\tilde{T}}\left(\frac{\partial \tilde{T}}{\partial t} + \tilde{u}\frac{\partial \tilde{T}}{\partial x} + \tilde{v}\frac{\partial \tilde{T}}{\partial y}\right) \tag{3.38}$$

The temperature derivatives are approximated using the explicit scheme and the spatial gradients by the central difference. In discretized form, Eq. 3.35 is written as

$$\begin{aligned}\frac{\varphi^{n}_{(i-1,j)} - 2\varphi^{n+1}_{(i,j)} + \varphi^{n}_{(i+1,j)}}{\Delta x^2} &+ \frac{\varphi^{n}_{(i,j-1)} - 2\varphi^{n+1}_{(i,j)} + \varphi^{n}_{(i,j+1)}}{\Delta y^2} \\ &= \frac{1}{\tilde{T}^{n}_{(i,j)}}\left(\frac{\tilde{T}^{n}_{(i,j)} - \tilde{T}^{n-1}_{(i,j)}}{\Delta t} + \tilde{u}^{n}_{(i,j)}\frac{\tilde{T}^{n}_{(i-1,j)} - \tilde{T}^{n}_{(i+1,j)}}{2\Delta x}\right. \\ &\left. + \tilde{v}^{n}_{(i,j)}\frac{\tilde{T}^{n}_{(i,j-1)} - \tilde{T}^{n}_{(i,j+1)}}{2\Delta y}\right)\end{aligned} \tag{3.39}$$

Rearranging,

$$\begin{aligned}\varphi^{n+1}_{(i,j)} = \frac{1}{2(1+\beta^2)}&\left[\varphi^{n}_{(i-1,j)} + \varphi^{n}_{(i+1,j)} + \beta^2\left(\varphi^{n}_{(i,j-1)} + \varphi^{n}_{(i,j+1)}\right)\right] \\ &- \frac{\Delta x^2}{\tilde{T}^{n}_{(i,j)}}\left(\frac{\tilde{T}^{n}_{(i,j)} - \tilde{T}^{n-1}_{(i,j)}}{\Delta t} + \tilde{u}^{n}_{(i,j)}\frac{\tilde{T}^{n}_{(i-1,j)} - \tilde{T}^{n}_{(i+1,j)}}{2\Delta x}\right. \\ &\left. + \tilde{v}^{n}_{(i,j)}\frac{\tilde{T}^{n}_{(i,j-1)} - \tilde{T}^{n}_{(i,j+1)}}{2\Delta y}\right)\end{aligned} \tag{3.40}$$

The circulation needs to be updated as well at each node during each time step using Eq. 3.36

$$\frac{\partial\tilde{\Gamma}}{\partial t}=\int\limits_{A}\frac{1}{\bar{\tilde{T}}}\left(\frac{\partial\tilde{T}}{\partial x}\vec{\imath}+\frac{\partial\tilde{T}}{\partial y}\vec{\jmath}\right)\times\left[\left(\frac{\partial u}{\partial t}+u\frac{\partial u}{\partial x}+v\frac{\partial u}{\partial y}\right)\vec{\imath}+\left(\frac{\partial v}{\partial t}+u\frac{\partial v}{\partial x}+v\frac{\partial v}{\partial y}\right)\vec{\jmath}\right]dA \quad (3.41)$$

Eq. 3.41 is developed as

$$\frac{\partial\Gamma}{\partial t}=\iint\frac{1}{\bar{\tilde{T}}}\left[\left(\frac{\partial\tilde{v}}{\partial t}+\tilde{u}\frac{\partial\tilde{v}}{\partial x}+\tilde{v}\frac{\partial\tilde{v}}{\partial y}\right)\frac{\partial\tilde{T}}{\partial x}-\left(\frac{\partial\tilde{u}}{\partial t}+\tilde{u}\frac{\partial\tilde{u}}{\partial x}+\tilde{v}\frac{\partial\tilde{u}}{\partial y}\right)\frac{\partial\tilde{T}}{\partial y}\right]dxdy \quad (3.42)$$

The temperature derivatives are approximated using the explicit scheme and the spatial gradients by the central difference. Discretizing Eq. 3.42 while assuming that each term within the integral is uniform in each grid surrounding a node, i.e. a staggered grid is used, the change in circulation at each node is obtained as

$$\begin{aligned}\Delta\tilde{\Gamma}=\frac{\Delta t}{\tilde{T}^{n}_{(i,j)}}\Bigg[\Bigg(&\frac{\tilde{v}^{n}_{(i,j)}-\tilde{v}^{n-1}_{(i,j)}}{\Delta t}+\tilde{u}^{n}_{(i,j)}\frac{\tilde{v}^{n}_{(i+1,j)}-\tilde{v}^{n}_{(i-1,j)}}{2\Delta x}\\&+\tilde{v}^{n}_{(i,j)}\frac{\tilde{v}^{n}_{(i,j+1)}-\tilde{v}^{n}_{(i,j-1)}}{2\Delta y}\Bigg)\frac{\tilde{T}^{n}_{(i+1,j)}-\tilde{T}^{n}_{(i-1,j)}}{2\Delta x}-\Bigg(\frac{\tilde{u}^{n}_{(i,j)}-\tilde{u}^{n-1}_{(i,j)}}{\Delta t}\\&+\tilde{u}^{n}_{(i,j)}\frac{\tilde{u}^{n}_{(i+1,j)}-\tilde{u}^{n}_{(i-1,j)}}{2\Delta x}\\&+\tilde{v}^{n}_{(i,j)}\frac{\tilde{u}^{n}_{(i,j+1)}-\tilde{u}^{n}_{(i,j-1)}}{2\Delta y}\Bigg)\frac{\tilde{T}^{n}_{(i,j+1)}-\tilde{T}^{n}_{(i,j-1)}}{2\Delta y}\Bigg]\Delta x\Delta y\end{aligned} \quad (3.43)$$

3.2 Scalar Field

The scalar field is governed by the general scalar transport equation defined as

$$\frac{\partial \rho \phi_\sigma}{\partial t} + \frac{\partial \rho u \phi_\sigma}{\partial x} + \frac{\partial \rho v \phi_\sigma}{\partial y} = -\frac{\partial}{\partial x}\left(\gamma_\sigma \frac{\partial \phi_\sigma}{\partial x}\right) - \frac{\partial}{\partial y}\left(\gamma_\sigma \frac{\partial \phi_\sigma}{\partial y}\right) + \rho S_\sigma \qquad (3.44)$$

For scalar fields governed by the enthalpy transport equation, ϕ_σ would represent the total specific enthalpy h. $\gamma_\sigma = \rho\Gamma_\sigma$ is the thermal molecular diffusivity coefficient with $\Gamma_\sigma = K/C_p$ where K is the thermal conduction coefficient and C_p is the specific heat at constant pressure. Γ_σ is related to the kinematic viscosity v via the Prandtl number Pr, as $\Gamma_\sigma = v/Pr$. S_σ represents the source term and is assumed to be negligible for low Mach number flows with negligible viscous dissipation and thermal radiation, i.e. $S_\sigma = 0$ (Jaberi et al., 1999). In the context of LES, Eq. 3.44 is filtered using the Favre filtered quantities for the scalar variable $\phi_\sigma = \tilde{\phi}_\sigma + \phi_\sigma''$ with $\tilde{\phi}_\sigma = \frac{\overline{\rho\phi_\sigma}}{\bar{\rho}}$, the filtered enthalpy transport equation becomes similar to the one presented in (Jaberi, et al. 1999) and is written as follow

$$\frac{\partial \bar{\rho}\tilde{\phi}_\sigma}{\partial t} + \frac{\partial \bar{\rho}\tilde{u}\tilde{\phi}_\sigma}{\partial x} + \frac{\partial \bar{\rho}\tilde{v}\tilde{\phi}_\sigma}{\partial y} = -\frac{\partial}{\partial x}\left(\gamma_\sigma \frac{\partial \tilde{\phi}_\sigma}{\partial x}\right) - \frac{\partial}{\partial y}\left(\gamma_\sigma \frac{\partial \tilde{\phi}_\sigma}{\partial y}\right) - \frac{\partial M_{\sigma,x}}{\partial x} - \frac{\partial M_{\sigma,y}}{\partial y} \qquad (3.45)$$

where $M_{\sigma,x} = \bar{\rho}\left(\widetilde{u\phi_\sigma} - \tilde{u}\tilde{\phi}_\sigma\right)$ and $M_{\sigma,y} = \bar{\rho}\left(\widetilde{v\phi_\sigma} - \tilde{v}\tilde{\phi}_\sigma\right)$ are the unresolved subgrid heat fluxes in x- and y-directions, respectively. By analogy with the SGS in the filtered vorticity equation, the subgrid heat fluxes $M_{\sigma,x}$ and $M_{\sigma,y}$ are modeled using the eddy diffusion concept for an anisotropic flow as

$$M_{x,\sigma} = -\gamma_{t_{\sigma,x}} \frac{\partial \tilde{\phi}_{\sigma}}{\partial x}$$

$$and \qquad (3.46)$$

$$M_{y,\sigma} = -\gamma_{t_{\sigma,y}} \frac{\partial \tilde{\phi}_{\sigma}}{\partial y}$$

Substituting Eq. 3.46 into Eq.3.45 and rearranging to get

$$\frac{\partial \bar{\rho}\tilde{\phi}_{\sigma}}{\partial t} + \frac{\partial \bar{\rho}\tilde{u}\tilde{\phi}_{\sigma}}{\partial x} + \frac{\partial \bar{\rho}\tilde{v}\tilde{\phi}_{\sigma}}{\partial y} = -\frac{\partial}{\partial x}\left[\left(\gamma_{\sigma} + \gamma_{t_{\sigma,x}}\right)\frac{\partial \tilde{\phi}_{\sigma}}{\partial x}\right] - \frac{\partial}{\partial y}\left[\left(\gamma_{\sigma} + \gamma_{t_{\sigma,y}}\right)\frac{\partial \tilde{\phi}_{\sigma}}{\partial y}\right] \qquad (3.47)$$

The probability density function (PDF) has been successfully used to predict the scalar field. In order to fit the PDF into the framework of large eddy simulation of variable temperature flow, a new approach based on the filtered mass density function (FMDF) (Jaberi, et al. 1999) has been introduced and defined as follows. The FMDF denoted by F_L is defined as

$$F_L(\xi; \boldsymbol{x}, t) = \int_{-\infty}^{+\infty} \rho(\boldsymbol{x}', t)\delta\left(\xi - \phi_{\sigma}(\boldsymbol{x}', t)\right) \mathrm{G}(\mathbf{x}' - \mathbf{x})\mathrm{d}\mathbf{x}' \qquad (3.48)$$

where δ is the Dirac delta function which represents the fine grained density of the scalar ϕ in one realization, ξ denotes the composition sample. Eq. 3.48 implies that the FMDF is the mass weighted spatially filtered value of the fine grained density, F_L gives the mass weighted probability density in the composition space of the fluid around $\boldsymbol{x}_i$ weighted by the filter G. F_L has all the properties of the probability density function. The transport equation for $F_L(\xi; \boldsymbol{x}, t)$ was obtained by Jaberi et al. (1999) as

$$\frac{\partial F_L}{\partial t}+\frac{\partial\left[\overline{u|\xi}\,F_L\right]}{\partial x}+\frac{\partial\left[\overline{v|\xi}\,F_L\right]}{\partial y}$$
$$=\frac{\partial}{\partial \xi}\left[\left(\overline{\frac{1}{\bar{\rho}}\frac{\partial}{\partial x}\left(\gamma_\sigma\frac{\partial \phi_\sigma}{\partial x}\right)|\xi}+\overline{\frac{1}{\bar{\rho}}\frac{\partial}{\partial y}\left(\gamma_\sigma\frac{\partial \phi_\sigma}{\partial y}\right)|\xi}\right)F_L\right] \tag{3.49}$$

This is an exact transport equation for the FMDF. The symbol $\overline{\boldsymbol{u}|\boldsymbol{\xi}}$ indicates the mass weighted filtered mean $\boldsymbol{u}$ conditional on the satisfaction of the constraint $\boldsymbol{\xi}$. The first term on LHS of Eq. 3.49 is the unsteady term and is closed. The unclosed subfilter scale convective and mixing is indicated respectively by the conditional filtered values of the second and third term on LHS of Eq. 3.49 and the first term on RHS of Eq. 3.49. Therefore these two terms have to be modeled.

3.2.1 Model for the Convective Term

The convective term is decomposed as (Jaberi, et al., 1999)

$$\overline{u|\xi}\,F_L=\tilde{u}\,F_L+\left[\overline{u|\xi}-\tilde{u}\right]F_L$$
$$and \tag{3.50}$$
$$\overline{v|\xi}\,F_L=\tilde{v}\,F_L+\left[\overline{v|\xi}-\tilde{v}\right]F_L$$

where the second term in RHS denotes the influence of SGS convective flux. This term is modeled as

$$\left[\overline{u|\xi}-\tilde{u}\right]F_L=-\gamma_{t_{\sigma,x}}\frac{\partial(F_L/\bar{\rho})}{\partial x}$$
$$and \tag{3.51}$$
$$\left[\overline{v|\xi}-\tilde{v}\right]F_L=-\gamma_{t_{\sigma,y}}\frac{\partial(F_L/\bar{\rho})}{\partial y}$$

3.2.2 Model for the Diffusion Term

The diffusion term in Eq. 3.49 is decomposed as

$$\begin{aligned}
&\frac{\partial}{\partial\xi}\left[\left(\overline{\frac{1}{\bar{\rho}}\frac{\partial}{\partial x}\left(\gamma_\sigma\frac{\partial\phi_\sigma}{\partial x}\right)|\xi}+\overline{\frac{1}{\bar{\rho}}\frac{\partial}{\partial y}\left(\gamma_\sigma\frac{\partial\phi_\sigma}{\partial y}\right)|\xi}\right)F_L\right]\\
&\qquad=\frac{\partial}{\partial x}\left(\gamma_\sigma\frac{\partial(F_L/\bar{\rho})}{\partial x}\right)+\frac{\partial}{\partial y}\left(\gamma_\sigma\frac{\partial(F_L/\bar{\rho})}{\partial y}\right)\\
&\qquad-\frac{\partial^2}{\partial\xi^2}\left[\overline{\left(\gamma_\sigma\left(\frac{\partial^2\phi_\sigma}{\partial x^2}+\frac{\partial^2\phi_\sigma}{\partial y^2}\right)\right)|\xi}\;\frac{F_L}{\bar{\rho}}\right]
\end{aligned}\tag{3.52}$$

The first and second term on RHS of this equation denotes the molecular diffusion in spatial transport of the FMDF and is in closed form. The second term represents the dissipative nature of subgrid scale mixing and needs to be modeled.

3.2.3 Modeled FMDF Equation

In the present study, the governing equation for the FMDF is obtained by substituting Eq. 3.50, Eq. 3.51 and Eq. 3.52 into Eq. 3.49 and rearranging to get

$$\begin{aligned}
&\frac{\partial F_L}{\partial t}+\frac{\partial[\tilde{u}\,F_L]}{\partial x}+\frac{\partial[\tilde{v}\,F_L]}{\partial y}\\
&\qquad=\frac{\partial}{\partial x}\left(\left(\gamma_\sigma+\gamma_{t_{\sigma,x}}\right)\frac{\partial(F_L/\bar{\rho})}{\partial x}\right)\\
&\qquad+\frac{\partial}{\partial y}\left(\left(\gamma_\sigma+\gamma_{t_{\sigma,y}}\right)\frac{\partial(F_L/\bar{\rho})}{\partial y}\right)\\
&\qquad-\frac{\partial^2}{\partial\xi^2}\left[\overline{\left(\gamma_\sigma\left(\frac{\partial^2\phi_\sigma}{\partial x^2}+\frac{\partial^2\phi_\sigma}{\partial y^2}\right)\right)|\xi}\;\frac{F_L}{\bar{\rho}}\right]
\end{aligned}\tag{3.53}$$

The solution of Eq. 3.53 gives all statistical information concerning the scalar field.

3.2.4 Molecular Mixing Model

The closure of the mixing term presented in Eq. 3.53 requires the joint statistics of ξ and its gradients, for which several model have been proposed by Dopazo (1994) and Pope (2000). In the present study, the modified curl model used by Wang and Milane (2006) is adopted and summarized here as follows. In the context of the Monte-Carlo technique the modified Curl model for the mixing term, $\frac{\partial^2}{\partial \xi^2}\left[\overline{\left(\gamma_\sigma\left(\frac{\partial^2 \phi_\sigma}{\partial x^2}+\frac{\partial^2 \phi_\sigma}{\partial y^2}\right)\right)|\xi}\ \frac{F_L}{\bar{\rho}}\right]$ is modeled by selecting pairs of particles randomly as

$$n_m = \beta\overline{\omega_f}N\Delta t \tag{3.54}$$

where n_m denotes the number of pairs of particles that will mix in a given grid, $\overline{\omega_f}$ is the mean mixing frequency in the grid and the coefficient β is a function of the mixing model. It has a value of 3 for the modified curl model. After mixing, the scalar variable ξ of each of the two particles in a mixing pair are given as

$$\begin{aligned} \xi_1^* &= \left[(1-\alpha_{curl})\xi_1 + \frac{\alpha_{curl}(\xi_1+\xi_2)}{2}\right] \\ \xi_2^* &= \left[(1-\alpha_{curl})\xi_2 + \frac{\alpha_{curl}(\xi_1+\xi_2)}{2}\right] \end{aligned} \tag{3.55}$$

where $\xi_1^*$and ξ_2^* denotes the scalar variables after mixing and ξ_1 and ξ_2 denotes the variables values before mixing. α_{curl} is a uniform random number between 0 and 1.

The mixing frequency $\overline{\omega_f}$ for the anisotropic flow considered in this study, is calculated at the nodes as

$$\overline{\omega_f} = \frac{1}{2}C_\phi\left[\frac{\left(\Gamma+\Gamma_{t_{\sigma,x}}\right)}{{\Delta_x}^2} + \frac{\left(\Gamma+\Gamma_{t_{\sigma,y}}\right)}{{\Delta_y}^2}\right] \tag{3.56}$$

where Δ_x and Δ_y are the filter sizes in x- and y-directions, respectively, used in SGS models. The mean mixing frequency, $\overline{\omega_f}$ used in Eq. 3.54 is calculated at the nodes and then transferred to particle locations using an area weighing interpolation scheme (Wang and Milane, 2006).

3.2.4.1 Temperatures of Mixed Particles

The temperature after mixing is calculated using the first law of thermodynamics written for the pair of mixing particles, assuming constant pressure process, therefore

$$\Delta H = \delta Q$$

where H is the enthalpy. Assuming heat transfer to neighboring particles is nil ($\delta Q = 0$), the first law becomes

$$\Delta H = 0$$

$$\text{i.e.}\quad H_A + H_B = H_A^* + H_B^*$$

where * indicates the state of particles after mixing. For an ideal gas

$$\Delta H = mC_p\Delta T \qquad (3.57)$$

where C_p, the specific heat at constant pressure is assumed to be constant (in the present study, the temperature difference is 50 K with temperature ranging between 303K to 353K which corresponds to C_p values for air of 29.075 to 29..2 KJ/Kmol-K) and m is the mass a particle mixing. Since equal mass of particles is assumed after and before mixing, therefore Eq. 3.57 implies that

$$\Delta T = 0,$$

$$\text{i.e.}\quad T_A + T_B = T_A^* + T_B^*$$

The modified curl's model implies that after mixing, the temperature of each particle is given as

$$T_A^* = \left[(1 - \alpha_{curl})T_A + \frac{\alpha_{curl}(T_A + T_B)}{2}\right] = T_A + \frac{\alpha_{curl}}{2}(T_B - T_A) \qquad (3.58)$$

and

$$T_B^* = \left[(1 - \alpha_{curl})T_B + \frac{\alpha_{curl}(T_A + T_B)}{2}\right] = T_B + \frac{\alpha_{curl}}{2}(T_A - T_B) \qquad (3.59)$$

3.2.5 Monte-Carlo Scheme

The solution of the scalar FMDF transport equation Eq. 3.53 is carried out by using the Monte Carlo technique. The Monte-Carlo particles are moved due to convection and diffusion, and their compositions are altered due to mixing process only in the non-reacting flow. The particles motion is due to molecular and subgrid diffusivities governed by the following stochastic differential equation (SDE) (Risken, 1989 and Gardiner, 1990)

$$d\boldsymbol{x}_i(t) = \boldsymbol{D}_i(\boldsymbol{x}(t), t)dt + \boldsymbol{E}(\boldsymbol{x}(t), t)d\boldsymbol{W}_i(t) \qquad (3.60)$$

where $\boldsymbol{x}_i$ is the Lagrangian position of a stochastic particle, $\boldsymbol{D}_i$ and $\boldsymbol{E}$ are the drift and diffusion coefficients, respectively, and $\boldsymbol{W}_i$ denotes the Wiener-Levy process (Karlin and Taylor 1981). A simple comparison between Eq. 3.60 and the spatial derivative terms in the FMDF transport equation Eq. 3.53 yields the expressions of the drift and diffusion coefficients

$$\boldsymbol{E} = \sqrt{\frac{2(\gamma_\sigma + \gamma_{t_\sigma})}{\bar{\rho}}} \qquad \boldsymbol{D}_i = \widetilde{\boldsymbol{u}}_i + \frac{1}{\bar{\rho}}\frac{\partial(\gamma_\sigma + \gamma_{t_\sigma})}{\partial \boldsymbol{x}_i} \qquad (3.61)$$

The molecular mixing term is implemented by mean of the Modified Curl model which consists of selecting particles in the ensemble to mix them and has been discussed in Section 3.2.4

3.3 Initial and Boundary Conditions

The computational domain shown in Figures 3.1(a) and (b) is used to solve the flow field and the scalar field of the thermal mixing layer experimented by Mizuno et al. (2005). The domain consists of a rectangular grid with uniform but different grid sizes in each direction ($\Delta x \neq \Delta y$). The lower left corner of the grid is located at $x = 1$ and $y = 1$. The boundary conditions for LES are the same as for the unfiltered case because they are assumed to be governed by the large scale.

3.3.1 Flow Field Initial and Boundary Condition

The Neumann conditions apply to the inflow and outflow boundaries with $\psi = 0$ at $y = 0$. At the inflow, two laminar boundary layers, developed on the high speed side and the low speed side of splitter plate, are represented by third-order polynomials and another third-order polynomial is used to patch the two boundary layers in order to avoid the accumulation of Monte-Carlo particles. The velocity profile also reflects the development of the wake at some distance from the edge of the splitter plate. Here assuming a third-order polynomial profile $\tilde{u}_{\omega} = ay + by^2 + cy^3$ and using the boundary conditions

$$\frac{\partial \tilde{u}_\omega}{\partial y} = 0, \text{at}\, y = \delta_{laminar}$$

$$\frac{\partial^2 \tilde{u}_\omega}{\partial y^2} = 0, \text{at}\, y = 0 \tag{3.62}$$

The laminar velocity profile is given as

$$\frac{\tilde{u}_\omega}{U} = \frac{3}{2}\frac{y}{\delta_{laminar}} - \frac{1}{2}\frac{y^3}{\delta_{laminar}^3} \tag{3.63}$$

where $U = U_H$ at $y > y_{sp}$ and $U = U_L$ at $y \leq y_{sp}$ and the thickness of the boundary layer $\delta_{laminar}$ is calculated using $(\delta_{laminar}/x) = 5.0/Re_x^{1/2}$ assuming $x = 0.5$ for this study. Therefore the boundary conditions at inflow are given as

$$\begin{aligned} \left(\frac{\partial \psi}{\partial y}\right)_{1,j} &= \left[\frac{3}{2}\frac{y}{\delta_{laminar}} - \frac{1}{2}\frac{y^3}{\delta_{laminar}^3}\right] U_H \qquad \text{at}\, y > y_{sp} \\ \left(\frac{\partial \psi}{\partial y}\right)_{1,j} &= \left[\frac{3}{2}\frac{y}{\delta_{laminar}} - \frac{1}{2}\frac{y^3}{\delta_{laminar}^3}\right] U_L \qquad \text{at}\, y \leq y_{sp} \end{aligned} \tag{3.64}$$

where subscript 'j' corresponds to the node in the y-direction, U_H and U_L are the velocities of the high speed side and the low speed side, respectively, y_{sp} is the splitter plate location in the y-direction. The outflow stream function profile corresponds to a profile for the velocity that is an error function as

$$\left(\frac{\partial \psi}{\partial y}\right)_{N,j} = \frac{\Delta U}{2} erf\left\{\sigma \frac{(y - y_{ov})}{x - x_v}\right\} + U_c \tag{3.65}$$

where subscript 'N' corresponds to the node in x-direction at the outflow, 'j' corresponds to the node in the y-direction, $\Delta U = U_H - U_L$ is the velocity difference across the layer, y_{ov} is the ordinate of centerline, x_v is the virtual origin, σ is the spreading parameter and $U_c = (U_H + U_L)/2$ is the average velocity. The dilatational velocity u_D is nil at the inflow, top and bottom boundaries, therefore a constant arbitrary value is assigned to the potential function φ along these boundaries. The convective outflow boundary condition is assumed for the potential function at the outflow boundary.

In addition, in order to simulate the Kelvin-Helmholtz instability mechanism, the profile may be augmented by a perturbation based on linear stability analysis (Monkewitz, 1982). In the vortex method, the Kelvin-Helmholtz instability may be simulated by moving vertically the vortex closest to the edge of the splitter plate by a small distance (perturbation) given by a sinusoidal function of time operating at the fundamental frequency (f) of the unforced mixing layer as

$$y(t) = Ax\, sin(2\pi f\ t) \qquad (3.66)$$

where $A = 0.5\, U_c\, \Delta t$ is the amplitude and x represents a small percentage of A, (i.e. $x = 3.0\%$ in this study). The fundamental frequency (f) is calculated using the following $f\theta_i/(2\ U_c) \approx 0.02$ (Oster and Wygnanski, 1982) where θ_i is the momentum thickness at the beginning of the region of linear growth. The factor A has been used by Inoue (1992) where a forced mixing layer was investigated. In this study, the small value of $x = 3.0\%$ introduced insures that the mixing layer is in the unforced mode.

The error-function outflow boundary condition has been adopted because it constrains the growth rate of the momentum thickness and yields a slope for the linear growth region in close agreement with the experiment as discussed in Abdolhosseini and Milane (2000). Furthermore, slip conditions are assumed for the top and bottom boundaries. The Dirichlet condition is used for the bottom boundary at $y_l = 1$ consistent with $\psi_{i,0} = 0$ at $y = 0$, as

$$\psi_{i,1} = y_l \times U_l \qquad (3.67)$$

And for the top boundary

$$\psi_{i,N} = U_l y_{sp} + U_h(y_{i,N} - y_{sp}) \tag{3.68}$$

where y_{sp} is the splitter plate y-location and N corresponds to the nodes at the top boundary.

Initially, the velocity discontinuity across the splitter plate is simulated using a vortex sheet, which is discretized into a row of point vortices. At time $t = 0$, the point vortices are equidistant at an interval $d = L/N_v$, where N_v is the number of vortices and L is the computational domain length. The vortex closest to the edge of the splitter plate is moved vertically using Eq.3.66 to initialize the Kelvin-Helmholtz instability. The total circulation in the computational domain is $L(U_h - U_l)$. The initial circulation is equally distributed among the N_v vortices as $\Gamma_\text{i} = L(U_h - U_l)/N_v = d(U_h - U_l)$. Furtermore, in order to satisfy the Kutta condition, a vortex with initial circulation Γ_i is introduced at the trailing edge of the splitter plate at the end of each time step $\Delta t = d/U_c$. The oldest vortex, i.e. the vortex with the largest residence time, is discarded from the calculations when a new vortex is introduced. The vortices can move freely in and out through the outflow boundary to avoid the collection of vortices at the end of the computational domain. The motion of the vortices outside the computational domain is assumed to be governed by the velocity at the outflow boundary.

3.3.2 Scalar Field Initial and Boundary Conditions

The flow parameters of the thermal mixing layer simulated is similar to the experiment of Mizuno et al. (2005) where a high speed cold flow at temperature T_h and a low speed hot flow at temperature T_l mix. The temperature profile at the inlet boundary is assumed to be an error function written as

$$T_{1,j} = \frac{\Delta T}{2} erf\{\sigma(y - y_{oT})/x_v\} + T_c \tag{3.69}$$

where subscript '1' corresponds to the inflow x-location and subscript 'j' corresponds to the nodes in the y-direction, $\Delta T = |T_h - T_l|$ is the temperature difference across the layer, $T_c = (T_h + T_l)/2$ is the average temperature, σ is the spreading rate and y_{oT} is the ordinate of centerline of temperature, different from the ordinate of centerline of velocity y_{ov}. The relation $y_{oT} \neq y_{ov}$ is similar to the cross-stream adjustment length used in the "wake-modified" inlet conditions by Sotierou and Ghoniem (1988), and also is necessary to obtain prediction that fit the experimental data. The outflow boundary condition is not specified (Eq. 3.53 is parabolic) because the displacement of scalars due to streamwise convection is very high compared to the displacement due to backward diffusion.

Particles that exit the top, bottom and the outflow domain boundaries are discarded from the calculation. At inflow the temperature of the introduced particles is defined by the inlet boundary condition.

3.4 Solution Procedure

The VIC algorithm developed by Wang and Milane (2006) is employed to solve for the velocity field and is extended for a low Mach number thermal mixing layer in such a way that, during each time step, the vorticity transport equation (Eq. 3.24) and the FMDF scalar transport equation (Eq. 3.53) are solved simultaneously to simulate the coupling effect between the scalar field and the flow field. Also, two interpolation techniques based on the area weighing scheme are used, one of them transfers velocity from nodes to vortex particles and vorticity from particles to nodes as described in Wang and Milane

(2006). The second scheme transfers vorticity from nodes to particles and is described in Shaikh (2006).

3.4.1 Flow Field Algorithm

The numerical algorithm devised to solve the governing equations is divided into four steps: initialization, predictor, corrector and time advancement. Due to the predictor-corrector scheme employed, at each time step two values of each variable are stored, i.e. the old values at time t and the predicted value denoted by (*). At the end of the corrector step, the old value is replaced with the new value at time $t + \Delta t$. The solution procedure is summarized in the following steps. Also a representative flowchart is provided in appendix A.2

Initialization

a) Initialize by placing the equidistant vortices at the level of the splitter plate and by assigning values for the temperature $\tilde{T}$, for the stream function ψ and for the potential function φ at the internal nodes together with the boundary conditions.

Predictor step

b) Transfer the vorticity from the vortex particles to the nodes using the interpolation scheme.

c) Solve the two Poisson's equations (Eq. 3.32 and Eq. 3.34) to get the stream and potential functions, using Gauss-Seidel iteration with a left-to-right sweep of the nodes and bottom-to-top sweep of the lines. Iteration convergence is obtained when the percent difference between consecutive ψ or φ is less than 0.001%.

d) Compute the velocity $\tilde{\boldsymbol{u}}(t) = \tilde{\boldsymbol{u}}_w(t) + \tilde{\boldsymbol{u}}_D\,(t)$ at the nodes.

e) Transfer the velocities at the location of each vortex $\tilde{\boldsymbol{u}}_{\boldsymbol{n}}(t)$ using the interpolation scheme.

f) Compute the SGS eddy viscosity using the Smagorinsky SGS model.

g) Compute the diffusion velocity $\tilde{\boldsymbol{u}}_{diff}(t)$ at the nodes.

h) Calculate the diffusion velocity at the location of each vortex $\tilde{\boldsymbol{u}}_{\boldsymbol{n},diff}(t)$ using the interpolation scheme.

i) Update the co-ordinates of the vortex particles, while keeping the circulation constant.

$$\boldsymbol{x}^*(\mathrm{t}+\Delta\mathrm{t}) = \boldsymbol{x}(\mathrm{t}) + \left(\tilde{\mathbf{u}}_{\mathrm{n}}(\mathrm{t}) + \tilde{\mathbf{u}}_{\mathrm{n,diff}}(\mathrm{t})\right)\Delta\mathrm{t}$$

j) Solve for the baroclinic term to find the change in the vorticity at the nodes

$$\frac{\partial\tilde{\omega}}{\partial t}(t) = \frac{\nabla\tilde{\mathrm{T}}(\mathrm{t})}{\tilde{\mathrm{T}}(\mathrm{t})} \times \frac{D\tilde{\boldsymbol{u}}(t)}{Dt}$$

k) Transfer the change in vorticity from nodes to particles using the interpolation scheme and update the vortex circulations $\tilde{\Gamma}^*(\mathrm{t}+\Delta\mathrm{t})$ for each vortex particle as

$$\tilde{\Gamma}^*(\mathrm{t}+\Delta\mathrm{t}) = \tilde{\Gamma}(\mathrm{t}) + \frac{\partial\tilde{\Gamma}}{\partial\mathrm{t}}(\mathrm{t})\Delta\mathrm{t}$$

l) Transfer the vorticity $\tilde{\omega}^*(\mathrm{t}+\Delta\mathrm{t})$ from vortex particles to nodes using the interpolation scheme.

m) Solve for the governing equation (FMDF) of the scalar field using the Monte Carlo technique discussed in the next Section 3.4.2 and update the temperature at the nodes $\tilde{\mathrm{T}}^*(\mathrm{t}+\Delta\mathrm{t})$

n) Given $\left(\boldsymbol{x}^*, \tilde{\omega}^*, \tilde{\mathrm{T}}^*\right)$ stored at every node in the domain thus ending the predictor substep.

Corrector step

o) The corrector substep starts by solving the stream and potential functions using the two Poisson's equations as in step c), but with the new values $(\boldsymbol{x}^*, \widetilde{\omega}^*, \widetilde{T}^*)$ found from the predictor substep.

p) Calculate the new velocity $\widetilde{\boldsymbol{u}}^*(t + \Delta \mathrm{t}) = \widetilde{\boldsymbol{u}}_w(t + \Delta \mathrm{t}) + \widetilde{\boldsymbol{u}}_D\,(t + \Delta \mathrm{t})$ at the nodes and then transfer using interpolation scheme to find the velocity $\widetilde{\boldsymbol{u}}_{\boldsymbol{n}}{}^*(t + \Delta \mathrm{t})$ at the location of each vortex.

q) Compute the SGS eddy viscosities using the Smagorinsky model.

r) Compute the diffusion velocity $\widetilde{\boldsymbol{u}}^*{}_{diff}(t)$ at the nodes.

s) Calculate the diffusion velocity at the location of each vortex $\widetilde{\boldsymbol{u}}^*{}_{n,diff}(t)$ using the interpolation scheme.

t) Update the co-ordinates of the vortices, while keeping the circulation constant.

$$\boldsymbol{x}(t + \Delta t) = \boldsymbol{x}(t) + \frac{\left(\widetilde{\mathbf{u}}_{\mathrm{n}}(\mathrm{t}) + \widetilde{\mathbf{u}}_{\mathrm{n,diff}}(\mathrm{t}) + \widetilde{\mathbf{u}}_{\mathrm{n}}{}^*(\mathrm{t} + \Delta \mathrm{t}) + \widetilde{\mathbf{u}}_{\mathrm{n,diff}}{}^*(\mathrm{t} + \Delta \mathrm{t})\right)}{2} \Delta t$$

u) Find the change in the vorticity at the nodes, by solving the baroclinic term

$$\frac{\partial \widetilde{\omega}^*}{\partial t}(t + \Delta \mathrm{t}) = \frac{\nabla \widetilde{T}^*(\mathrm{t} + \Delta \mathrm{t})}{\widetilde{T}^*(\mathrm{t} + \Delta \mathrm{t})} \times \frac{D\widetilde{\boldsymbol{u}}^*(t + \Delta \mathrm{t})}{Dt}$$

v) Transfer the change in vorticity from nodes to particles using the interpolation scheme to calculate the change in circulation $\frac{\partial \widetilde{\Gamma}^*}{\partial t}(\mathrm{t} + \Delta \mathrm{t})$ at each vortex particles and then update the vortices circulations

$$\widetilde{\Gamma}(\mathrm{t} + \Delta \mathrm{t}) = \widetilde{\Gamma}(\mathrm{t}) + \frac{1}{2}\left(\frac{\partial \widetilde{\Gamma}}{\partial t}(\mathrm{t}) + \frac{\partial \widetilde{\Gamma}^*}{\partial t}(\mathrm{t} + \Delta \mathrm{t})\right) \Delta \mathrm{t}$$

w) Solve for the governing equation (FMDF) of the scalar field using the Monte Carlo technique discussed in the next Section 3.4.2 and update the temperature at the nodes $\widetilde{T}(\mathrm{t} + \Delta \mathrm{t})$

x) End the corrector substep by storing the values $\boldsymbol{x}(\mathrm{t}+\Delta\mathrm{t}), \tilde{\omega}(\mathrm{t}+\Delta\mathrm{t}), \tilde{\mathrm{T}}(\mathrm{t}+\Delta\mathrm{t})$ at the nodes.

Time advancement

y) Introduce a new vortex at the edge of the splitter plate and discard the oldest one.

z) March in time by repeating the calculations from step b) through z).

3.4.2 Scalar Field Algorithm

The scalar field is defined by solving the FMDF transport equation Eq. 3.53 using the Monte-Carlo scheme discussed in details in Wang (2005). Briefly, the steps are as follow

1- Initialize the Monte-Carlo particles in the computational domain by prescribing particles to each grid cell.

2- Assign initial temperature to each particle using the temperature profile adopted in this study (Eq. 3.69)

3- Calculate $\boldsymbol{D}_i$, $\boldsymbol{E}$ (Eq. 3.61) and the mixing frequency $\overline{\omega_f}$ (Eq. 3.56).

4- Transfer $\boldsymbol{D}_i$ and $\boldsymbol{E}$ from the nodes to particle locations using the interpolation scheme (Wang and Milane, 2006) and then displace the particles using the stochastic differential equation (Eq. 3.60).

5- Transfer the mixing frequency from the nodes to particles using the interpolation scheme (Wang and Milane, 2006) and then calculate the arithmetic average mixing frequency $\overline{\omega_f}$ at each node.

6- Calculate the number of mixing pairs n_m using the Modified Curl model (Eq. 3.54). The pairs are selected randomly and new temperatures are assigned following Eq. 3.58 and Eq. 3.59.

7- March in time by repeating steps 3 to 7.

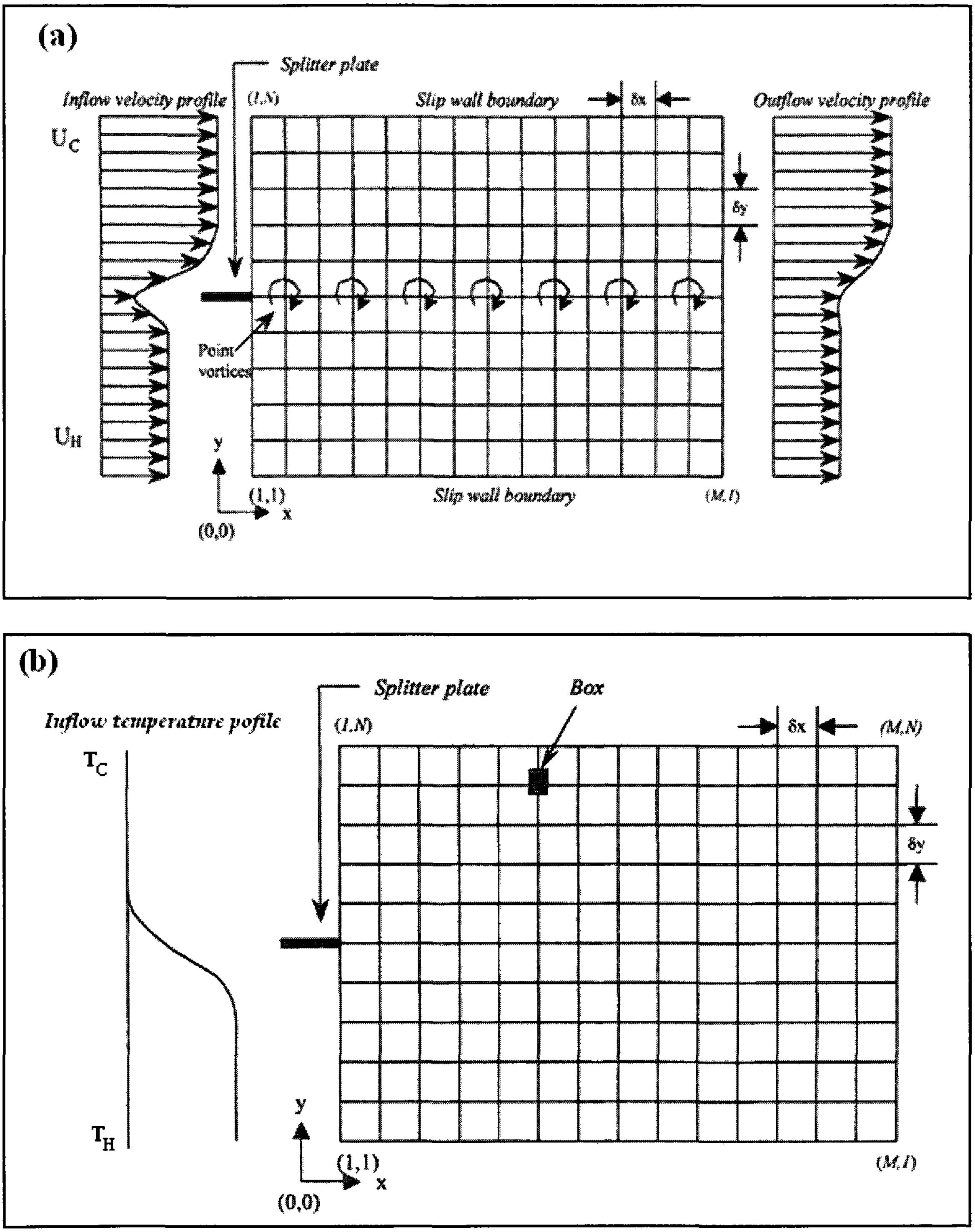

Figure 3-1: Thermal mixing layer (a) flow field computational domain, rectangular grid, initial position of the vortices, and boundary conditions. (b) Scalar field computational domain, rectangular grid, box and boundary condition.

Chapter 4

FORMULATION FOR INCOMPRESSIBLE REACTIVE FLOW AND SCALAR FIELDS

This chapter discusses the filtered incompressible vorticity and scalar transport equations and their modeling approaches as they are applied to a two-dimensional isothermally reacting mixing layer. The incompressible formulations are, in reality, just a special case of the compressible ones obtained by assuming constant density. The flow field governing equations and modeling are presented in Section 4.1. The scalar field governing equations and modeling are discussed in Section 4.2. The initial and boundary conditions for the isothermally reacting mixing layer under study are presented in Section 4.3. The solution procedures for the flow and scalar fields are stated in Section 4.4.

4.1 Flow Field

The continuity and the time dependent vorticity transport equations for an incompressible flow with constant viscosity are given as

$$\frac{\partial \boldsymbol{u}_i}{\partial \boldsymbol{x}_i} = 0 \tag{4.1}$$

$$\frac{\partial \boldsymbol{\omega}_i}{\partial t} + \boldsymbol{u}_j \frac{\partial \boldsymbol{\omega}_i}{\partial \boldsymbol{x}_j} = \boldsymbol{\omega}_j \frac{\partial \boldsymbol{u}_i}{\partial \boldsymbol{x}_j} + \nu \frac{\partial^2 \boldsymbol{\omega}_i}{\partial \boldsymbol{x}_j{}^2} \tag{4.2}$$

respectively, where $\boldsymbol{\omega}_i$ represents the components of the vorticity $\boldsymbol{\omega}$, the viscosity term is derived later in the viscosity section, $\boldsymbol{u}_i$ is the velocity vector, and ν is the kinematic viscosity. The left hand side includes the unsteady term and the convection term, whereas, the right side includes the vortex stretching and the viscous diffusion terms. For a two-dimensional flow in the x-y plane, the vorticity vector will be reduced to one component in the z- direction perpendicular to x-y plane, and the stretching term vanishes from the vorticity equation which becomes:

$$\frac{\partial \omega}{\partial t} + \boldsymbol{u}_j \frac{\partial \omega}{\partial \boldsymbol{x}_j} = \nu \frac{\partial^2 \omega}{\partial \boldsymbol{x}_j{}^2} \tag{4.3}$$

Combining Eq. 4.1 with Eq. 4.2, another form of the vorticity equation is obtained

$$\frac{\partial \omega}{\partial t} + \frac{\partial \mathbf{u}_j \omega}{\partial \boldsymbol{x}_j} = \frac{\partial}{\partial \boldsymbol{x}_j}\left(\nu \frac{\partial \omega}{\partial \boldsymbol{x}_j}\right) \tag{4.4}$$

Eq. 4.4 can be rewritten as

$$\frac{\partial \omega}{\partial t} + \frac{\partial}{\partial \boldsymbol{x}_j}\left(\boldsymbol{u}_j \omega - \nu \frac{\partial \omega}{\partial \boldsymbol{x}_j}\right) = 0 \tag{4.5}$$

Eq. 4.5 is similar to the one used by Ogami et al. (1991) in their development of the diffusion velocity method.

4.1.1 The Filtered Incompressible Vorticity Equation

The LES equations are obtained by applying a low-pass spatial filter G of width Δ to the vorticity transport equation. This eliminates scales smaller than Δ. Mathematically, the filtered field for any quantity $\phi(x,y,t)$, is given by

$$\bar{\phi} = \iint \phi(\zeta,\eta,t)\, G(x-\zeta, y-\eta)\, d\zeta\, d\eta$$

where G(x,y) is the spatial filter shape. Such a filter will be called a "bar-filter". Scales of motion, such as velocity and vorticity, are then decomposed into a gridscale $\bar{f}$ (overline) and subgrid-scale part f'(superscript $'$).

$$\omega = \bar{\omega}(x,y,t) + \omega'(x,y,t)$$

$$\mathbf{u} = \bar{\mathbf{u}}(x,y,t) + \mathbf{u}'(x,y,t)$$

The filtered continuity equation and the filtered transport equation for the spanwise vorticity component $\bar{\omega}_z$, are (Wang and Milane 2006) and (Cottet1996)

$$\frac{\partial \bar{u}}{\partial x} + \frac{\partial \bar{v}}{\partial y} = 0 \tag{4.6}$$

$$\frac{\partial \bar{\omega}}{\partial t} + \bar{u}\frac{\partial \bar{\omega}}{\partial x} + \bar{v}\frac{\partial \bar{\omega}}{\partial y} = \nu\frac{\partial^2 \bar{\omega}}{\partial x^2} + \nu\frac{\partial^2 \bar{\omega}}{\partial y^2} - \frac{\partial A}{\partial x} - \frac{\partial B}{\partial y} \tag{4.7}$$

respectively, where

$$A = \overline{u\omega_z} - \bar{u}\,\bar{\omega} \tag{4.8}$$

$$B = \overline{v\omega} - \bar{v}\bar{\omega} \tag{4.9}$$

are the unresolved SGS terms which need to be modeled in order to solve the filtered vorticity equation numerically.

4.1.2 SGS Eddy Viscosity Model

The terms A and B in Eq. 4.7 are the SGS vorticity stresses. Their net effect is to transfer energy from the large scales to the small scales. By analogy with the SGS Reynolds stresses in the filtered momentum, The SGS vorticity stresses are modeled using the eddy viscosity concept for an anisotropic flow as

$$-A = \nu_{t_x} \frac{\partial \bar{\omega}}{\partial x} \tag{4.10}$$

$$-B = \nu_{t_y} \frac{\partial \bar{\omega}}{\partial y} \tag{4.11}$$

Substituting Eq. 4.10 and Eq. 4.11 into the Eq. 4.7 to get

$$\frac{\partial \bar{\omega}}{\partial t} + \bar{u}\frac{\partial \bar{\omega}}{\partial x} + \bar{v}\frac{\partial \bar{\omega}}{\partial y} = \nu \frac{\partial^2 \bar{\omega}}{\partial x^2} + \nu \frac{\partial^2 \bar{\omega}}{\partial y^2} + \frac{\partial}{\partial x}\left(\nu_{t_x}\frac{\partial \bar{\omega}}{\partial x}\right) + \frac{\partial}{\partial y}\left(\nu_{t_y}\frac{\partial \bar{\omega}}{\partial y}\right) \tag{4.12}$$

Rearranging, the final form of the filtered vorticity equation is

$$\frac{\partial \bar{\omega}}{\partial t} + \bar{u}\frac{\partial \bar{\omega}}{\partial x} + \bar{v}\frac{\partial \bar{\omega}}{\partial y} = \frac{\partial}{\partial x}\left(\left(\nu + \nu_{t_x}\right)\frac{\partial \bar{\omega}}{\partial x}\right) + \frac{\partial}{\partial y}\left(\left(\nu + \nu_{t_y}\right)\frac{\partial \bar{\omega}}{\partial y}\right) \tag{4.13}$$

In the present work the Smagorinsky and the dynamic eddy viscosity models are employed. These SGS models have been implemented for the incompressible vorticity equation by Wang and Milane (2006) and they are presented in the following two sections for completeness of the text. While the Smagorinsky model formulations are independent of the density and can be applied for both incompressible and variable density flows, the dynamic SGS model is affected by the variable density (Vreman, Geurts and Kuerten 1997). This is the reason why the dynamic eddy viscosity model was only used in the incompressible (i.e. constant density) formulations.

4.1.2.1 Smagorinsky SGS Model

The Smagorinsky model is an eddy-viscosity model, where the effect of the subgrid scales is modeled purely as an enhanced diffusivity for the large-scale flow. The eddy viscosities ($\boldsymbol{\nu}_{t_j}$) for the Smagorinsky SGS model, shown in Eq. 4.13, are expressed, following Sagaut (2002) for an anisotropic flow as:

$$\nu_{t_x} = C_r^2 (\Delta^3)^{\frac{2}{9}} \Delta_x^{\frac{4}{3}} (2S_{ij}S_{ij})^{\frac{1}{2}}$$

$$\mathit{and} \qquad (4.14)$$

$$\nu_{t_y} = C_r^2 (\Delta^3)^{\frac{2}{9}} \Delta_y^{\frac{4}{3}} (2S_{ij}S_{ij})^{\frac{1}{2}}$$

Eq. 4.14 has been extended to anisotropic flow by simply using different filter sizes Δ_x and Δ_y in x- and y-direction respectively, $\Delta = \left(\Delta_x \Delta_y\right)^{1/2}$ or $\Delta = \max\left(\Delta_x, \Delta_y\right)$, and the modulus of strain rate for 2D flow $|\bar{S}| = \left(2S_{ij}S_{ij}\right)^{\frac{1}{2}}$ is given by

$$(2S_{ij}S_{ij})^{\frac{1}{2}} = \left[2\left(\frac{\partial \bar{U}}{\partial y}\right)^2 + \frac{1}{2}\left(\frac{\partial \bar{U}}{\partial y} + \frac{\partial \bar{V}}{\partial x}\right)^2\right]^{\frac{1}{2}}$$

$$\left[2\left(\frac{\partial \bar{V}}{\partial x}\right)^2 + \frac{1}{2}\left(\frac{\partial \bar{U}}{\partial y} + \frac{\partial \bar{V}}{\partial x}\right)^2\right]^{\frac{1}{2}} \qquad (4.15)$$

The SGS model constants depend on the type of the governing equations being vorticity or momentum equations and on the type of the SGS model used. In the current study, the constant for the Smagorinsky SGS model and the expression of the constant for the dynamic SGS model have been chosen following the work of (Mansfield, Knio and Meneveau 1998) where the constant $C_r = 0.12$, in Smagorinsky SGS model, has been obtained by balancing enstrophy production and dissipation for homogenous isotropic flow.

4.1.2.2 Dynamic SGS Model

In the dynamic SGS model implementation, C_r is calculated at each node for each time step. As shown in (Mansfield, Knio and Meneveau 1998), two equations are generated: the first one is the filtered vorticity equation using the physical filter size Δ and the second is obtained by filtering the filtered vorticity equation using an additional 'test' filter with a size of $\Delta' > \Delta$ and in particular $\Delta' = 2\Delta$. Then the first equation is filtered again using the test filter and the result is subtracted from the second equation, assuming the same subgrid scale model in both equations. This yields to an expression for the constant as

$$l = C_r^2 m$$

Where

$$l = l^c + l^s$$

$$m = m^D + m^Z$$

For a 2D simulation

$$l^s = 0$$

$$l^c = e_z \left\{ \overline{\bar{u} \frac{\partial \overline{\omega_z}}{\partial x}} + \overline{\bar{v} \frac{\partial \overline{\omega_z}}{\partial y}} - \bar{\bar{u}} \frac{\partial \overline{\overline{\omega_z}}}{\partial x} - \bar{\bar{v}} \frac{\partial \overline{\overline{\omega_z}}}{\partial y} \right\}$$

$$m^Z = 0$$

and

$$m^D = e_z\,\Delta^2 \frac{\partial}{\partial x}\overline{\left\{|\bar{S}|\frac{\partial \overline{\omega_z}}{\partial x}\right\}} + e_z\,\Delta^2 \frac{\partial}{\partial y}\overline{\left\{|\bar{S}|\frac{\partial \overline{\omega_z}}{\partial y}\right\}} - e_z\,\Delta'^2 \frac{\partial}{\partial x}\left\{|\bar{\bar{S}}|\frac{\partial \overline{\overline{\omega_z}}}{\partial x}\right\}$$

$$- e_z\,\Delta'^2 \frac{\partial}{\partial y}\left\{|\bar{\bar{S}}|\frac{\partial \overline{\overline{\omega_z}}}{\partial y}\right\}$$

For the 2D simulation the constant C_r is uniquely specified, unlike 3D- simulation where the constant is over-specified and error minimization is invoked. For any variable $\overline{\emptyset}$ calculated at the nodes, double filtering is calculated using the differential interpretation of the filter in which the second order terms are neglected (Sagaut, 2002), for both the top hat filter and the Gaussian filter $\overline{\overline{\emptyset}}$ is given as:

$$\overline{\overline{\emptyset}} = \overline{\emptyset} + \frac{\Delta}{24}\left[\frac{\partial^2 \overline{\emptyset}}{\partial x^2} + \frac{\partial^2 \overline{\emptyset}}{\partial y^2}\right]$$

And the product of two double filtered terms as:

$$\overline{\overline{\emptyset}}\,\overline{\overline{\eta}} = \bar{\phi}\,\bar{\eta} + \frac{\Delta^2}{24}\bar{\eta}\left[\frac{\partial^2 \overline{\emptyset}}{\partial x^2} + \frac{\partial^2 \overline{\emptyset}}{\partial y^2}\right] + \frac{\Delta^2}{24}\bar{\phi}\left[\frac{\partial^2 \bar{\eta}}{\partial x^2} + \frac{\partial^2 \bar{\eta}}{\partial y^2}\right]$$

$$+ \left(\frac{\Delta^2}{24}\right)^2 \left[\frac{\partial^2 \overline{\emptyset}}{\partial x^2} + \frac{\partial^2 \overline{\emptyset}}{\partial y^2}\right]\left[\frac{\partial^2 \bar{\eta}}{\partial x^2} + \frac{\partial^2 \bar{\eta}}{\partial y^2}\right]$$

4.1.3 Fractional Step

Similar to what was discussed in Section 3.1.3 for the compressible flow case, the method of fractional steps is used for the incompressible flow simulation. Therefore, Eq. 4.13 is split into two fractional steps:

$$\frac{\partial \bar{\omega}}{\partial t} + \bar{u}\frac{\partial \bar{\omega}}{\partial x} + \bar{v}\frac{\partial \bar{\omega}}{\partial y} = 0 \tag{4.16}$$

$$\frac{\partial \bar{\omega}}{\partial t} = \frac{\partial}{\partial x}\left(\left(\nu + \nu_{t_x}\right)\frac{\partial \bar{\omega}}{\partial x}\right) + \frac{\partial}{\partial y}\left(\left(\nu + \nu_{t_y}\right)\frac{\partial \bar{\omega}}{\partial y}\right) \tag{4.17}$$

In the first substep, the transport of vorticity due to convection is obtained from the solution of Eq. 4.16 in a similar fashion to what has been discussed in Section 3.1.3.1 with the only difference that for incompressible flows, the velocity field has only a solenoidal component therefore the stream function ψ is defined such that

$$\bar{u} = \nabla \times \psi$$

$$\bar{u} = \frac{\partial \psi}{\partial y} \; and \; \bar{v} = -\frac{\partial \psi}{\partial x} \tag{4.18}$$

For a two-dimensional flow, the vorticity vector reduces to one component in the z-direction perpendicular to the xy-plane (the plane of motion)

$$\bar{\omega} = \frac{\partial \bar{v}}{\partial y} - \frac{\partial \bar{u}}{\partial x} \tag{4.19}$$

Combining Eq. 4.18 and 4.19, the following Poisson equation is obtained

$$\nabla^2 \psi = -\bar{\omega} \tag{4.20}$$

Eq. 4.20 is then used to retrieve the convective velocity field from the vorticity.

In the second fraction step, the diffusion and SGS terms effects are simulated in a similar fashion as in Section 3.1.3.3, i.e. using the diffusion velocity method for Eq. 4.17 which with some manipulation is rewritten as

$$\frac{\partial \bar{\omega}}{\partial t} + \frac{\partial}{\partial \boldsymbol{x}_j}\left[\left(-\frac{\left(\nu + \boldsymbol{\nu}_{t_j}\right)}{\bar{\omega}}\frac{\partial \bar{\omega}}{\partial \boldsymbol{x}_j}\right)\bar{\omega}\right] = 0$$

and the diffusion velocities are

$$\tilde{\boldsymbol{u}}_{diff} = -\frac{\left(\nu + \boldsymbol{\nu}_{t_j}\right)}{\tilde{\omega}}\frac{\partial \tilde{\omega}}{\partial \boldsymbol{x}_j} \tag{4.21}$$

4.2 Scalar Field

The scalar field of the incompressible flow is governed by the scalar transport equation obtained from Eq. 3.44 by assuming a constant density and using the incompressible continuity equation (Eq. 4.1) to get

$$\frac{\partial \phi}{\partial t}+\frac{\partial u\phi}{\partial x}+\frac{\partial v\phi}{\partial y}=-\frac{\partial}{\partial x}\left(\Gamma\frac{\partial \phi}{\partial x}\right)-\frac{\partial}{\partial y}\left(\Gamma\frac{\partial \phi}{\partial y}\right)+S_\alpha \tag{4.22}$$

For the incompressible reactive flow situation, the scalar variable ϕ would represent the species mass fraction "Y_α”, with S_α being the reaction rate, Γ is the molecular mass diffusion coefficient related to the viscosity ν via the turbulent Schmidt number Sc_t, as $\Gamma = \nu/Sc_t$. In LES context Eq. 4.22 is filtered to become

$$\frac{\partial \bar{\phi}}{\partial t}+\frac{\partial \bar{\mathrm{u}}\bar{\phi}}{\partial x}+\frac{\partial \bar{\mathrm{v}}\bar{\phi}}{\partial y}=-\frac{\partial}{\partial x}\left(\Gamma\frac{\partial \bar{\phi}}{\partial x}\right)-\frac{\partial}{\partial y}\left(\Gamma\frac{\partial \bar{\phi}}{\partial y}\right)-\frac{\partial N_x}{\partial x}-\frac{\partial N_y}{\partial y}+\bar{S}_\alpha \tag{4.23}$$

Where the mass fraction and the reaction rate are decomposed as $\phi = \bar{\phi} + \phi'$ and $S_\alpha = \bar{S}_\alpha + S'_\alpha$, and the terms $N_x = \overline{\mathrm{u}\phi} - \bar{\mathrm{u}}\bar{\phi}$ and $N_y = \overline{\mathrm{v}\phi} - \bar{\mathrm{v}}\bar{\phi}$ are the unresolved subgridmass flux in x- and y-directions, respectively. Similar to what is done for the terms M_x and M_y in the compressible part of this study, the subgrid mass fluxes N_x and N_y are modeled using the eddy diffusion concept for an anisotropic flow as

$$\begin{gathered} N_x = -\Gamma_{\mathrm{t_x}}\frac{\partial \bar{\phi}}{\partial x} \\ and \\ N_y = -\Gamma_{\mathrm{t_y}}\frac{\partial \bar{\phi}}{\partial y} \end{gathered} \tag{4.24}$$

Substituting Eq. 4.24 into Eq. 4.25, to get

$$\frac{\partial \bar{\phi}}{\partial t}+\frac{\partial \bar{\mathrm{u}}\bar{\phi}}{\partial x}+\frac{\partial \bar{\mathrm{v}}\bar{\phi}}{\partial y}=-\frac{\partial}{\partial x}\left[\left(\Gamma+\Gamma_{\mathrm{t_x}}\right)\frac{\partial \bar{\phi}}{\partial x}\right]-\frac{\partial}{\partial y}\left[\left(\Gamma+\Gamma_{\mathrm{t_y}}\right)\frac{\partial \bar{\phi}}{\partial y}\right]+\bar{S}_\alpha \tag{4.25}$$

To predict the large scale scalar field, a filtered probability density function (FDF) is introduced (Colucci et al., 1998) and is similar to the large eddy probability density function (LEPDF) presented by Gao and O'brien (1993). Let $\phi(\boldsymbol{x}, t)$ denotes the scalar array; the FDF denoted by P_L is defined as

$$P_L(\xi; \boldsymbol{x}, t) = \int_{-\infty}^{+\infty} \delta\big(\xi - \phi(\boldsymbol{x}', t)\big)\, \mathrm{G}(\mathbf{x}' - \mathbf{x})\mathrm{d}\mathbf{x}' \tag{4.26}$$

Where

$$\delta\big(\xi - \phi(\boldsymbol{x}', t)\big) = \prod_{\alpha=1}^{\mathrm{N_S}} \delta\big(\xi_\alpha - \phi_\alpha(\boldsymbol{x}, t)\big) \tag{4.27}$$

δ is the Dirac delta function and represents the fine grained density of the scalar ϕ in one realization, ξ denotes the composition sample and N_s is the number of species. Eq. 4.26 implies that the FDF is the spatially filtered value of the fine grained density, P_L gives the probability density in the composition space of the fluid around x weighted by the filter G. The FDF transport equation can be obtained from the FMDF equation (Eq. 3.49) by assuming a constant density and using the incompressible continuity equation (Eq. 4.1). The FDF transport equation is

$$\begin{aligned} &\frac{\partial P_L}{\partial t} + \frac{\partial\left[\overline{\mathrm{u}|\boldsymbol{\xi}}\, P_L\right]}{\partial x} + \frac{\partial\left[\overline{\mathrm{v}|\boldsymbol{\xi}}\, P_L\right]}{\partial y} \\ &\qquad = \frac{\partial}{\partial \xi_\alpha}\left[\left(\overline{\frac{\partial}{\partial x}\left(\Gamma\frac{\partial \phi}{\partial x}\right)|\xi} + \overline{\frac{\partial}{\partial y}\left(\Gamma\frac{\partial \phi}{\partial y}\right)|\xi}\right) P_L\right] - \frac{\partial \overline{S_\alpha} P_L}{\partial \xi_\alpha} \end{aligned} \tag{4.28}$$

Where the symbol $\overline{\boldsymbol{u}|\boldsymbol{\xi}}$ indicates the filtered mean $\overline{\boldsymbol{u}}$ conditional on the satisfaction of the constraint $\boldsymbol{\xi}$, similar to what has been developed in the compressible flow case (Section 3.2); the convective term is decomposed via

$$\begin{aligned} &\overline{u|\xi}\, P_L = \bar{u}\, P_L + \left[\overline{u|\xi} - \bar{u}\right] P_L \\ &\text{and} \\ &\overline{v|\xi}\, P_L = \bar{v}\, P_L + \left[\overline{v|\xi} - \bar{v}\right] P_L \end{aligned} \tag{4.29}$$

Where the second term in the right hand side denotes the influence of SGS convective flux, this term is modeled as

$$\begin{aligned} &\left[\overline{u|\xi} - \bar{u}\right] F_L = -\Gamma_{t_x} \frac{\partial (P_L)}{\partial x} \\ &\text{and} \\ &\left[\overline{v|\xi} - \bar{v}\right] F_L = -\Gamma_{t_y} \frac{\partial (P_L)}{\partial y} \end{aligned} \tag{4.30}$$

The closure for the conditional subgrid diffusion is based on the modified curl model, which involves the decomposition of the diffusion term in Eq. 4.28 as follows

$$\begin{aligned} \frac{\partial}{\partial \xi_\alpha} &\left[\left(\overline{\frac{\partial}{\partial x}\left(\Gamma \frac{\partial \phi}{\partial x}\right) |\xi} + \overline{\frac{\partial}{\partial y}\left(\Gamma \frac{\partial \phi}{\partial y}\right) |\xi} \right) P_L \right] \\ &= \frac{\partial}{\partial x}\left(\Gamma \frac{\partial (P_L)}{\partial x}\right) + \frac{\partial}{\partial y}\left(\Gamma \frac{\partial (P_L)}{\partial y}\right) \\ &- \frac{\partial^2}{\partial \xi^2}\left[\overline{\left(\Gamma \left(\frac{\partial^2 \phi}{\partial x^2} + \frac{\partial^2 \phi}{\partial y^2}\right)\right) |\xi}\; P_L \right] \end{aligned} \tag{4.31}$$

The first and second term on RHS of Eq. 4.31 denotes the molecular diffusion in spatial transport of the FDF and is in closed form. The third term represents the dissipative nature of the subgrid scale mixing and needs to be modeled.

4.2.1 Modeled FDF Equation

By substituting Eq. 4.29, 4.30 and 4.31 into Eq.4.28, the modeled FDF transport equation is obtained as

$$\begin{aligned}\frac{\partial P_L}{\partial t}+\frac{\partial[\bar{\mathrm{u}}\,P_L]}{\partial x}+\frac{\partial[\bar{\mathrm{v}}\,P_L]}{\partial y}\\ =\frac{\partial}{\partial x}\left(\left(\Gamma+\Gamma_{\mathrm{t_x}}\right)\frac{\partial(P_L)}{\partial x}\right)+\frac{\partial}{\partial y}\left(\left(\Gamma+\Gamma_{\mathrm{t_y}}\right)\frac{\partial(P_L)}{\partial y}\right)\\ -\frac{\partial^2}{\partial\xi_\alpha\partial\xi_\beta}\left[\overline{\left(\Gamma\left(\frac{\partial\phi_\alpha}{\partial x}\frac{\partial\phi_\beta}{\partial x}+\frac{\partial\phi_\alpha}{\partial y}\frac{\partial\phi_\beta}{\partial y}\right)\right)|\xi}\,P_L\right]\\ -\frac{\partial(\bar{S}P_L)}{\partial\xi}\end{aligned}\tag{4.32}$$

The solution of Eq. 4.32 gives all statistical information concerning the reactive scalar field.

4.2.2 Monte-Carlo Scheme

The solution of the scalar FDF transport equation Eq. 4.32 is carried out by the same procedure used to solve the FMDF equation described earlier. The Monte-Carlo particles are moved either by convection or diffusion, and their compositions are altered due to mixing and chemical reaction. The particles motion due to convection, molecular and subgrid diffusivities is governed by the following stochastic differential equation (SDE) (Risken, 1989 and Gardiner, 1990)

$$d\boldsymbol{x}_i(t)=\boldsymbol{D}_i{}'(\boldsymbol{x}(t),t)dt+\boldsymbol{E}'(\boldsymbol{x}(t),t)d\boldsymbol{W}_i(t)\tag{4.33}$$

where $\boldsymbol{x}_i$ is the Lagrangian position of a stochastic particle, $\boldsymbol{D}_i{}'$ and $\boldsymbol{E}'$ are the drift and diffusion coefficients, respectively, and $\boldsymbol{W}_i$ denotes the Wiener-Levy process (Karlin and Taylor 1981). A simple comparison between Eq. 4.33 and the spatial derivative terms in the FDF transport equation Eq. 4.32 yields the expressions for the drift and the diffusion coefficients

$$\boldsymbol{E}' = \sqrt{2(\Gamma + \Gamma_T)} \qquad \boldsymbol{D}_i' = \bar{\boldsymbol{u}}_i + \frac{\partial(\Gamma + \Gamma_T)}{\partial x_i} \tag{4.34}$$

As for the species compositions in the particles, they are affected by the molecular mixing and chemical reaction terms denoted by the third and forth terms on the RHS of Eq. 4.32, respectively. The mixing term is unclosed and needs to be modeled whereas the reaction term is in closed form.

4.2.3 Molecular Mixing Model

The mixing term in the modeled FDF transport equation (Eq. 4.32)

$$\frac{\partial^2}{\partial \xi_\alpha \partial \xi_\beta}\left[\overline{\left(\Gamma\left(\frac{\partial \phi_\alpha}{\partial x}\frac{\partial \phi_\beta}{\partial x} + \frac{\partial \phi_\alpha}{\partial y}\frac{\partial \phi_\beta}{\partial y}\right)\right)|\xi}\, P_L\right]$$

is modeled using modified curl model as described by (Wang and Milane 2006) and has already been presented in Section 3.2.4.

4.2.3.1 Mass Conservation of the Mixing Model

The Monte-Carlo particles introduced to simulate the scalar field are assumed to be of equal masses. The mixing process assumes that two particles mix and separate instantaneously and the masses of each particle after mixing are equal and identical to the mass of particles prior to mixing. To illustrate mass conservation during binary mixing, particles which include three non-reactive species have been considered in the manipulation below. This can be easily extended to any number of species.

Assume a particle A of mass m_A composed of three species α, β and γ; m_A is equal to the sum of the masses of the species in particle A. Therefore $m_A = m_{A,\alpha} + m_{A,\beta} + m_{A,\gamma}$. Particle A is mixing with particle B having a mass $m_B = m_A$. Also, particle B is composed of species $\alpha, \beta\ and\ \gamma$ thus $m_B = m_{B,\alpha} + m_{B,\beta} + m_{B,\gamma}$. It is noted that, the mass fractions of each species in particle A and B are in general different i.e. $m_{A,\alpha} \neq m_{B,\alpha}$, $m_{A,\beta} \neq m_{B,\beta}$, $and\ m_{A,\gamma} \neq m_{B,\gamma}$. Using the modified Curl model, the masses of species α in particles A* and B* after mixing are

$$\begin{aligned} m^*_{A,\alpha} &= \left[(1-\alpha_{curl})m_{A,\alpha} + \frac{\alpha_{curl}(m_{A,\alpha}+m_{B,\alpha})}{2}\right] \\ &= m_{A,\alpha} + \frac{\alpha_{curl}}{2}(m_{B,\alpha} - m_{A,\alpha}) \\ m^*_{B,\alpha} &= \left[(1-\alpha_{curl})m_{B,\alpha} + \frac{\alpha_{curl}(m_{A,\alpha}+m_{B,\alpha})}{2}\right] \\ &= m_{B,\alpha} + \frac{\alpha_{curl}}{2}(m_{A,\alpha} - m_{B,\alpha}) \end{aligned} \tag{4.35}$$

Furthermore, the total mass of the particle A* is equal to

$$m^*_A = m^*_{A,\alpha} + m^*_{A,\beta} + m^*_{A,\gamma} \tag{4.36}$$

Substituting Eq. 3.58 into Eq.3.59 for each species

$$\begin{aligned} m^*_A = m_{A,\alpha} + \frac{\alpha_{curl}}{2}(m_{B,\alpha} - m_{A,\alpha}) + m_{A,\beta} + \frac{\alpha_{curl}}{2}(m_{B,\beta} - m_{A,\beta}) + m_{A,\gamma} \\ + \frac{\alpha_{curl}}{2}(m_{B,\gamma} - m_{A,\gamma}) \end{aligned}$$

By developing and rearranging, the mass of particle A* is

$$\begin{aligned} m^*_A &= (m_{A,\alpha} + m_{A,\beta} + m_{A,\gamma}) \\ &\quad + \frac{\alpha_{curl}}{2}\left[(m_{B,\alpha}+m_{B,\beta} + m_{B,\gamma}) - (m_{A,\alpha}+m_{A,\beta} + m_{A,\gamma})\right] \end{aligned}$$

Therefore,

$$m^*_A = m_A + \frac{\alpha_{curl}}{2}(m_B - m_A) = m_A = m_B = m^*_B = m$$

Furthermore, since $m_A = m_B$, therefore

$$m_A^* = m_A = m_B = m_B^*$$

In conclusion, the masses of particles are conserved after mixing. Frozen mixing is assumed first followed by chemical reaction. Therefore, the chemical reactions that occur inside each particle will only alter the composition and the mass fraction of each species while conserving the total mass of the particle.

4.2.4 Reaction Term Solution

As mentioned, one of the advantages of using the FDF method to solve for the scalar field is that the reaction term $\bar{S}_\alpha$ is in closed form. For the bimolecular reaction, $a + b \rightarrow c + d$ considered in this study, the source term is expressed as

$$\bar{S}_a = \bar{S}_b = -kX_aX_b \tag{4.37}$$

where k is the reaction rate and is assumed to be constant for the isothermal flow considered in this section of this study, X_a and X_b are the concentrations of species a and b respectively. The reaction terms are implemented by altering the composition of the particles using

$$\frac{d\phi_{A,\alpha}}{dt} = \bar{S}_{A,\alpha} \tag{4.38}$$

Eq. 4.38 describes the change of the mass fraction of species 'α' due to chemical reaction in particle 'A'. In simulating the reaction using the Monte Carlo technique, the species depleted or formed by chemical reactions are tracked. The mass fraction Y_α and the mole fraction X_α are needed to implement the mixing and reaction processes, respectively. Also, the mass fraction Y_α of species α, is related to its mole fraction X_α as

$$\phi_\alpha \equiv Y_\alpha = X_\alpha \frac{M_{w_\alpha}}{M_{w_{mix}}} \tag{4.39}$$

where $M_{w_{mix}}$ is the molecular weight of the species mixture given as

$$M_{w_{mix}} = \sum_{\alpha=1}^{N_s} X_\alpha M_{w_\alpha}$$

4.3 Initial and Boundary Conditions

The computational domain used to solve the two-dimensional flow and scalar fields of the isothermally reacting mixing layer experimented by Masutani and Bowmann (1986) is shown in Figure 4.1. It consists of a rectangular region covered by a uniform mesh system with different grid sizes in each direction (i.e. $\Delta x \neq \Delta y$). The lower left corner of the grid is located at $x = 1$ and $y = 1$.

4.3.1 Flow Field Initial and Boundary Conditions

The incompressible isothermal reacting mixing layer flow field is constructed with the same initial and boundary conditions as the thermal mixing layer flow discussed in Section 3.3.1. With the difference that in the incompressible formulation there is no dilatational velocity (i.e. $\tilde{u}_D = 0$), therefore the flow field is described only with the stream function ψ. Also, the Favre filtered solenoidal velocity $\tilde{u}_\omega$ in Section 3.3.1 is replaced with the bar filtered velocity $\bar{u}$.

4.3.2 Scalar Field Initial and Boundary Conditions

The scalar field configuration studied in this part of this work corresponds to the experiment of Masutani and Bowmann (1986) where the concentration structure and data on the dynamical variables are measured for a gas phase, reacting mixing layer flow. The simulation consisted of a mixing layer with two co-flowing streams with N_2 as a carrier gas in which NO and O_3 were introduced respectively into the upper and lower stream. The dominant reaction path is

$$NO + O_3 + N_2 \rightarrow NO_2 + O_2 + N_2$$

Masutani and Bowmann (1986) have indicated that in their experiment, this reaction occurs rapidly and irreversibly in dilute concentrations and have measured the temperature rise in the flow to be equal to 7 K, therefore, the isothermal flow condition can be assumed. The rate of depletion of O_3 and NO is

$$\bar{S}_{O_3} = \bar{S}_{NO} = -kX_{O_3}X_{NO}$$

where $X_{O_3}$and X_{NO} are the molar concentration of species O_3 and NO, respectively. The inlet boundary conditions have an error function profile given as

$$X_{\alpha(1,j)} = \frac{\Delta X_\alpha}{2} erf\left\{\frac{\sigma'(y - y'_{oc})}{x'_v}\right\} + X_{\alpha_c} \qquad \text{with } \alpha = NO \text{ or } O_3 \tag{4.40}$$

where subscript '$(1,j)$' corresponds to the inflow nodes, X_α denotes concentration of the species α, $\Delta X_\alpha = X_{\alpha_l} - X_{\alpha_h}$ is the concentration difference across the layer, the term $X_{\alpha_c} = (X_{\alpha_l} + X_{\alpha_h})/2$ is the average concentration, σ' is the spreading rate of the reacting mixing layer, y'_{oc} is the ordinate of centerline of the scalar field $y'_{oc} \neq y_{ov}$. The outflow boundary condition is not specified (Eq. 4.32 is parabolic) because the displacement of particles due to streamwise convection is very high, as compared to the displacement of concentration due to diffusion. Therefore, the concentration values in the downstream flow do not have any significant upstream effect.

4.4 Solution Procedure

The VIC algorithm and the Monte Carlo technique developed by Wang and Milane (2006) are used and extended to solve for the isothermal chemically reacting mixing layer. Since the chemical reaction is assumed to be isothermal, the scalar field does not affect the flow variables (i.e. passive scalars). Therefore, during each time step, the flow field is solved using the predictor-corrector scheme and then the velocity obtained is used in the solution of the scalar field. The same interpolation schemes discussed in Section 3.4 are employed to transfer flow and scalar variables between the Eulerian nodes and the Lagrangian vortices and Monte Carlo particles.

4.4.1 Flow Field Algorithm

During each time step, the vorticity transport equation (Eq. 4.13) is solved using the VIC algorithm (Wang and Milane, 2006). The solution procedure is summarized in the following steps. Also a representative flowchart is provided in appendix A.1

Initialization

a) Initializing by placing the equidistant vortices at the level of the splitter plate and by assuming arbitrary values for ψ at the internal nodes together with the boundary conditions.

Predictor step

b) Transfer the vorticity from the vortex particles to the nodes using the interpolation scheme.

c) Solve the Poisson's equations (Eq. 4.20) using Gauss-Seidel iteration with a left-to-right sweep of the nodes and bottom-to-top sweep of the lines. Iteration convergence is obtained when the percent difference between consecutive ψ is less than 0.001%.

d) Compute the velocities $\bar{\boldsymbol{u}}(t)$ at the nodes (Eq. 4. 18)

e) Transfer the velocities to the location of each vortex $\bar{\boldsymbol{u}}_n(t)$ using the interpolation scheme.

f) Compute the SGS eddy viscosities using the Smagorinsky or the dynamic SGS models, and then compute the diffusion velocity $\bar{\boldsymbol{u}}_{diff}(t)$ at the nodes.

g) Transfer the diffusion velocity to the location of each vortex $\bar{\boldsymbol{u}}_{n,diff}(t)$ using the interpolation scheme.

h) Update the co-ordinates of the vortices, while keeping the circulation constant

$$x^*(t+\Delta t) = x(t) + \left(\bar{\boldsymbol{u}}_n(t) + \bar{\boldsymbol{u}}_{n,diff}(t)\right)\Delta t$$

Corrector step

i) The corrector substep starts by transferring the new vorticity field from the new located vortices to the nodes by repeating step b). Then solve the Poisson's equation (Eq. 4.20).

j) Compute the new velocities $\bar{\boldsymbol{u}}^*(t+\Delta\mathrm{t})$ at the nodes (Eq. 4. 18).

k) Compute the SGS eddy viscosities using the Smagorinsky or the dynamic SGS models, and then compute the diffusion velocity $\bar{\boldsymbol{u}}^*{}_{diff}(t+\Delta t)$ at the nodes.

l) Transfer the diffusion velocity to the location of each vortex $\bar{\boldsymbol{u}}^*{}_{n,diff}(t+\Delta t)$ using the interpolation scheme.

m) Update the co-ordinates of the vortices, while keeping the circulation constant.

$$x(t+\Delta t) = x(t) + \frac{\left(\bar{\boldsymbol{u}}(t) + \bar{\boldsymbol{u}}_{diff}(t) + \bar{\boldsymbol{u}}^*(t+\Delta t) + \bar{\boldsymbol{u}}^*_{n,diff}(t+\Delta t)\right)}{2}\Delta t$$

Time advancement

n) Introduce a new vortex at the edge of the splitter plate and discard the oldest one.

o) March in time by repeating the calculations from step b) through o).

4.4.2 Scalar Field Algorithm

The scalar field is defined by solving the FDF transport equation Eq. 4.32 using the Monte-Carlo scheme discussed in details in Wang (2005). Briefly, the steps are as follow

1- Initialize the number of particles in the computational domain by prescribing particles to each grid cell and assign initial concentration to each particle using the error function profiles Eq. 4.40.

2- Calculate $\boldsymbol{D}_i'$, $\boldsymbol{E}'$ from Eq. 4.34 and the mixing frequency $\overline{\omega_f}$ using Eq. 3.56.

3- Transfer $\boldsymbol{D}_i'$ and $\boldsymbol{E}'$ from the nodes to particle locations using the interpolation scheme and then move the particles using Eq. 4.33.

4- Transfer the mixing frequency from the nodes to particles using the interpolation scheme and calculate the arithmetic average mixing frequency $\overline{\omega_f}$ in each grid.

5- Calculate the number of mixing pairs $n_m$using the Modified Curl model. The pairs are selected randomly and new concentrations assigned for each species in each particle.

6- March in time by repeating steps 3 to 6 is performed only within the defined range of time steps.

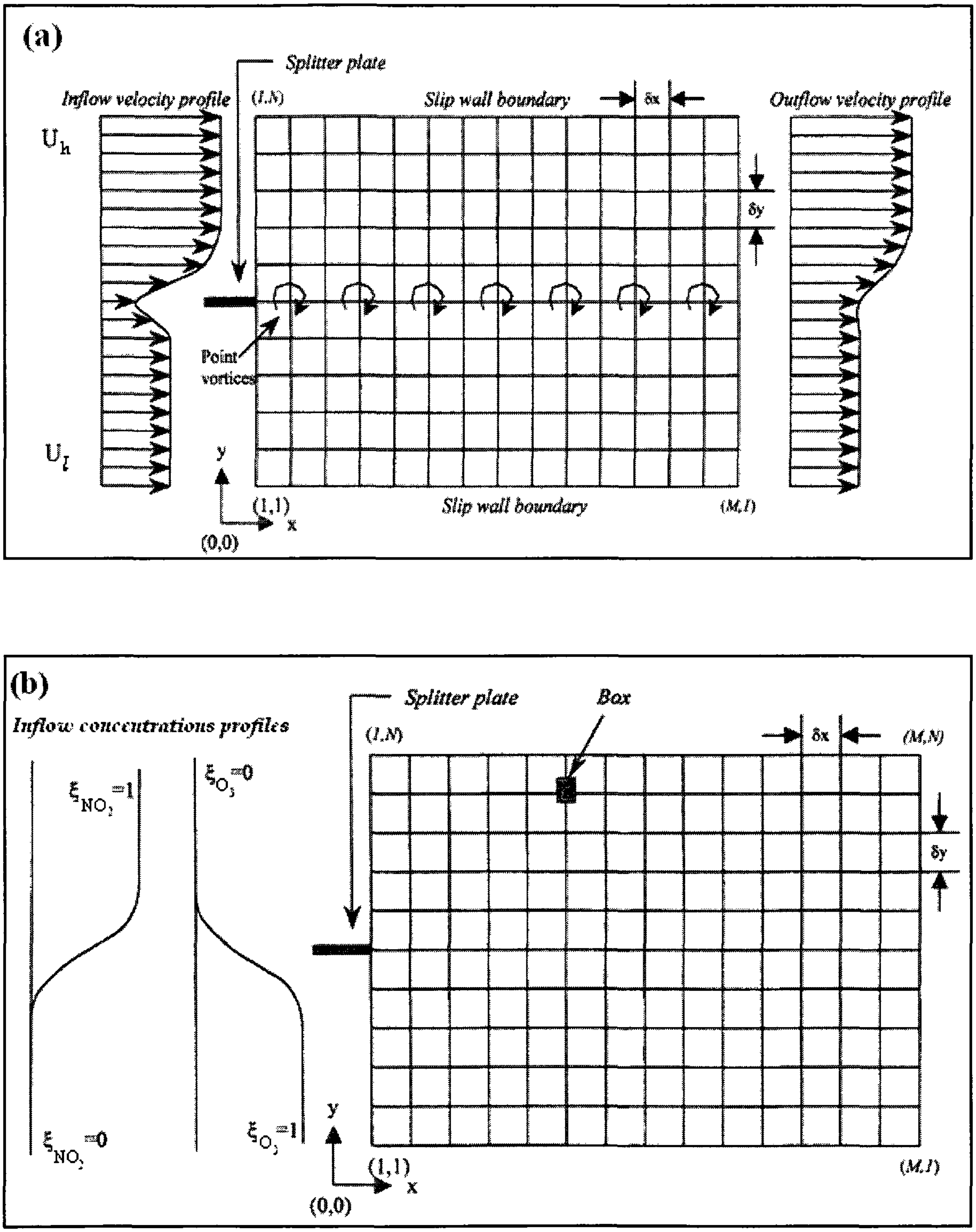

Figure 4-1: Chemically reacting mixing layer with no heat release (a) flow field computational domain, rectangular grid, initial position of the vortices, and boundary conditions. (b) Scalar field computational domain, rectangular grid, box and boundary condition.

Chapter 5

ISOTHERMAL NON-REACTING AND REACTING MIXING LAYER

5.1 Flow Field for Non-Reacting and Reacting Mixing Layer

In this section, the flow field results of the non-reacting mixing layer simulation are presented. Also since the reacting flow is assumed to be isothermal, the flow field will remain the same for the reacting mixing layer simulation. The results selected to describe the flow field include: the location of vortex particles, the vorticity contours, the mean flow velocity, the vorticity thickness, the root-mean-square (rms) velocities fluctuations and the negative cross-stream correlation.

5.1.1 Numerical Parameters

The flow configuration studied in this work represents a mixing layer similar to the experiment of Masutani and Bowmann (1986) (M&B). The profiles from the experiment of M&B are shown in the following sections as reference only because direct comparison between unfiltered experimental data and LES (i.e. filtered) results is not ideal. The ratio of the free-stream mean velocities $r = U_h/U_l$ was fixed at 2, with the top stream velocity $U_h = 6\, m/s$ faster than the bottom stream velocity $U_l = 3\, m/s$. The reported results are for a viscous flow condition with $\nu = 15.69 \times 10^{-2}\, cm^2/s$ (the kinematic viscosity of N_2 at 27 °C).

For the base run, the computational flow domain consists of 210x210 nodes forming an anisotropic uniform mesh with an aspect ratio $a_{xy} = \frac{\Delta x}{\Delta y} = 2$; $\Delta x = 0.5\, cm$ and $\Delta y = 0.25\, cm$ being the grid size in x- and y-directions, respectively. The aspect ratio is chosen to be consistent with what Kaltenbach (1977) has reported on the representation of shear flows being most economical when anisotropic grid ($a_{xy} > 1$) is used because it produces adequate values for ratios of Reynolds stresses when LES is used. Anisotropic grid has been used in LES of channel flow by Deardoff (1970) with $a_{xy} = 2$ and Shumann (1975) with $a_{xy} = 3.7$. For the LES runs, in this study, the filter sizes are set to twice the grid size in each direction, i.e. $\Delta_x = 2\Delta x$ and $\Delta_y = 2\Delta y$.

At the level of the splitter plate an initial vortex sheet is introduced consisting of $N_v = 3150$ equidistant vortex particles. Therefore, the circulation of each vortex particle is $\Gamma_i = \frac{(U_h - U_l) \times N_x \times \Delta x}{N_v} = 9.95 \times 10^{-4}\, m^2/s$, with N_x being the number of grid in the x-direction. The residence time is $t_{res} = \frac{N_x \times \Delta x}{U_{avg}} = 0.23\, sec.$, while the time step is calculated as $\Delta t = \frac{d}{U_{avg}} = 1.11 \times 10^{-4}\, s$, where d is the initial spacing between the vortices.

The flow is allowed to develop for two residence times (i.e. $2N_v$ time steps) before the statistical information are calculated. The mean flow quantities are obtained using time averaging over the next four residence times, the root-mean-square (rms) velocity fluctuations, the negative cross-stream correlation and the rms vorticity fluctuations are calculated using time-averaging over the next eight residence times.

The base run is performed using the dynamic SGS model; the results obtained are presented in Sections 5.1.2 to 5.1.5. LES results using the Smagorinsky SGS model are discussed in Section 5.1.6. Comparison between LES results and results with no SGS are discussed in Section 5.1.7.

5.1.2 Vortex Particles Location

The development of the mixing layer structure is presented in Figure 5-1 by displaying the instantaneous locations of all the vortex particles used in the computations at five different times. The plot shows the roll-up and pairing of large vortical structures along the two distinct ranges of the mixing layer: initially the particles are organized into semi-round structures prior to the first roll-up, then large eddies are formed by pairing process. Pairing starts as soon as eddies reach their maximum growth, and continues to join two eddies into a larger structure. As noticed by Ghoniem and Heidarinejad (1990), few eddies are observed to escape pairing at least in the range of the computational domain and pairing of more than two eddies are seen occasionally.

5.1.3 Mean Velocity and Vorticity Thickness

In Figures 5-2(a) and (b), the calculated normalized mean velocities are plotted against the similarity variable at four downstream locations and compared to the measured results of M&B and the LES results of Zhou and Pereira (2000) (Z&P), respectively. The similarity variable is given as $\eta_v = \frac{(y-y_0)}{(x-x_v)}$, with y_0 being the lateral location where the streamwise mean velocity corresponds to the centerline velocity $U_{avg} = \frac{1}{2}(U_h + U_l)$ and x_v being the virtual origin of the velocity field defined as the x-location where the centerline velocity intersects the horizontal line at the level of the splitter plate. Figures 5-2(a) and (b) show that the calculated normalized mean velocity profiles are in good agreement with the experimental results of M&B and the calculated results of Z&P, respectively, in the self-preserving region, which extends from $0.4 \leq x/H_x \leq 0.6$.

The self-preserving region corresponds to the region of linear growth of the vorticity thickness δ_ω shown in Figure 5-3. The vorticity thickness is computed as

$$\delta_\omega = \frac{\Delta U}{(\partial \bar{U}/\partial y)_{max}}$$

where $(\partial \bar{U}/\partial y)_{max}$ is the maximum gradient of the mean velocity $\bar{U}$. Figure 5-3 shows the downstream evolution of the vorticity thickness. The growth rate of the vorticity thickness $d\delta_\omega/dx$ is about 0.062 in the region $0.4 \leq x/H_x \leq 0.6$. This is less than the value of 0.0706 found by M&B but close to the value of 0.0603 obtained by Brown and Roshko (1974). M&B indicated that the growth of their layer was about 15-20% larger than the value measured by the majority of other experiments. The difference in the layer growth rate may be due to a possible establishment of an acoustic field within the experiment of M&B. This acoustic field can enhance the growth of the layer by initiating early roll-up and pairing of vortices. The effect of the difference in the growth rate will appear when comparing other flow statistics.

5.1.4 Root-Mean-Square Velocity Fluctuations and Negative Cross-Stream Correlations

As shown in Figures 5-4(a) and (b), the normalized rms longitudinal velocity fluctuations $(u'_{rms}/\Delta U)$ agree well with the experimental results of M&B and the calculated results of Z&P in the self-preserving region. The values of u'_{rms} in the simulation increase along the stream-wise direction whereas it decreases in the experimental data. Similar behavior is found in the numerical work of Ghoniem and Heidarinajad (1990), who argued that the experimental trend is caused by dissipation due to molecular diffusion. The normalized lateral velocity fluctuations $(v'_{rms}/\Delta U)$ in Figure 5-4(c) are consistent with previous 2D simulations of Wang and Milane (2006).

The measurements for the Reynolds shear stress $\left(-\overline{u'v'}/\Delta U^2\right)$ are not reported in M&B. However in Figure 5-4(d), the peak values for the Reynolds shear stresses $(-\overline{u'v'}/\Delta U^2 = 0.015)$ are consistent with previous simulations of Wang and Milane (2006). Furthermore they are comparable with the peak of 0.013 obtained in the experiment of Oster and Wygnanski (1982) for a velocity ratio of 0.6, which is slightly different than the value of 0.5 used in the present simulation.

The agreement between the numerical and experimental results could have been improved if $(y - y_0)$, in the similarity variable η_v, was normalized with respect to the local vorticity thickness δ_ω instead of $(x - x_v)$, since this would have absorbed the impact of the difference between the spread rates of the numerical and experimental results. Other factors, which might have contributed to the difference between the numerical predictions and the experimental data, include the relative amplitude of noise in the numerical and experimental results, the scatter in experimental results, the finite probe size of the measurement device and the finite sample used in averaging the experimental and numerical results.

5.1.5 LES Results

LES results using Smagorinsky SGS are shown in Figures 5-5(a)-(d) together with the experimental results of M&B and the LES results of Z&P. Figures 5-5(a) and (b) show that the normalized mean velocity results indicate adequate self-similar profiles in the region $0.4 \leq x/H_x \leq 0.7$ consistent with the region of nearly linear growth of the vorticity thickness shown in Figure 5-3. In Figures 5-5(c) and (d), the longitudinal rms velocity fluctuations profiles indicate a self-similar trend and are in agreement with the experimental results of M&B and the LES results of Z&P.

5.1.6 SGS Effects

In order to emphasize the dissipative effect of the SGS models on the flow field results, three runs are made and compared: a run without SGS, a run with the dynamic SGS model and a run with the Smagorinsky SGS model.

5.1.6.1 Vorticity Contours

In the present two-dimensional study and due to the inflow mean profile, the spanwise vorticity is initially negative (i.e. clockwise) implying that the vorticity remains negative during the calculations. Figures 5-6(a)-(c) show the magnitude of the spanwise vorticity contours as they develop downstream for the three cases under study. The contours spread and broaden in the free stream as they develop from the edge of the splitter plate. The maximum vorticity contour level decreases as SGS models are applied consistent with their dissipative nature (see legend): it attained 1700 for the case without SGS in Figure 5-6(a), 1600 for the case with dynamic eddy viscosity SGS model in Figure 5.6(b) and 1400 for the case Smagorinsky SGS model in Figure 5-6(c). Close-up of chosen downstream locations between $x/H_x = 0.7$ and 0.8 are scaled identically and shown in Figures 5-7(a)-(c). For the case without SGS model, the vorticity contours peak at a value of 700 as indicated in Figure 5-7(a), whereas the contours peak drops to values of 600 and 300 when the dynamic eddy viscosity SGS model and the Smagorinsky SGS model are used, in Figure 5-7(b) and (c), respectively. Furthermore, the Smagorinsky SGS model is shown to be more dissipative than the dynamic eddy viscosity SGS model, similar results were reported by Wang and Milane (2006).

5.1.6.2 Root-Mean-Square Velocity and Vorticity Fluctuations, and Negative Cross-Stream Correlations

Comparison between profiles of various statistics for the three runs, at the downstream location $x/H_x = 0.6$, is shown in Figures 5-8(a)-(d). The peaks of the normalized u'_{rms} and v'_{rms}, shown in Figures 5-8(a) and (b), respectively, are higher for

LES with dynamic eddy viscosity model as compared to the case with Smagorinsky SGS model, but lower than the case without SGS model. This is again consistent with the fact that the dynamic eddy viscosity model is less dissipative than Smagorinsky SGS model (Vreman et al., 1997). The peaks of the negative cross-stream correlation $\left(-\overline{u'v'}/\Delta U^2\right)$ and the rms vorticity fluctuation ω'_{rms} in Figures 5-8(c) and (d), respectively, are lowered as the dissipative effect of SGS is increased, consistent with the lower contour level peaks in Figures 5-6(a)-(c) and 5-7(a)-(c).

5.1.6.3 Vorticity Thickness

Figure 5-9 shows the downstream evolution of the vorticity thicknesses for the three runs with and without SGS modeling. Consistent with other flow results discussed in the previous two sections, the profiles reveal slightly higher vorticity thickness in the self preserving region for the run with Smagorinsky SGS model due to the higher dissipation this model imposes on the flow. Moreover, the downstream evolution of vorticity thickness grows at a faster rate past the self preserving region $x/H_x > 0.6$ due to end effects caused by the outflow boundary condition (Abdolhosseini et al., 2000).

5.2 Scalar Field for Non-Reacting and Reacting Isothermal Mixing Layer

In this section, the scalar fields of the non-reacting and reacting isothermal mixing layers are discussed. The numerical parameters used to describe the scalar fields are presented in Section 4.2.1; scalar field results for non-reacting and reacting flows are presented in Sections 4.2.2 and 4.2.3, respectively.

5.2.1 Numerical Parameters

Simulations of the scalar field are conducted on a rectangular computational domain identical to the flow field computational domain. The initial number of particles per grid is $N_g = 36$ which is within the range of 20-200 suggested by Jaberi et al. (1999). The scalar field variables and statistics are approximated at the nodes using particles located in rectangular boxes centered at nodes. The box size is set to be less than half of the grid size to avoid overlapping. The approximation becomes more accurate as the box size is decreased and as the number of particles in the box is increased. In this study, the box size is set to 0.4 of the grid size. The value of y'_{oc} used in Eq. 4.40 is set to $26.05\ cm$.

The FDF solution requires specifying the constants Sc_t and C_ϕ. The constant C_ϕ is set to a value of $C_\phi = 3.0$. The values of the constant C_ϕ fall within the range $0.6 < C_\phi < 3.1$ suggested by Pope (1985). The turbulent Schmidt number employed is $Sc_t = 0.7$ similar to the one used in Z&P.

To achieve statistically stationary solutions, the Monte-Carlo simulation is run for 14 residence times. Similar to the flow field run, the first two residence times ensured the development of the flow. Then the mean concentrations are computed over the next four residence times. The rms concentration fluctuations and PDFs are computed over the last eight residence times. The base run consists of the run using the dynamic SGS model.

5.2.2 Non-Reacting Mixing Layer

Results of the non-reacting mixing layer are obtained from simulations in which only O_3 species were introduced into the low speed (3m/s) stream with initial concentration of $X_{O_{3,\infty}} = 1000\, ppmV$. At the inflow boundary, the distribution of the concentration immediately downstream of the splitter plate is described by an error function with $y'_{oc} = 26.05\ cm$ used in Eq. 4.40.

The normalized mean concentration and rms concentration fluctuations are presented in Section 4.2.2.1; the instantaneous concentration profiles in Section 4.2.2.2; the FDF results in Section 4.2.2.3; the LES results in Section 4.2.2.4 and the SGS effects are discussed in Section 4.2.2.5.

5.2.2.1 Normalized Mean Concentration and RMS Concentration Fluctuations

Figures 5-10(a) and (b) show the normalized mean O3 concentration ($\bar{\xi}_{O_3} = X_{O_3} / X_{O_{3,\infty}}$) plotted as a function of the similarity variable $\eta_c = \frac{(y-y_c)}{(x-x_{vc})}$, where y_c and x_{vc} are the concentration analogues of y_0 and x_v. Figures 5-10(a) and (b) show that the mean concentration profiles calculated have achieved similarity for $0.45 \leq x/H_x \leq 0.6$, and are close to the experimental values of M&B and to the calculated results of Z&P, respectively. The concentration spread appears to extend further on the high speed side ($\eta_c > 0$) than on the low speed side ($\eta_c < 0$). This shows that the mixing layer entrains more particles from the high speed stream than from the low speed stream. The mean concentration profiles exhibit triple inflection point for $x/H_x = 0.5$, 0.6 and 0.75 similar to the results of M&B and Z&P. However, for $x/H_x = 0.45$, the triple inflection point is less pronounced, because the flow is still developing.

The normalized rms concentration fluctuations profiles ($\xi_{O_3,rms}$) for O3 species are shown in Figures 5-10(c) and (d) as a function of η_c at four different downstream locations. The rms concentration fluctuations profile is an indication to the degree of homogeneity of the flow: it has a maximum value of 0.5 when mixing two streams of immiscible substances and a value of zero when only homogeneous fluid appears. The calculated rms concentration fluctuations never attain the value of 0.5, and are slightly higher than the experimental results of M&B but in good agreement with the calculated results of Z&P. As expected, the rms concentration profiles exhibit a bimodal shape with respect to $\eta_c = 0$, with values on the high speed side ($\eta_c > 0$) lower than the values on the low speed side ($\eta_c < 0$) due to mixing asymmetry. This indicates that the rate of entrainment of high speed fluid exceeds the rate of entrainment of the low speed fluid.

5.2.2.2 Instantaneous Concentration and Vortex Structure

The enlarged and detailed concentration contours of the non-reacting, premixing transition mixing layer are visualized in Figure 5-11 between $x/H_x = 0.41$ and 0.48. The large scale concentration structures and the finite-thickness diffusion zones are clearly visible. There is a continuous distorted interface between the regions of unmixed fluids and a nearly homogeneous core consisting of mixed fluid. This observation suggests that, prior to mixing transition, the fluid in the plane mixing layer exists in three states: tongues of unmixed free-stream fluid stretching all the way across the layer; finite-thickness diffusion zones of mixed fluid which border the volumes of unmixed fluids; and cores of mixed fluid of nearly homogeneous composition.

The evolution of the concentration contours is shown in Figures 5-12 at five different times. Figures 5-12 suggest, in consistency with the experimental observations, that entrainment and mixing of free-stream fluid are achieved by a process of engulfment, diffusional mixing and ingestion into the homogeneous core flow regions. In this process, free-stream fluid penetrates deep within the mixing region, drawn in by the velocity field induced by the primary vortices. These volumes of gas from the two feeder streams are brought into contact and interfacial diffusional mixing zones form. These regions with a finite-thickness are characterized by large continuous spatial gradients of concentration. The continuous gradients imply that molecular diffusion is a major mechanism for mixing in these interfacial regions. Eventually, the mixed fluid is incorporated into the cores. It is noted that during vortex pairing events, large volumes of free-stream fluid characterized by thick tongues of unmixed fluid may bypass the diffusional mixing process and be drawn directly into the core regions.

Figures 5-13 show the instantaneous concentration of O_3 at different downstream locations, superimposed on the instantaneous distribution of the vortex. The locations are chosen across the midsection of the vortex in Figures 5-13(a)-(c), and across the braids in Figures 5-13(d)-(f). The instantaneous concentration profiles reveal that, even at sections far downstream of the splitter plate, zones of completely unmixed fluid still exist within the layer. These zones correspond to the gulfs or "tongues", of pure fluid brought into the layer from either side by the inviscid mechanism of entrainment (Ghoniem and Heidarinejad, 1990). Across the braids, the instantaneous concentration changes between the free stream values within a distance comparable to the initial mixing layer thickness described by the error function profile.

5.2.2.3 Filtered Probability Density Function

Each particle of the ensemble N (total number of particles in the box centered at each node) is identified by a value of the concentration $0 \le X_{O_3} \le 1000$ ppmv which is normalized to give $0 \le \xi_{O_3} \le 1$. In order to obtain the probability, the range of ξ_{O_3} is subdivided into 100 windows, so that any particle belongs in an interval based on its value of ξ_{O_3}. The probability of finding a particle with concentration ξ_{O_3} falling in a given window interval is written as,

$$P(\xi_{O_3})\Delta\xi_{O_3} = \frac{n}{N}$$

where n is the number of elements in the window interval and $P(\xi_{O_3})$ is the FDF. The behavior of the ensemble of FDFs can be characterized as marching and non-marching. For marching FDFs, the most probable value on each side of the layer is closer to the free stream value of that side, whereas for the non-marching FDFs, the most probable value of the scalar is substantially independent of the position in the layer.

A representative three-dimensional plot for the FDF of the mixture fraction is presented in Figure 5-14 for the downstream location $x/H_x = 0.55$. Mixture fraction FDFs at other downstream locations $0.4 \leq x/H_x \leq 0.75$ were qualitatively similar. In these three-dimensional plots, the filtered probability density is given as a function of the normalized concentration ξ_{O_3} and the similarity coordinate η_c. The plot shows the evolution of the FDF of ξ_{O_3} across the mixing layer. The spikes in the FDF at $\xi_{O_3} = 1$ and 0, which persist for some distance into the layer indicate the presence of pure unmixed fluid from either of the free stream. The presence of a third peak in the FDF between concentration ξ_{O_3} of 0 and 1 indicate that a preferred concentration $\xi_{O_3,p}$ exists in the mixed fluid. The establishment of a preferred mean concentration $\xi_{O_3,p}$ is caused by the mechanism of asymmetric mixing. Mixing asymmetry which arises due to the asymmetric growth of eddies during the initial stages of the roll-up, is indicated by the fact that the profiles are not symmetric around the line $\xi_{O_3} = 0.5$. The normalized preferred mean concentration is the value of ξ most likely to be found within the cores of the structures. The value of $\xi_{O_3,p}$ at a given streamwise location in the flow does not vary across the mixing layer, an indication that the FDF is non-marching.

Figures 5-15(a)-(d) show the FDFs at selected downstream locations for $x/H_x = 0.4,\ 0.5,\ 0.6$ and 0.75. Figures 5-15(a)-(d) reveal that the value of the preferred concentration $\xi_{O_3,p}$ increases with downstream evolution of the mixing layer, it varies from a value of approximately 0.25 at $x/H_x = 0.4$ to a value of 0.3 at $x/H_x = 0.75$. This indicates an increasing proportion of low-speed fluid in the homogeneous zones with increasing distance from the splitter plate. Also, since $\xi_{O_3,p} \leq 0.3$, therefore, the mixed fluid in the layer comprises less fluid from the low-speed feed stream than from the high-speed feed stream, similar behavior have been reported by M&B.

5.2.2.4 LES Results Using the Smagorinsky SGS Model

Figures 5-16(a) and (b) show the normalized mean O_3 concentrations for the LES runs using the Smagorinsky SGS model, together with the experimental results of M&B and the calculated LES results of Z&P, respectively. The Figures show that LES results using Smagorinsky SGS model attain self-similarity in the downstream region $0.4 \leq x/H_x \leq 0.6$ and are in good agreement with both the experimental results of M&B and the calculated results of Z&P. Figures 5-16(c) and (d) show that the rms O_3 concentration fluctuations profiles indicate a self similar trend and are close to the experimental data of M&B and the calculated results of Z&P. Moreover, in Figure 5-16(d), the LES results using the Smagorinsky SGS model indicate lower rms concentration fluctuations when compared to the results of Z&P. This may lead to the conclusion that the Smagorinsky SGS model is more dissipative than the structure-function model employed by Z&P.

5.2.2.5 SGS Effects

Figures 5-17(a)-(f) reveal the effect of SGS models under study by comparing the profiles of mean concentration and rms concentration fluctuations, using three different runs: without SGS modeling, with Smagorinsky SGS model having $C_r = 0.12$ and with the Dynamic Eddy Viscosity SGS model, at three different locations downstream of the splitter plate corresponding to $x/H_x = 0.4, 0.5$ and 0.6. In Figures 5.17(a), (b) and (c), the mean concentration exhibits triple inflection point for all the three runs in the high speed side region. The inflection point of the run without SGS modeling at about $\eta_c = 0.04$ is slightly further to high speed side than that of Dynamic eddy viscosity and Smagorinsky SGS models.

The profiles of rms concentration fluctuations are shown in Figures 5-17(d), (e) and (f). The profiles for the Smagorinsky SGS model run are lower than the profiles of the Dynamics eddy viscosity model and of the simulation without SGS modeling. This is due to the fact that the Smagorinsky SGS model is more dissipative and consequently yields higher mixing frequency thus the flow tends to be more homogeneous than the other two simulations.

Figures 5-18(a)-(d) reveal the effect of the SGS models on the filtered probability density function at four different downstream locations in the high speed side region ($\eta_c > 0$). The results of Smagorinsky SGS model indicates a most probable and highest preferred concentration $\xi_{O_3,p}$ compared to the other two runs. The dynamic eddy viscosity SGS model shows some dissipative effect marked by a slightly higher peak than the run without SGS model. Comparison of the PDF and FDFs for the three runs shows that the more dissipative SGS model yields a preferred concentration $\xi_{O_3,p}$ with a higher peak in PDF and a value closer to the mean concentration value of $\xi_{O_3} = 0.5$. Results in the low speed side region ($\eta_c < 0$) are similar to high speed side region ($\eta_c > 0$).

5.2.3 Reacting Mixing Layer

The Damköhler number Da is defined as

$$Da \equiv \frac{\tau_m}{\tau_c} = \frac{characteristic\ mixing\ time}{characteristic\ chemical\ time}$$

By this definition, $Da \ll 1$ implies frozen chemistry and $Da \gg 1$ implies fast chemistry. The characteristic chemical times in the present simulations may be estimated from

$$\tau_c \equiv 1/kX_{NO,\infty}$$

where $X_{NO,\infty} = 8500\, ppmv$ is the mole fraction of the rich reactant in the upper free stream conditions, and k is the chemical reaction rate. Broadwell and Breidenthal (1982) have suggested two timescales brackets for the mixing times in boundary free mixing zones. The Eddy turnover (or the cascade time),

$$\tau_\delta \approx \delta_\omega/\Delta U$$

and the small-scale diffusion time,

$$\tau_{\lambda_0} \approx \tau_\delta\, Sc\, Re^{-\frac{1}{2}}$$

Where Sc is the Schmidt number, Re is the Reynolds number and τ_{λ_0} is the time required to diffuse across the Kolmogorov scale. M&B stated that in the conditions of their experiment $\tau_\delta/\tau_{\lambda_0} = 30$, suggesting that the rate limiting the mixing step is characterized by τ_δ. Therefore

$$Da = \frac{\tau_\delta}{\tau_c}$$

The vorticity thickness used in the present calculation of τ_δ is taken as the average thickness in the self-similarity region $0.4 \leq \mathrm{x}/\mathrm{H_x} \leq 0.6$, where the results are presented.

In the present calculation of the reacting mixing layer, O_3 was injected into the low-speed stream, and NO in excess of stoichiometric proportion was injected into the high speed stream. The carrier gas is N_2. The ratio of reactant concentration, (X_{O_3}/X_{NO}) is 0.118 with $X_{O_3} = 1000\,ppmV$ and $X_{NO} = 8500\,ppmV$. The dominant reaction path between O_3 and NO is $\mathrm{NO} + \mathrm{O_3} \rightarrow \mathrm{NO_2} + \mathrm{O_2}$. The reaction rate is set to $k = 0.41\ (ppmV.s)^{-1}$ corresponding to $Da = 30.5$, similar to the value used in the LES of Z&P and consistent with the experiment of M&B.

The normalized mean reactant and product concentrations are presented in Section 5.2.3.1; the instantaneous concentration profiles and contour plots are displayed in Section 5.2.3.2; the FDF results are presented in Section 5.2.3.3; the LES results using the Smagorinsky SGS model are presented in Section 5.2.3.4 and the SGS effects on the reactive scalar field results are discussed in Section 5.2.3.5.

5.2.3.1 Normalized Mean Reactant and Product Concentration

In Figures 5-19(a) and (b), the normalized mean reactant O_3 concentration are plotted as a function of the similarity variable η_c, at four downstream locations. Also included in the figure is the profile of O_3 concentration for the non reactive flow at the location $x/H_x = 0.55$, shown as a solid black line. The profiles appear to attain similarity for $0.4 \leq x/H_x \leq 0.6$ and are in good agreement with the experimental data of M&B and the calculated results of Z&P. As anticipated, chemical reaction depletes the mean O_3

concentration in the layer. The triple inflection point that once was present in the concentration profile for the non-reactive flow has vanished to leave behind a smooth error function–like profile for the reactive flow. This indicates the depletion of O_3 species in the cores of the vortex structures due to chemical reaction. Also, it is noted the substantial decrease in the values of the mean concentration when comparing the non-reactive flow profile to the reactive flow results; for instance, at $\eta_c = 0$ which is defined as the location where the normalized mean concentration has a value of 0.5 for the non-reactive flow, the results for the chemically reacting mixing layer show a 50% decrease with a value of 0.25.

The product (NO_2) concentration is normalized by the mean value of the O_3 mole fraction in the free stream

$$\xi_{NO_2} = \frac{X_{NO_2}}{X_{O_3,\infty}}$$

In Figures 5-19(c) and (d), the calculated mean normalized product concentration ($\bar{\xi}_{NO_2}$) profiles show a slight increase in mean concentration values with downstream evolution of the flow. This is due to the fact that the reaction $\mathrm{NO} + \mathrm{O}_3 \rightarrow \mathrm{NO}_2 + \mathrm{O}_2$ is irreversible for the present conditions, therefore once the product species are formed, they behave as inert scalars, being dispersed by macroscopic and molecular transport and accumulated within the mixing region. At $x/H_x = 0.55$ the product concentration results show a good accuracy with the data measured in the experiment of M&B and the calculated results of Z&P.

5.2.3.2 Instantaneous Concentration and Vortex Structure

Figures 5-20(a) and (b) show the instantaneous concentration contours of reactant (O_3) and product (NO_2) in the plane-reacting mixing layer. A comparison of the reactive and non-reactive concentration ξ_{O_3} structure (see Figures 5-20(a) and 5-12, respectively) shows that significant amount of O_3 in the mixing region are consumed.

Reactant species must be mixed at the molecular level for reaction to occur. The free-stream fluid that has been entrained into the mixing layer, but remains unmixed (corresponding to $\xi_{O_3} = 1$ in the tongues structures), will not undergo reaction. However, Figure 5-20(a) shows that in reacting flows there is an apparent depletion of unmixed reactants, especially in the thin tongues structures formed by vortex roll-up in the early stage of the mixing layer. Assuming that the interfacial diffusion zones are regions of chemical activity, an explanation for this observation may be proposed. Chemical reaction serves as a sink for reactants, which can produce an increase in the concentration gradients in the vicinity of reaction zones in non-premixed systems. The increased gradient will result in enhanced diffusive transport of reactants in the vicinity of reaction zones, resulting in the apparent depletion of unmixed reactants. The residual non-reacted reactant O_3 is located only in the finite-thickness interfacial diffusion zones and in the tongues of the unmixed fluid induced by large vortex pairing events, further downstream the splitter plate. These tongues contained enough volumes of free-stream fluid and were able to bypass the 'corrosion' or depletion effect due to chemical reaction and molecular diffusion.

Figure 5-20(b) reveals that most of the produced NO_2 is formed in the interfacial layer marked with a darker region, i.e. higher product (NO_2) concentration. This is due to the fact that under the present conditions with $Da = 30.5$, chemical-reaction times are short relative to the contact time of free-stream reactants in the interfacial zones. The homogeneous core regions act as repositories for fluid consisting of product species, residual rich reactants and diluents gas.

Figures 5-21(a)-(f) show the instantaneous concentration of O_3 at different downstream locations superimposed on the instantaneous distribution of the vortex. The locations are chosen across the midsection of the vortex in Figures 5-21(a)-(c), and across the braids in Figures 5-21(d)-(f). The instantaneous concentration profiles confirm the depletion of the lean reactant O_3 species in the vortex structures. The profiles in Figures 5-21(a)-(c) show a peak indicating the presence of O_3 in the thick tongues formed mainly during vortex pairing. Across the braids, the instantaneous concentration are described by an error function-like profile characterized by steep changes between the free stream values within a smaller distance as compared with the non-reactive concentration profiles in Figures 5-13. This indicates the presence of large O_3 concentration gradients in the interfacial layer.

Figures 5-22(a)-(f) show the instantaneous concentration of the product NO_2 at different downstream locations superimposed on the instantaneous distribution of the vortex. The locations are chosen across the midsection of the vortex in Figures 5-22(a)-(c), and across the braids in Figures 5-22(d)-(f). The instantaneous product concentration profiles show that vortex structures retain the larger volumes of product species and act as homogeneous depositories of the chemically reacted mixed fluid. The locations of the peaks in the product concentration profiles correspond to the interfacial diffusion zones in the vortex structure and across the braids, in consistency with the dark region shown in Figure 5.20(b) indicating the active regions of chemical reaction.

5.2.3.3 Probability Density Function for Reactive Flow

Figure 5.23 represents a three-dimensional plot for the FDF of the mixture fraction for the downstream location $x/H_x = 0.55$. The plot shows the evolution of the FDF of ξ_{O_3} across the mixing layer. A comparison of the reactive FDFs scalar (Figure 5-23) with those of the non-reactive scalar (Figure 5-14) at the same locations shows significant reduction of the probability densities for $0 < \xi_{O_3} < 1$, corresponding to depletion of volume of mixed reactant O_3 in the reacting layer, similar behavior have been reported by M&B.

Figures 5-24(a)-(d) show the FDFs of the reacting mixing layer for different values of η_c at selected downstream locations, $x/H_x = 0.4, 0.5, 0.6$ and 0.75. They reveal U-shape FDFs confirming the high rate of consumption of O_3 in the mixing layer. The O_3 species are only present in the tongues of unmixed fluid stretching across the layer and displayed as a spike at $\xi_{O_3} = 1$.

5.2.3.4 LES Results

Figures 5-25(a)-(b) and (c)-(d) show the normalized mean reactant O_3 and product NO_2 concentrations profiles, for the LES runs with Smagorinsky SGS model, respectively, together with the experimental results of M&B and the calculated LES results of Z&P. Figures 5-25(a) and (b) show that LES results using Smagorinsky SGS models attain self-similarity in the downstream region $0.4 \leq x/H_x \leq 0.6$. The results in Figure 5-25(b) show somewhat lower values of O_3 concentration for $\eta_c > 0$ when compared to the LES results of Z&P which are higher than the experimental results of M&B. In Figure 5-25(c) the normalized mean product concentration profile showed slightly higher values for $\eta_c > 0$ than the experimental results of M&B. The Smagorinsky SGS results, in Figures 5-25 (a)-(d), reflect the dissipation induced by this SGS model causing more mixing in the flow and consequently more consumption of reactant species and higher production of product species, i.e. lower O_3 concentration and higher NO_2 concentration values as compared to the experimental results of M&B and LES results of Z&P.

5.2.3.5 SGS Effects

A comparison of the results obtained using the three runs with different SGS models reveals the effect of SGS on the reactive scalar field. The profiles of the mean reactant O_3 concentration (Figure 5-26(a)-(b)), the rms reactant O_3 concentration fluctuations (Figure 5-26(c)-(d)) and the mean product NO_2 concentration (Figure 5-26(e)-(f)) are plotted against the reactive similarity variable η_c at the downstream locations $x/H_x = 0.45$ and 0.55 for three different runs: without SGS modeling, with Smagorinsky SGS model and with the dynamic eddy viscosity SGS model. In Figures 5-26(a) and (b), the mean concentration of O_3 shows lower values for the run with Smagorinsky SGS model due to higher mixing that in turn accelerates the depletion of O_3 species by enhancing chemical reaction.

The rms concentration fluctuations profiles of O_3 in Figures 5-26(c) and (d) show that the results for the Smagorinsky SGS model run are lower than the profiles of the two other runs. This is due to the fact that the Smagorinsky SGS model is more dissipative and consequently yields to more mixing thus the flow tends to be more homogeneous than the other two simulations.

As expected, the mean concentration profiles of the product NO_2 shown in Figures 5-26(e) and (f) indicate higher values for the run with Smagorinsky SGS model due to the higher dissipation, and therefore enhanced chemical reaction and production of NO_2. The results, for the other two runs 'no SGS' and 'dynamic Eddy viscosity SGS' models are close to each other.

Figures 5-27(a)-(d) reveal the effect of the SGS models on the probability density function and on the filtered density function plotted at four different downstream locations in the low speed side region $\eta_c = -0.01$. Comparison of the probability and filtered density function for the three runs with different SGS models under study shows that higher dissipation induced from the SGS model yields a higher FDF values for the mixed flow $0 < \xi_{O_3} < 1$. The results of Smagorinsky SGS model indicates a most probable mixed flow compared to the other two runs. Also the dynamic eddy viscosity SGS model shows more probable values for $0 < \xi_{O_3} < 1$ than the values of the run without SGS modeling.

5.2.4 Damköhler Number Effects

In this section, the effect of Da number on the scalar field is investigated for cases ranging from frozen chemistry to fast chemistry conditions. To this end, three additional runs are made. Two of them introduced lower concentration of NO reactant in the upper free stream conditions causing slower reaction mechanism corresponding to $Da = 1.0$ and 0.1. The third run simulated the limit of fast chemistry reactive mixing layer with $Da = \infty$, modeled in such a way that any mixed reactants are immediately transformed into products and characterized by a reaction sheet replacing the interfacial diffusional reaction zones between the two free streams.

The normalized mean concentration, the rms concentration fluctuations (Sections 5.2.4.1 and 5.2.4.2), the instantaneous concentration contours and profiles (Section 5.2.4.3) and the FDF results (Section 5.2.4.4) are shown and compared between five different runs: the non-reactive scalar (representing the limit of frozen chemistry $Da = 0$), the fast reaction run ($Da = \infty$) and three finite-rate chemistry runs with $Da = 30.5$, 1.0 and 0.1.

5.2.4.1 Mean Reactant, Product Concentrations and RMS Reactant Concentration Fluctuations.

Figures 5-28(a) and (d) show the normalized mean reactant O_3 concentration profiles $\bar{\xi}_{O_3}$ for $Da = 1.0$ and 0.1, respectively. The $\bar{\xi}_{O_3}$ profiles are plotted against the reactive similarity variable η_c. It is observed that the profiles are self-similar in the downstream locations $0.4 \leq x/H_x \leq 0.6$. For the case with $Da = 0.1$ (Figure 5-28(d)), a triple inflection point is observed in the upper side of the mixing layer ($\eta_c > 0$) indicating the presence of homogeneous core regions with a preferred concentration.

The normalized rms concentration fluctuations of O_3 ($\xi_{O_{3,rms}}$) results for Da = 1.0 and 0.1, are plotted as a function of the reactive similarity variable in Figures 5-28(b) and (e), respectively. Self-similar profiles are shown for $0.4 \leq x/H_x \leq 0.6$. The profiles of $\xi_{O_{3,rms}}$ in Figure 5-28(e) show the tendency for a second peak formation similar to the bimodal shape of rms concentration fluctuations profile of the non-reacting mixing layer (see Figure 5-10(c)).

The normalized mean product NO_2 concentration profiles $(\bar{\xi}_{NO_2})$ are displayed in Figures 5-28(c) and (f), at four downstream locations. The profiles of $\bar{\xi}_{NO_2}$ appear to attain similarity. However a slight increase in the product concentration is observed with downstream evolution of the mixing layer due to the irreversibility of the chemical reaction.

5.2.4.2 Effect of Da on the Mean Reactant and Product Concentrations and RMS Reactant Concentration Fluctuations

The results of five different runs are compared at the downstream location $x/H_x = 0.55$ to reveal the effect of Da. Three runs are made with finite-rate chemical reaction with $Da = 0.1, 1.0$ and 30.5. The other two runs represent the limiting case of non-reactive mixing layer and fast reaction, i.e. $Da = 0$ and ∞, respectively.

The mean reactant O_3 concentration profiles are shown in Figure 5-29(a) for the five different runs. As expected, it is observed that the mean reactant O_3 concentration has lower values as Da is increased, reflecting the higher consumption of O_3 as chemical reaction is enhanced. The triple inflection point appearing in the non-reactive profile is less pronounced with $Da = 0.1$ and it disappears completely when $Da \geq 1$ leaving a smooth error-function-like profile indicating the absence of the preferred O_3 concentration in the core regions of the vortical structures.

The rms concentration fluctuations of O_3 are shown in Figure 5-29(b) for the five runs. It is observed that for $\eta_c > 0$, the $\xi_{O_{3,\mathrm{rms}}}$ values decrease with increasing Da number. At $\eta_c = 0$, $\xi_{O_3,\mathrm{rms}}$ remains constant for all the runs and it increases with increasing Da for $\eta_c < 0$. The bimodal shape of $\xi_{O_{3,\mathrm{rms}}}$ profile presented in the non-reactive case is progressively transformed to unimodal shape with enhanced reaction having a higher peak skewed toward the lower side of the mixing layer indicating the presence of steeper gradient at the boundary of the lean reactant free-stream. It is noted the proximity of the results for the run with $Da = 30.5$ to the fast reaction results.

Figure 5-29(c) shows the mean product concentration profiles for the different runs under study, along with the prediction of the fast-chemistry product concentration calculated following the methodology of Bilger (1980) and presented in the work of M&B. Figure 5-29(c) displays a marked increase in both the peak value of $\bar{\xi}_{NO_2}$ and the total (integrated) amount of product in the layer. The fast reaction limit shows a profile that is similar in shape but lower in comparison with the calculations presented by M&B. At the fast reaction limit the product concentration profile is skewed toward the lean-reactant bearing free stream, thus indicating the shift in the reaction mechanism to the interface with the lean-reactant fluid, where reactants are mixed at stoichiometric proportions.

5.2.4.3 Instantaneous Concentration Contours and Profiles

The instantaneous concentration contours of reactant (O_3) and product (NO_2) in the plane-reacting mixing layer are shown in Figures 5-30(a)-(d) for two runs with $Da = 0.1$ and 1.0, respectively. A comparison between Figures 5-30(a) and (b) and Figure 5-20(a)

$(Da = 30.5)$ reveals that reactant O_3 are increasingly present in the mixing layer as Da is decreased, approaching the case of frozen chemistry $(Da = 0.1)$, where reactants are observed to coexist since reaction proceeds too slowly to deplete the lean mixed reactant.

The manner in which fluid from the free streams is ingested into the core regions determines whether these regions will be active centers of reaction. If chemical-reaction times are short relative to the contact time of free-stream reactants in the interfacial zones, then fluid that is incorporated into the core regions will comprise product species, residual rich reactants and diluents gas. In this situation, the homogeneous core regions will be repositories for reacted fluid and reaction will be confined to the interfacial layer. However, when fresh reactants are ingested directly into the core regions for cases with low Da, these core regions will become active centers of reaction. By comparing the darker contours in Figure 5-30(c) and (d), the shift of the product formation from the interfacial zones towards the core regions is observed when Da is decreased from 1.0 to 0.1.

Close-ups of the reactant (O_3) concentration contour plots are visualized in Figures 5-31(a) and (b) for the cases with $Da = 30.5$ and 0.1, respectively. It is shown that for high Da numbers, O_3 species are depleted in the core regions and they exist only in the tongues of pure unmixed free-stream fluid and in the thin reactive interfacial zones marked by progressively continuous concentration gradients. For the slow reaction regime results presented in Figure 5-31(b) with $Da = 0.1$, mixed O_3 species spread across the mixing layer leading to a distributed-like reaction flame regime. Pockets or islands of mixed reactants are clearly spotted in the core regions of the vortex structures.

Figures 5-32(a) and (b) show close-ups of the product (NO_2) concentration contours for the runs with $Da = 30.5$ and 0.1, respectively. For $Da = 30.5$, peaks of NO_2 concentrations (dark contours in Figure 5-32(a)) are found within the interfacial zones, where the production takes place, and within the core regions where the products are stored. For $Da = 0.1$, Figure 5-32(b) shows that the product contours become very brushy, with lower concentration values in the interfacial zones, and darker (high NO_2 concentrations) core regions where the products are mainly formed and stored. Figure 5-32(b) shows a pattern of product pockets that is similar to the pattern of pockets of the reactant concentration contours displayed in Figure 5-31(b).

The instantaneous concentration profiles of reactant O_3 are shown in Figures 5-33(a)-(f) for $Da = 30.5, 1.0$ and 0.1 at different downstream locations, superimposed on the instantaneous distribution of the vortex particles. The locations are chosen across the midsection of the vortices in Figures 5-33(a), (c) and (e), and across the braids in Figures 5-33(b), (d) and (f). For $Da = 30.5$ and 1.0 in Figures 5.33(a) and (c), the lean reactant O_3 species are completely depleted in the vortex structures as shown by the concentration profiles. Whereas for the case with $Da = 0.1$ shown in Figure 5-33(e), O_3 species are still noticed in the core regions. Across the braids, the instantaneous concentrations are described by an error function-like profile characterized by steep changes between the free stream values indicating the thickness of the interfacial zones. These interfacial zones tends to be broader when Da number is decreased as can be observed by comparing Figure 5-33(b) to Figures 5-33(d) and (f).

Figures 5-34(a)-(f) show the instantaneous concentration profiles of product NO_2 at different downstream locations superimposed on the instantaneous distribution of the vortex particles. The downstream locations are chosen across the midsection of the vortex in Figures 5-34(a), (c) and (e), and across the braids in Figures 5-34(b), (d) and (f) for $Da = 30.5, 1.0$ and 0.1, respectively. The product concentration profiles have lower values with lower Da numbers, because the reaction is slower. In the core regions of the vortex structures the concentration profiles become smoother with less fluctuations as Da is decreased. This is due to the fact that at low Da numbers the reaction zones are distributed across the mixing layer and not limited within the interfacial zones.

5.2.4.4 Probability Density Function

Figures 5-35(a) and (b) show the FDFs of the reactant O_3 species for the reactive mixing layer simulation with $Da = 1.0$ for different values of η_c at selected downstream locations $x/H_x = 0.5$ and 0.6, respectively. The Figures reveal U-shape profiles indicating the depletion of O_3 species in the mixing layer. However, the profiles show slightly more probable mixed particles, i.e. $0 < \xi_{O_3} < 1$, as compared to the results of the chemically reacting mixing layer with $Da = 30.5$ shown in Figures 5-25(a)-(d).

Figures 5-35(c) and (d) show the FDFs of the reactant O_3 species for the reacting mixing layer simulation with $Da = 0.1$ for different values of η_c at downstream locations $x/H_x = 0.5$ and 0.6, respectively. The profiles show a third peak in the FDF for ξ_{O_3} between 0 and 1 indicating the presence of O_3 species in the homogeneous core regions with a preferred concentration $\xi_{O_3,p}$ close to the value of 0.15. A slight increase in the value of $\xi_{O_3,p}$ with downstream evolution of the mixing layer is observed by comparing Figure 5-35(c) to 5-35(d). This indicates an increasing proportion of low-speed fluid in the homogeneous zones with increasing distance from the splitter plate.

The FDFs shown in Figures 5-35(c) and (d) with $Da = 0.1$ reveal lower value and higher peak of $\xi_{O_3,p}$ present in the core regions of the mixing layer as compared to the FDFs results of the non-reacting mixing layer at downstream locations $x/H_x = 0.5$ and 0.6 shown in Figures 5-15(b)-(c), respectively. The lower $\xi_{O_3,p}$ value reflects the consumption of O_3 species by chemical reaction. Whereas the higher probability of the $\xi_{O_3,p}$ for $\eta_c > 0$ maybe due to the fact that chemical reaction shifts the values of η_c toward the O_3 (lean reactant) bearing free-stream.

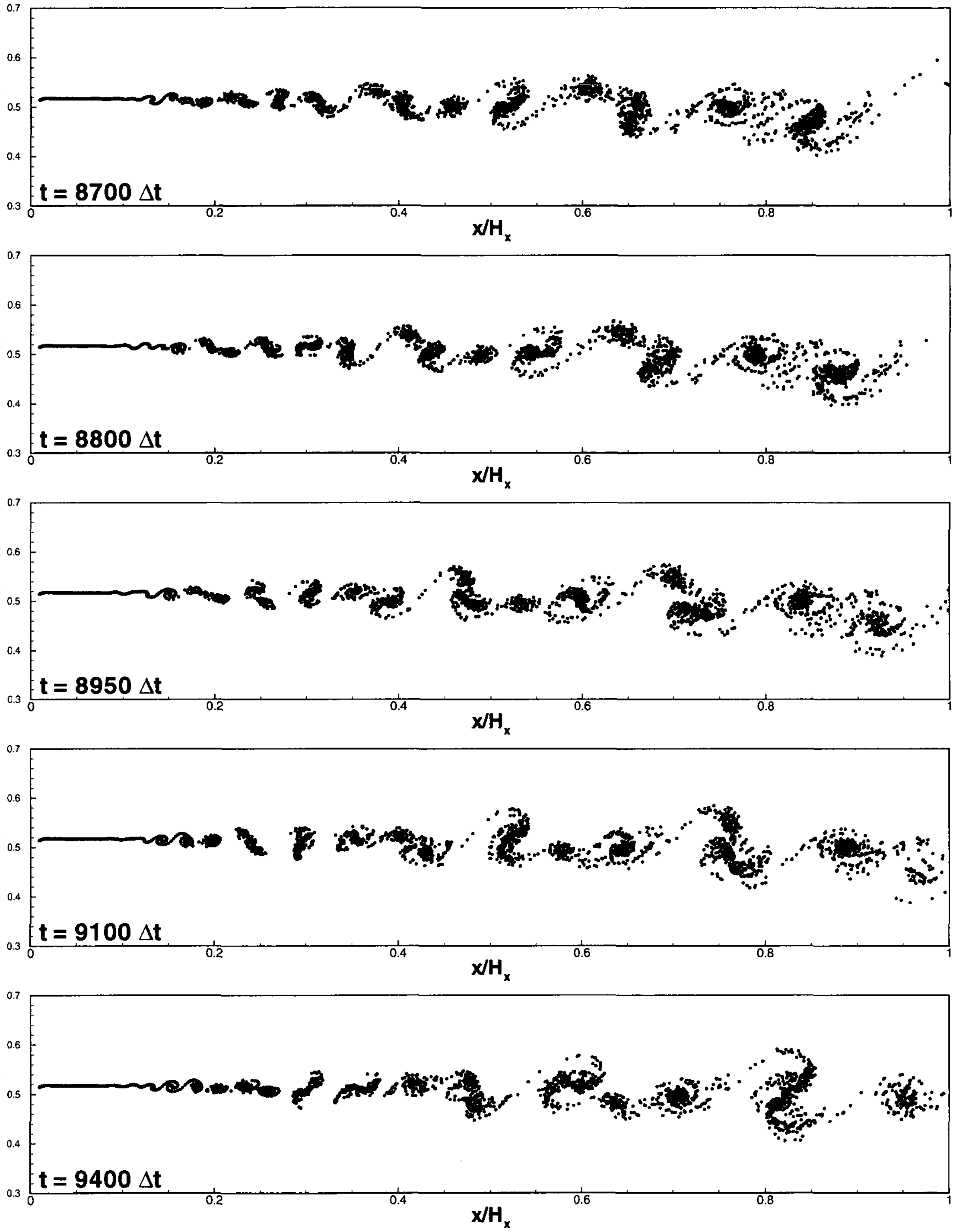

Figure 5-1: Location of the vortex particles at five consecutive times.

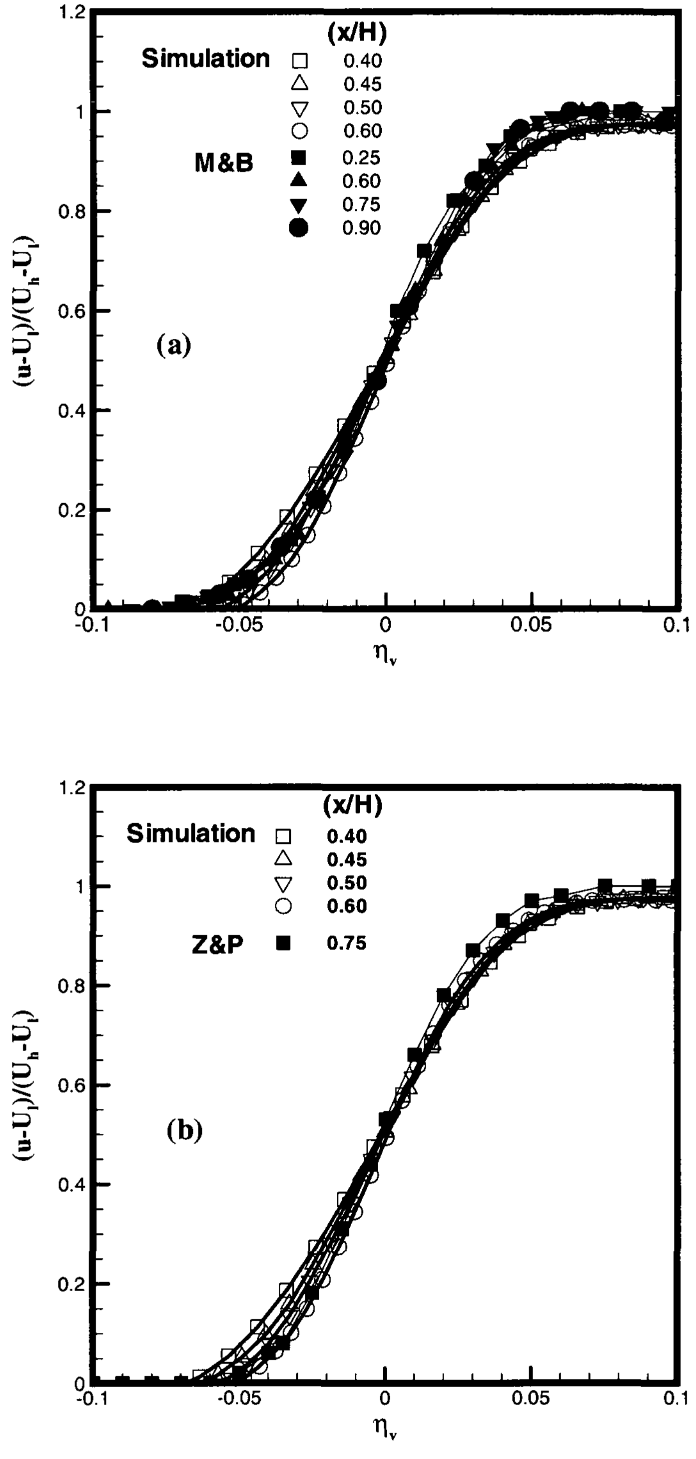

Figure 5-2: Comparison of the normalized calculated mean stream-wise velocity profiles (open symbols) with (a) the measured results of M&B, (dark symbols) and (b) the calculated results of Z&P at different downstream locations.

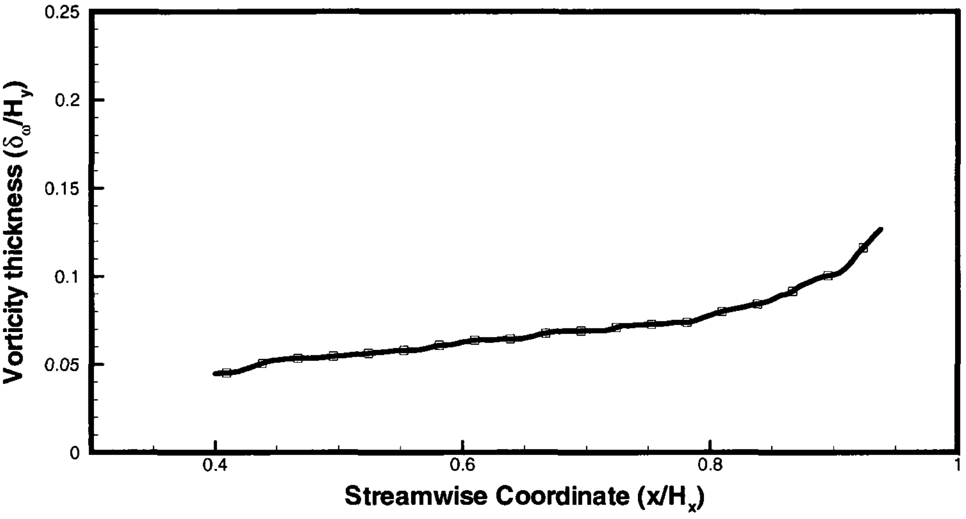

Figure 5-3: Downstream evolution of vorticity thickness.

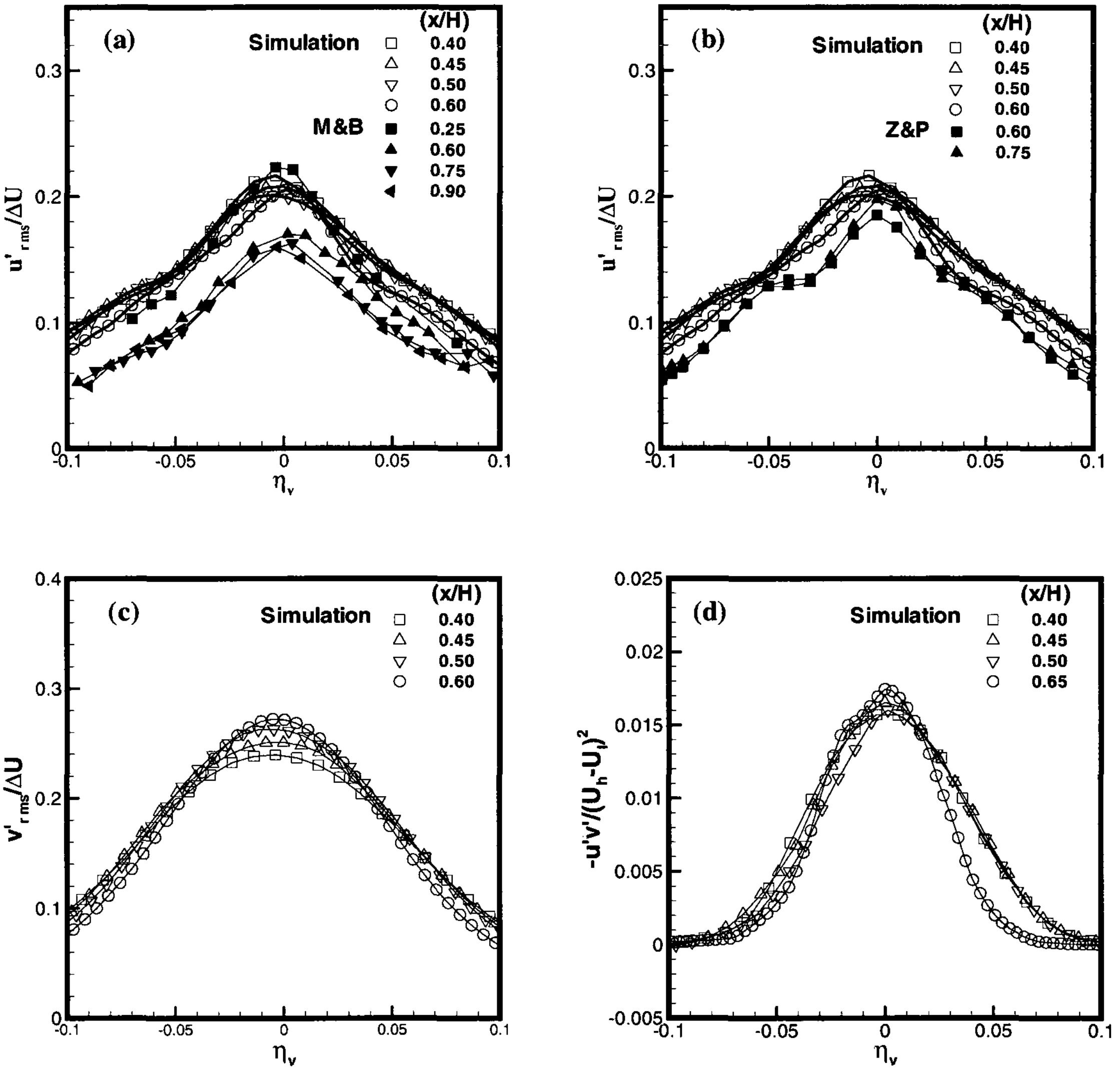

Figure 5-4: Normalized velocity profiles at four downstream locations for the base run: (a) rms longitudinal velocity fluctuations compared to measured results (M&B, dark symbols), (b) rms longitudinal velocity fluctuations compared to calculated results (Z&P, dark symbols), (c) rms lateral velocity fluctuations and (d) negative cross-stream correlation.

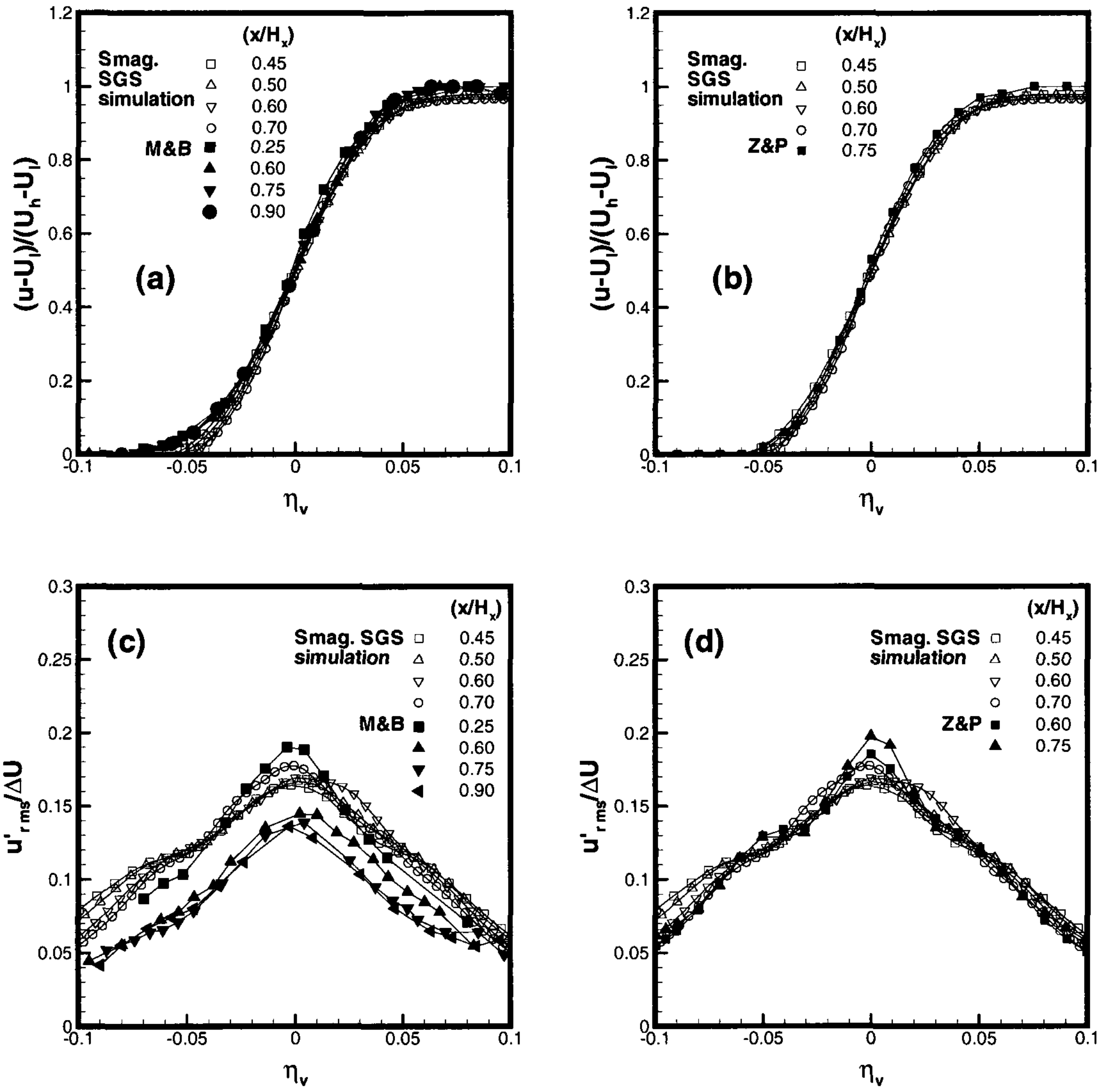

Figure 5-5: LES results using the Smagorinsky SGS model. Normalized mean velocity compared to: (a) experimental results of M&B, (b) calculated results of Z&P; rms longitudinal velocity fluctuations compared to: (c) experimental results of M&B, and (d) to calculated results of Z&P.

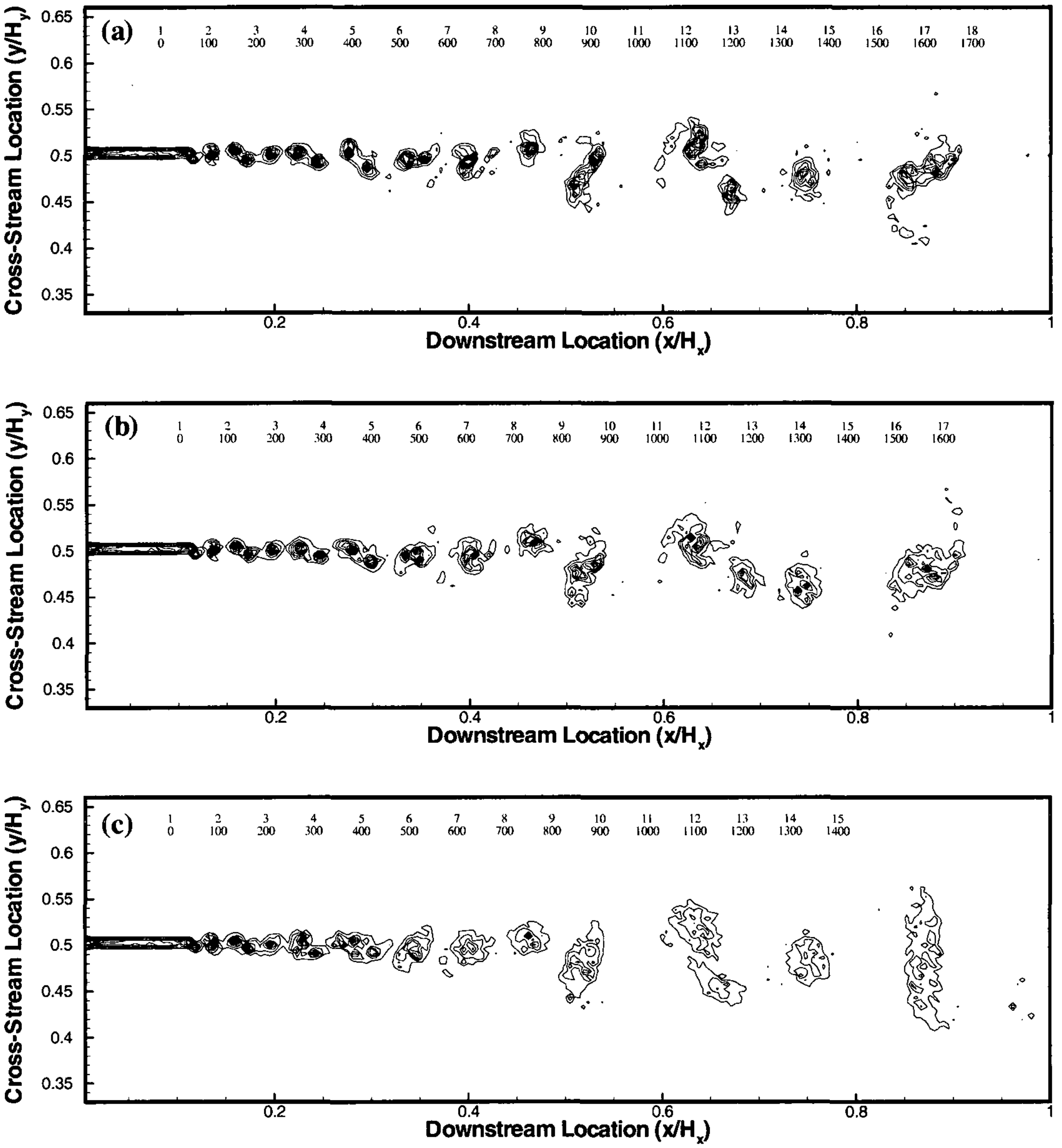

Figure 5-6: Vorticity contours for case: (a) run without SGS, (b) with dynamic Eddy viscosity SGS (base run) and (c) with Smagorinsky SGS. Contour-level increment is 100.

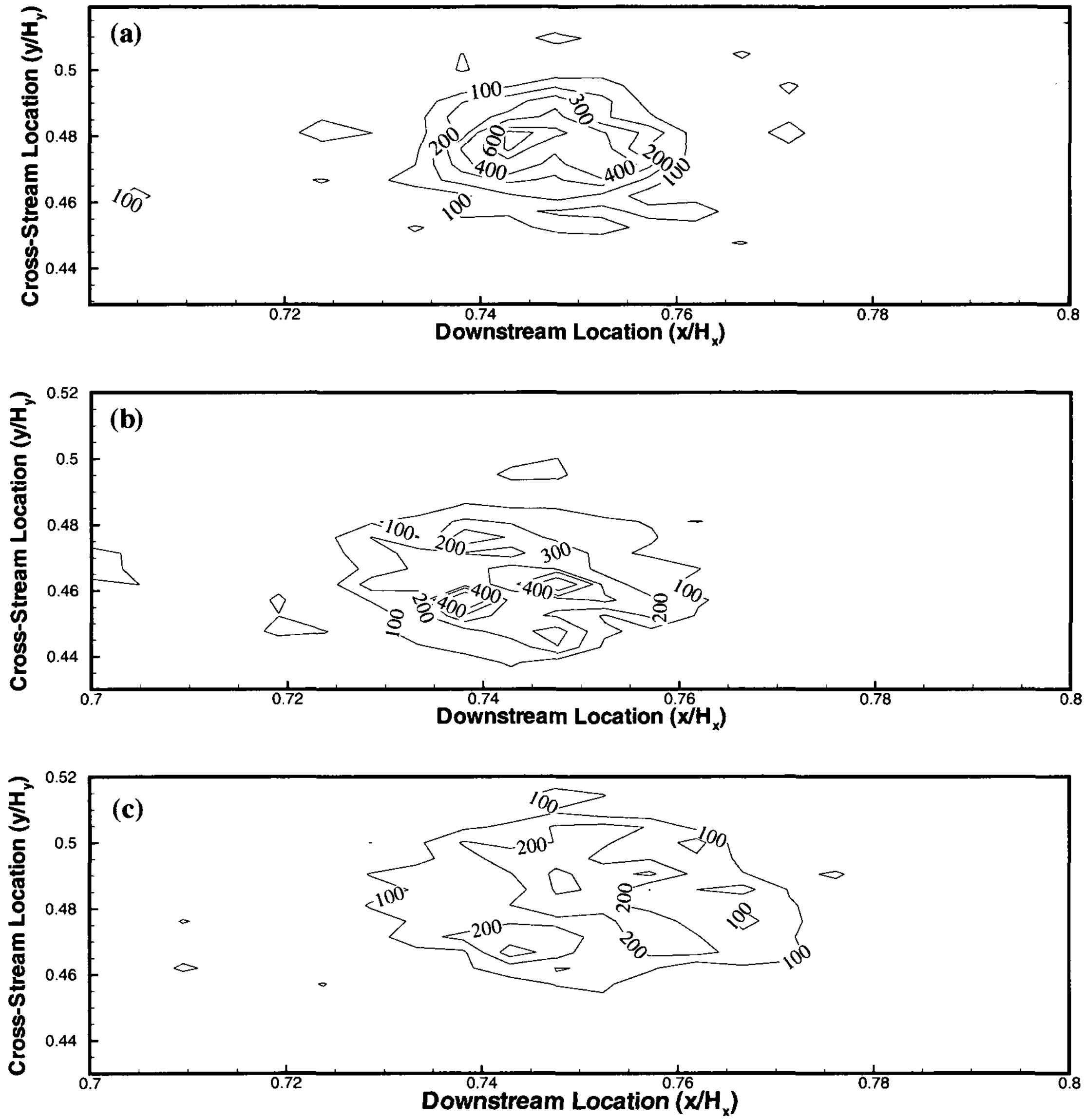

Figure 5-7: Close-ups of vorticity contours at selected downstream location for: (a) run without SGS, (b) run with dynamic Eddy viscosity SGS (base run) and (c) run with Smagorinsky SGS. Contour-level increment is 100.

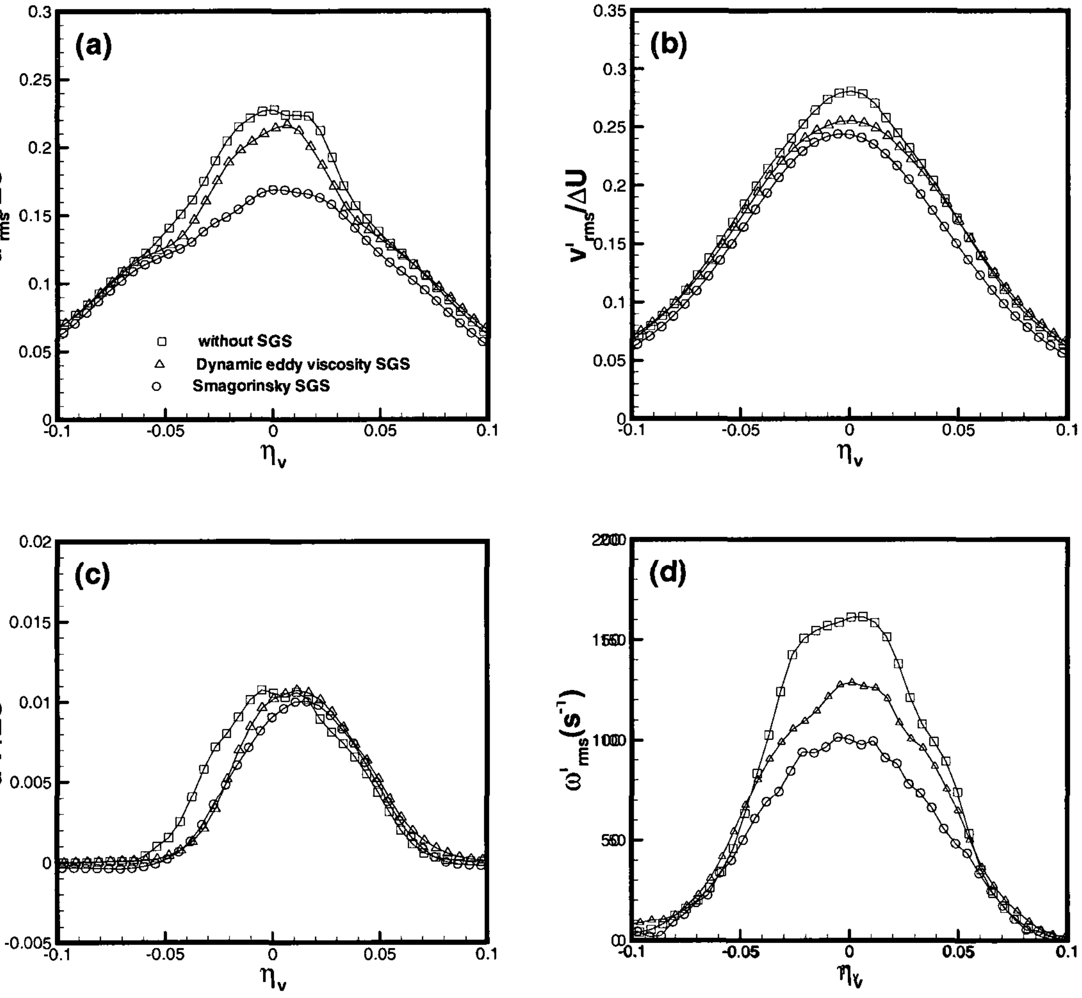

Figure 5-8: Comparison of profiles with and without SGS model: (a) rms longitudinal velocity fluctuations, (b) rms lateral velocity fluctuations, (c) negative cross-stream correlation and (d) rms vorticity fluctuations at $x/H_x = 0.6$.

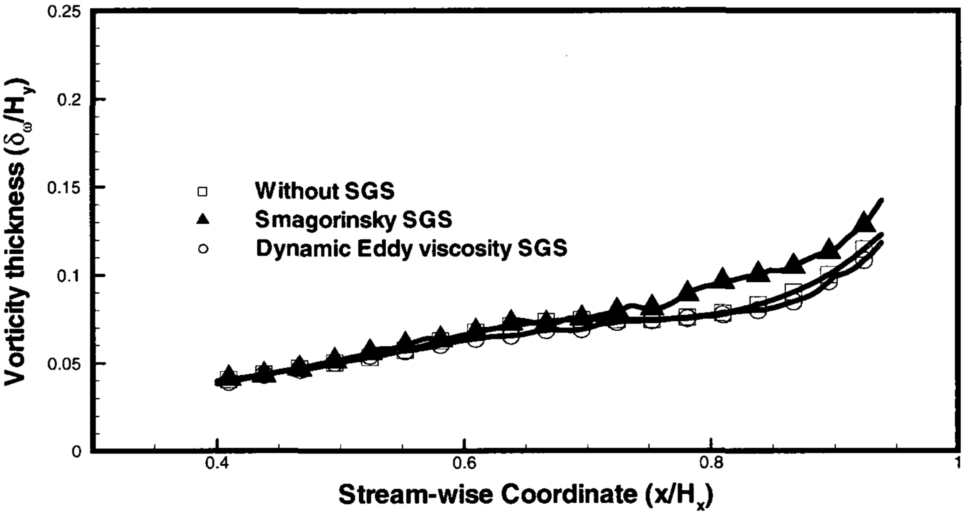

Figure 5-9: Comparison of the downstream evolution of (a) the momentum thickness and (b) the vorticity thickness for runs with and without SGS models.

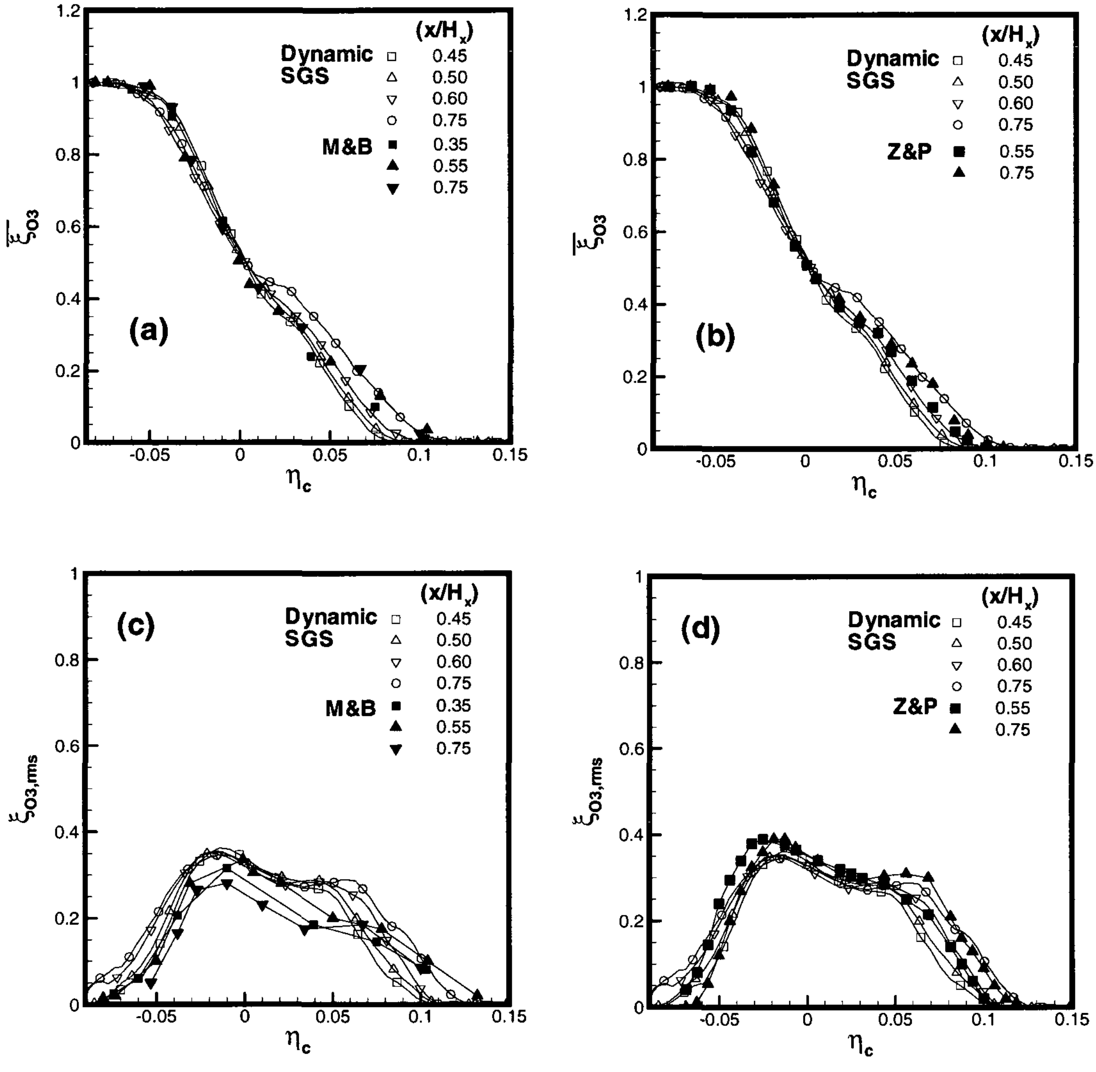

Figure 5-10: The base run non-reactive scalar field results for O_3 at different downstream locations: Normalized mean concentration profiles compared to (a) experimental results of M&B, (b) calculated LES results of Z&P and the normalized rms concentration fluctuations compared to (c) experimental results of M&B and (d) the calculated LES results of Z&P.

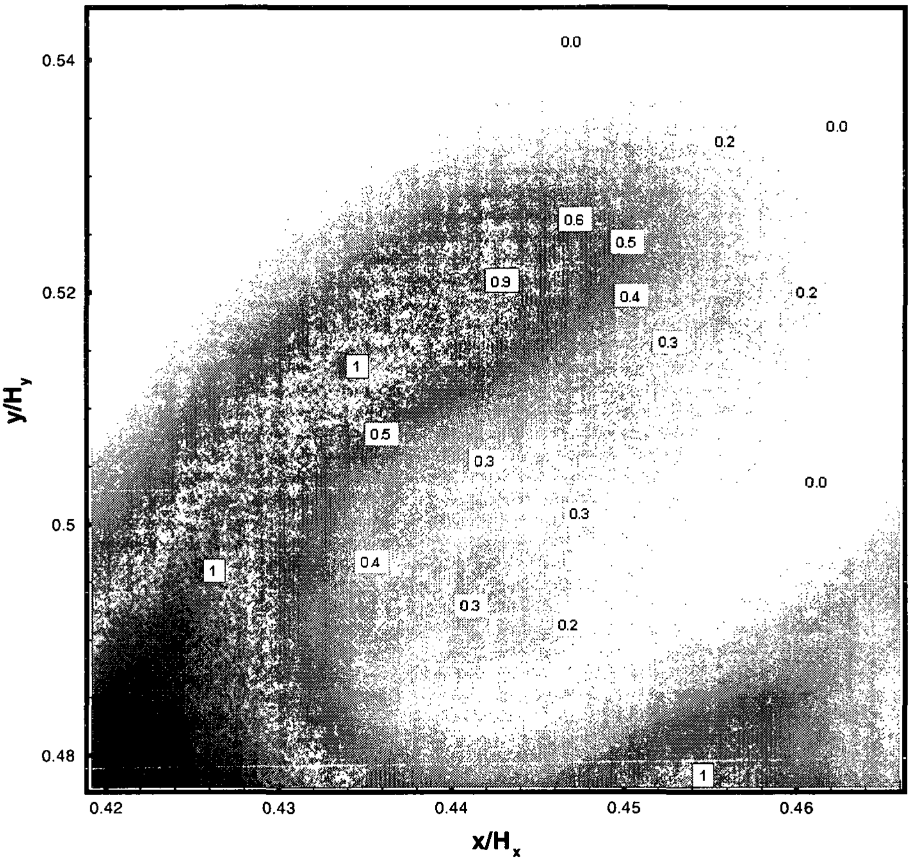

Figure 5-11: Enlarged visualization of calculated instantaneous concentration structure of mixture fraction of O_3 species in the non-reactive plane mixing layer.

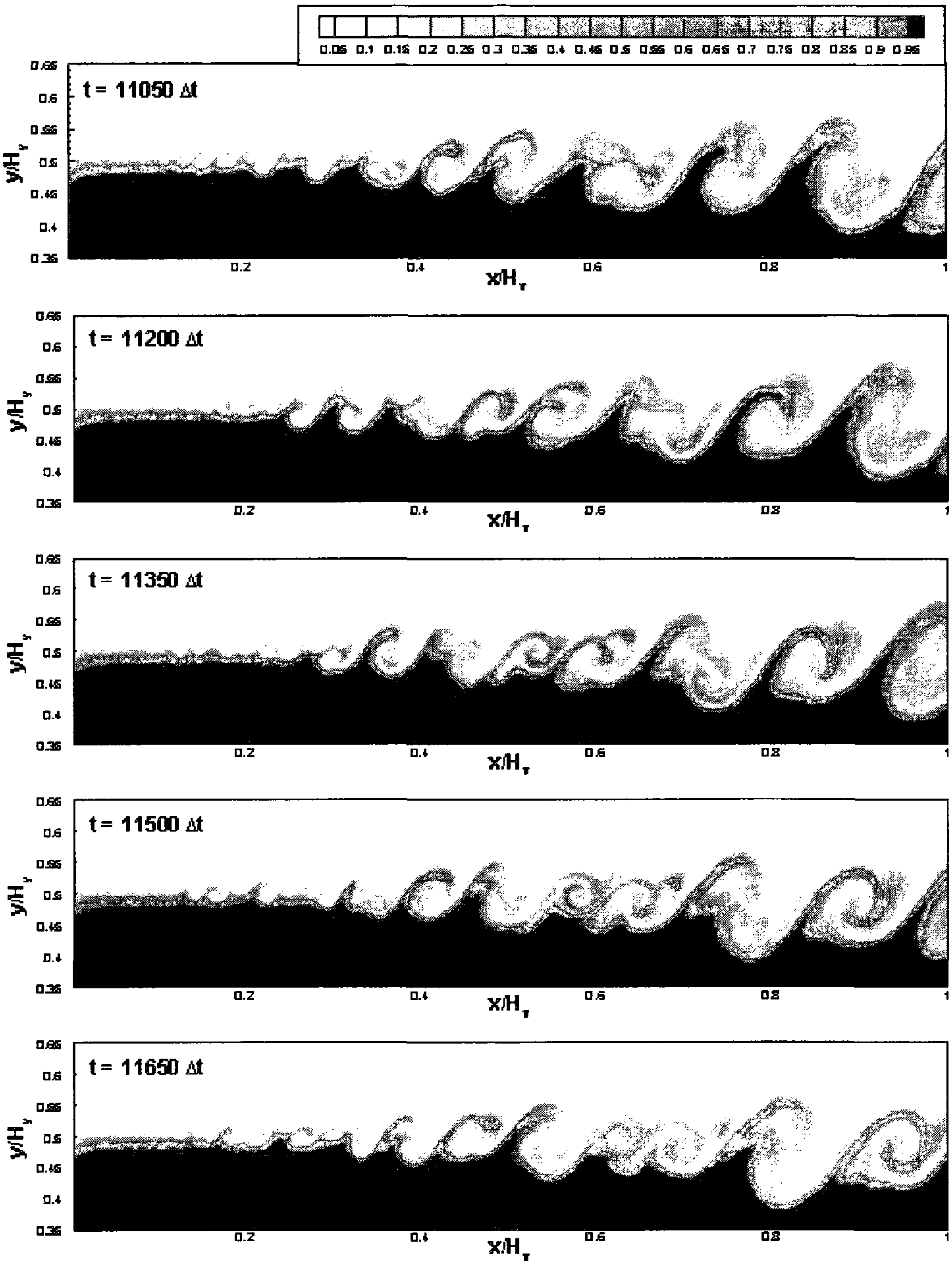

Figure 5-12: Evolution of the instantaneous concentration structure of O_3 at five different times.

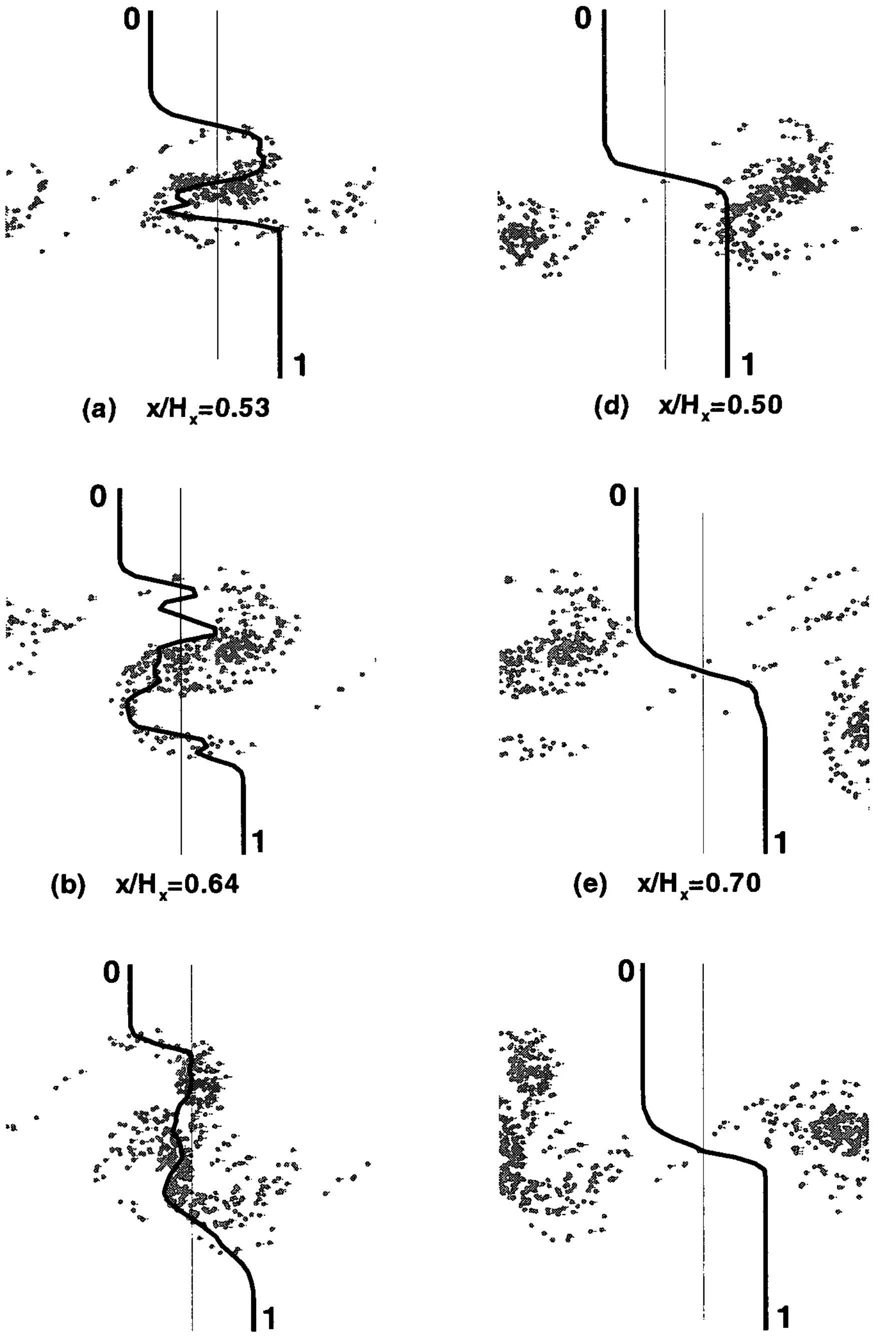

(a) $x/H_x=0.53$ (d) $x/H_x=0.50$

(b) $x/H_x=0.64$ (e) $x/H_x=0.70$

(c) $x/H_x=0.78$ (f) $x/H_x=0.85$

Figure 5-13: Instantaneous concentration profiles of O_3 for the non-reacting flow superimposed on the vortex element at different downstream locations: (a), (b) and (c) across the midsection of the vortex structures; (d), (e) and (f) across the braids.

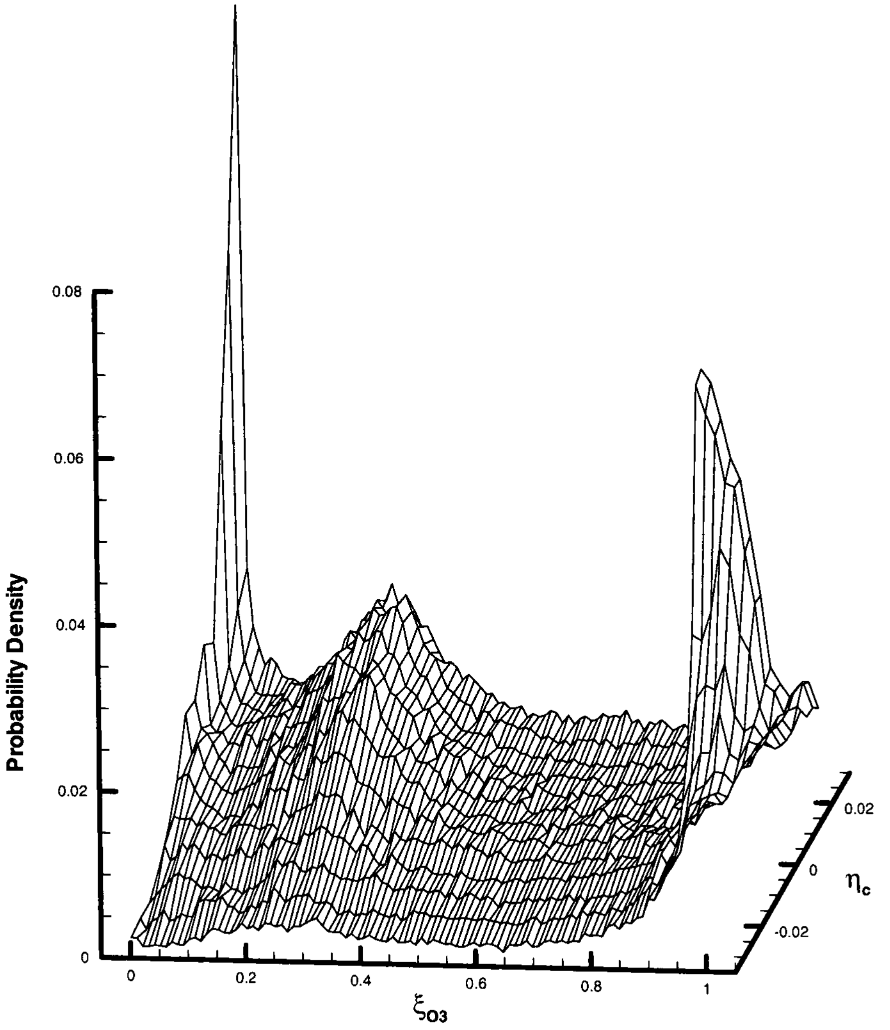

Figure 5-14: Mixture fraction (concentration) P.D.F. of O_3 for the non-reactive flow at downstream location $x/H_x = 0.55$.

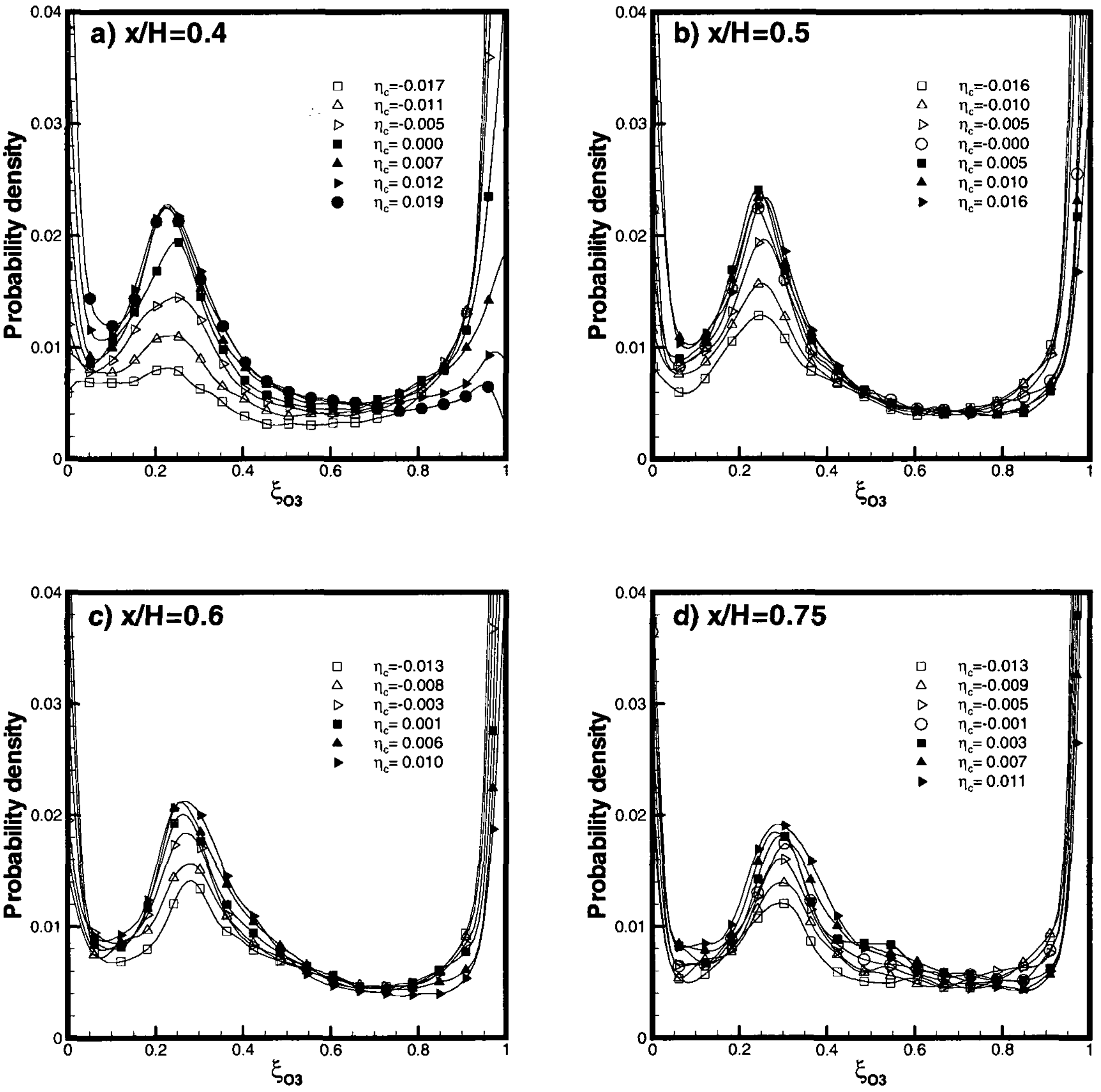

Figure 5-15: Probability density function (PDF) at several cross-stream locations for non-reactive flow: (a) $x/H_x = 0.4$, (b) $x/H_x = 0.5$, (c) $x/H_x = 0.6$ and (d) $x/H_x = 0.75$.

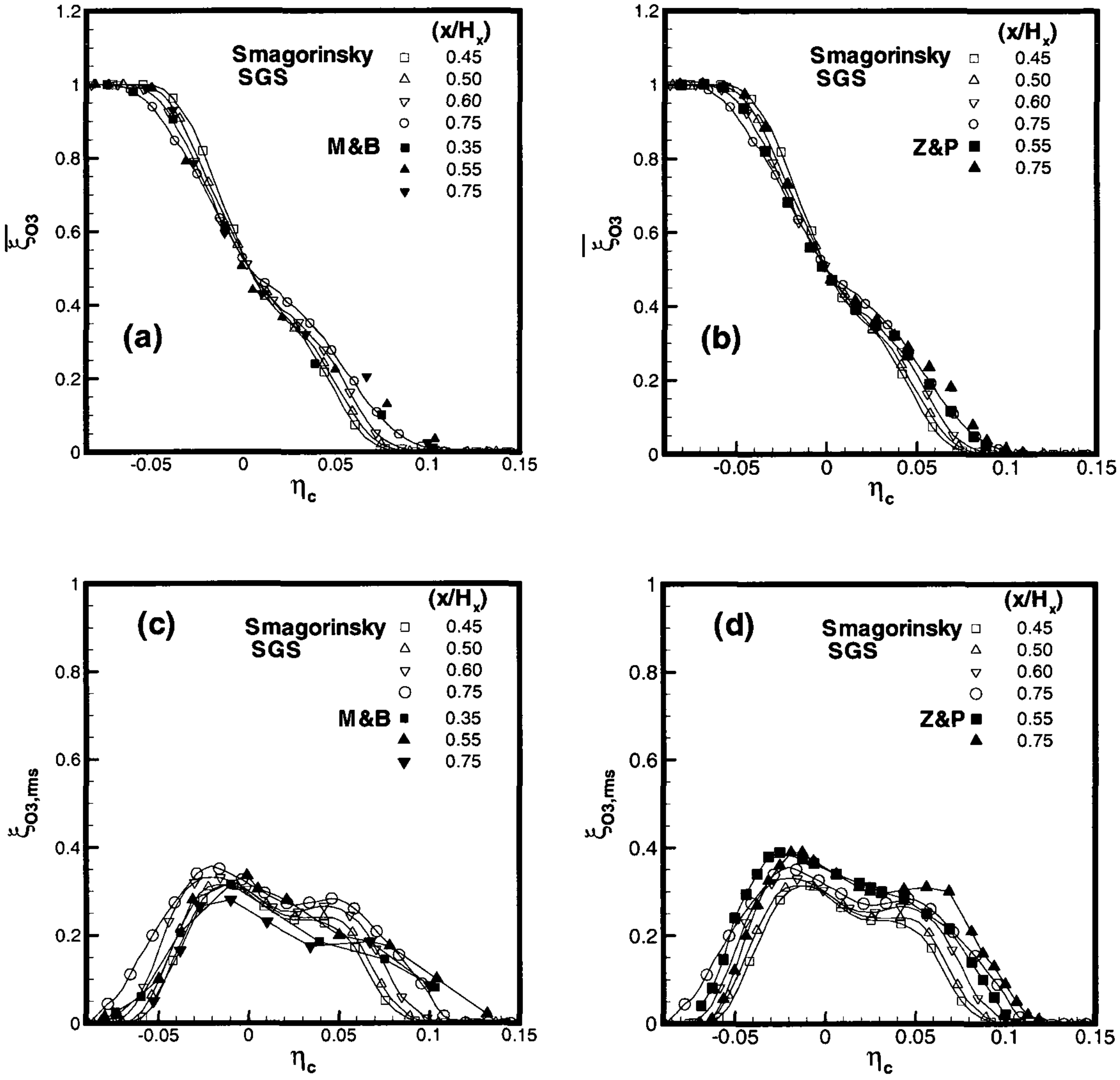

Figure 5-16: LES results using Smagorinsky SGS model for the non-reactive flow: Normalized mean concentration of O_3 compared to (a) experimental results of M&B, (b) LES results of Z&P; and the rms concentration fluctuations of O_3 compared to (c) experimental results of M&B (d) LES results of Z&P.

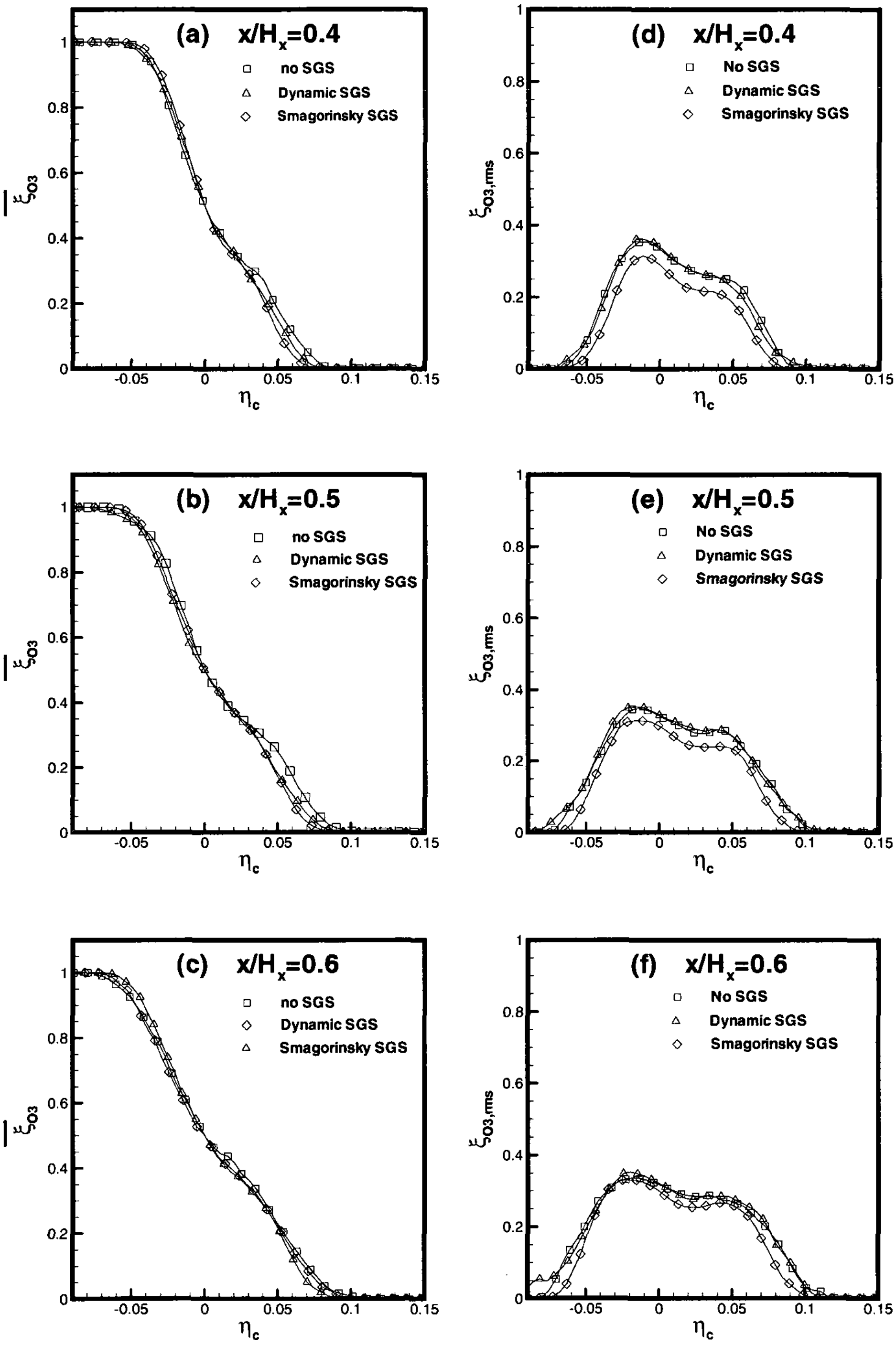

Figure 5-17: Effect of SGS on the normalized mean concentration of O_3 at selected downstream locations: (a) $x/H_x = 0.4$ (b) $x/H_x = 0.5$ (c) $x/H_x = 0.6$, and on the rms concentration fluctuations at: (d) $x/H_x = 0.4$ (e) $x/H_x = 0.5$, (f) $x/H_x = 0.6$ for the non-reactive flow.

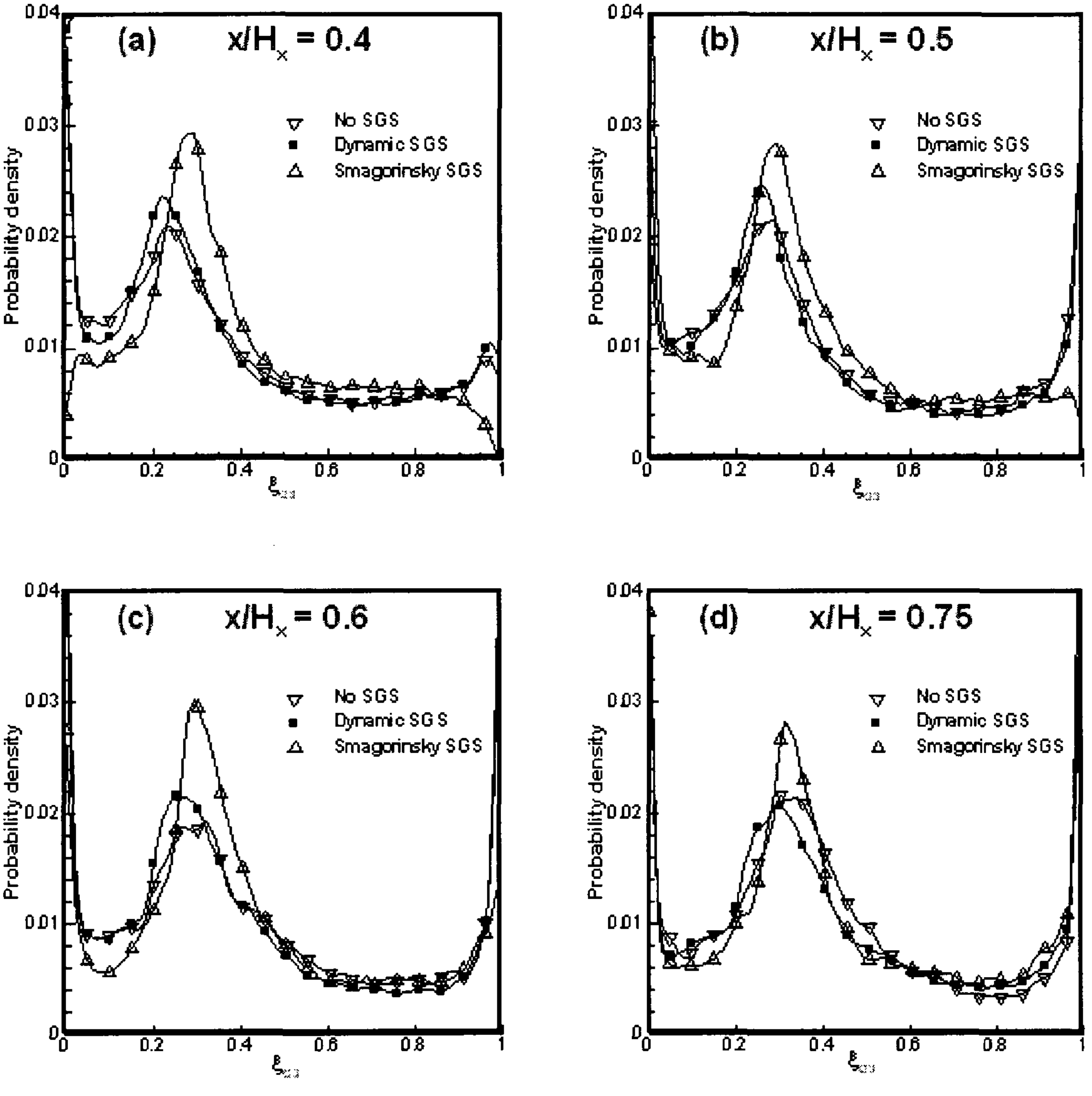

Figure 5-18: Effect of SGS on the probability density function of the mixture fraction of O_3 for $\eta_c = 0.01$ at downstream locations: (a) $x/H_x = 0.4$, (b) $x/H_x = 0.5$, (c) $x/H_x = 0.6$ and (d) $x/H_x = 0.75$.

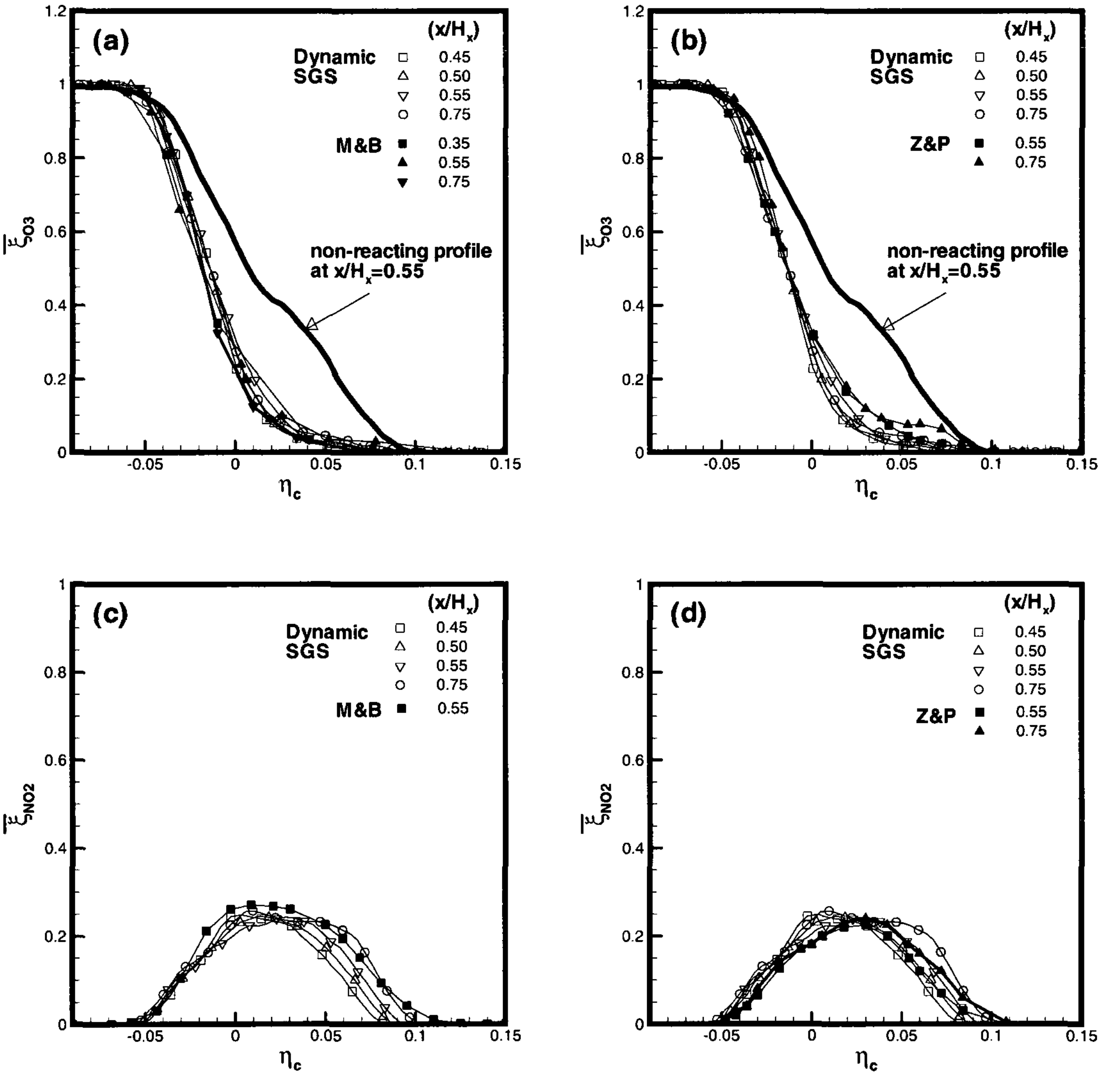

Figure 5-19: LES results for the reacting mixing layer using the dynamic SGS model at different downstream locations: the normalized mean reactant O_3 concentration profiles compared to (a) experimental results of M&B (b) LES results of Z&P; and the normalized mean product NO_2 concentration profiles compared to (c) experimental results of M&B (d) LES results of Z&P.

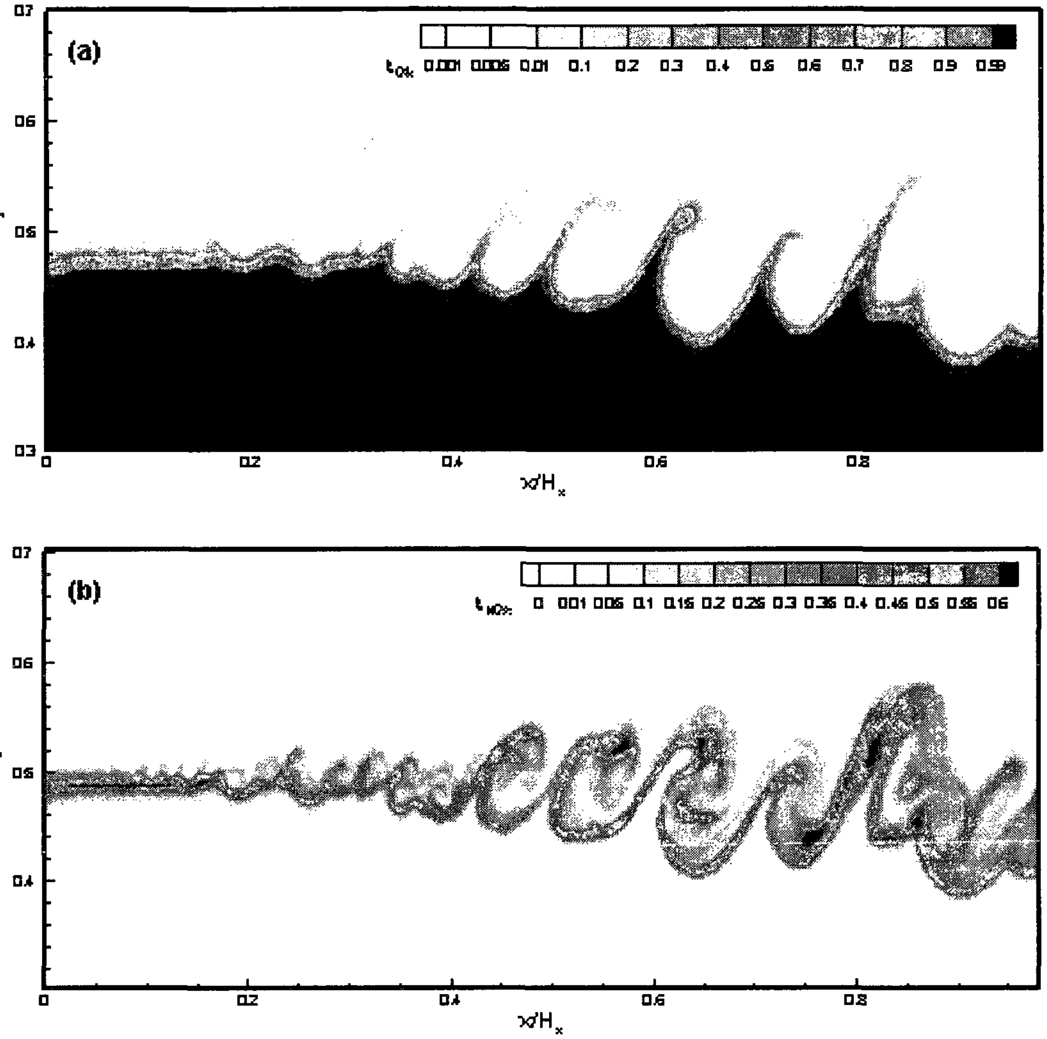

Figure 5-20: Calculated instantaneous normalized concentration contours of (a) reactant O_3 and (b) product NO_2 in a reacting plane mixing layer, for $Da = 30.5$.

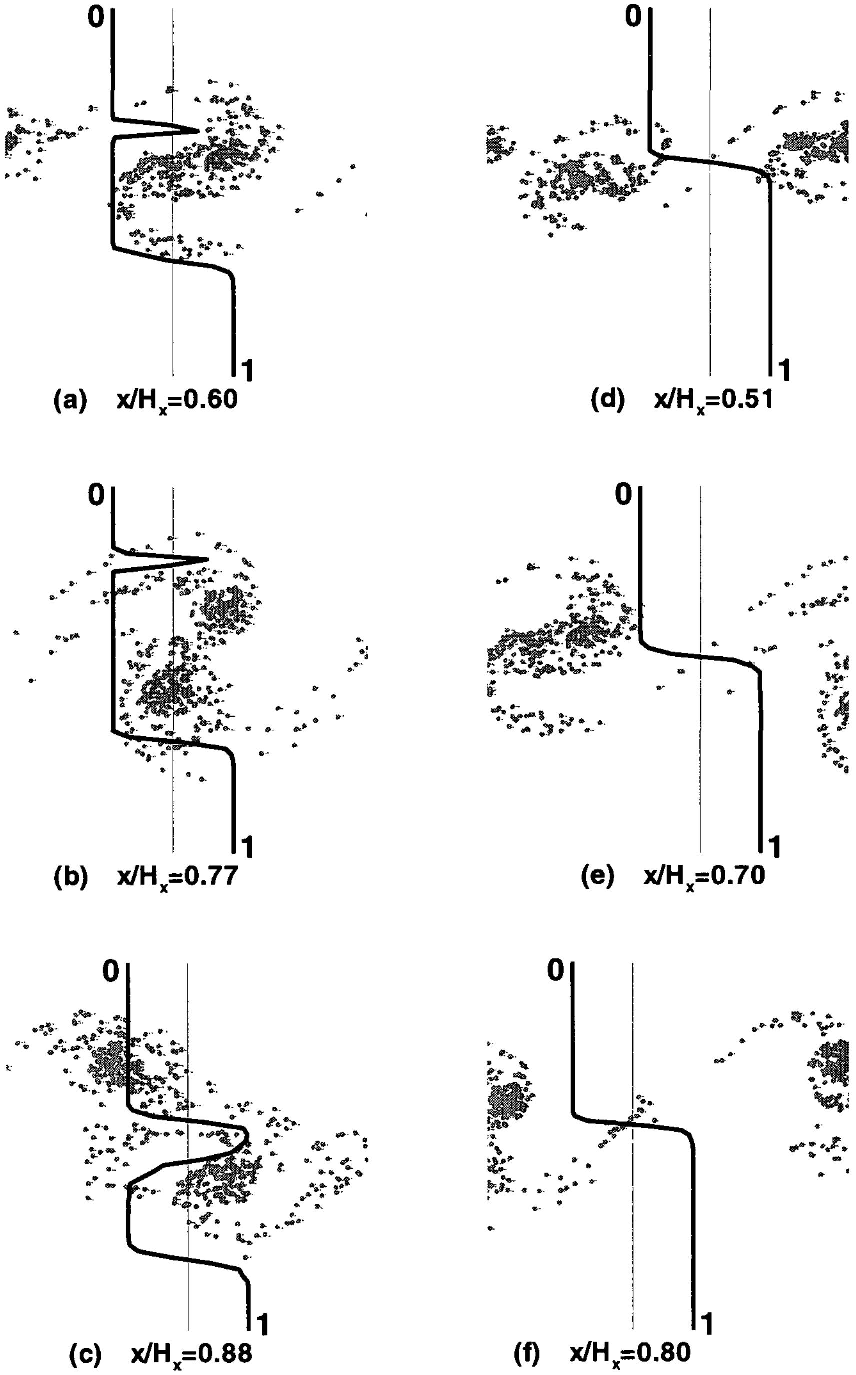

(a) $x/H_x=0.60$

(d) $x/H_x=0.51$

(b) $x/H_x=0.77$

(e) $x/H_x=0.70$

(c) $x/H_x=0.88$

(f) $x/H_x=0.80$

Figure 5-21: Instantaneous concentration profiles of the reactant O_3 for the reacting flow superimposed on the vortex particles structure at different downstream locations: (a), (b) and (c) across the midsection of the vortex structures; (d), (e) and (f) across the braids.

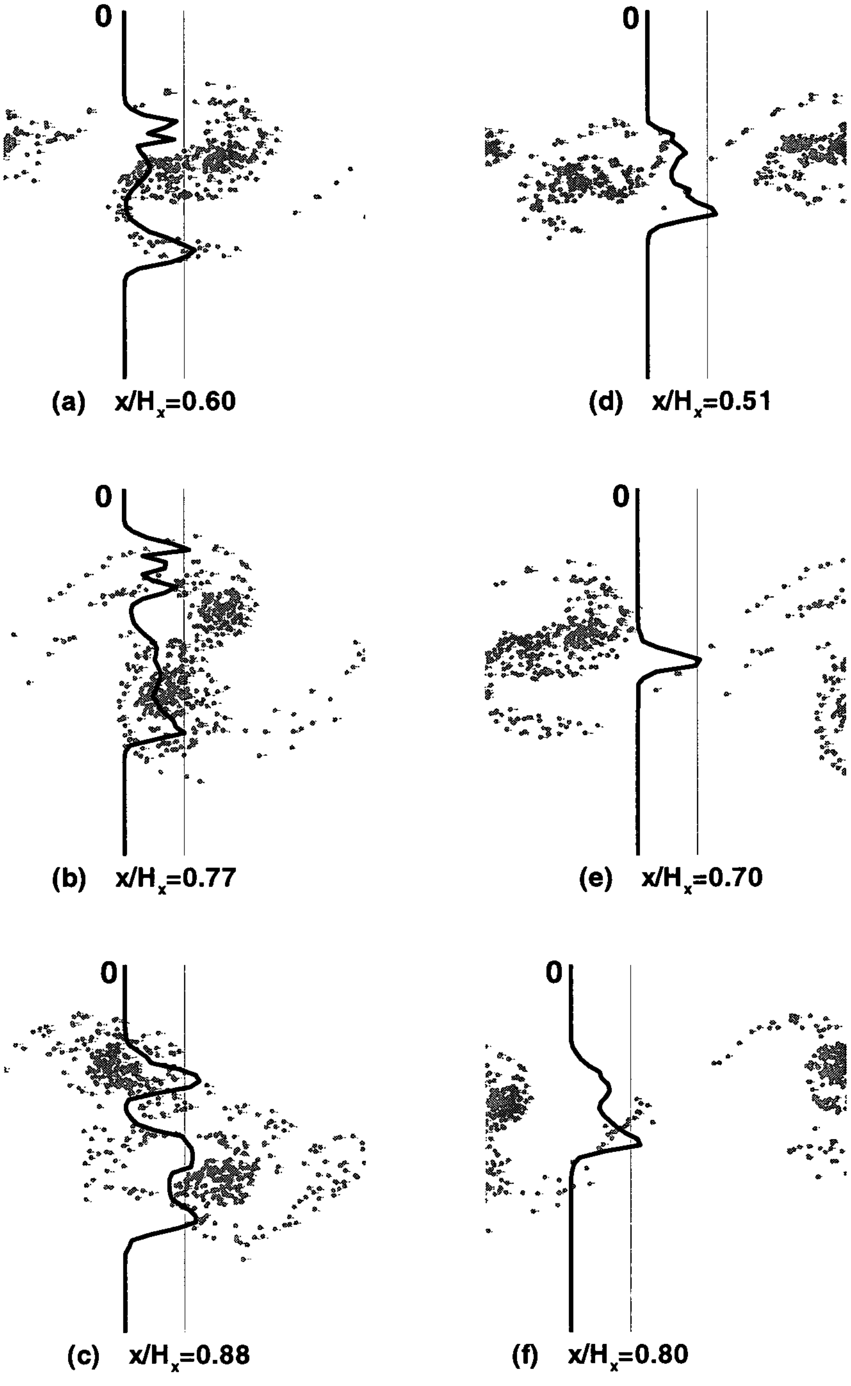

(a) $x/H_x=0.60$ (d) $x/H_x=0.51$

(b) $x/H_x=0.77$ (e) $x/H_x=0.70$

(c) $x/H_x=0.88$ (f) $x/H_x=0.80$

Figure 5-22: Instantaneous concentration profiles of the product NO_2 for the reacting flow superimposed on the vortex particles structure at different downstream locations: (a), (b) and (c) across the midsection of the vortex structures; (d), (e) and (f) across the braids.

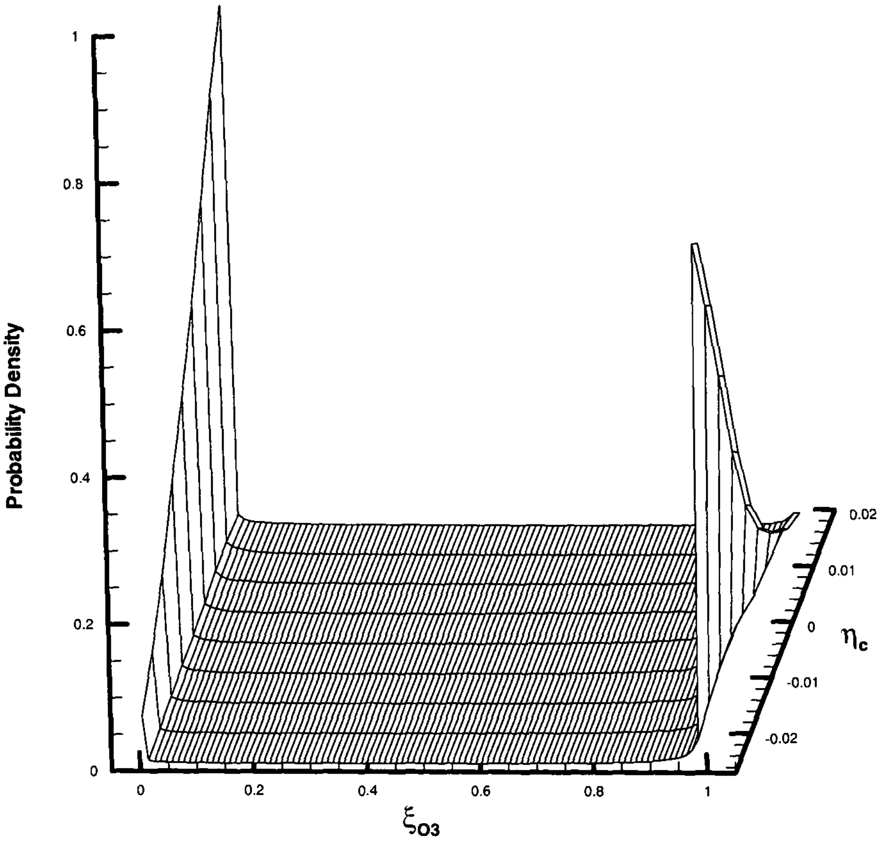

Figure 5-23: Mixture fraction (concentration) PDF of O_3 for the reactive flow at downstream location $x/H_x = 0.55$.

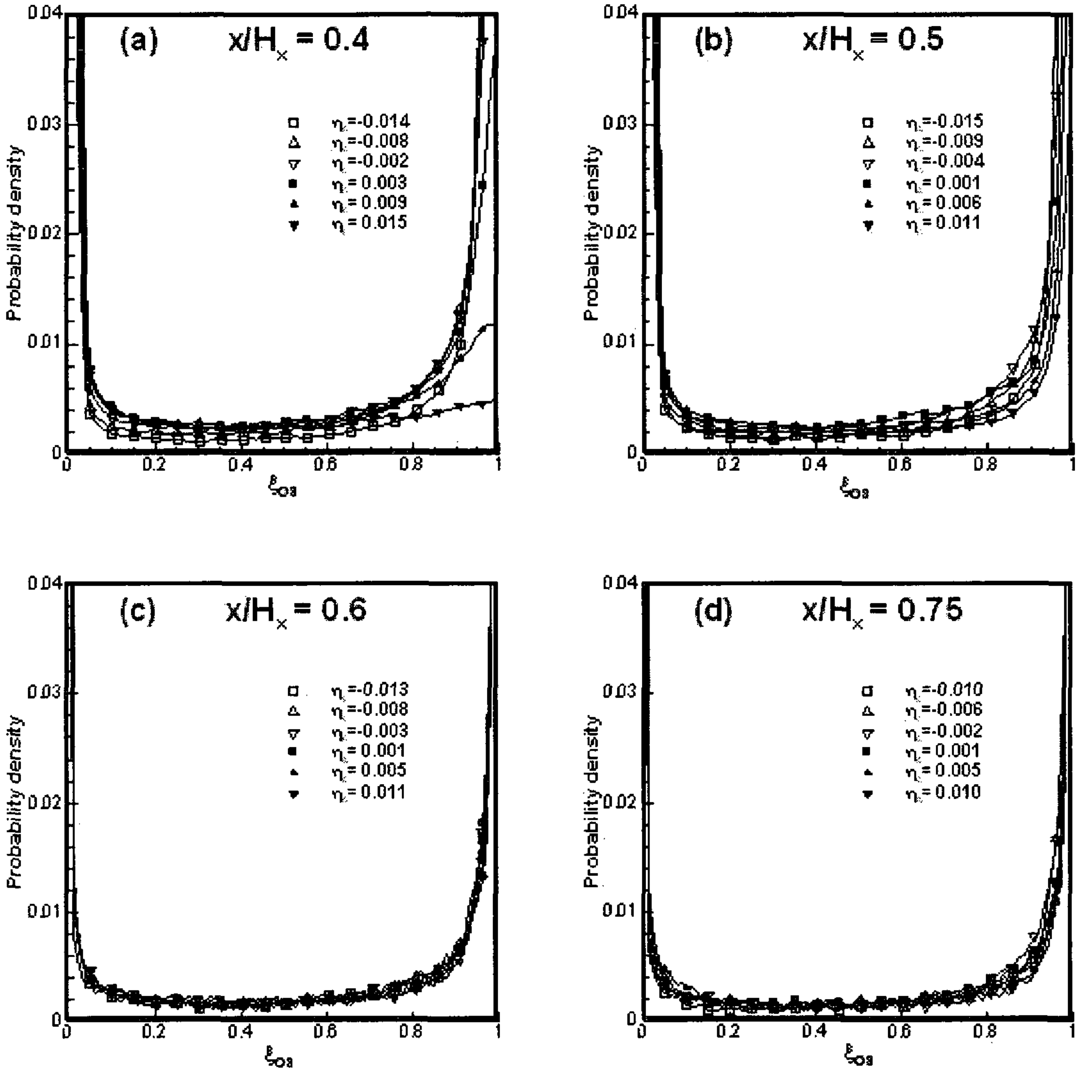

Figure 5-24: Probability density function (PDF) at several cross-stream locations for reactive flow: (a) $x/H_x = 0.4$, (b) $x/H_x = 0.5$, (c) $x/H_x = 0.6$ and (d) $x/H_x = 0.75$.

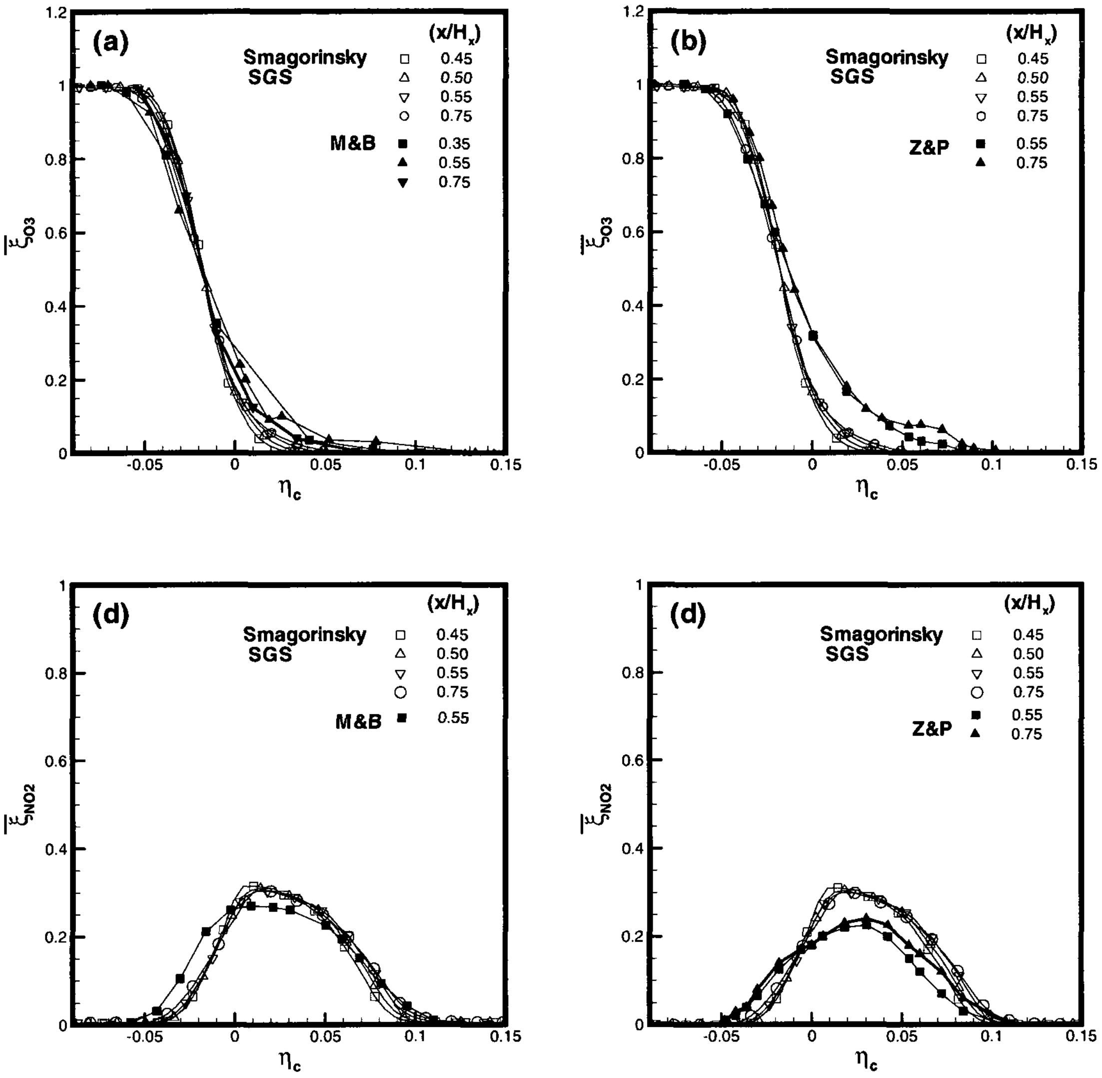

Figure 5-25: LES results for the reacting mixing layer using the Smagorinsky SGS model at different downstream locations: the normalized mean reactant O_3 concentration profiles compared to (a) experimental results of M&B (b) LES results of Z&P; and the normalized mean product NO_2 concentration profiles compared to (c) experimental results of M&B (d) LES results of Z&P.

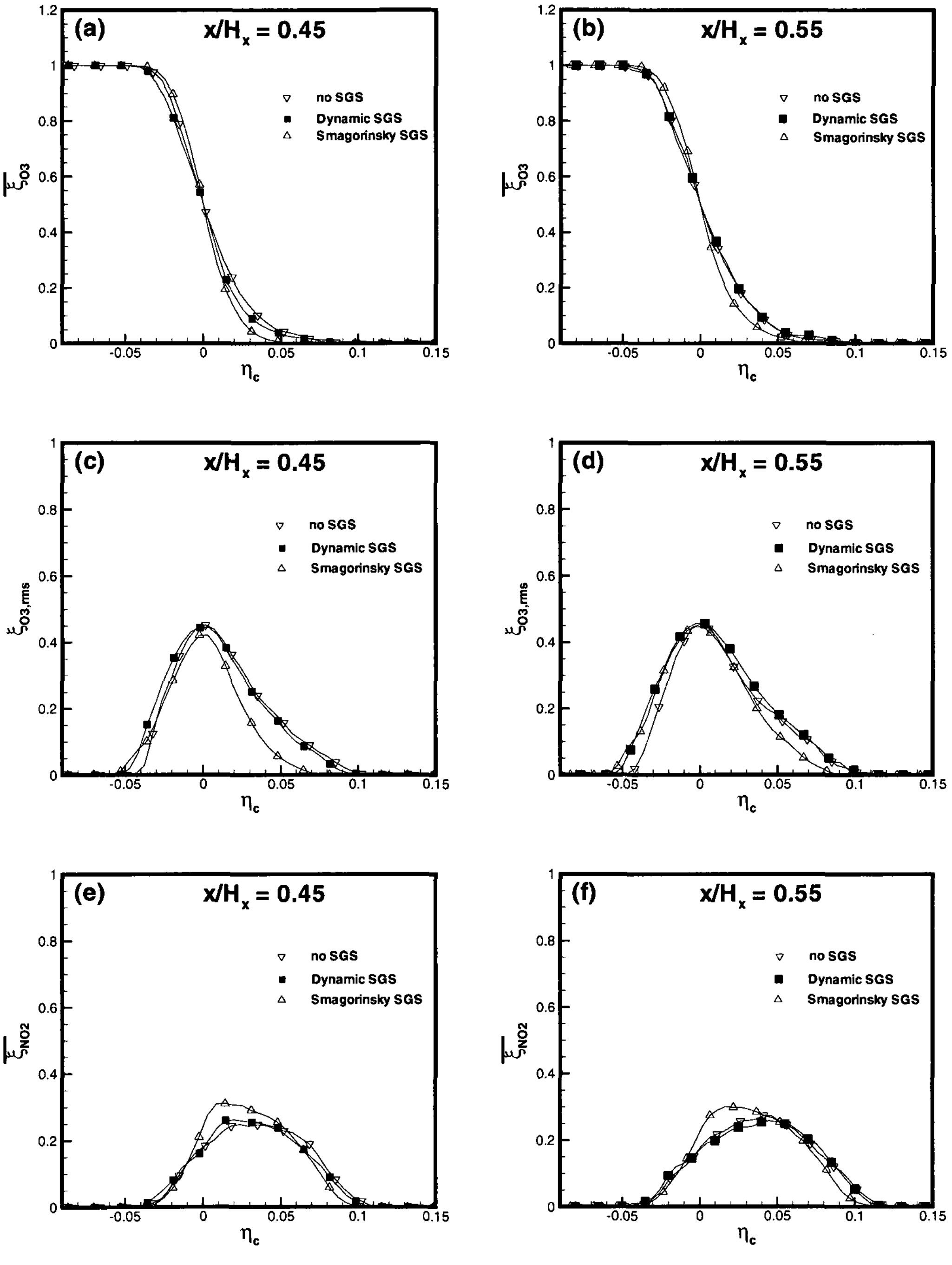

Figure 5-26: Effect of SGS on the reactive mixing layer; normalized mean concentration of O_3 at downstream locations: (a) $x/H_x = 0.45$ (b) $x/H_x = 0.55$; normalized rms O_3 concentration fluctuations at: (d) $x/H_x = 0.45$ (d) $x/H_x = 0.55$; normalized mean concentration of NO_2 at: (e) $x/H_x = 0.45$ (f) $x/H_x = 0.55$.

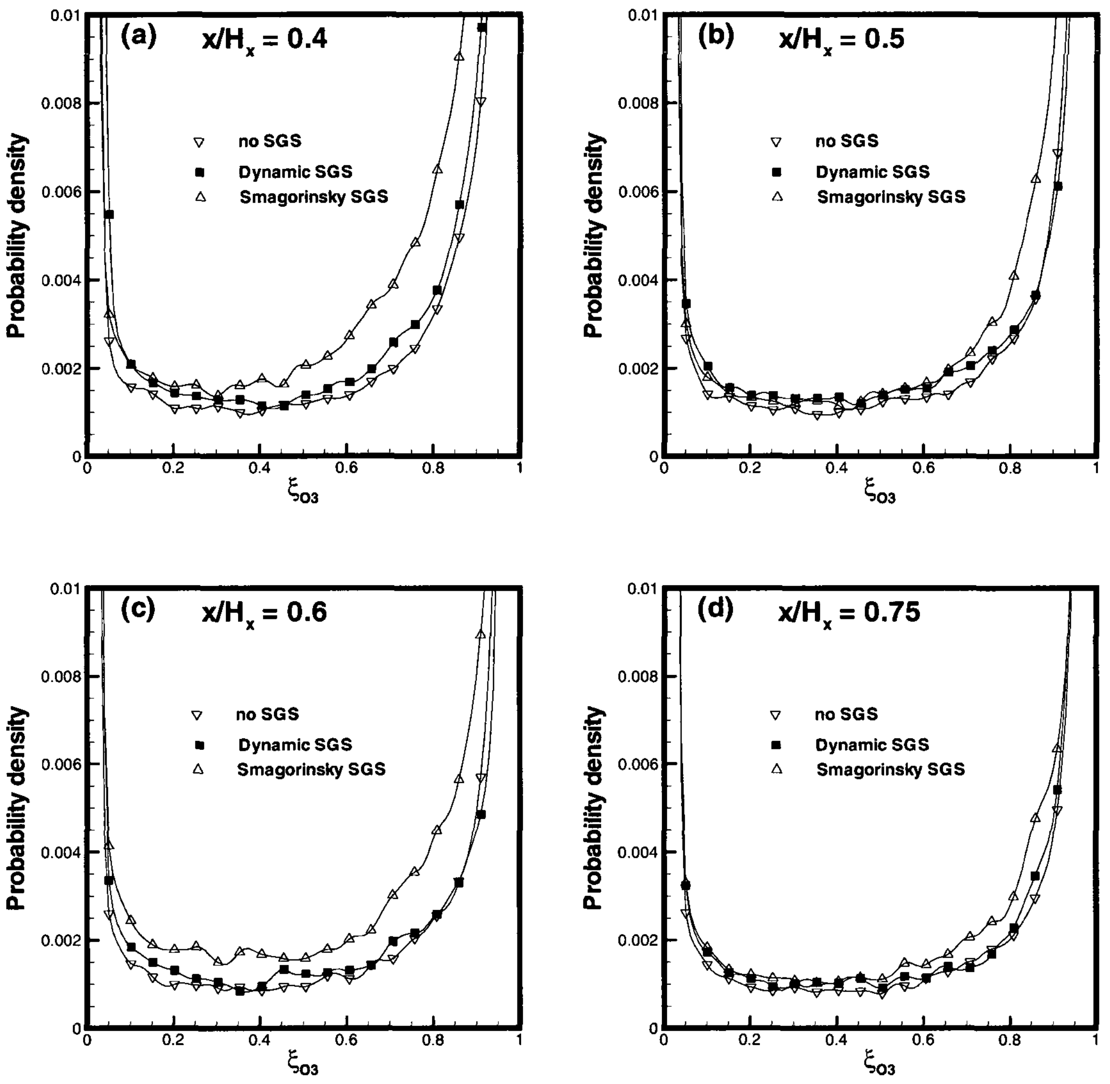

Figure 5-27: Effect of SGS on the PDF of the mixture fraction of O_3 for the reactive mixing layer at $\eta_c = -0.01$ at downstream locations: (a) $x/H_x = 0.4$, (b) $x/H_x = 0.5$, (c) $x/H_x = 0.6$ and (d) $x/H_x = 0.75$

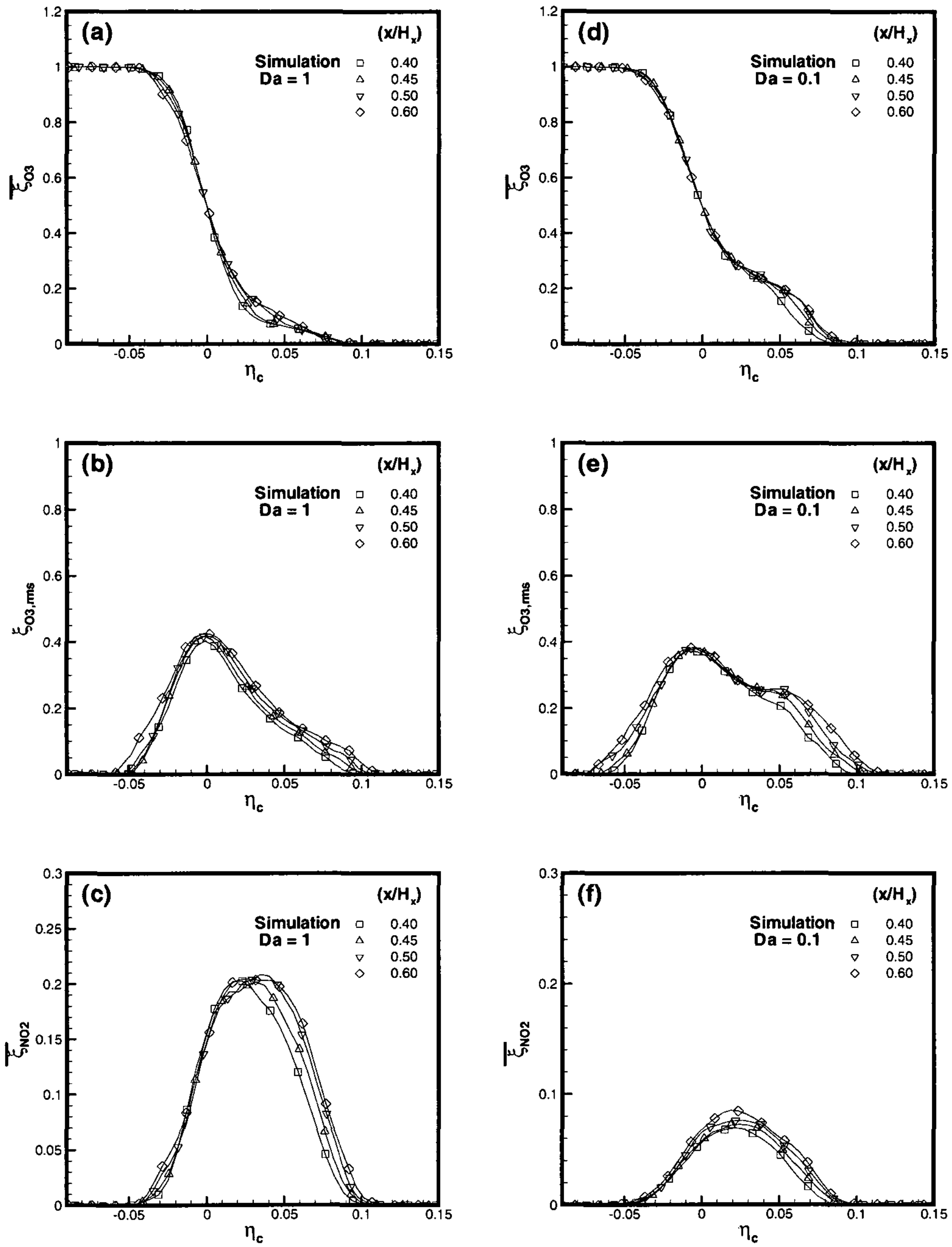

Figure 5-28: Normalized mean concentration of O_3 at selected downstream locations with: (a) $Da = 1.0$ (d) $Da = 0.1$; normalized rms concentration fluctuations of O_3 with: (b) $Da = 1.0$ (e) $Da = 0.1$; normalized mean concentration of NO_2 with: (c) $Da = 1.0$ (f) $Da = 0.1$.

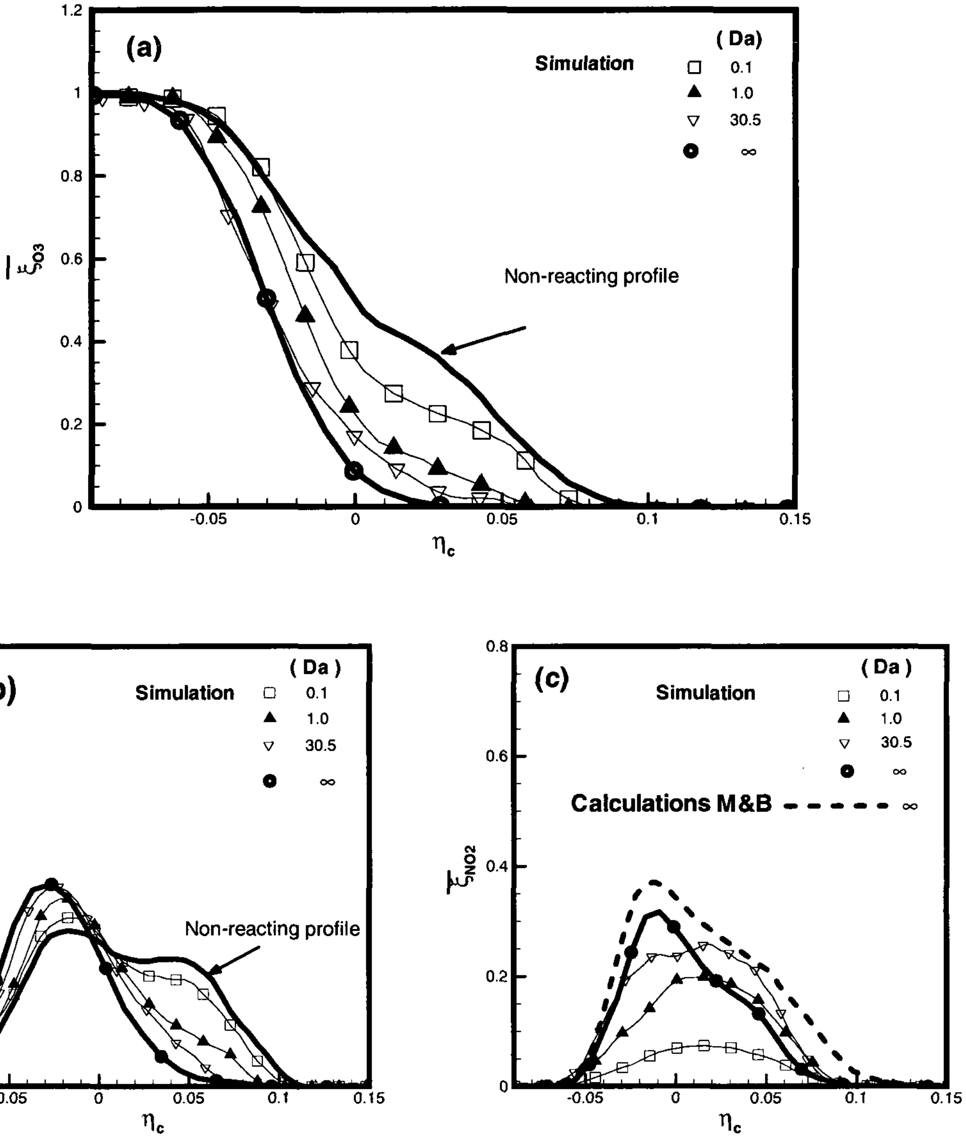

Figure 5-29: Effect of Da (a) normalized mean concentration profiles of O_3, (b) normalized rms concentration fluctuations of O_3 and (c) normalized mean concentration profiles of NO_2 at downstream locations $x/H_x = 0.55$.

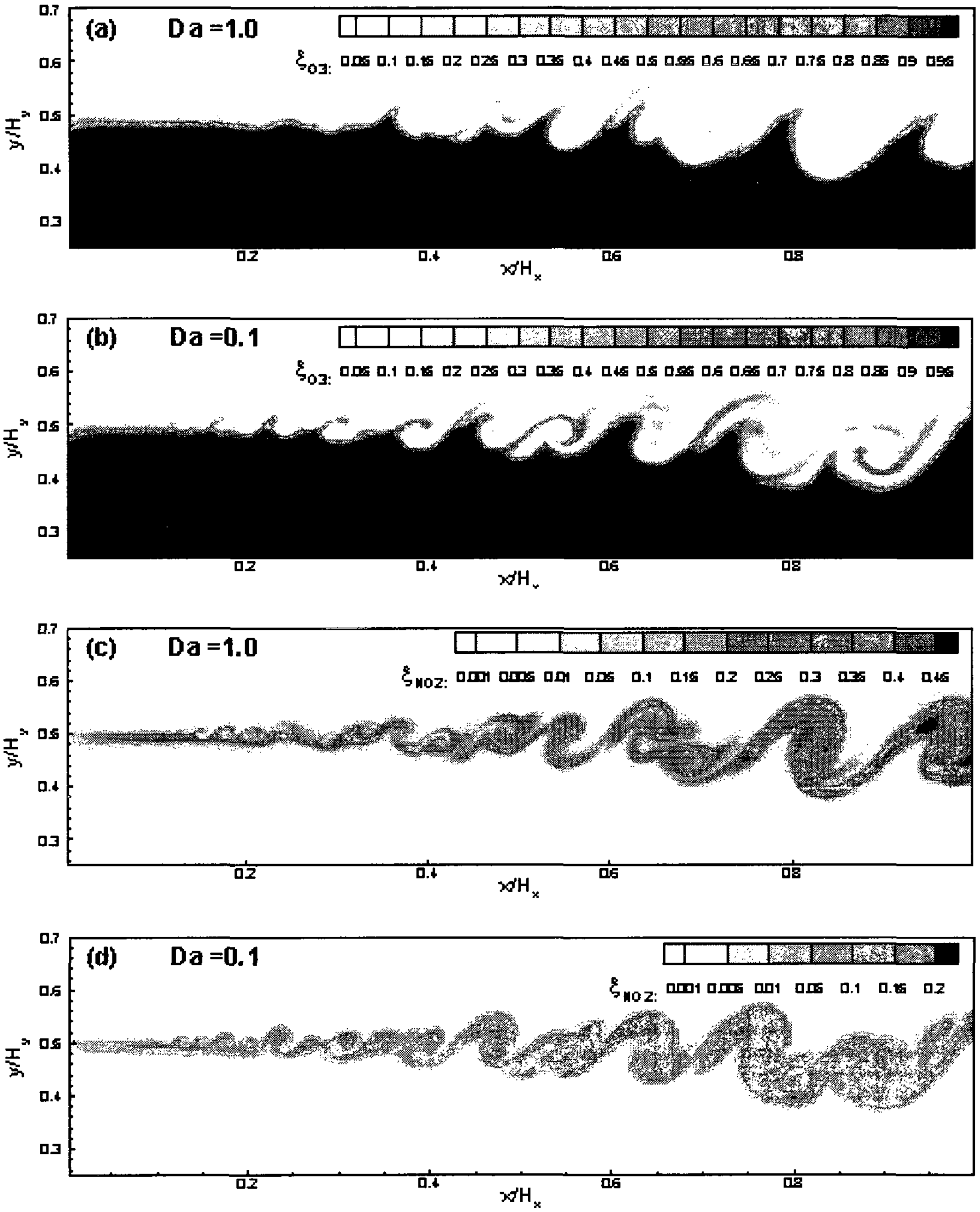

Figure 5-30: Instantaneous normalized concentration contours of the reactant O_3 for reactive mixing layer with (a) $Da = 1.0$ and (b) $Da = 0.1$ and of the product NO_2 with (c) $Da = 1.0$ and (d) $Da = 0.1$.

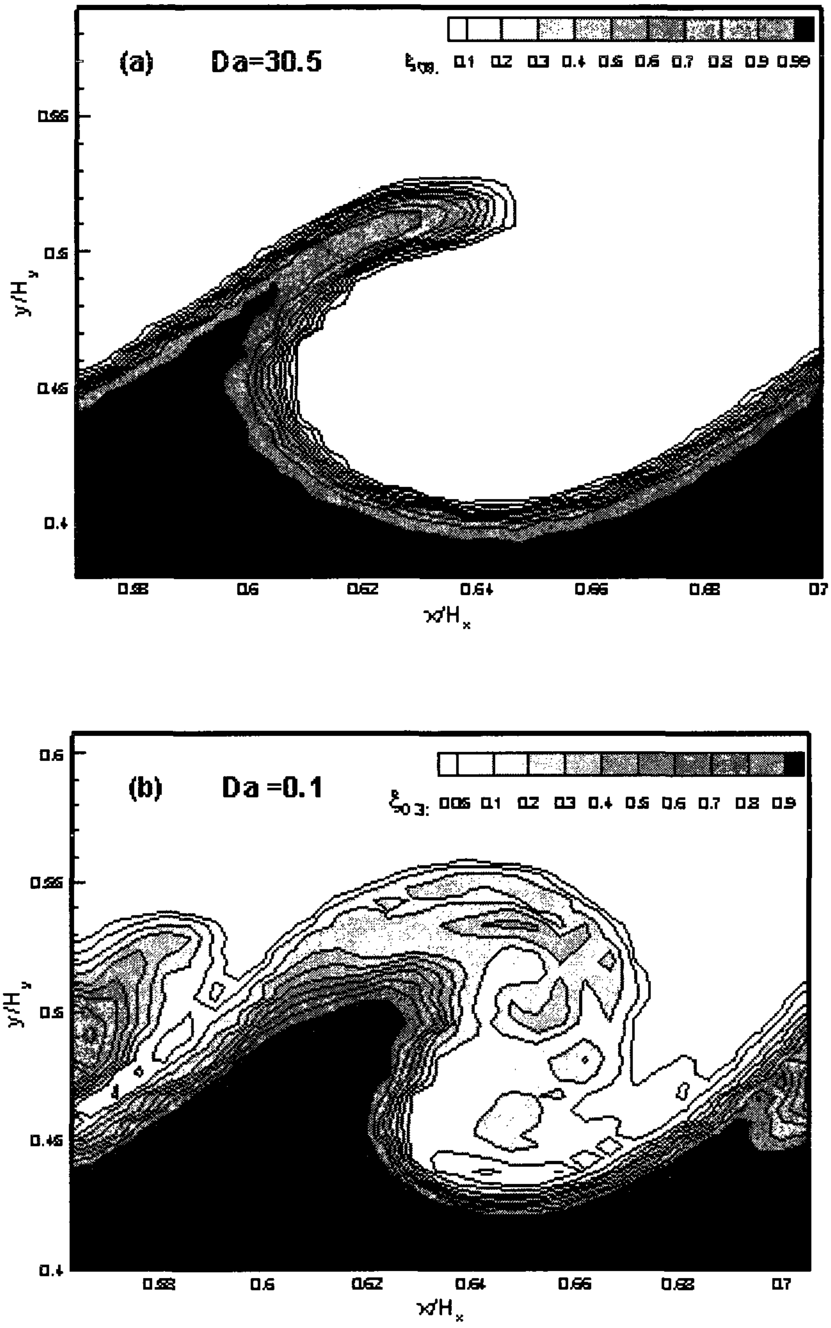

Figure 5-31: Enlarged visualization of calculated instantaneous concentration contours of mixture fraction of O_3 for the reactive plane mixing layer with (a) $Da = 30.5$ and (b) $Da = 0.1$.

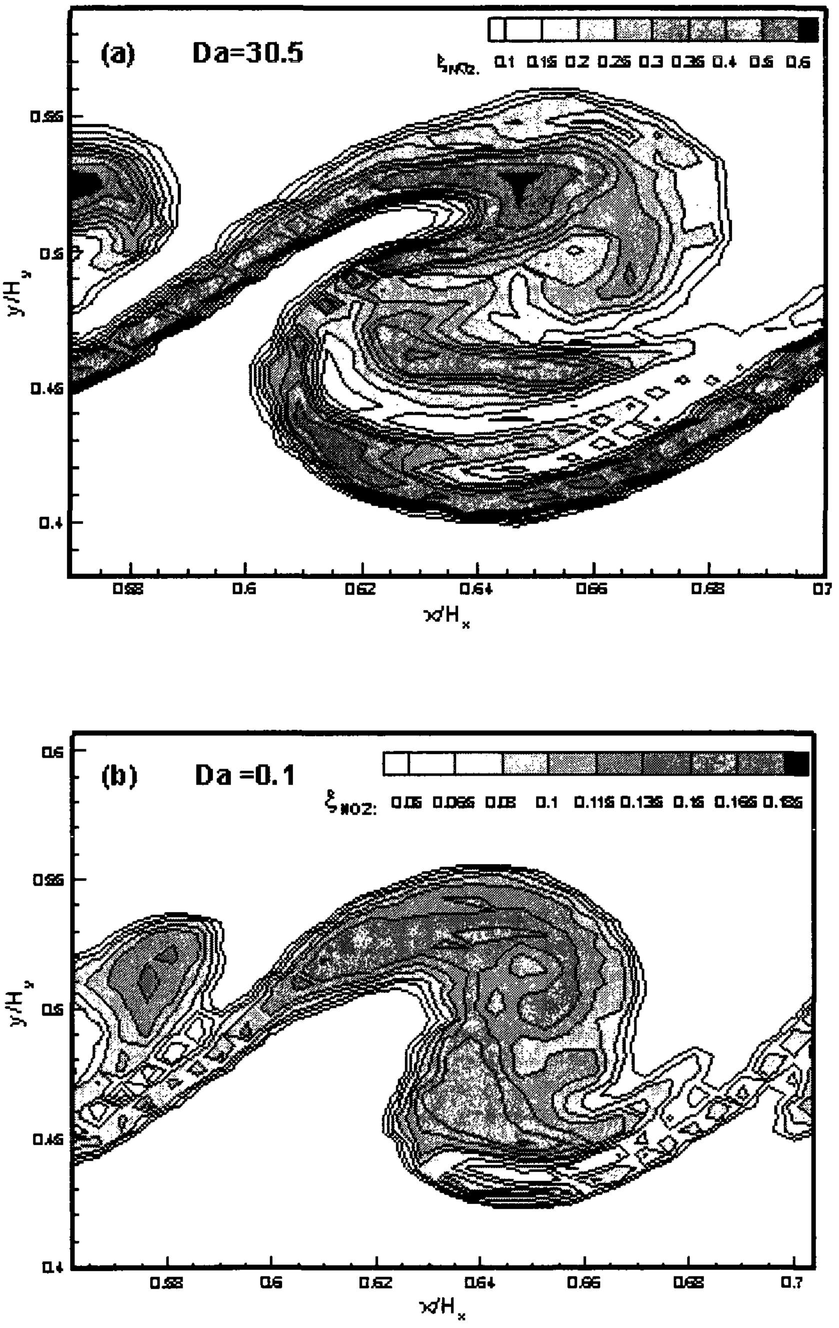

Figure 5-32: Enlarged visualization of normalized calculated instantaneous concentration contours of product NO_2 for the reactive plane mixing layer with (a) $Da = 30.5$ and (b) $Da = 0.1$.

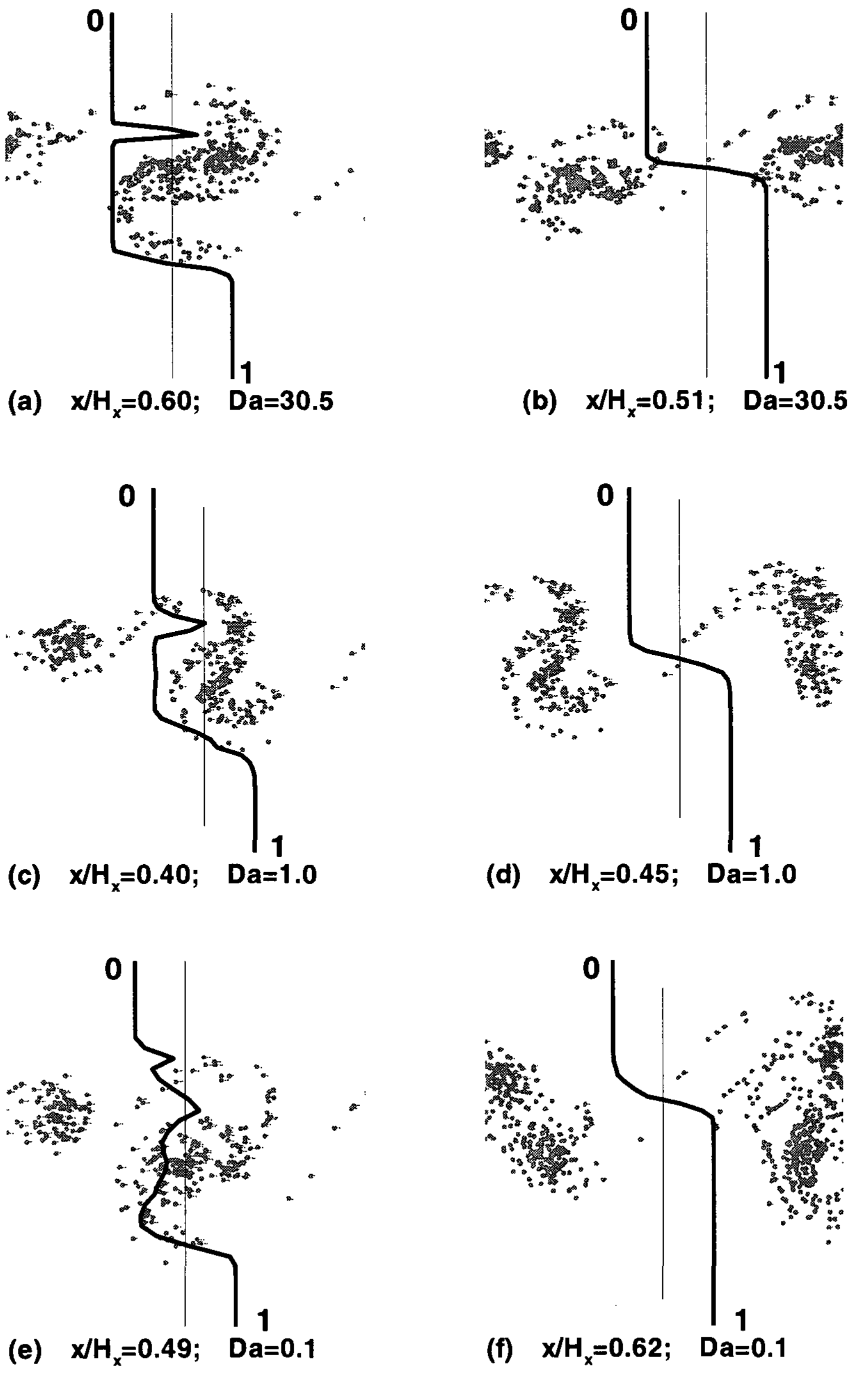

(a) x/H$_x$=0.60; Da=30.5 (b) x/H$_x$=0.51; Da=30.5

(c) x/H$_x$=0.40; Da=1.0 (d) x/H$_x$=0.45; Da=1.0

(e) x/H$_x$=0.49; Da=0.1 (f) x/H$_x$=0.62; Da=0.1

Figure 5-33: Instantaneous concentration profiles of reactant O_3 for the reacting flow superimposed on the vortex particles structure: across the midsection of the vortex with (a) $Da = 30.5$, (c) $Da = 1.0$ and (e) $Da = 0.1$; and across the braids with (b) $Da = 30.5$, (d) $Da = 1.0$ and (f) $Da = 0.1$ at different downstream locations.

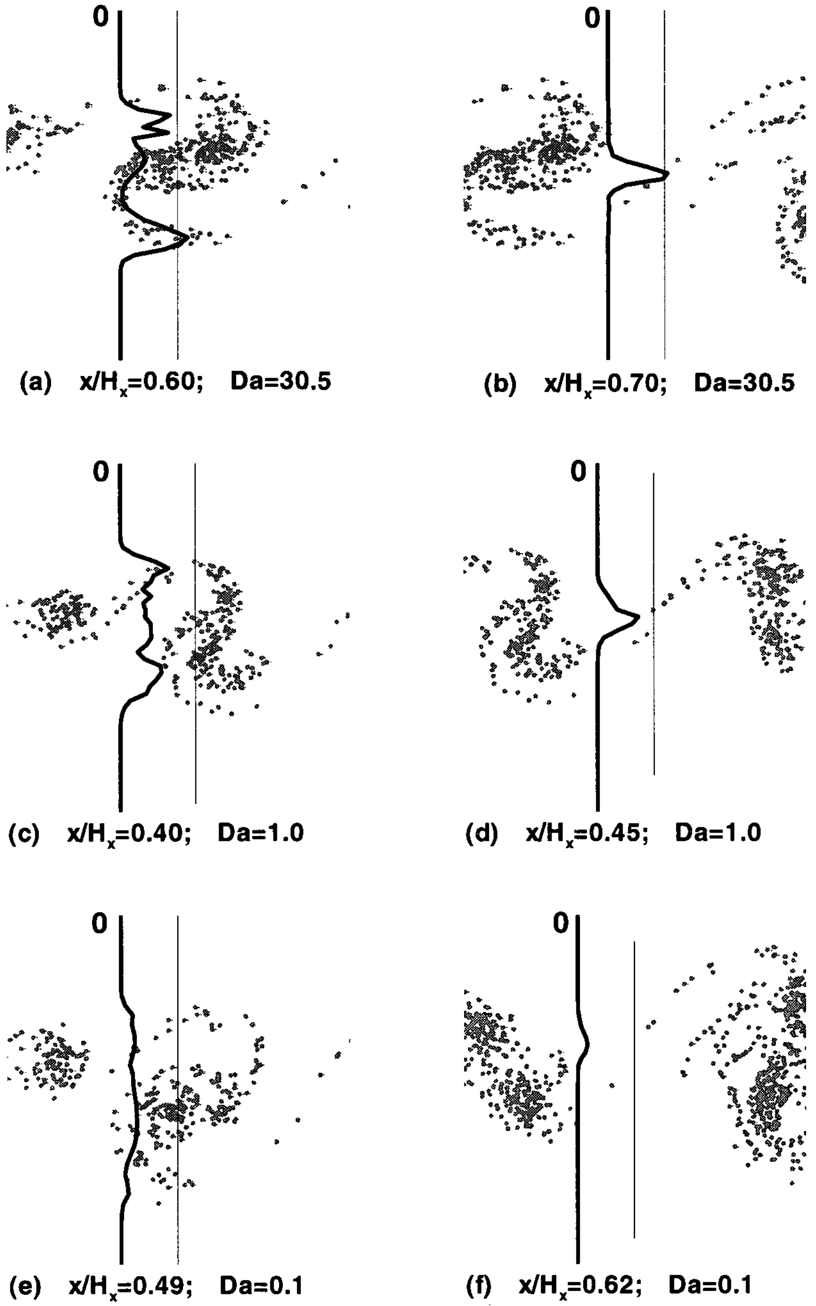

(a) x/H_x=0.60; Da=30.5 (b) x/H_x=0.70; Da=30.5

(c) x/H_x=0.40; Da=1.0 (d) x/H_x=0.45; Da=1.0

(e) x/H_x=0.49; Da=0.1 (f) x/H_x=0.62; Da=0.1

Figure 5-34: Instantaneous concentration profiles of product NO_2 for reacting flow superimposed on the vortex particles structure: across the midsection of the vortex with (a) $Da = 30.5$, (c) $Da = 1.0$ and (e) $Da = 0.1$; and across the braids with: (b) $Da = 30.5$, (d) $Da = 1.0$ and (f) $Da = 0.1$ at different downstream locations.

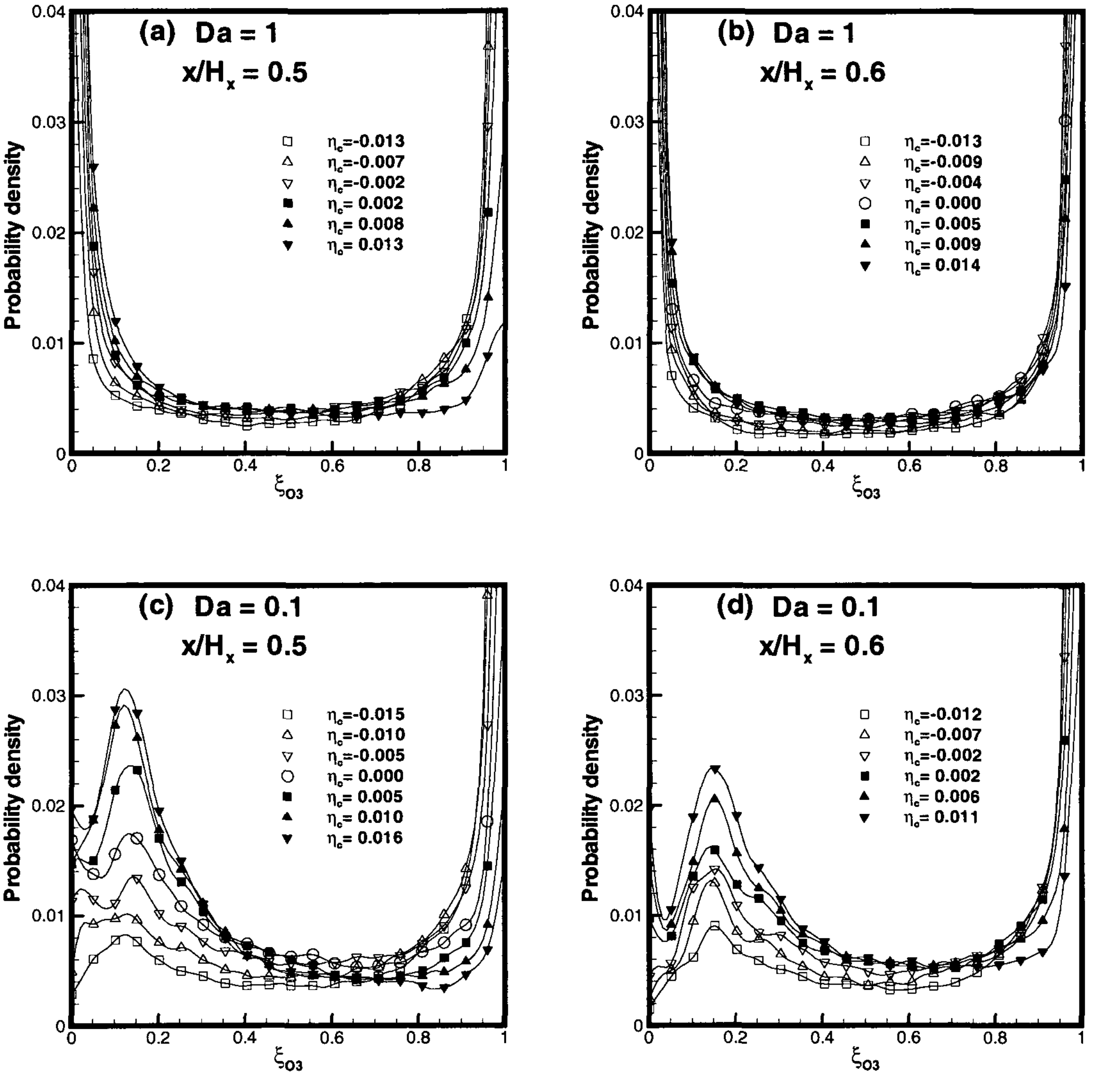

Figure 5-35: PDF of O_3 concentration for reactive flow at several cross-stream locations: (a) $x/H_x = 0.5$ & $Da = 1.0$, (b) $x/H_x = 0.6$ & $Da = 1.0$, (c) $x/H_x = 0.5$ & $Da = 0.1$ and (d) $x/H_x = 0.6$ & $Da = 0.1$.

Chapter 6

THERMAL MIXING LAYER

6.1 Flow Field of the Isothermal Mixing Layer

The results of the isothermal mixing layer are presented in this section: Firstly, to ensure the self-similarity characteristic of the mixing layer prior to introducing the temperature gradient in the flow field, and secondly to show the effect of the temperature gradient on the flow field by comparing the isothermal with the thermal mixing layers results. The numerical parameters used to describe the flow field are presented in Section 6.1.1; the location of vortex particles are presented in Section 6.1.2; the momentum and vorticity thicknesses are discussed in Section 6.1.3; the mean flow, rms velocities fluctuations and negative cross-stream correlations are presented in Section 6.1.4.

6.1.1 Numerical Parameters

The flow configuration (see Figure 3-1(a)) represents a mixing layer similar to that of the experiment of Mizuno et al. (2005). The ratio of the free-stream mean velocities $r = U_C/U_H$ was fixed at 2 with $U_C = U_h = 4\,m/s$ being the top cold stream mean velocity and $U_H = U_l = 2\,m/s$ being the lower hot stream mean velocity. Both top and bottom streams of the isothermal mixing layer consisted of air at $303\,°K$ with the kinematic viscosity $\nu = 16 \times 10^{-6}\,m^2/s$.

The computational flow domain used consisted of 210×210 nodes forming an anisotropic uniform mesh with an aspect ratio $a_{xy} = \frac{\Delta x}{\Delta y} = 2$ similar to the mesh used in simulating the reactive mixing layer presented previously in Chapter 5, with $\Delta x = 0.5\,cm$ and $\Delta y = 0.25\,cm$ being the grid size in x- and y-directions, respectively.

The initial vortex sheet, introduced at the level of the splitter plate, consisted of $N_v = 3150$ equidistant vortex particles. The circulation of each vortex particle is $\Gamma_i = 6.62 \times 10^{-4}\,m^2/s$, the residence time is $t_{res} = 0.23\,sec.$ and the time step is $\Delta t = 1.11 \times 10^{-4}\,s$. The value of y_{ov} used in Eq. 3.65 is set to $26.14\,cm$.

The LES was performed using the Smagorinsky SGS model. The flow was allowed to develop for two residence times before the statistical information were calculated. The mean flow quantities were obtained using time averaging over the next four residence times, the rms velocities fluctuations and the negative cross-stream correlations were calculated over the last eight residence times.

6.1.2 Vortex Particles Locations

The development of the mixing layer structure is presented in Figure 6-1 by displaying the instantaneous locations of all the vortex particles used in the computations at five different times. The plot shows the roll-up and pairing of large vortical structures in a similar manner to that discussed in Section 5.1.2 for the isothermal non-reacting mixing layer.

6.1.3 Vorticity Thickness

Figure 6-2 shows the downstream evolution of the normalized vorticity thickness (δ_ω) for the isothermal mixing layer. The vorticity thickness evolves in a nearly linear trend in the self-preserving region, i.e. $0.4 < x/H_x < 0.8$, with a growth rate of 0.065 comparable to the value of 0.062 found in the non-reacting mixing layer presented previously in Chapter 5.

6.1.4 Mean Velocity, RMS Velocities Fluctuations and Cross-Stream Correlations

Figure 6-3(a) shows the normalized mean velocity profiles plotted against the similarity variable η_v at five downstream locations. The Figure shows that the mean velocity profiles attain self similarity.

The normalized rms longitudinal $(u'_{rms}/\Delta U)$ and lateral $(v'_{rms}/\Delta U)$ velocity fluctuations are shown in Figure 6-3(b) and (c), respectively, as a function of η_v. The u'_{rms} and v'_{rms} profiles appear to attain self-similarity in the downstream region 0.5 <

$x/H_x < 0.7$ with peak values of 0.17 and 0.23, respectively. The normalized Reynolds shear stresses ($\overline{u'v'}/\Delta U^2$) profiles are shown in Figure 6-3(d). The $\overline{u'v'}$ profiles indicate adequate self-similarity in the downstream region where the data are presented.

6.2 Flow Field of the Thermal Mixing Layer

In this section, the thermal mixing layer flow field is investigated by simulating the work of Mizuno et al (2005) which consists of mixing hot and cold air streams in a simple mixing layer. The temperature difference between the two streams is set to $\Delta T = 50\,°K$. The numerical parameters are specified in Section 6.2.1, the vortex particle locations are presented in Section 6.2.2 and the flow statistics are discussed and validated in Section 6.2.3.

6.2.1 Numerical Parameters

The simulation of the thermal mixing layer is conducted using the computational domain sketched in Figure 3-1(a). It represents a mixing layer similar to that of the experiment of Mizuno et al. (2005). The ratio of the free-stream mean velocities $r = U_C/U_H$ is fixed at 2, with $U_C = 4$ m/s being the cold top stream mean velocity associated with a temperature $T_C = 303$ °K and $U_H = 2$ m/s being the lower hot stream mean velocity associated with a temperature $T_H = 353$ °K. Both top and bottom stream consists of air. The characteristic length $D_x = 0.1\,m$ is used in the normalization of the results presented in the work of Mizuno et al. (2005); D_x being half the height of the experimental setup. In order to interpret the effect of the volumetric expansion and the baroclinic reduction /generation terms, simplifications are introduced in the molecular transport properties. All particles are assumed to have the same diffusion coefficient D therefore the effects of differential diffusion are thereby eliminated. The kinetic viscosity is assumed to remain constant equal to $\nu = 16 \times 10^{-6}\ \mathrm{m}^2/\mathrm{s}$. Also, the Prandtl number Pr and the specific heat C_p of the mixture are assumed to be constant. The approximate value $Pr = 0.7$ for air is employed.

The computational flow domain consists of 210×210 nodes forming an anisotropic uniform mesh with an aspect ratio $a_{xy} = \frac{\Delta x}{\Delta y} = 2$ similar to the mesh used in simulating the isothermal flow field in Section 6.1.

The initial vortex sheet, introduced at the level of the splitter plate, consists of $N_v = 3150$ equidistant vortex particles. The circulation of each vortex particle is calculated to be $\Gamma_i = 6.62 \times 10^{-4}\ m^2/s$, the residence time is $t_{res} = 0.23\ sec.$ and the time step is $\Delta t = 1.11 \times 10^{-4}\ s$. The value of y_{ov} used in Eq. 3.65 is set to $26.14\ cm$.

The LES is performed using the Smagorinsky SGS model. The flow is allowed to develop for two residence times before the statistical information are calculated. The mean flow quantities are obtained using time averaging over the next four residence times, the rms velocities fluctuations and the negative cross-stream correlations are calculated over the last eight residence times.

6.2.2 Vortex Particles Locations and Vorticity Thickness

The development of the thermal mixing layer structure is presented in Figure 6-4 by displaying the instantaneous locations of the vortex particles used in the computation at five different times. Three distinct regions can be observed for the thermal mixing layer under study. The first region is characterized by a flow with vortex particles almost aligned. Comparison between Figure 6-4 and Figure 6-1 indicates that this region gets shorter when the temperature difference between the upper and the lower streams is increased. In the second region i.e. $0.1 < x/H_x < 0.35$, the vortex particles start to organize into semi-round structures prior to the first roll-up. In the third region, i.e. $x/H_x > 0.35$, the mixing layer becomes fully developed and continues to expand due to vortex pairing and amalgamation. In this fully developed region, the self-similarity in the mixing layer prevails. The vorticity thickness exhibit a nearly linear growth in this region i.e. $0.35 < x/H_x < 0.7$ as shown in Figures 6-5(a) and (b). The growth rate of the vorticity thickness for the thermal mixing layer is 0.059.

6.2.3 Flow Statistics

The flow statistics obtained from the simulation of the thermal mixing layer are compared with the experimental data of Mizuno et al. (2005) in the initial region of the mixing layer and then they are presented in the fully developed region to address the self-similarity of the mixing layer. The mean longitudinal velocity is discussed in Section 6.2.3.1, the rms longitudinal and lateral velocities fluctuations are discussed in Section 6.2.3.2 and the negative cross-stream correlations are presented in Section 6.2.3.3. Self-similar profiles are shown in Section 6.2.3.4.

6.2.3.1 Mean Longitudinal Velocity

The normalized mean longitudinal velocity profiles are compared with the experimental results of Mizuno et al. (2005) at four downstream locations $x/D_x = 0.35, 0.5, 1.0$ and 2.0 in Figures 6-6(a), (b), (c) and (d), respectively. In Figures 6-6(a) and (b), the numerical results show a minimum value similar to the experimental results but at a slightly lower lateral position. Figures 6-6(c) and (d) indicate that the experimental mixing layer thickness is larger than the numerical one and this is marked by the broader velocity profile separating the two free-streams values. Moreover, it is noted that the experimental mixing layer develops at a faster rate than the numerical simulation. Therefore, it is suggested to compare the experimental and the numerical profiles at different downstream positions but with the same approximate spread in the y-direction. For this reason, the experimental results in Figure 6-10(d) are different than the calculated results at $x/D_x = 2.0$ but show a better fit with the numerical results at the downstream location $x/D_x = 4.0$.

6.2.3.2 RMS Longitudinal and Lateral Velocities Fluctuations

The normalized rms longitudinal and lateral velocities fluctuations are compared with the experimental results of Mizuno et al. (2005) in Figures 6-7(a)-(d) and Figures 6-8(a)-(d) at four downstream locations. It is apparent that the numerical results differ from the experimental results in the initial stage of the mixing layer. This deviation may be attributed to two main reasons.

Firstly, Figures 6-7(a)-(d) and 6-8(a)-(d) show that all the profiles of the calculated rms longitudinal and lateral velocity fluctuations show a similar trend but are shifted back from the experimental results by a constant value all the way across the mixing layer. Looking closely at the profiles for $x/D_x = 0.35$ and 0.5 (Figures 6-7(a) and (b) and Figures 6-8(a) and (b), respectively) at the range outside the mixing layer; i.e. $y/D_x > 0.2$ and $y/D_x < -0.2$, the experimental results show a non-zero turbulence values. This indicates that the free-streams were not turbulence free in Mizuno et al. (2005).

Secondly, the difference in the spread rate between the numerical and experimental results needs to be accounted for. The agreement between the numerical and experimental results would have been improved substantially if the downstream positions were normalized with respect to the momentum thickness $\theta(x)$. Mizuno et al. (2005) stated that the thermal mixing layer development is accelerated in the region after $x/D_x = 1.0$. It is shown that the experimental results in Figure 6-8(d) and Figure 6-9(d) are close to the numerical results at the downstream location $x/D_x = 4.0$, where the mixing layer is nearly fully developed.

6.2.3.3 Negative Cross-Stream Correlations

In Figures 6-9(a)-(d), the normalized negative cross-stream correlations $(-\overline{u'v'}/{U_C}^2)$ profiles are presented and compared to the experimental results of Mizuno et al. (2005) at four downstream locations. Figures 6-9 (a) and (b) show adequate agreement between the experimental and numerical results at the downstream locations $x/D_x = 0.35$ and 0.5. The profiles exhibit an S-shape having the zone of positive Reynolds stress in the high speed side of the flow. At the downstream locations $x/D_x = 1.0$ and 2.0 (Figures 6-9(c) and (d) respectively), the numerical results are different from the experimental data and this may be due to the difference in the spread between the experimental and simulated mixing layers. The experimental data in Figure 6-9(d) are shown to have a better fit with the calculated $-\overline{u'v'}/{U_C}^2$ profiles further downstream, i.e. at $x/D_x = 4.0$, corresponding to a more developed region of the simulated mixing layer.

6.2.3.4 Flow Field Self-Similarity

Figure 6-10(a) shows the normalized mean longitudinal velocity profiles plotted against the similarity variable η_v, at six downstream locations. The profiles appear to attain self-similarity for the downstream region $0.55 < x/\mathrm{H}_\mathrm{x} < 0.75$, i.e. $5.8 < x/D_\mathrm{x} < 7.8$ which corresponds to the fully developed mixing layer region and where the momentum and vorticity thicknesses evolve linearly.

Figures 6-10(b) and (c) show the normalized u'_{rms} and v'_{rms} profiles plotted against the similarity variable η_v, at six downstream locations. The profiles are adequately self-similar in the self-preserving region i.e. $0.55 < x/H_x < 0.75$, i.e. $5.8 < x/D_\mathrm{x} < 7.8$.

Figure 6-10(d) shows the $-\overline{u'v'}/\Delta U^2$ profiles plotted against the similarity variable η_v, at six downstream locations. The profiles appear to attain self-similarity in the downstream region $0.55 < x/H_x < 0.75$, i.e. $5.8 < x/D_\mathrm{x} < 7.8$ which corresponds to the self-preserving region of the mixing layer.

6.3 Scalar Field of the Thermal Mixing Layer

In this section the scalar field results of the thermal mixing layer are presented. The numerical parameters used to describe the scalar field are stated in Section 6.3.1; instantaneous temperature contours and profiles are discussed in Section 6.3.2; the mean temperature and rms temperature fluctuations and the turbulent heat fluxes results are presented and compared to experimental data in Section 6.3.3; the filtered mass weighted probability density function is discussed in Section 6.3.4.

6.3.1 Numerical Parameters

The scalar field of the thermal mixing layer is solved using the Monte-Carlo technique on rectangular computational domain identical to the one used to solve the flow field and sketched in Figure 3-1(b). The number of particles per grid is $N_g = 36$. Boxes centered at nodes are used to approximate scalar field variables and statistics. The box size is set to 40% of the grid size identical to the scalar field solution of the reactive mixing layer in Chapter 5. The turbulent Prandtl number employed is $Pr_t = 0.7$ and the constant $C_\emptyset$ is set to a value of 3.0. To achieve statistically stationary solutions, The Monte-Carlo simulation is run for 14 residence times. Similar to the flow field run, the first two residence times ensured the development of the flow. Then the mean temperatures are computed over the next four residence times. The rms temperature fluctuations, turbulent heat fluxes and FMDFs are computed over the last eight residence times. The LES is performed using the Smagorinsky SGS model.

6.3.2 Instantaneous Temperature and Vortex Structure

The downstream evolution of the temperature contours is shown in Figures 6-11 at five consecutive times. The three phases of the mixing layer are observed, i.e. the tongues of unmixed free stream fluid stretching all the way across the layer, the finite thickness heat diffusion zones and the cores of mixed fluid of nearly homogeneous composition.

Figures 6-12(a)-(f) show the instantaneous temperature profiles at different downstream locations superimposed on the instantaneous distribution of the vortex particles. The locations are chosen across the midsection of the vortex in Figures 6-12(a)-(c), and across the braids in Figures 6-12(d)-(f). The instantaneous temperature profiles reveal that, even at sections far downstream of the splitter plate, free-stream unmixed fluid from both sides is still engulfed and incorporated into the vortex layer by the entrainment and pairing mechanism. Across the braids, the instantaneous temperature changes between the free streams values within a distance comparable to the initial shear layer thickness described by the inlet temperature error function profile.

6.3.3 Normalized Mean Temperature, RMS Temperature Fluctuations and Turbulent Heat Flux

The normalized mean temperature profiles are compared with the experimental results of Mizuno et al. (2005) at four downstream locations $x/D_x = 0.35, 0.5, 1.0$ and 2.0 in Figures 6-13(a), (b), (c) and (d), respectively. In Figures 6-13(a), (b) and (c), the numerical results show a satisfactory agreement with the experimental results. Figure 6-13(d) indicates that the experimental temperature profiles are laterally more stretched than the numerical one. Moreover, the experimental results in Figure 6-13(d) differ from the calculated results at $x/D_x = 2.0$ but show a better fit with the numerical results at the downstream location $x/D_x = 4.0$. This is an indication that the experimental mixing layer develops at a faster rate than the numerical simulation.

The normalized rms temperature fluctuations are compared with the experimental results of Mizuno et al. (2005) in Figures 6-14(a)-(d) at four downstream locations. The calculated T'_{rms} results are close to the experimental data for $x/D_x = 0.35, 0.5$ and 1.0. For $x/D_x = 2.0$, Figure 6-14(d) shows that there is a difference between experimental data and numerical results. Figure 6-14(d) shows a better fit between the experimental data at $x/D_x = 2.0$ and the numerical results at $x/D_x = 4.0$ which corresponds to a more developed region in the simulated mixing layer.

The normalized longitudinal heat flux $(\overline{u'T'})$ are compared with the experimental results of Mizuno et al. (2005) in Figures 6-15(a)-(d) at four downstream locations. For $x/D_x = 0.35$ and 0.5, in Figures 6-15(a) and (b), respectively, the $\overline{u'T'}$ profiles exhibit an S-shape having a dip of positive values in the lower stream. As shown in Figures 6-15(c) and (d), for $x/D_x = 1.0$ and 2.0 respectively, the dip in the lower stream is more pronounced and the calculated $\overline{u'T'}$ exhibit a two-maxima with a saddle point profiles different from the experimental trend. An explanation for the numerical results behavior is proposed in the next Section 6.3.4.

The lateral distributions of the normalized lateral turbulent heat flux $(\overline{v'T'})$ are compared with the experimental data of Mizuno et al. (2005) in Figures 6-16(a)-(d). The calculated $\overline{v'T'}$ results are close to the measured data for $x/D_x = 0.35$ and 0.5, shown in Figures 6-16(a) and (b), respectively. Figures 6-16(c) and (d) indicate that the calculated $\overline{v'T'}$ values are different from the experimental data; this may be attributed to the differences in the spread rate between the experimental and the simulated mixing layer. Also, Figure 6-16(d) indicates that the experimental results match the calculated one at $x/D_x = 4.0$ rather than 2.0. This indicates that the numerical results develop at a slower rate than the experimental results.

6.3.4 Scalar Field Self-Similarity

Figure 6-17(a) shows the normalized mean temperature profiles plotted against the similarity variable η_T, at five downstream locations. The similarity variable is given as $\eta_T = \frac{(y-y_T)}{(x-x_{vT})}$, where x_{vT} and y_T the virtual origin of the temperature field and the ordinate of the centerline, respectively. The profiles appear to attain self-similarity for the downstream region $0.55 < x/\mathrm{H}_x < 0.75$, i.e. $5.8 < x/D_x < 7.8$, which corresponds to the fully developed mixing layer region and where the vorticity thickness evolves linearly as shown in Figure 6-5.

Figure 6-17(b) shows the normalized rms temperature fluctuations profiles plotted against the similarity variable η_T, at five downstream locations. The profiles appear to attain self-similarity in the self preserving region, i.e. $0.55 < x/H_x < 0.75$.

Figures 6-17(c) and (d) show the longitudinal and the lateral heat fluxes profiles, respectively, plotted against the similarity variable η_T. The $\overline{u'T'}$ and $\overline{v'T'}$ profiles appear to be self-similar in the fully developed region corresponding to $0.6 < x/H_x < 0.75$, i.e. $6.3 < x/D_x < 7.8$.

Moreover, in Figure 6-17(c) the $\overline{u'T'}$ profiles indicate positive values for $\eta_T < 0$ and then negative values for the region where $0 < \eta_T < 0.05$, followed by a positive bump for $0.05 < \eta_T < 0.1$. This trend in the $\overline{u'T'}$ profiles can be justified by considering the turbulent motion of a fluid particle. To this end, Figure 6-18 displays the mean temperature $\overline{T}$ contours along with two fluid particles (A and B) transported by a turbulent flow. It is assumed that each particle moves randomly, while conserving its temperature, at least as long as required for moving over one average distance from its original position (Tavoularis, 2007). It is noted that the line $\eta_T = 0$ corresponds to the line of constant average mean temperature i.e. $\overline{T}_{avg} = 328\ °K$.

For $\eta_T < 0$, considering particle A has a positive $u' > 0$, it moves downstream where the local mean $\overline{T}$ is smaller than its own temperature, so that the particle contributes a positive fluctuation, i.e. $T' = T - \bar{T} > 0$, to the local flow. Similarly it generates a negative fluctuation($T' < 0$) if it has a negative $u' < 0$, i.e. it moves upstream towards higher local mean temperature. Therefore for $\eta_T < 0$, the average turbulent heat flux of particle A will likely be positive, i.e. $\overline{u'T'} > 0$. The opposite would happen for particle B moving in the region $0 < \eta_T < 0.05$. If particle B has a positive $u' > 0$ it moves downstream towards a region of higher local mean temperature and it generates a negative fluctuation $T' < 0$ to the local average and vice versa. Therefore the average turbulent heat flux in the region $0 < \eta_T < 0.05$ will most likely be negative. The positive values of $\overline{u'T'}$ in the region $0.05 < \eta_T < 0.1$ are consistent with the third inflection point in the mean temperature profiles (Figure 6-17(a)) and with the second peak in the rms temperature fluctuations profiles (Figure 6-17(b)).

Similarly, the positive values of $\overline{v'T'}$ shown in Figure 6-17(d) can also be justified. If particle A has a positive $v' > 0$, it will be moves upward towards a region of lower local mean temperature and it contributes a positive fluctuation ($T' > 0$) to the local average. The opposite would happen if particle A has negative $v' < 0$, it will be moving downward towards a higher local mean temperature region and then it generates a negative fluctuation. Therefore, the average lateral turbulent heat flux $\overline{v'T'}$ is expected be positive in the mixing layer.

6.3.5 Filtered Mass Weighted Probability Density Function (FMDF)

Figures 6-19(a)-(d) show the FMDFs at selected downstream locations for $x/H_x = 0.5, 0.6, 0.7$ and 0.75. The FMDF profiles show the presence of a preferred temperature T_p marked with a peak in the temperatures between the two free-stream values. As expected, Figures 6-19(a)-(d) reveal that the value of the preferred temperature that exists in the nearly homogeneous core regions of the vortex layer $T_p = 320°K$ corresponds to the third of the temperature difference between the two free streams, i.e. $(T_p - T_C)/(T_H - T_C) = 0.33$. The fact that the preferred temperature value doesn't vary along with η_T indicates that the FMDFs are non-marching. Contrary to the observation made on the preferred concentration for the non-reactive scalar in Section 5.2.2.3, the preferred temperature value does not vary with the downstream locations. This can be attributed to the fact that the large scale eddies pairing mechanism that was responsible of incorporating more fluids from the lower stream toward the core regions is reduced.

6.4 Effect of Temperature Difference

In this section, the effect of temperature difference on the flow field of the thermal mixing layer is investigated. To this end, three additional runs are made by varying the lower hot stream temperature in such a way that $\Delta T = 5, 10$ and $30°K$. These three runs are then compared with the isothermal mixing layer and the thermal mixing layer with $\Delta T = 50°K$ previously discussed in Section 6.1 and 6.2, respectively. The effect of temperature difference on the vorticity structure and contours is investigated in Section 6.4.1. Section 6.4.2 discusses the effect of temperature difference on the momentum and vorticity thicknesses and comparison of the flow field results for the five runs is presented in Section 6.4.3.

6.4.1 Vorticity Contours

Figures 6-20(a)-(e) display the downstream evolution of the vorticity contours for the five runs investigated. It is noted that as the temperature difference ΔT increases, the initial region is destabilized earlier. The initial region carries higher vorticity as ΔT increases (see legend) due to both volumetric expansion (or contraction) and baroclinic generation (or destruction) (see Eq. 3.24). However as the flow develops downstream, the vorticity is almost insensitive to ΔT as shown in the close up vorticity contours in Figures 6-21(a)-(e). This implies that the vortical structures in the downstream positions expand as ΔT increases in order to conserve the circulation. The conservation of circulation for the five runs is confirmed in Figure 6-22.

As mentioned before, temperature effect on the vorticity field is mainly due to two mechanisms: volumetric expansion and baroclinic generation. It is noted that the volumetric expansion increases the area and therefore decreases the vorticity, whereas the volumetric contraction reduces the area and therefore increases the vorticity to preserve the circulation. This mechanism does not alter the vorticity sign. However, the baroclinic generation term is strongly directional, i.e. it changes the vorticity sign. Therefore it modifies the vorticity in regions where the fluid acceleration and the density gradient vectors are misaligned. In the present two-dimensional study and due to the free stream velocity configuration, the spanwise vorticity is initially negative, i.e. clockwise. The contribution of the baroclinic term tends to improve the amalgamation of vortical structures when it generates negative vorticity and to inhibit their interactions when it generates positive vorticity (Soteriou and Ghoniem, 1995). Due to the fact that the baroclinic generation term is responsible for the positive vorticity surrounding the vortical structures, it resists the clockwise pairing action of neighboring structures. This is noticed in Figure 6-20(e) where the pairing process of the vortical structures is inhibited. This inhibition tends to reduce the entrainment of the free streams fluids. This may be the reason why the preferred temperature does not vary along the streamwise direction as noted in the FDF discussed in Section 6.3.4.

6.4.2 Vorticity Thickness

Figure 6-23 shows a comparison of the normalized vorticity thickness for the five runs under study. It is noted that the vorticity thickness profiles show higher values as ΔT increases. However they indicate a slower growth rate in the fully developed region i.e. $0.55 < x/H_x < 0.75$. For $x/H_x > 0.8$, the values are ignored due to end effects.

6.4.3 Flow Statistics

Figures 6-24(a)-(d) display the flow field results for the five runs with different lower stream temperature under study at the downstream location $x/H_x = 0.6$ in the self-similar region. The normalized mean velocity profiles shown in Figure 6-24(a) reflect the increase in the spread as ΔT increases, in agreement with the increase of the vorticity thickness in Figure 6-23. Figures 6-24(b) and (c) show the normalized rms longitudinal and lateral velocity fluctuations, respectively, both quantities show a slight increase in the peak when the temperature difference is increased. The negative cross stream correlation profiles are presented in Figure 6-24(d). The trend of the peak values is opposite to the trend of the peaks in u'_{rms} and v'_{rms}, i.e. the peak decreases with increasing ΔT.

6.5 SGS Effects

In order to emphasize the dissipative effect of the Smagorinsky SGS model on the thermal mixing layer results, two runs are made: a run without SGS model and another run with Smagorinsky SGS model. The temperature difference between the cold and the hot air streams is set to $\Delta T = 50°K$.

6.5.1 Vorticity Contours

Figures 6-25(a) and (b) illustrate the downstream evolution of the vorticity contours for the runs with and without SGS model, respectively. Comparison between Figure 6-25(a) and Figure 6-25(b) indicates the drop in the vorticity values depicted by the decrease in the maximum contour level when using the Smagorinsky SGS model (see legend): it attained 850 for the case without SGS model and 700 for the case with Smagorinsky SGS model. This drop is due to the dissipative effect induced by the SGS model. Close up of chosen downstream locations between $x/H_x = 0.62$ and 0.74 in the self similar region are shown in Figures 6-25(c) and (d) for the runs with Smagorinsky SGS model and the run without SGS model, respectively. For the run with Smagorinsky SGS model, the contour levels are shown to be broader with a lower peak value of 200 when compared to the run without SGS model that has a peak value of 300 in the selected downstream region.

6.5.2 Vorticity Thickness

Figures 6-26 shows the downstream evolution of the vorticity thickness for the two runs with and without SGS model. The vorticity thickness shows slightly higher values for the case with Smagorinsky SGS model in comparison to the case without SGS model and this is consistent with the added dissipation by the Smagorinsky SGS model employed that tends to expand the mixing layer.

6.5.3 Flow Field Results

Comparison between profiles of various flow statistics for the two runs with and without SGS model is illustrated in Figures 6-27(a)-(d) at the downstream location $x/H_x = 0.6$ located in the self-similar region. Figure 6-26(a) shows the normalized mean velocity for the two runs under study. It indicates a slight deviation between the two profiles with the values for the Smagorinsky SGS run being lower in the upper stream region ($\eta_v > 0$) and higher in the lower stream region ($\eta_v < 0$) as compared to the values of the run without SGS model. This indicates that the profiles with SGS model spread more in the free streams. As expected, the normalized rms longitudinal velocity fluctuations shown in Figure 6-27(b) indicate lower values for the run with Smagorinsky SGS model than the run without SGS model. This is due to the dissipation effect of the SGS model. Furthermore, the normalized rms lateral velocity fluctuations and cross-stream correlations in Figures 6-27(c) and (d), respectively, show lower values for the run with Smagorinsky SGS model compared to the run without SGS model.

6.5.4 Scalar Field Results

Figures 6-28(a)-(d) reveal the effect of the SGS model on the scalar field by comparing profiles of the normalized mean temperature, the rms temperature fluctuations and the longitudinal and lateral heat fluxes for the two runs with and without SGS model at the downstream location $x/H_x = 0.6$. The run with Smagorinsky SGS model yields lower mean temperature values than the run without SGS in the regions $\eta_v < 0$ and $\eta_v > 0.05$. This is due to the dissipation effect of the Smagorinsky SGS model which tends to enhance heat transfer or in other terms to broaden the mixing layer as indicated by the vorticity thickness in Figure 6-26. As expected, the rms temperature fluctuations and the heat fluxes values are decreased under the effect of the induced dissipation when using the Smagorinsky SGS model.

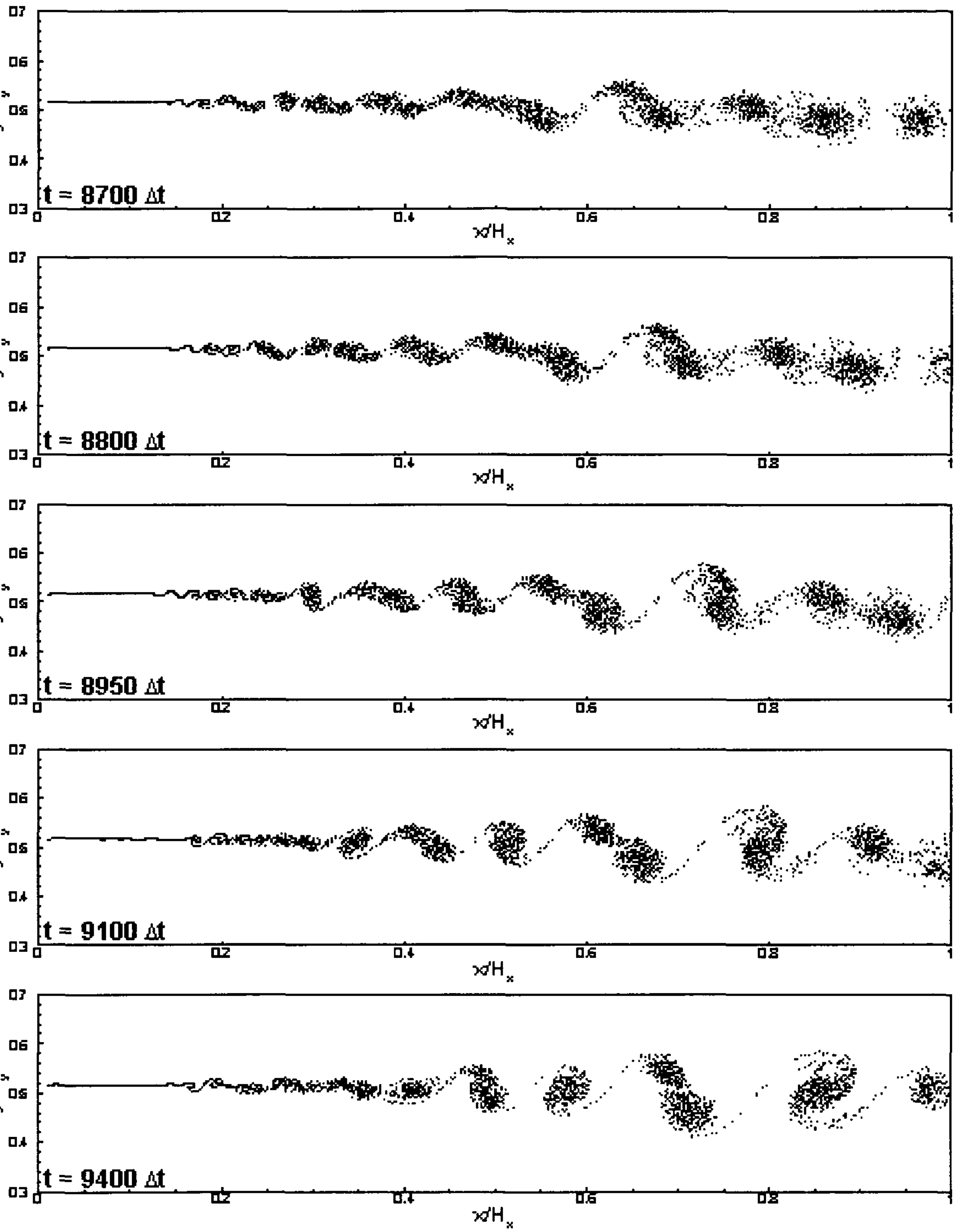

Figure 6-1: Location of the vortex particles for the isothermal mixing layer at five consecutive times.

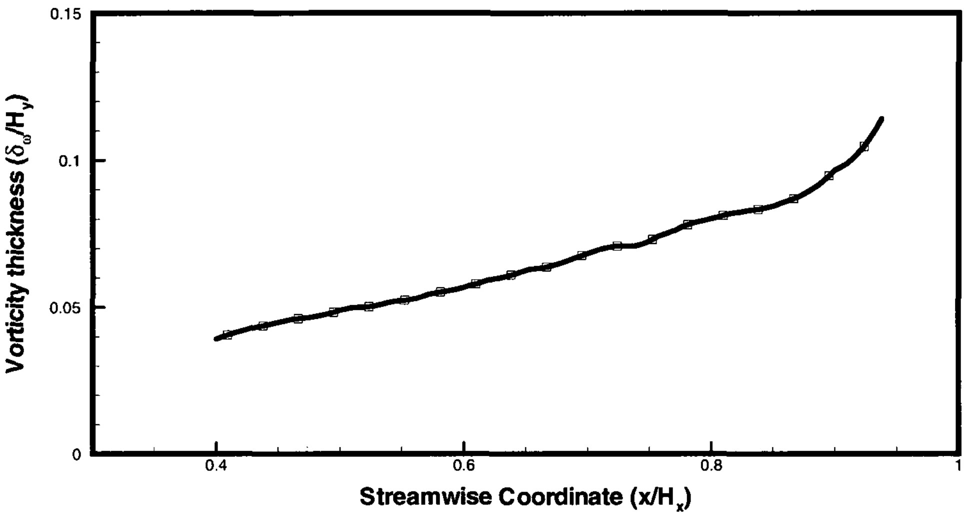

Figure 6-2: Downstream evolution of the isothermal mixing layer vorticity thickness.

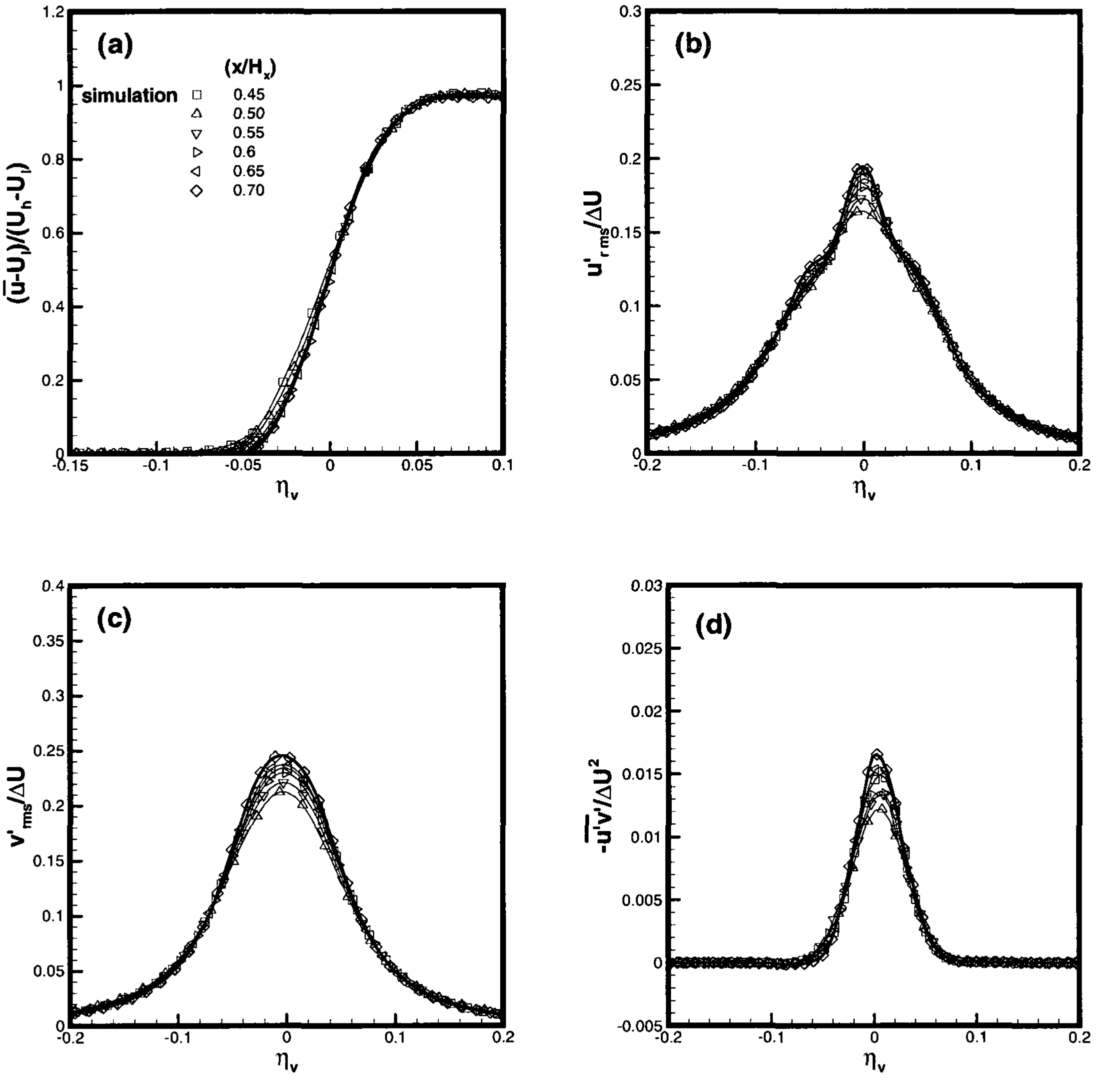

Figure 6-3: Normalized profiles at four downstream locations for the isothermal mixing layer run: (a) mean longitudinal velocity,(b)rms longitudinal velocity fluctuations, (c) rms lateral velocity fluctuations and (d) negative cross-stream correlation.

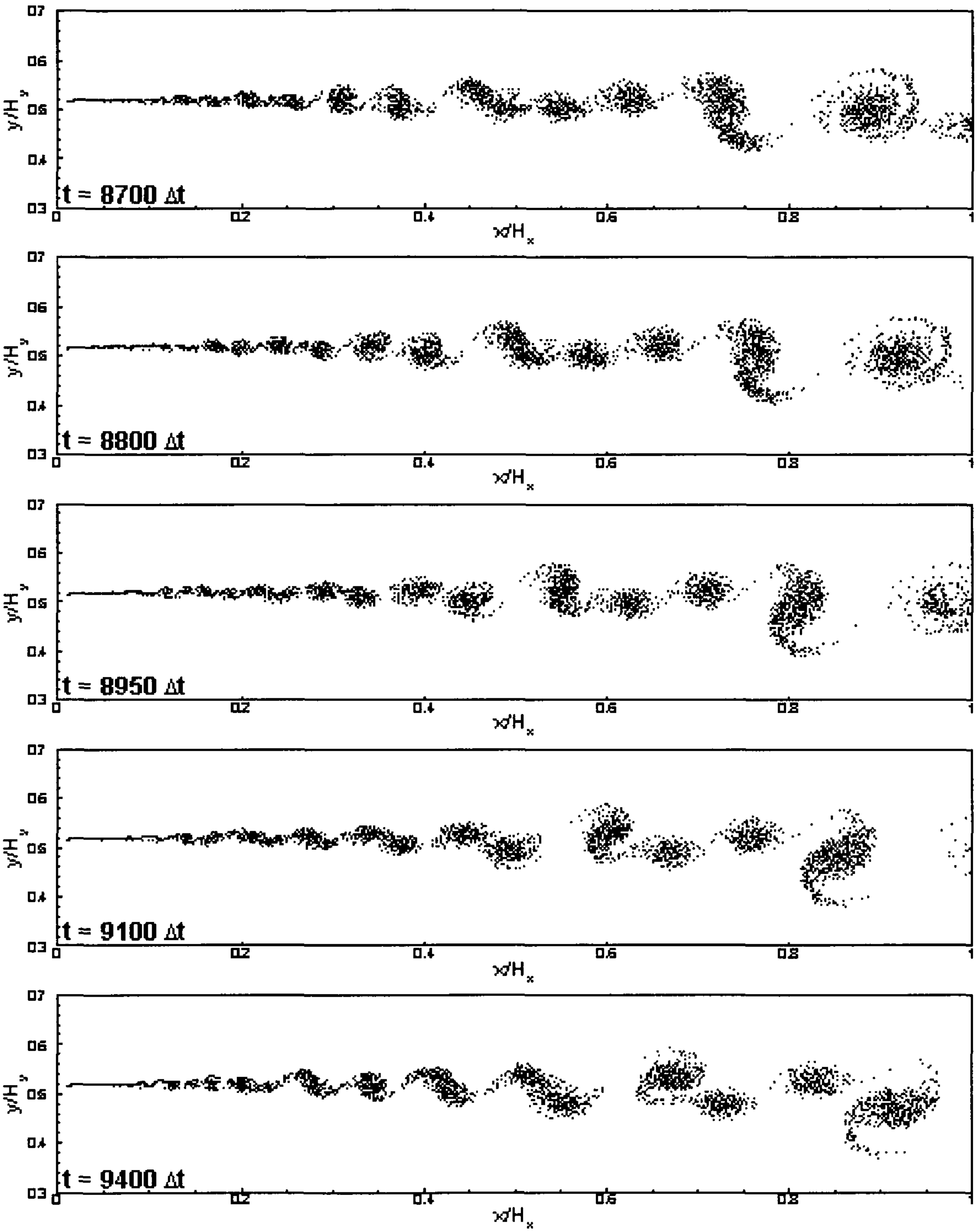

Figure 6-4: Location of the vortex particles for the thermal mixing layer at five consecutive times.

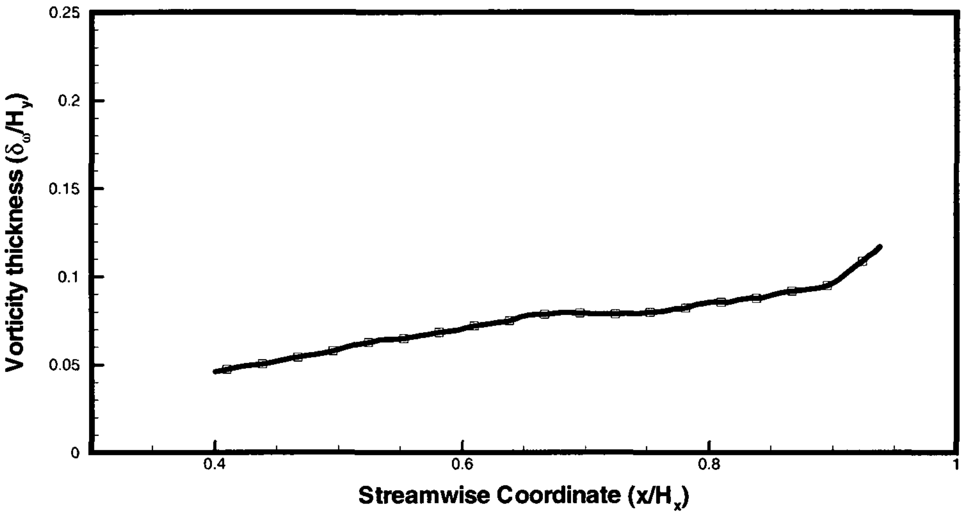

Figure 6-5: Downstream evolution of the thermal mixing layer vorticity thickness.

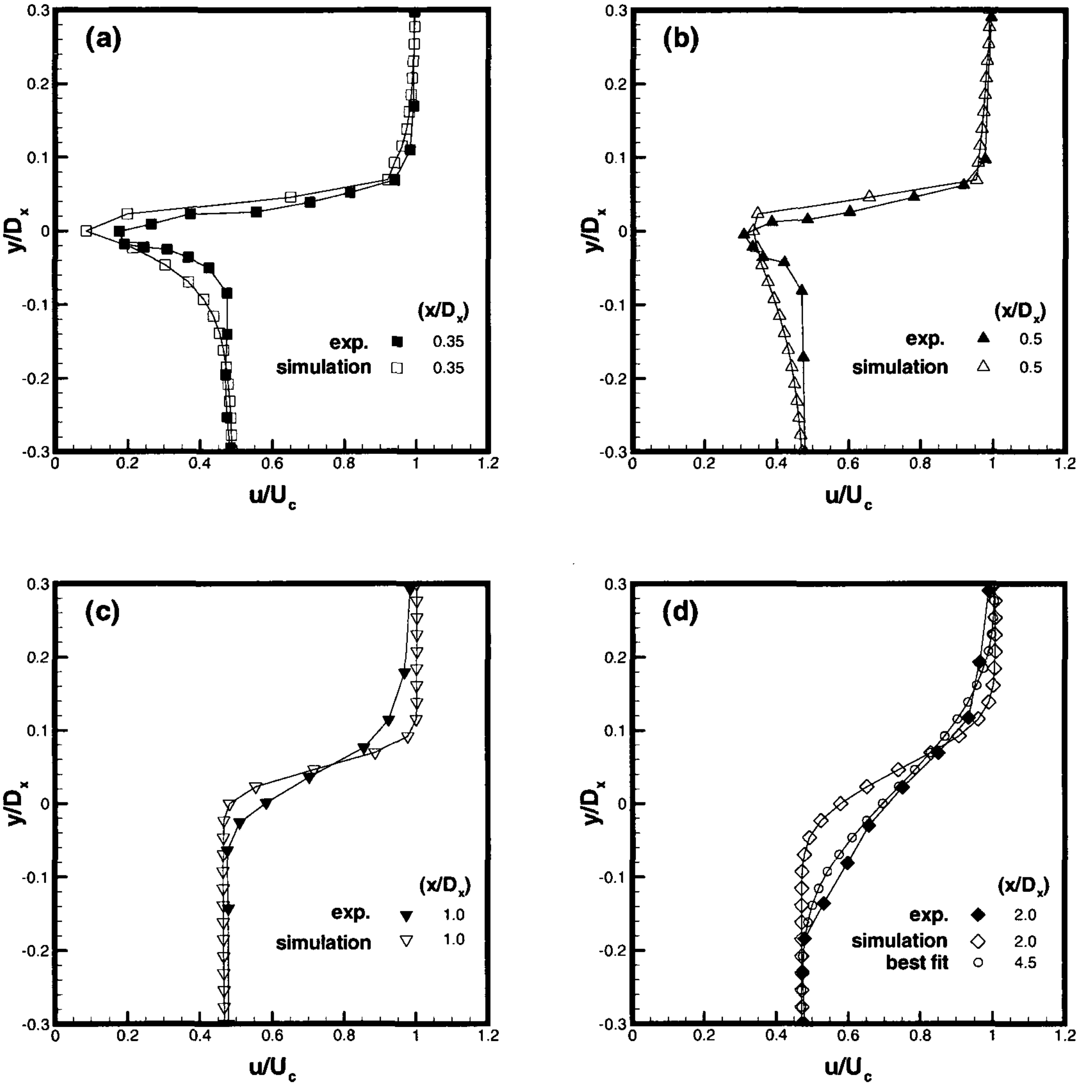

Figure 6-6: Lateral Distribution of normalized mean longitudinal velocity profiles compared to experimental results (Mizuno et al., dark symbols) at: (a) $x/D_x = 0.35$, (b) $x/D_x = 0.5$, (c) $x/D_x = 1.0$ (d) $x/D_x = 2.0$.

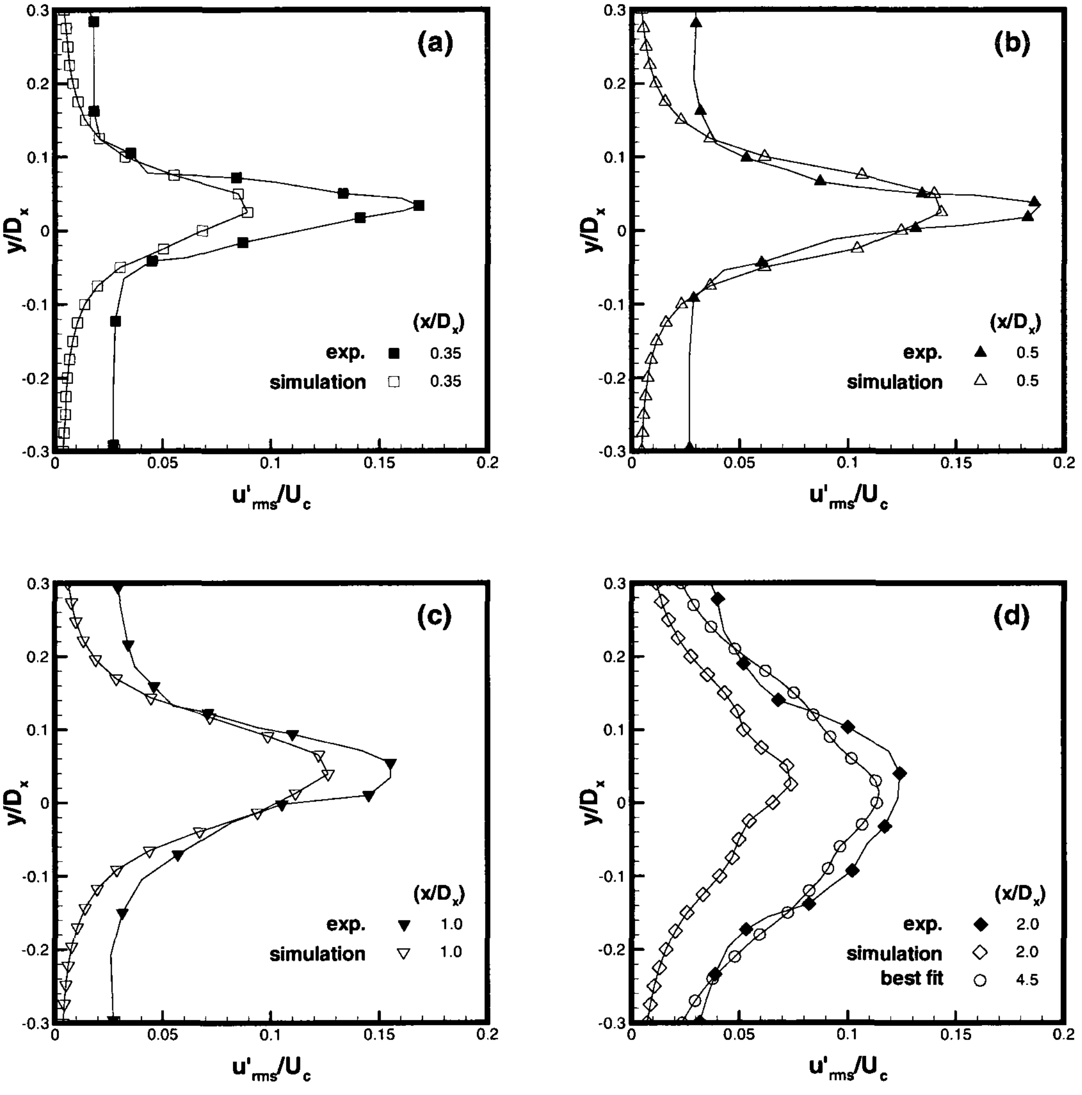

Figure 6-7: Lateral Distribution of normalized rms longitudinal velocity fluctuations profiles compared to experimental results (Mizuno et al., dark symbols) at: (a) $x/D_x = 0.35$, (b) $x/D_x = 0.5$, (c) $x/D_x = 1.0$ (d) $x/D_x = 2.0$.

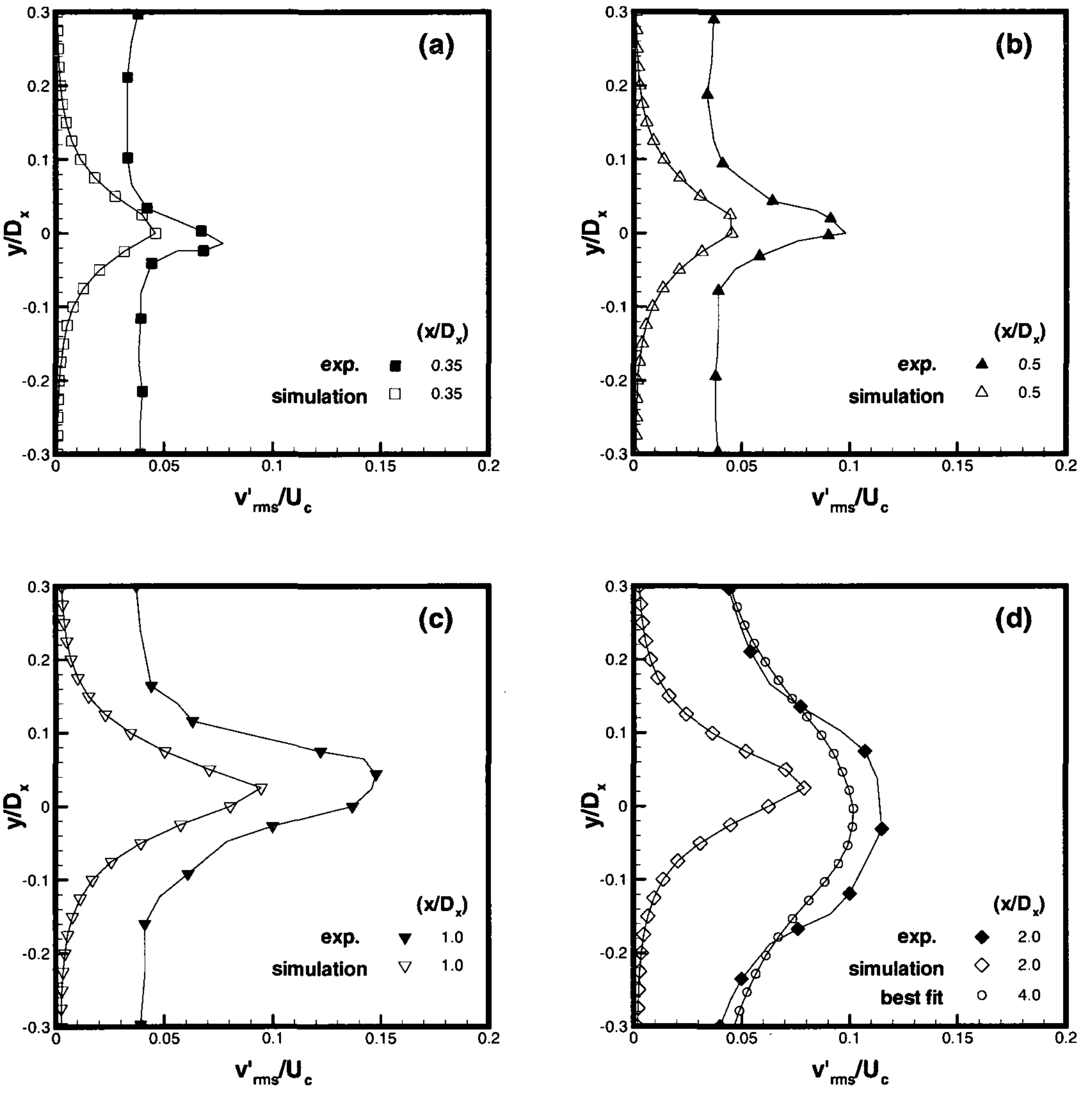

Figure 6-8: Lateral Distribution of normalized rms lateral velocity fluctuations profiles compared to experimental results (Mizuno et al., dark symbols) at: (a) $x/D_x = 0.35$, (b) $x/D_x = 0.5$, (c) $x/D_x = 1.0$ (d) $x/D_x = 2.0$.

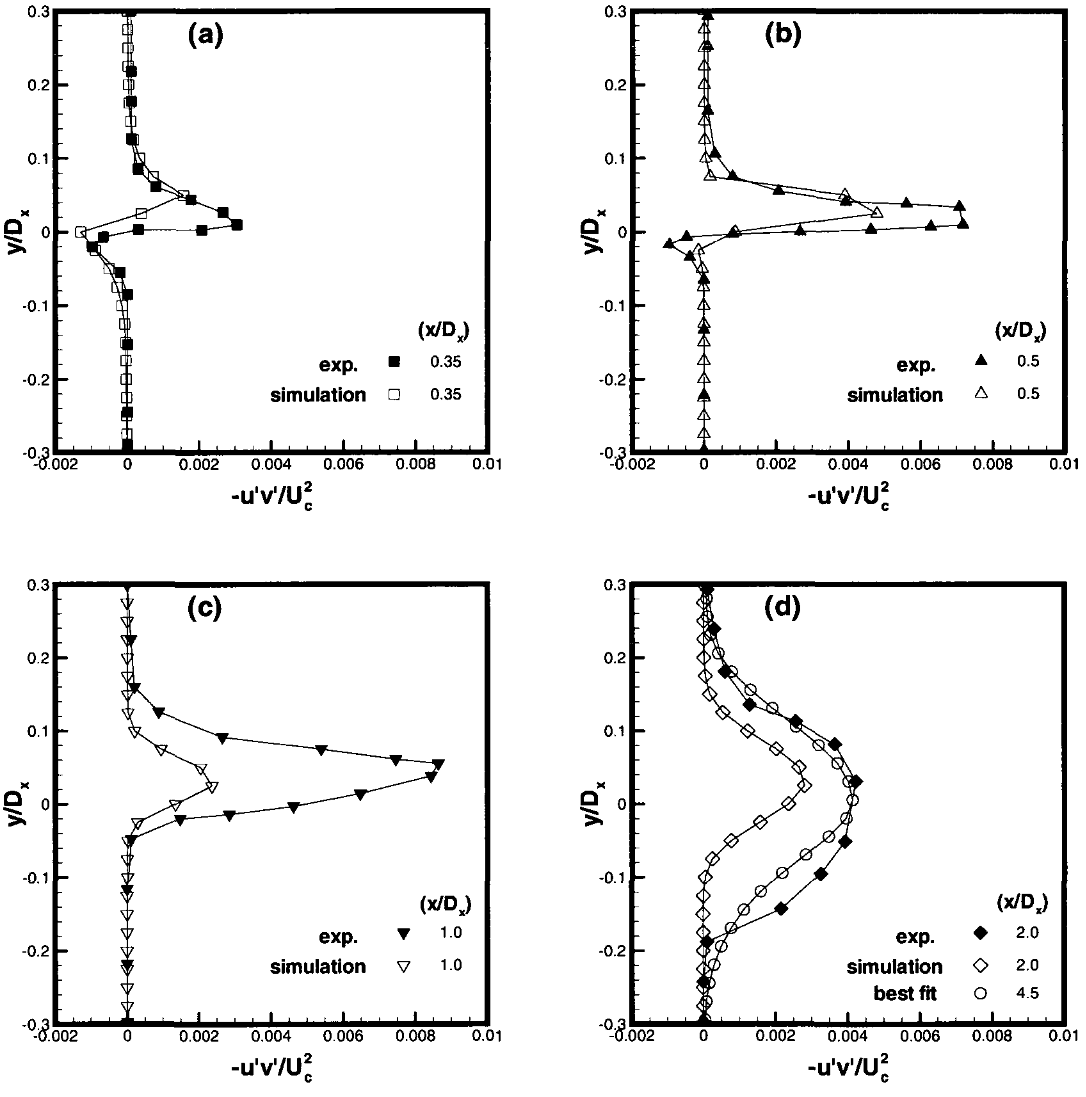

Figure 6-9: Lateral Distribution of normalized negative cross-stream correlation profiles compared to experimental results (Mizuno et al., dark symbols) at: (a) $x/D_x = 0.35$, (b) $x/D_x = 0.5$, (c) $x/D_x = 1.0$ (d) $x/D_x = 2.0$.

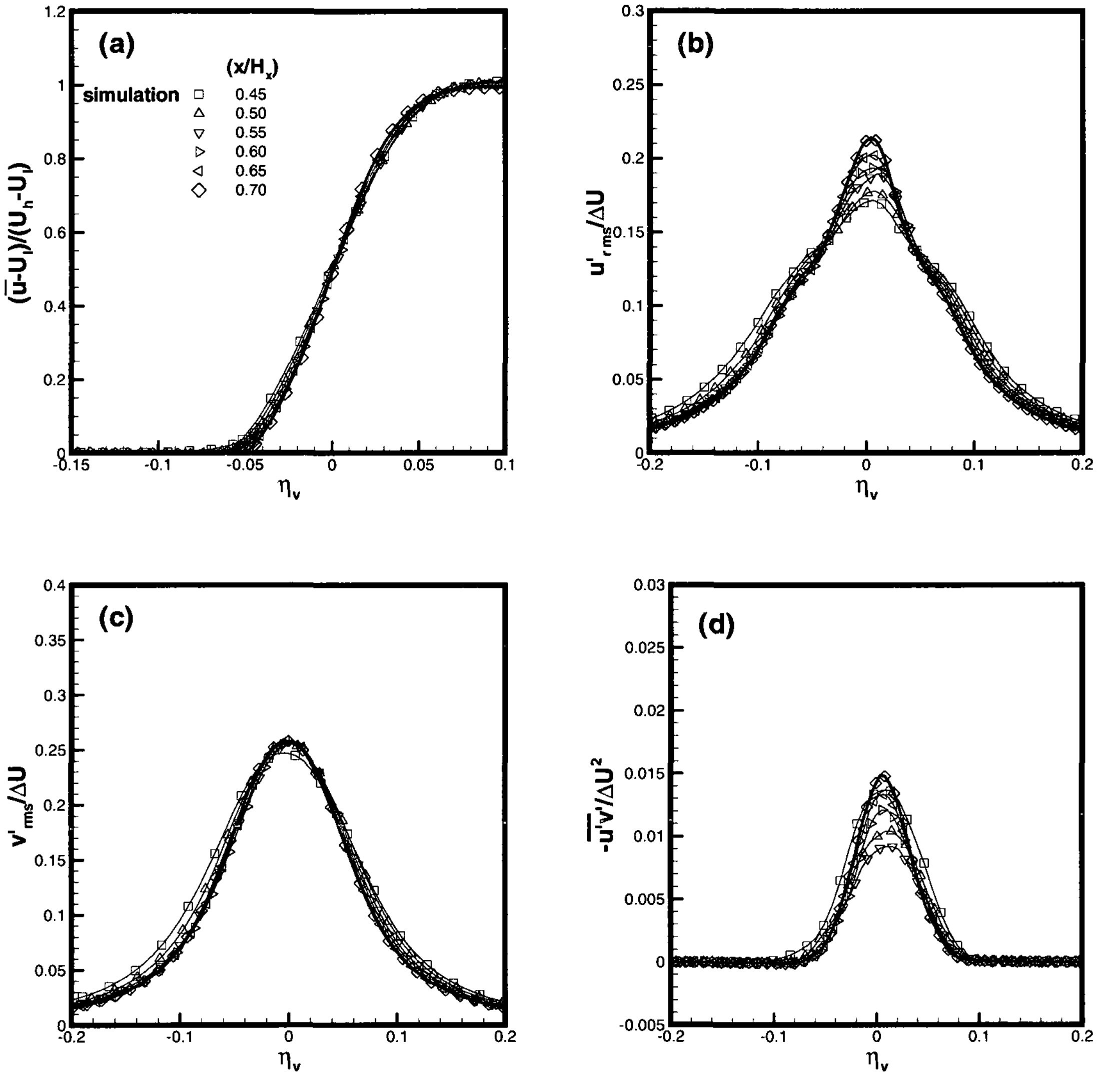

Figure 6-10: Normalized profiles at multiple downstream locations for the thermal mixing layer: (a) mean longitudinal velocity, (b) rms longitudinal velocity fluctuations, (c) rms lateral velocity fluctuations and (d) negative cross-stream correlation.

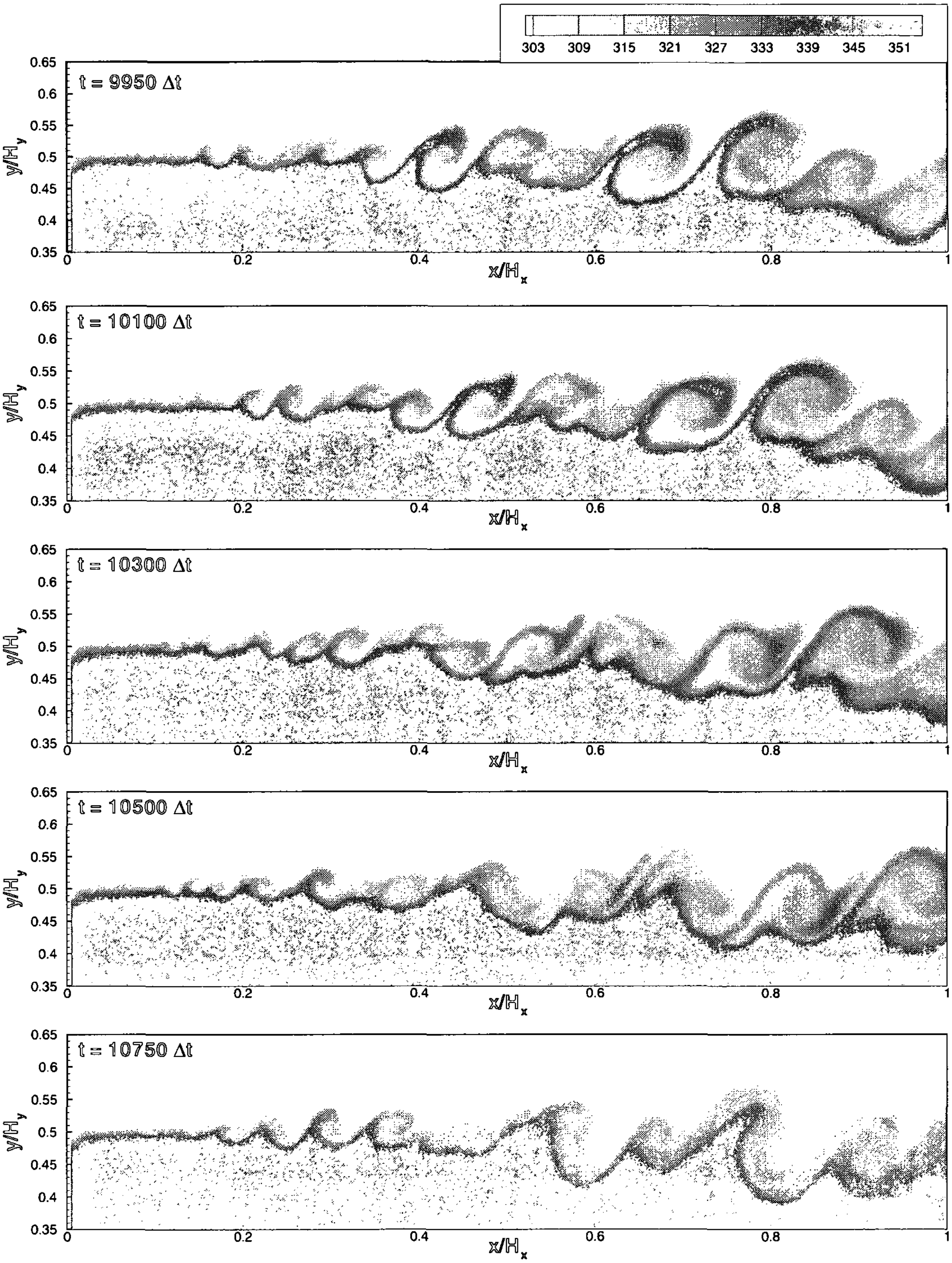

Figure 6-11: Evolution of the instantaneous temperature structure at five consecutive times.

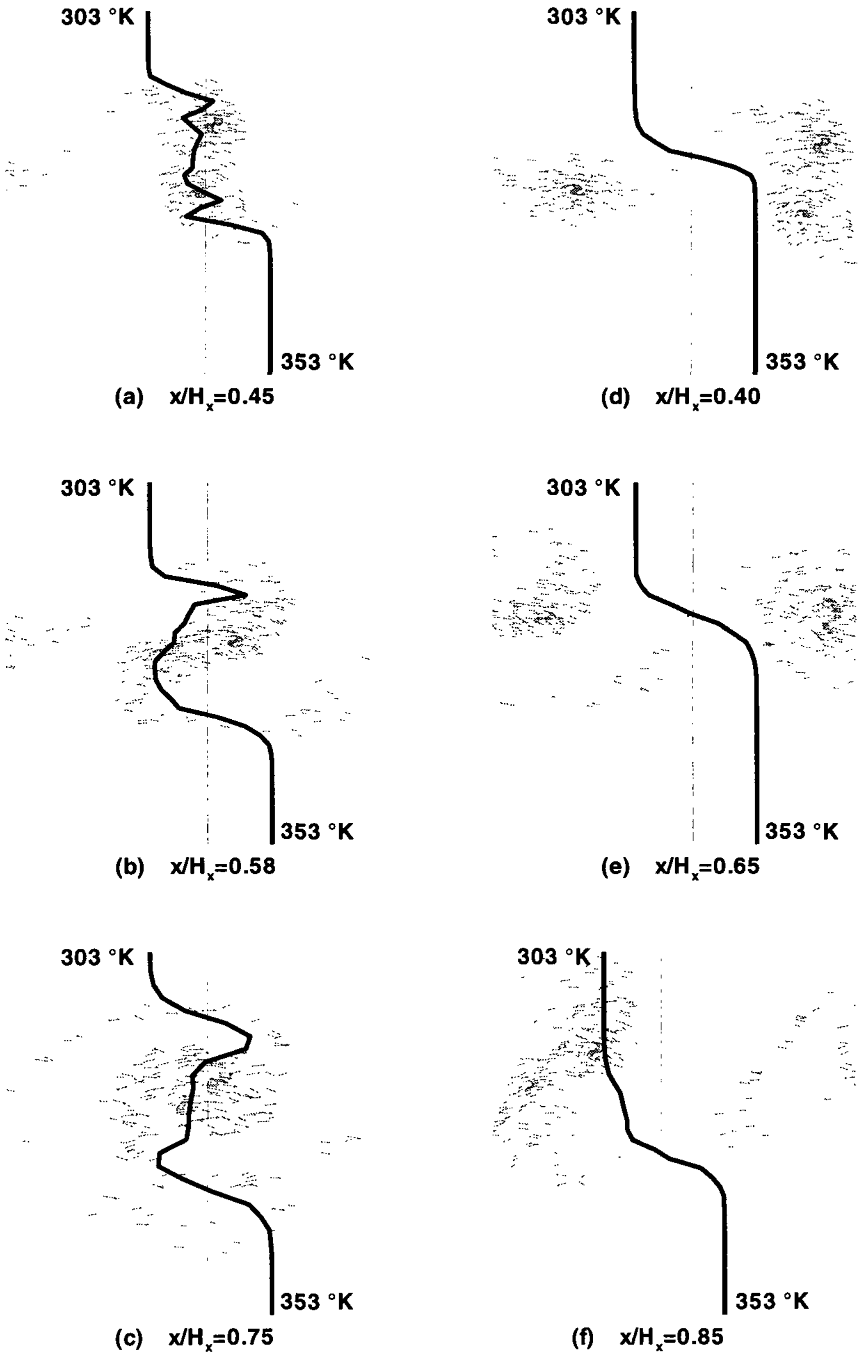

Figure 6-12: Instantaneous temperature profiles superimposed on the vortex elements shown with their instantaneous velocities at different downstream locations: (a), (b) and (c) across the midsection of the vortex structures; (d), (e) and (f) across the braids.

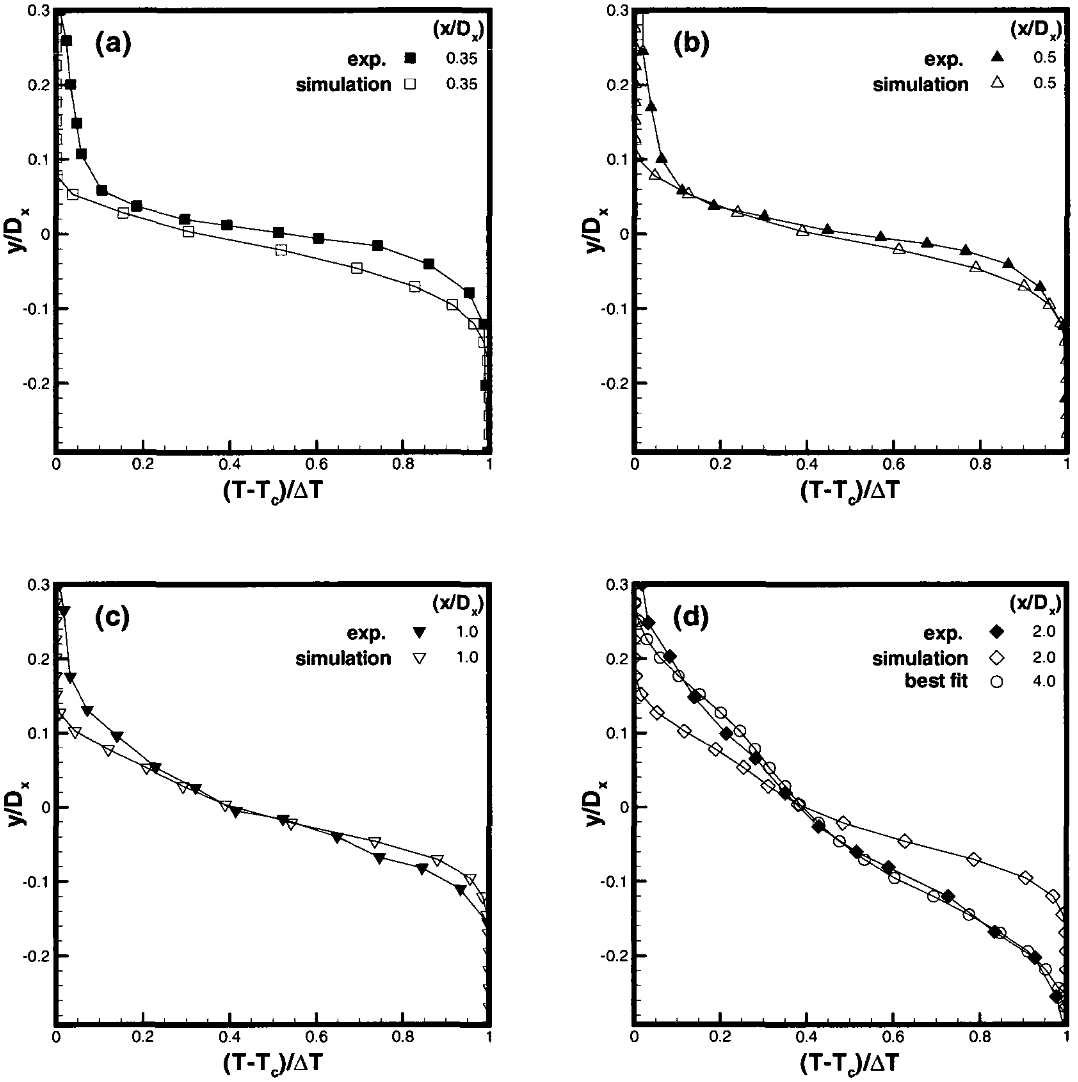

Figure 6-13: Lateral Distribution of normalized mean temperature profiles compared to experimental results (Mizuno et al., dark symbols) at: (a) $x/D_x = 0.35$, (b) $x/D_x = 0.5$, (c) $x/D_x = 1.0$ (d) $x/D_x = 2.0$.

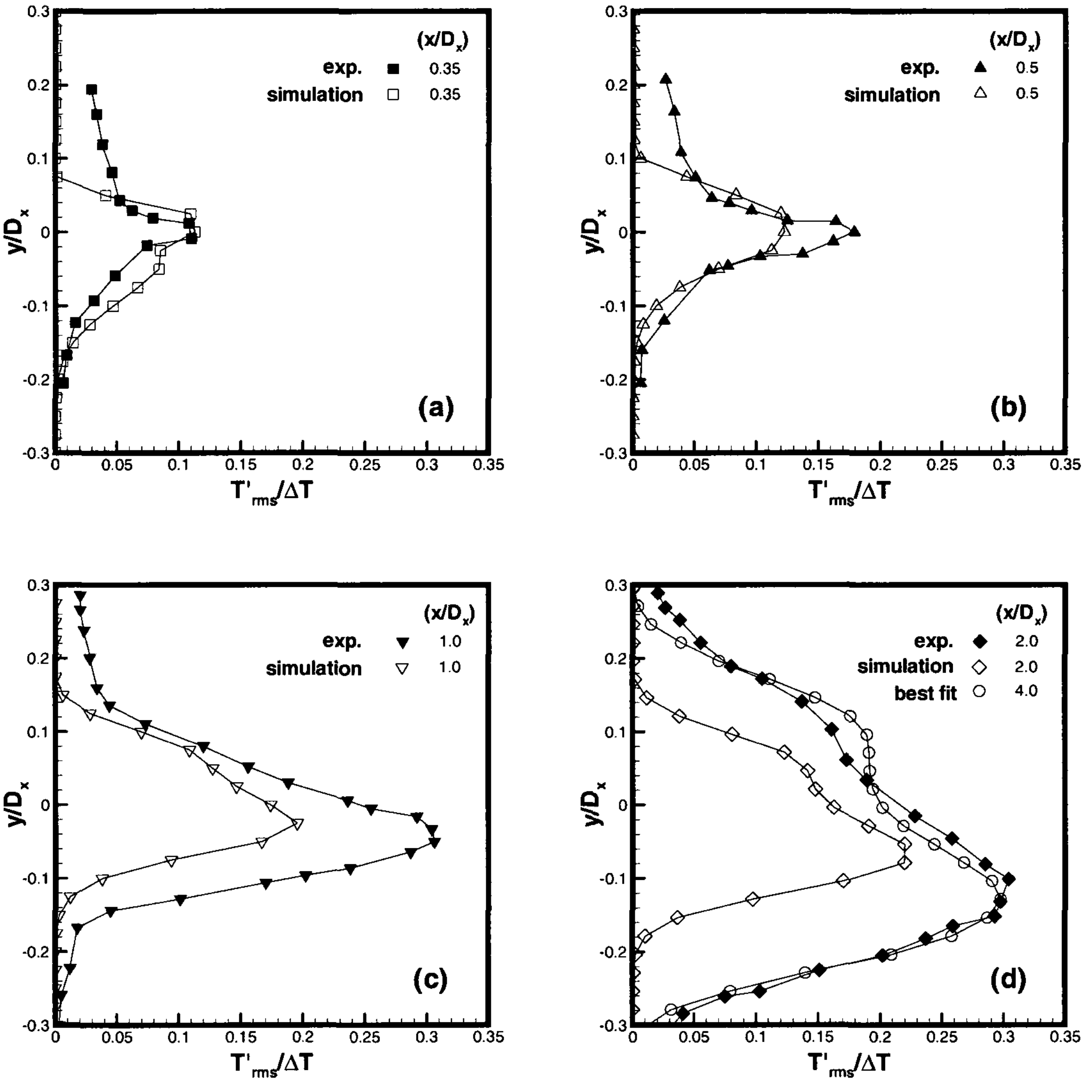

Figure 6-14: Lateral Distribution of normalized rms temperature profiles compared to experimental results (Mizuno et al., dark symbols) at: (a) $x/D_x = 0.35$, (b) $x/D_x = 0.5$, (c) $x/D_x = 1.0$ (d) $x/D_x = 2.0$.

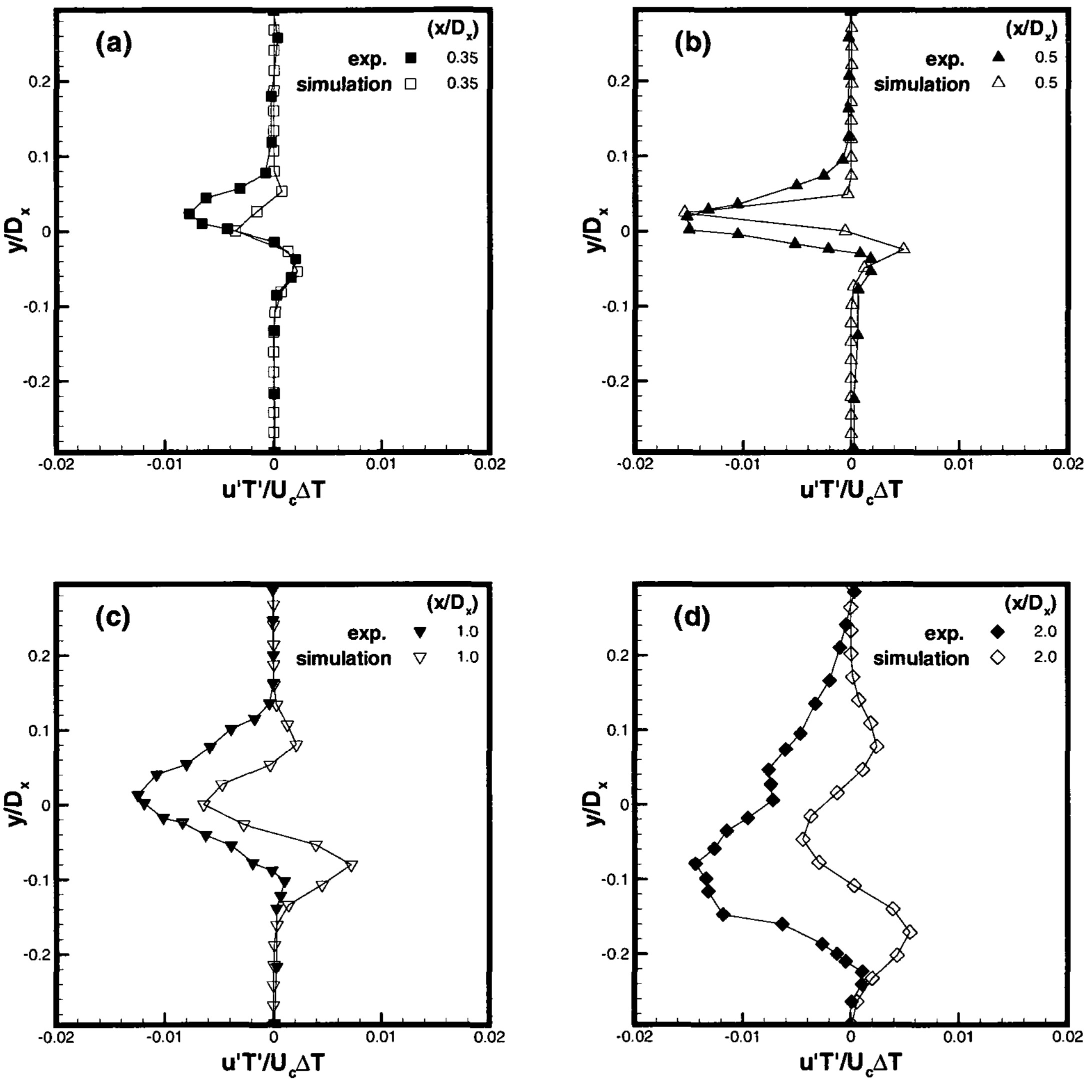

Figure 6-15: Lateral Distribution of normalized longitudinal turbulent heat flux profiles compared to experimental results (Mizuno et al., dark symbols) at: (a) $x/D_x = 0.35$, (b) $x/D_x = 0.5$, (c) $x/D_x = 1.0$ (d) $x/D_x = 2.0$.

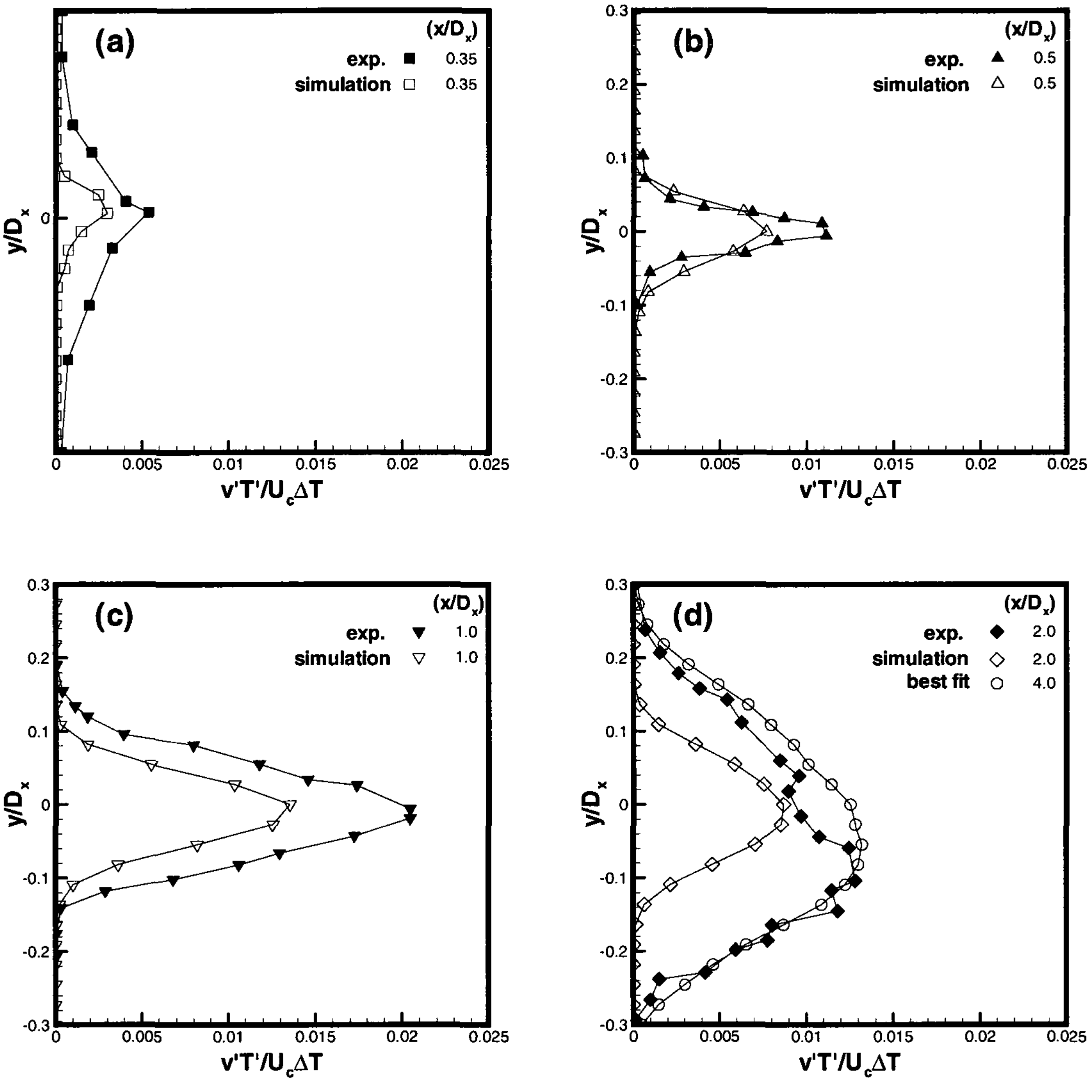

Figure 6-16: Lateral Distribution of normalized lateral turbulent heat flux profiles compared to experimental results (Mizuno et al., dark symbols) at: (a) $x/D_x = 0.35$, (b) $x/D_x = 0.5$, (c) $x/D_x = 1.0$ (d) $x/D_x = 2.0$.

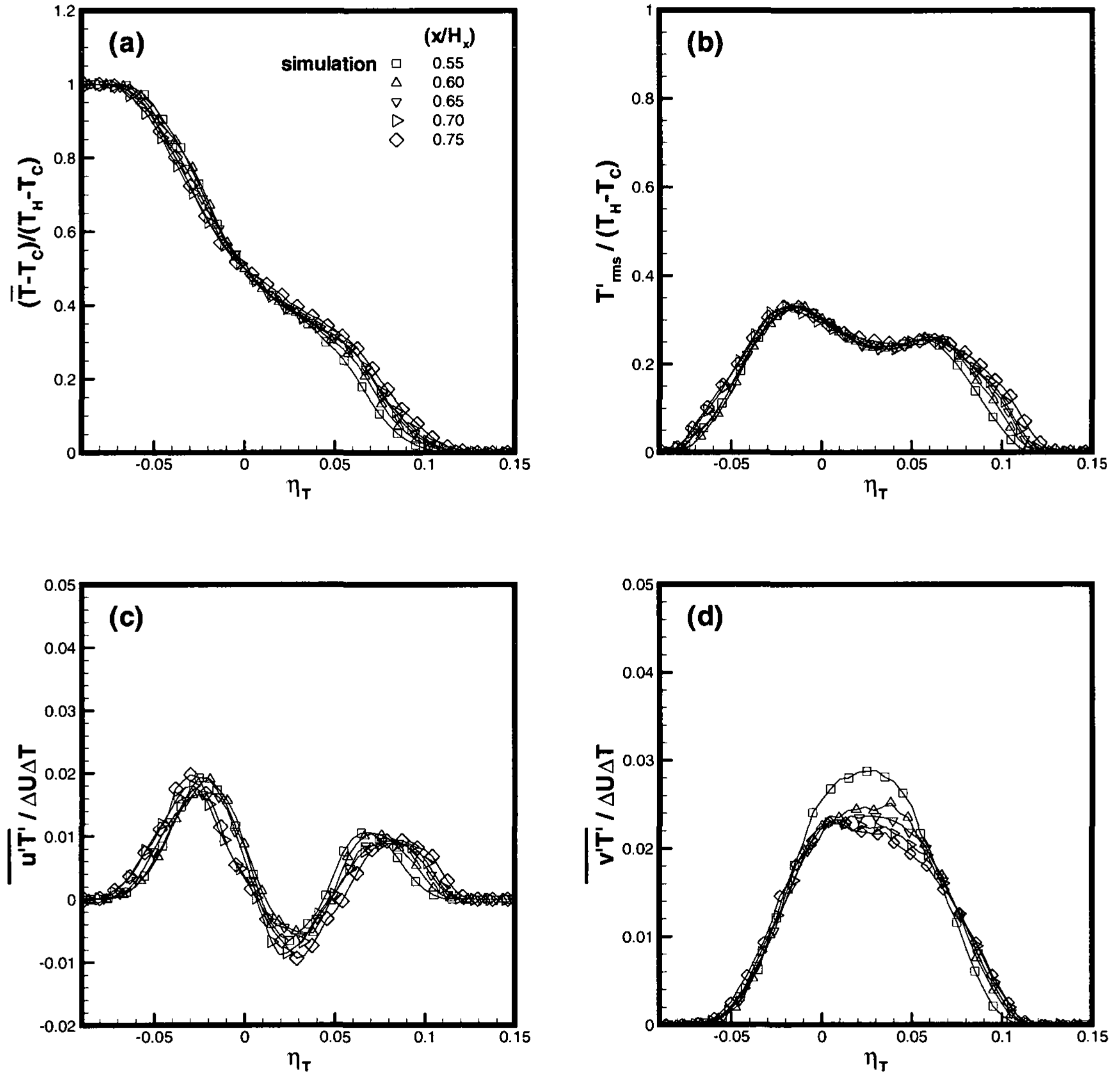

Figure 6-17: The base run scalar field normalized results at different downstream locations: (a) mean temperature, (b) rms temperature, (c) longitudinal turbulent heat flux and (d) lateral turbulent heat flux.

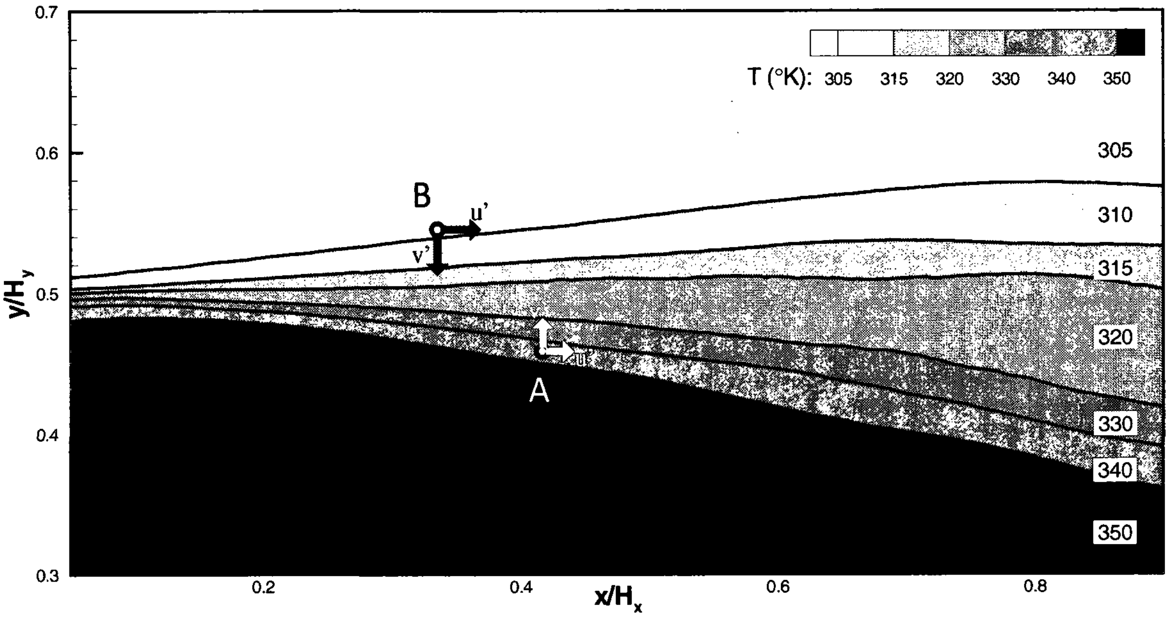

Figure 6-18: Mean temperature contours for the thermal mixing layer $\Delta T = 50°K$

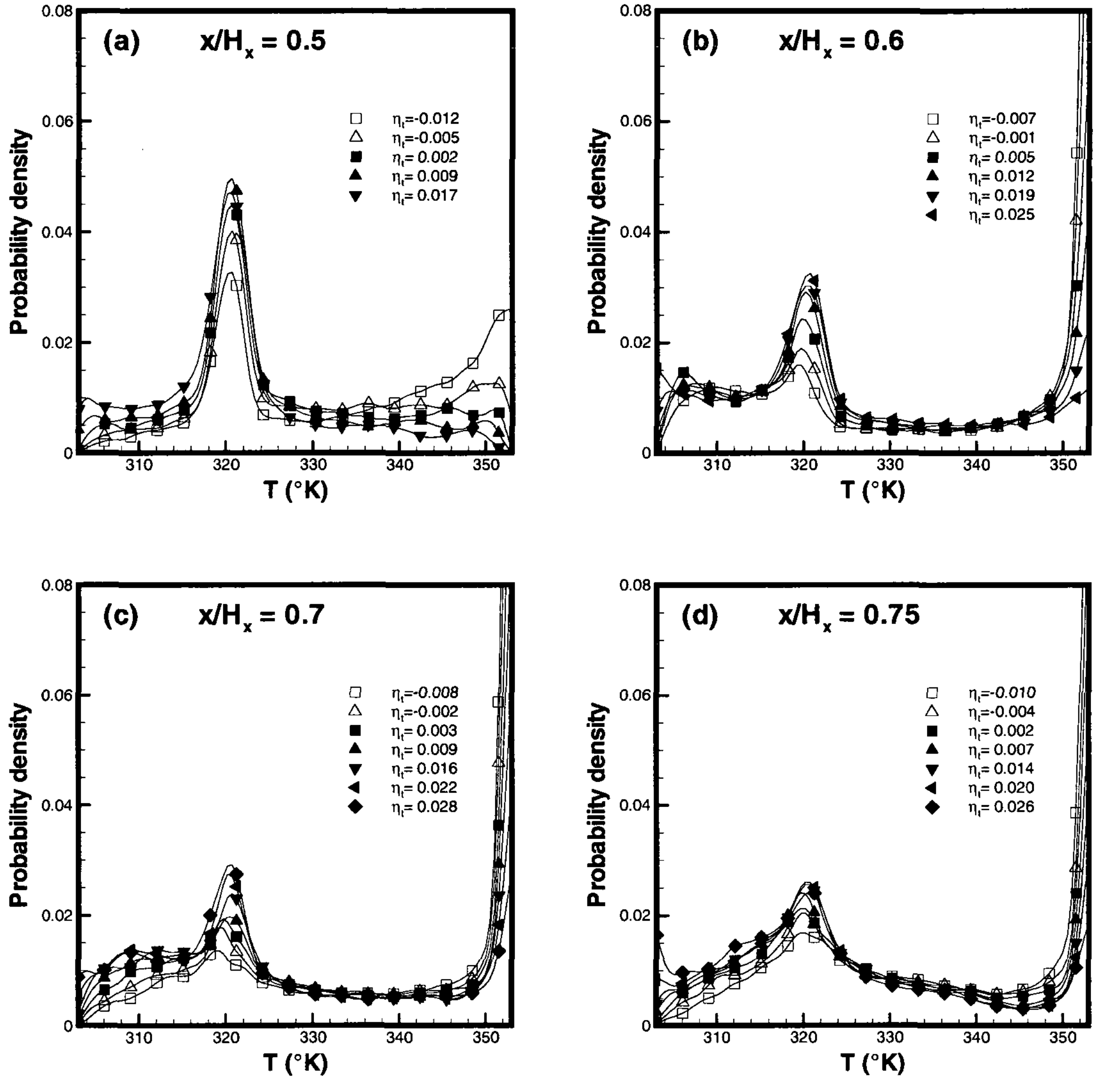

Figure 6-19: Probability density function at several cross-stream locations for the base run: (a) $x/H_x = 0.5$, (b) $x/H_x = 0.6$, (c) $x/H_x = 0.7$ and (d) $x/H_x = 0.75$

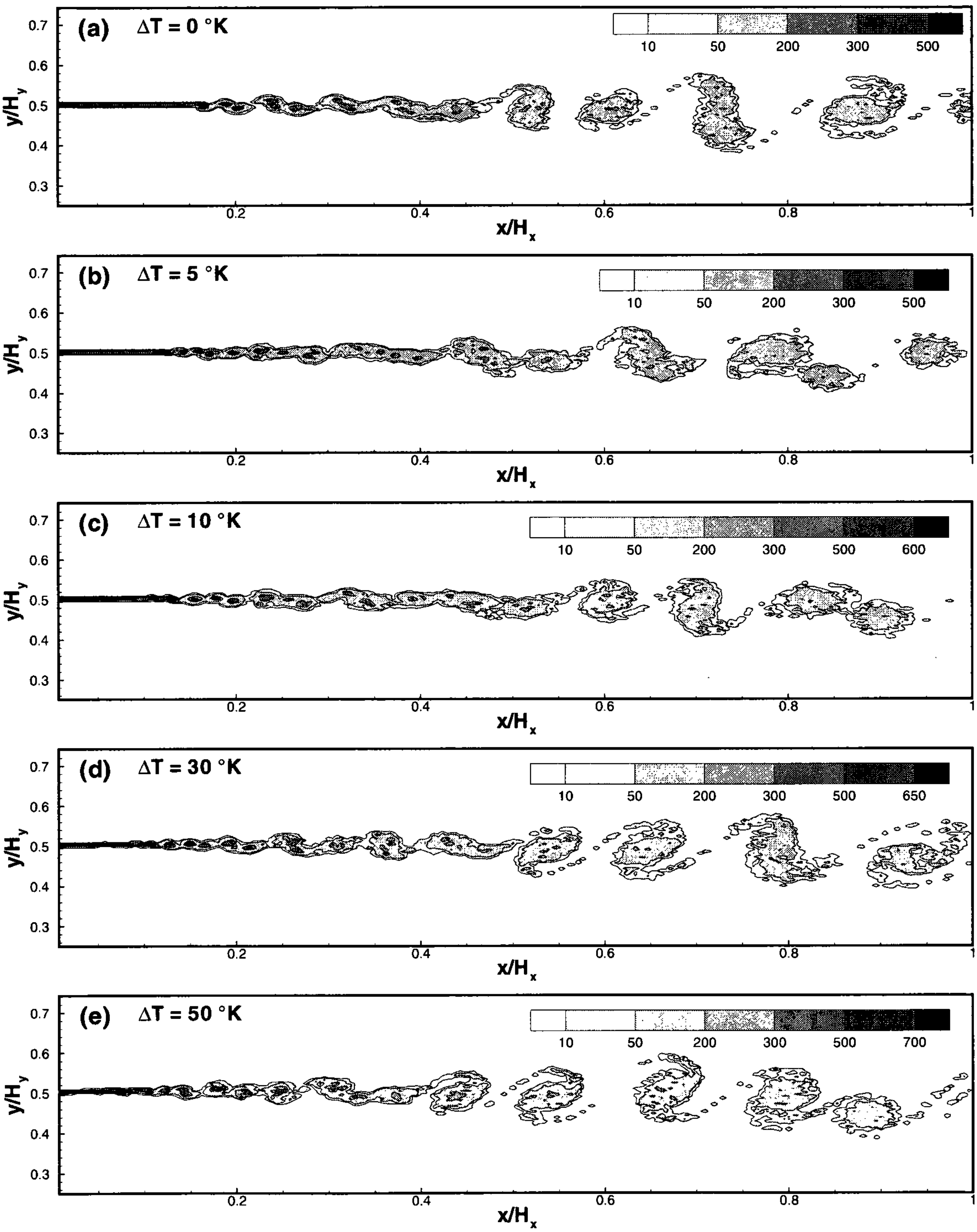

Figure 6-20: Downstream evolution of the vorticity contours for five different runs with diverse temperature differences.

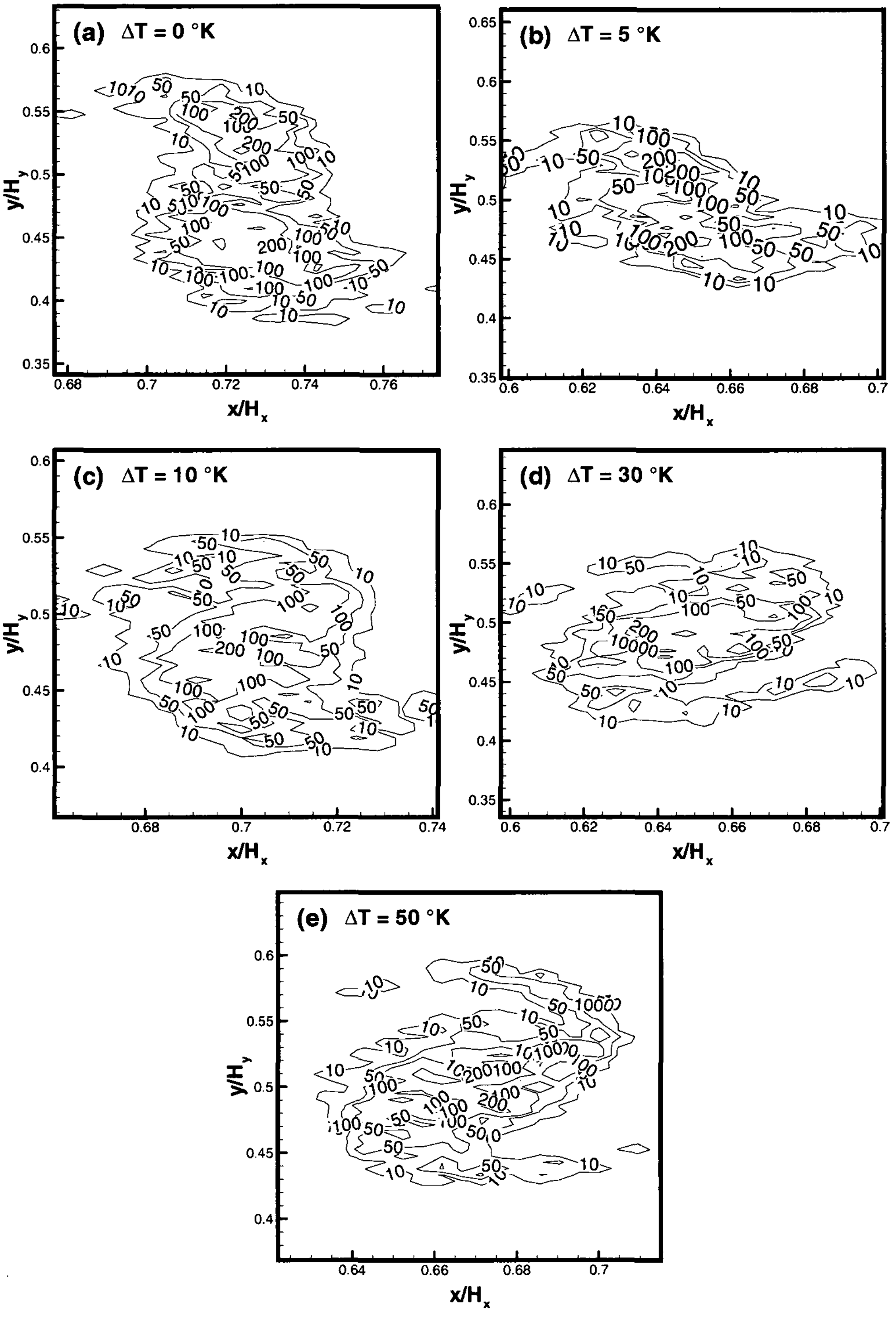

Figure 6-21: Close-ups of vorticity contours at selected downstream location for runs with diverse temperature differences.

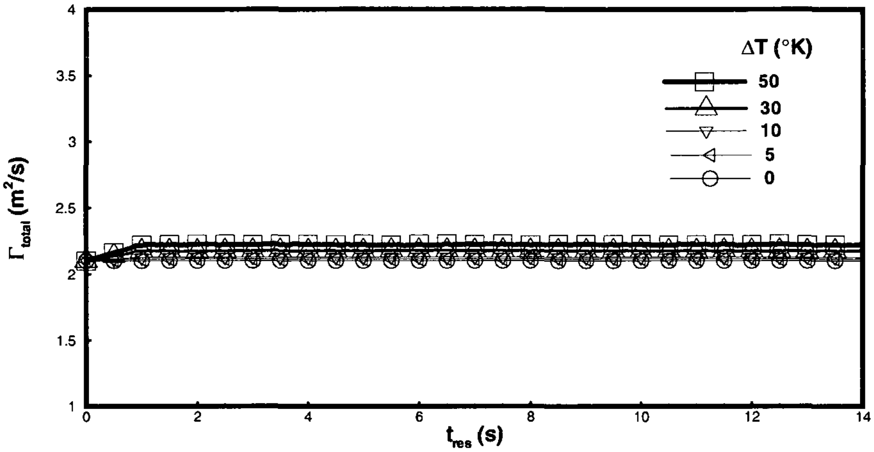

Figure 6-22: Comparison of the total domain circulation for runs with diverse temperature differences.

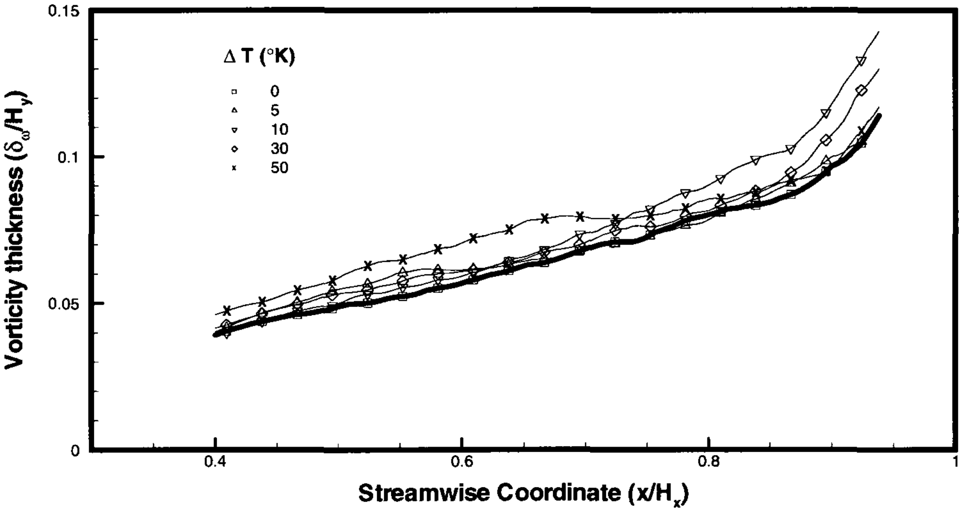

Figure 6-23: Comparison of the downstream evolution of the vorticity thickness for runs with diverse temperature differences.

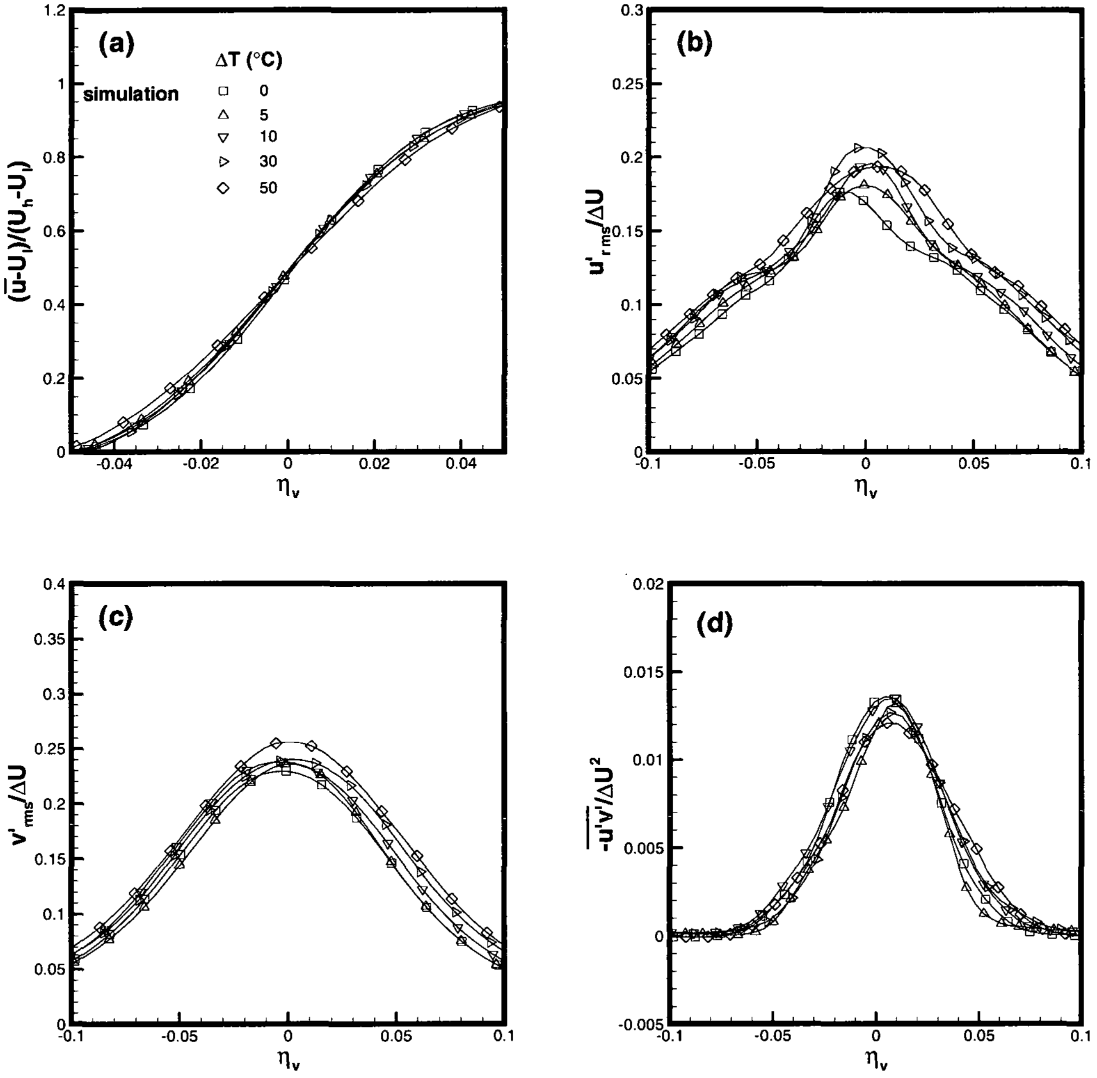

Figure 6-24: Comparison of the flow field results for runs with diverse temperature differences: (a) normalized mean longitudinal velocity, (b) normalized rms longitudinal velocity fluctuations, (c) normalized rms lateral velocity fluctuations and (d) normalized negative cross-stream correlation at $x/H_x = 0.6$

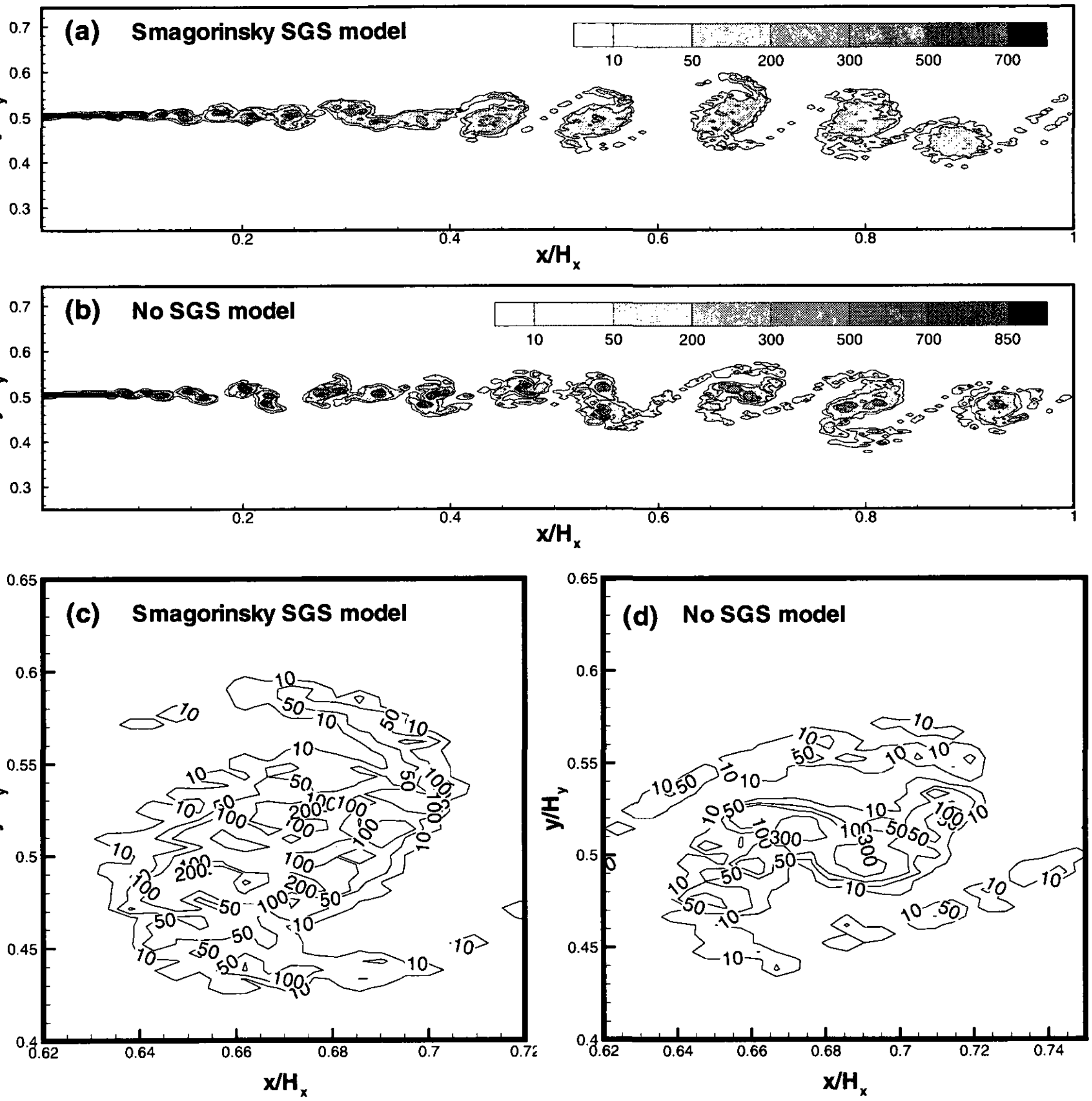

Figure 6-25: Comparison of the downstream evolution of vorticity contours for run (a) with Smagorinsky SGS model and (b) without SGS model; Close-ups of vorticity contours at selected downstream location for run (c) with Smagorinsky SGS model and (d) without SGS model.

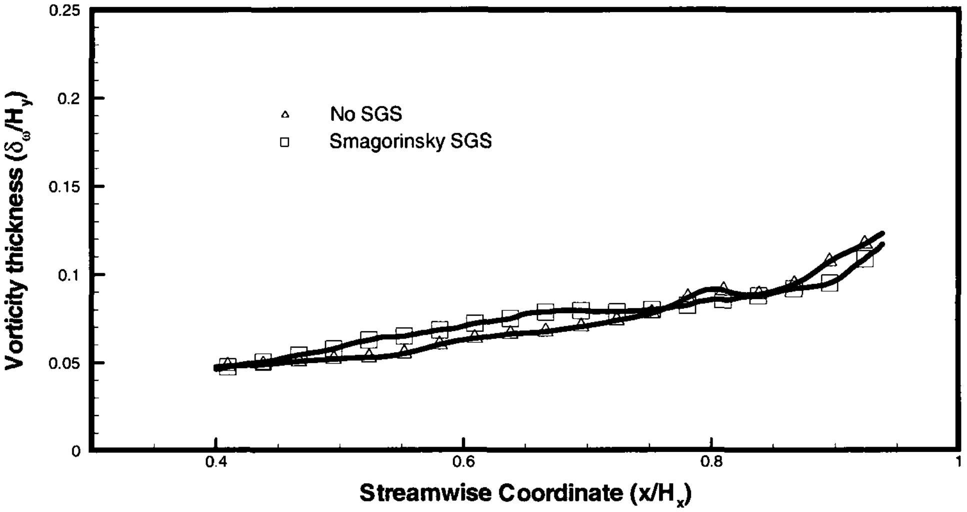

Figure 6-26: Comparison of the downstream evolution of the vorticity thickness for runs with and without SGS modeling.

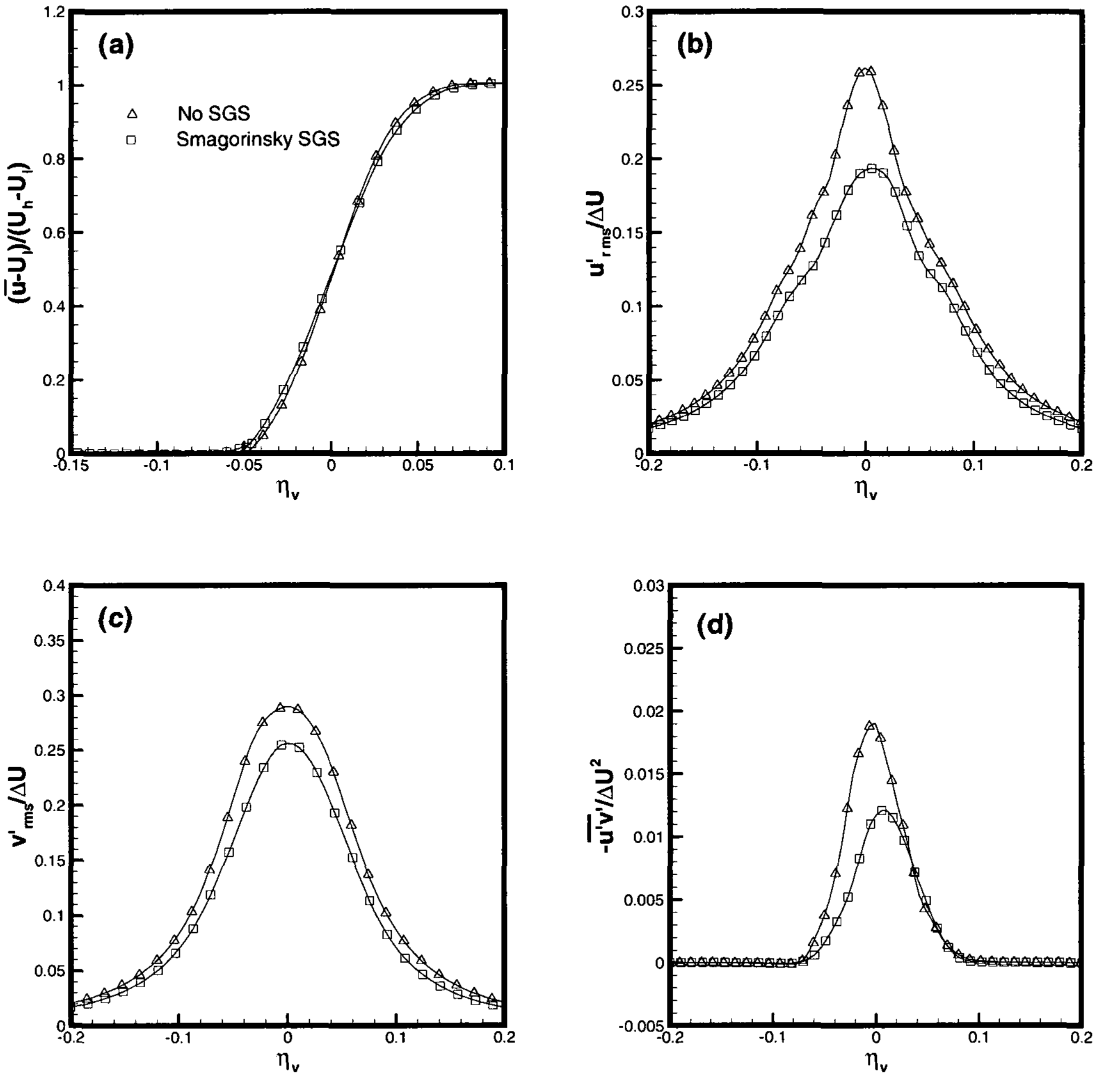

Figure 6-27: Comparison of flow field normalized results with and without SGS modeling: (a) mean longitudinal velocity, (b) rms longitudinal velocity fluctuations, (c) rms lateral velocity fluctuations and (d) negative cross-stream correlation at $x/H_x = 0.6$.

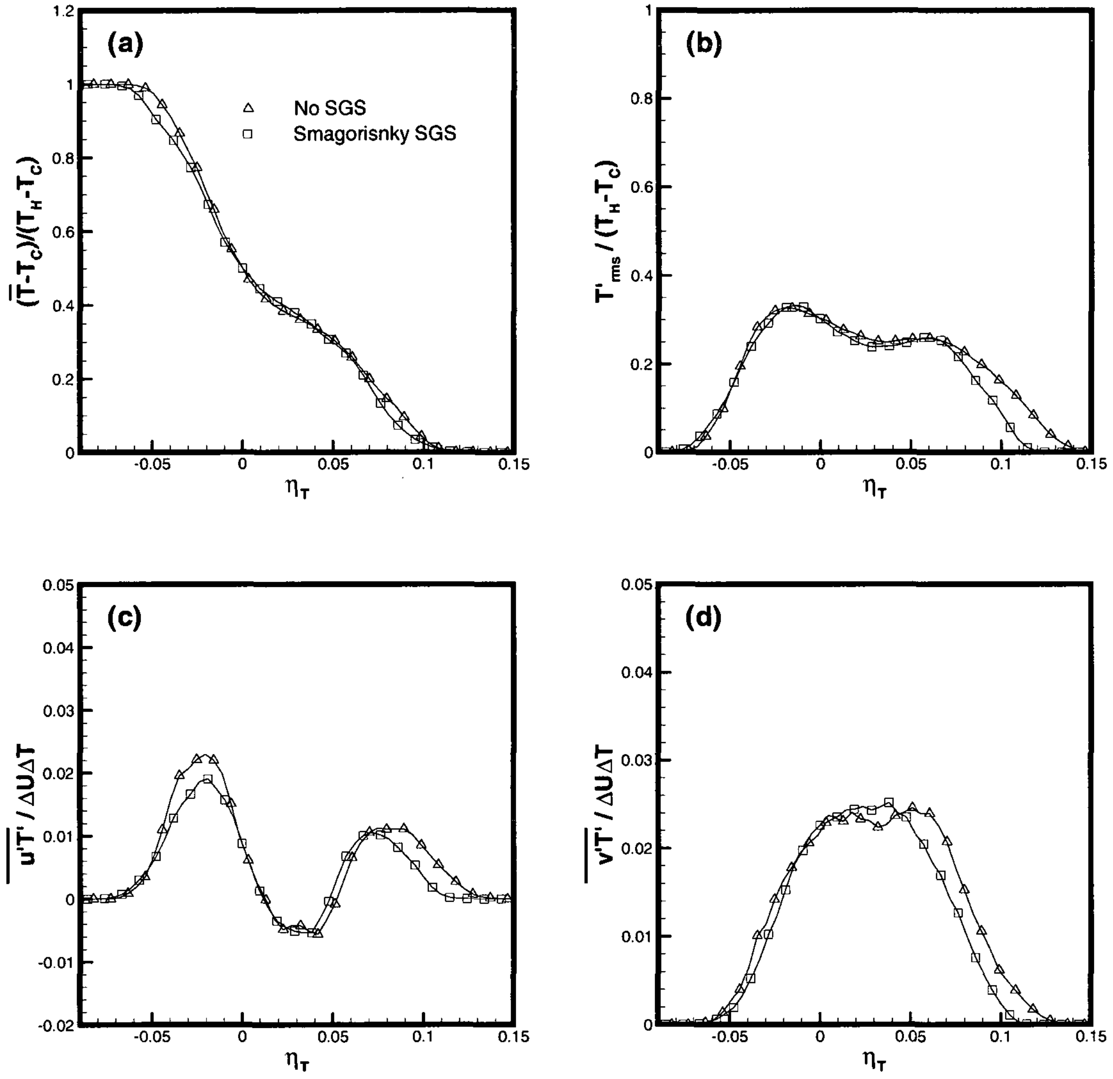

Figure 6-28: Comparison of scalar field normalized results with and without SGS modeling: (a) mean temperature, (b) rms temperature, (c) longitudinal turbulent heat flux and (d) lateral turbulent heat flux at $x/H_x = 0.6$

Chapter 7

SUMMARY AND CONCLUSIONS

This study has focused on the application of large eddy simulation to the prediction of both the chemically reacting with no heat release mixing layer and the thermal mixing layer. The filtered vorticity transport equation has been coupled with the filtered mass weighted density function (FMDF) transport equation to predict the flow and scalar fields. The filtered vorticity transport has been formulated using diffusion-velocity method and then solved using the vortex-in-cell scheme in conjunction with both Smagorinsky and dynamic eddy viscosity subgrid scale models. The filtered mass weighted density function transport equation is solved using the Lagrangian Monte-Carlo method. The flow field results, i.e. mean velocity, rms longitudinal and lateral velocities fluctuations and the cross-stream correlation and the scalar field results, i.e. the mean concentration, rms concentration fluctuations, mean temperature, rms temperature fluctuations and longitudinal and lateral heat fluxes are compared to previous experimental and numerical data. While comparison between experimental data and LES (filtered) results is not ideal, other possible factors that might have contributed to the differences between the numerical predictions and the experimental data include: the difference between the flow development of the numerical and experimental results, the relative amplitude of noise in the numerical and experimental results, the finite probe size of the measurement device and the finite sample used in averaging the experimental and numerical results. The main results of this work are summarized below.

7.1 Chemically Reacting Mixing Layer with No Heat Release

The incompressible filtered vorticity transport equation and the filtered density function (FDF) in conjunction with the dynamic eddy viscosity SGS model, presented in Chapter 4, are used to calculate the flow and scalar fields of the isothermal chemically reacting mixing layer. The mean velocity, rms velocities fluctuations, cross stream correlation, mean concentration and rms concentrations results relaxed to self similar profiles. Also, they are in agreement with the experimental results of Masutani and Bowmann (1986) and the calculated results of Zhou and Perreira (2001) in the self similar region, i.e.$0.4 \leq x/H_x \leq 0.6$, which corresponds to the region of linear growth of the vorticity thickness.

The SGS effect on the flow and scalar fields' results is investigated by comparing the three runs: without SGS model, with the dynamic SGS model and with the Smagorinsky SGS model. The Smagorinsky SGS model is shown to be more dissipative than the dynamic SGS model.

The mixing has a greater effect on scalar field within the vortex structure as compared to the braid regions. For the non reacting mixing layer, the mean concentration profiles had triple inflection point, the rms concentration fluctuations profiles had bimodal shapes and the FDFs profiles showed a peak for $0.25 < \xi < 0.3$, indicating the presence of a preferred concentration established in the core of the vortex structures. For the reacting case, the effect of Damköhler number (Da) on the scalar field results is investigated by comparing the results of four chemically reacting mixing layers with different Da to the results of the non-reacting mixing layer. For high Da, the reaction zones are mainly limited to the thin reacting interfacial zones, whereas for low Da, the reacting zones are spread as reacting pockets within the vortical structures. The triple inflection point in the mean concentration profiles has vanished along with the preferred peak in the FDFs profiles when Da is increased. Also, the rms concentration fluctuations bimodal shape is replaced by unimodal shape skewed towards the lower stream indicating the depletion of the lean reactant in the mixing layer when Da is increased.

7.2 Thermal mixing layer

The low Mach number compressible Favre filtered vorticity transport equation and the filtered mass weighted density function in conjunction with the Smagorinsky SGS model, presented in Chapter 3, are used to calculate the flow and scalar fields of the thermal mixing layer. Taking into account the turbulence noticed in the free streams of the experimental mixing layer, the mean velocity, longitudinal and lateral velocities fluctuations, cross stream correlation, mean temperature, rms temperature and longitudinal and lateral heat fluxes results showed adequate agreement with the experimental data of Mizuno et al. (2005) in the region $0.35 \leq x/D_x \leq 2.0$, where the flow has not yet reached self-similarity. The numerical results reached self-similarity when $5.8 \leq x/D_x \leq 7.8$, which is beyond the region where the data are reported by Mizuno et al. (2005). The mean temperature profiles had triple inflection point, the rms temperature profiles exhibited bimodal shapes and the FMDFs profiles have a peak around the normalized temperature value $(T - T_C)/\Delta T = 0.33$ indicating the presence of a preferred temperature in the cores of the vortex structures. This preferred temperature does not vary with downstream position implying that the fluid entrainment from the hot and cold free streams remains in the same proportion as the flow develops.

The effect of vorticity-temperature interaction, i.e. the volumetric expansion and baroclinic generation of vorticity, on the flow field is also investigated by mixing a cold and a hot stream with temperature differences of 0, 5, 10, 30 and 50°K. The mixing layer is destabilized earlier as ΔT is increased. Also, pairing of vortical structures is inhibited when $\Delta T = 50°K$ is compared to the isothermal run $(\Delta T = 0°K)$.

The effect of the SGS model is investigated by comparing the two runs: without SGS model and with Smagorinsky SGS model. The vorticity thickness is increased with lower vorticity values when the SGS model is used. Also, the rms flow and temperature fluctuations showed lower values for the run with Smagorinsky SGS model than the run without SGS model.

7.3 Recommendations

The numerical results obtained are encouraging. Therefore further studies may include combining the code for chemical reaction with no heat release with the code of thermal flow to predict the exothermic reactive flow. Also, extension to 3D flow can be done by accounting for the third dimension and including the stretching term in the vorticity equation. Future runs using parallel computations are recommended particularly in order to improve memory capabilities.

REFERENCES

Abdolhosseini, R., and R.E. Milane. "On the Effect of Vortex Grid Density in the Vortex-in-Cell Smulation of Mixing Layer." *International Journal of Fluid Dynamics* 13 (2000): 161-183.

Baig, A. m., and R. E. Milane. "Vortex-In-Cell and Probability Density Approach for a passive scalar field in a mixing layer." *J. Computational Fluid Dynamics* 18, no. 3 (2004): 247-263.

Baker, G. R., and J. T. Beale. "Vortex blobs methods applied to interfacial motion." *J. Comput. Phys.* 196 (2004): 233-258.

Bardina, J., J. H. Ferziger, and W. C. Reynolds. "Improved subgrid models for Large Eddy Simulation." *AIAA*, 1980: 80-1357.

Bilger, R. "Turbulent Reacting Flows." Chap. 3. Springer, 1980.

Bilger, R. W. "Conditional moment closure for turbulent reacting flow." *Phys. Fluid* 5 (1993): 436-444.

Birdsal, C. K., and D. Fuss. "Clouds-in-clouds, clouds-in-cells physics for many-body plasma simulations." *Journal of Computational Physics* 3 (1969): 494-511.

Brown, G. L. "The entrainment and large structure in turbulent mixing layers." *In Proc. 5th Australasian Conf. on Hydraulics and Fluid Mechanics*, 1974: 352-359.

Brown, G. L., and A. Roshko. "On Density Effects and Large Structure in Turbulent Mixing Layers." *J. Fluid Mech.* 57 (1974): 785-796.

Chang, C. H. H., W. J. A. Dahm, and G. Tryggvason. "Lagrangian model simulations of molecular mixing, including finite rate chemical reactions, in a temporally developing shear layer." *Phys. Fluids A* 3, no. 5 (1991): 1300-1311.

Chang, Y. C., T. Y. Hou, B. Merriman, and S. Osher. "A level set formulation of Eulerian interface capturing methods for incompressible fluid flows." *J. Comput. Phys.* 124 (1996): 449-464.

Christiansen, J. P. "Numerical simulation of hydrodynamics by the method of point vortices." *Journal of Computationsl Physics* 13 (1973): 363-379.

Colucci, P.J., F.A. Jaberi, P. Givi, and S.B. Pope. "Filtered Density Function for Large Eddy Simulation of Turbulent Reacting Flows." *Physics of Fluids* 10(2) (1998): 499-515.

Cottet, G.H. "Artificila Viscosity Models for Vortex and Particle Methods." *Journal of Computational Physics* 127 (1996): 299-308.

Cottet, G.H., and P.D. Koumoutsakos. *Vortex Methods: Theory and Practice.* Cambridge: Cambridge University Press, 2000.

Dahm, W. J. A. "Effects of heat release on turbulent shear flows. Part 2. Turbulent mixing layer and the equivalence principle." *J. Fluid Mech.* 540 (2005): 1-19.

De Sousa, F. S., et al. "A front-tracking/front-capturing method for the simulation of 3D multi-fluid flows with free surfaces." *J. Comput. Phys.* 198 (2004): 469-499.

Degond, P., and S. Mas-Gallic. "The Weighted Particle Method for convection-diffusion equations. Part 1: The case of isotropic viscosity." *Mathematics of Computation* 53, no. 188 (1989): 485-507.

Dimotakis, P. E. "Entrainment and growth of a fully-developed, two-dimensional shear layer." *AIAA J.* 24 (1986): 1791-1796.

Dimotakis, P. E. "Turbulent free shear layer mixing and combustion." *Prog. Astronaut. Aeronaut* 137 (1991): 265-340.

Dopazo, C. "Recent Developments in PDF Methods." Chap. 7 in *Turbulent Reactive Flows*, 375-474. Academic Press., 1994.

Esmaeeli, A., and G. Tryggvason. "A front tracking method for computations of boiling in complex geometries." *Intl. J. Multiphase Flow* 30 (2004): 1037-1050.

Ferchichi, M., and S. Tavoularis. "Evolution of a thermal mixing layer in uniformly sheared turbulent flow." *Phys. Fluids A* 4, no. 5 (1992): 997-1006.

Gao, F., and E.E. O'brien. "A Large-Eddy Simulation Scheme for Turbulent Reacting flows." *Physics of Fluids A* 5, no. 6 (1993): 1282-1284.

Gardiner, C.W. *Handbook of Stochastic Methods.* New York: Springer, 1990.

Ghoneim, A.F. "Lectures in applied mathematics." 24 (1986): 238.

Ghoneim, A.F., and G. Heidarinejad. "Effect of Two-Dimensional Shear Layer Dynamics on Mixing and Combustion at Low Heat Release." *Combustion Science and Technologies* 72 (1990): 79-99.

Ghoneim, Ahmed F., and Kenneth K. Ng. "Numerical study of the dynamics of a forced shear layer." *Physics of Fluids* 30, no. 3 (1986): 706-721.

Ghoniem, A. F., G. Heidarinejad, and A. Krishnan. "Numerical simulation of a thermally stratified shear layer using the vortex element method." *J. Comput. Phys.* 79 (1988): 135-166.

Green, Sheldon I. *Fluid Vortices. Fluid mechanics and its applications.* Vol. 30. Kluwer Academic Publishers, 1995.

Greengard, C. "The core spreading vortex method approximates the wrong equation." *Journal of Comput. Phys.* 61 (1985): 345-348.

Harlow, F. H. "The Particel-in-Cell method for two dimensional hydrodynamic problems." Los Alamos Scientific Laboratory, 1956.

Hermanson, J. C., and P. E. Dimotakis. "Effects of heat release in a turbulent, reacting shear layer." *J. Fluid Mech.* 199 (1989): 333-375.

Inoue, O. "Doubl-frequency forcing on spatially growing mixing layers." *J. Fluid Mech.* 234 (1992): 553-581.

Inoue, O., and A. Leonard. "Vortex Simulation of Forced/ Unforced Mixing Layers." *AIAA J.* 26, no. 11 (1987): 1417.

Jaberi, F.A., P.J. Colucci, S. James, P. Givi, and S.B. Pope. "Filtered Mass Density Function for Large-Eddy-Simulation of Turbulent Reacting Flows." *Journal of Fluid Mechanics* 401 (1999): 85-121.

Karlin, S., and H.M. Taylor. *A Second Course in Stochastic Processes.* New york: Academic, 1981.

Klimenko, A. "Multicomponent diffusion of various admixtures in turbulent flow." *Fluid Dyn.* 25, no. 3 (1990): 3-10.

Knio, O. M., and A. F. Ghoneim. "The three-dimensional structure of periodic vorticity layers under non-symmetric conditions." *J. Fluid Mech.* 243 (1992): 353-392.

Knio, O. M., and A. F. Ghoniem. "Vortex simulation of a three-dimensional reacting shear layer with infinite-rate kinetics." *AIAA J.* 30, no. 1 (1992): 105-116.

Konrad, J.H. "An experimental investigation of mixing in two-dimensional turbulent shear flows with applications to diffusion-limited chemical reactions." PhD thesis, California Institute of Technology, 1976.

Lakkis, I., and A.F. Ghoneim. "Axisymmetric Vortex Method for low-Mach number, Diffusoin-Controlled Combustion." *Journal of Compututional Physics* 184 (2003): 435-475.

LaRue, J. C., P. A. Libby, and D. V. R. Seshadri. "Further results on the thermal mixing layer downstream of a turbulence grid." *Phys. Fluids* 24 (1981): 1927.

Leonard, A. "Vortex methods for flow simulation." *J. Comp. Phys.* 37 (1980): 289-335.

Lessani, B., J. Ramboer, and C. Lacor. "Efficient Large-eddy Simulations of Low Mach Number Flows Using Preconditioning and Multigrid." *International Journal of Computational Fluid Dynamics* 18, no. 3 (2004): 221-233.

Lin, P., and D. T. Pratt. "Numerical simulation of a plane turbulent mixing layer, with applications to isothermal, rapid reactions." *AIAA Pap. 87-0224*, 1987.

Lozano, A., A. García-Olivares, and C. Dopazo. "The instability growth leading to a liquid sheet breakup." *Phys. Fluids* 10, no. 9 (1998): 2188-2197.

Lundgren, T.S. "Model Equation for Nonhomogeneous turbulence." *Physics of Fluids* 12 (1969): 485-497.

Ma, B.-K., and Z. Warhaft. "Some aspects of the thermal mixing layer in grid turbulence." *Phys. Fluids* 29 (1986): 3114.

Mansfield, J. R., O. M. Knio, and C. Meneveau. "A Dynamic LES Scheme for the Vorticity Transport Equation: Formulation and a Priori Tests." *Journal of Computational Physics* 145 (1998): 693-730.

Mansour, N. N., P. Moin, W. C. Reynolds, and J. H. Ferziger. "Improved Method for Turbulence. Tub. Shear Flow I." 1979: 386-401.

Masutani, S.M., and C.T. Bowman. "The structure of a chemically reacting plane Mixing Layer." *Journal of Fluid Mechanics* 172 (1986): 93-126.

McMurtry, P. A., J. J. Riley, and R. W. Metcalfe. "Effects of heat release on the large-scale structure in turbulent mixing layers." *J. Fluid Mech.* 199 (1989): 297-332.

Milane, R.E. "Large Eddy Simualtion (2D) using Diffusion-Velocity Method and Vortex-In-Cell." *International Journal for Numerical Methods in Fluids* 44 (2004): 837-860.

Milane, R.E., and S. Nourazar. "Large-Eddy-Simulation of Mixing Layer using Vortex Method: Effect of Subgrid-Scale Model on early Development." *Mechanics Research Communication* 24, no. 2 (1997): 215-221.

Milane, R.E., and S. Nourazar. "On the Turbulent Diffusion Velocity in Mixing Layer simulated using the Vortex Method and the Subgrid Scale Vorticity Model." *Mechanics Research Communication* 22, no. 4 (1995): 327-333.

Mizuno, Yasuhiro, Hideo Asano, Katsuyoshi Tada, Masafumi Hirota, Hiroshi Nakayama, and Shunsaku Hirayama. "Turbulent Mixing of Hot and Cold Air in HVAC Unit for Automobile (Thermal Mixing in Planar Shear Layer)." *Transactions of the Japan Society of Mechanical Engineers. B* 71, no. 701 (2005): 215-222.

Möbus, H., P. Gerlinger, and D. Brüggeman. "Comparison of Eulerian and Lagrangian Monte Carlo PDF Methods for Turbulent Diffusion Flame ." *Combustion and FLame* 124 (2001): 519-534.

Najm, H. N., R. B. Milne, K. D. Devine, and S. N. Kempa. "A coupled Lagrangian-Eulerian scheme for reacting flow modeling." *ESAIM Proc. 7*, 1999: 304-313.

Ogami, Y., and Akamatsu. "Viscous Flow Simulation using the Discrete Vortex Model - The Diffusion Velocity Method." *Computers and Fluids* 19 (1991): 433-441.

Oster, D., and I. Wygnanski. "The Forced Mixing Layer between Parallel Streams." *Journal of Fluid Mechanics* 123 (1982): 91-130.

Ould-Salihi, M. L., G.-H. Cottet, and M. E. Hamraoui. "Blending finite-difference and vortex methods for incompressible flow computations." *SIAM J. Sci. Comput.* 22, no. 5 (2000): 1655-1674.

Peters, N. "Laminar diffusion flamelet models in non-premixed models in turbulent combustion." *Prog. Energy Combust. Sci.* 10 (1984): 319-339.

Peters, N. "Laminar flamelet concepts in turbulent combustion." *Proc. Combust. Inst.* 21 (1986): 1231-1250.

Piomelli, U. "Large-Eddy and direct simulation of turbulent flows." *9eme conference annuelle de la Société Canadienne de CFD.* 2001.

Pope, S.B. "Lagrangian PDF Methods for Turbulent Flows." *Annuel Review of Fluid Mechanics* 26 (1994): 23-63.

Pope, S.B. "PDF Methods for Turbulent Reactive Flows." *Prog. Energy Combust. Sci.* 11 (1985): 119-192.

Reinaud, J., L. Joly, and P. Chassaing. "Numerical simulation of a variable-density mixing-layer." *ESAIM Proc. 7*, 1999: 359-368.

Risken, H. *The Fokker-Planck Equation, Methods of Solution and Applications.* New York: Springer, 1989.

Sagaut, Pierre. *Large Eddy Simulation for Incompressible Flows.* Second Edition. Torino: Springer, 2002.

Sekar, B., and H. S. Mukunda. "A computational study of direct simulation of high speed mixing layers without and with chemical heat release ." *Proc. Combust. Inst.* 23 (1990): 707–713.

Shaikh, Adeel. "Comparing Methods for Subgrid Stresses in Large Eddy Simulations Based on Vortex-In-Cell with Application to Mixing layer." M. Eng. report, Ottawa-Carleton Institute for Mechanical and Aerospace Engineering, 2006.

Soteriou, M., and A. F. Ghoneim. "Numerical simulation of unsteady combustion using the transport element method." *ESAIM Proc. 1*, 1996: 429-446.

Soteriou, M., and A. F. Ghoniem. "Effects of the free-stream density ratio on free and forced spatially-developing shear layers." *Phys. Fluids* 30 (1995): 2036–2051.

Tacina, K. M., and W. J. A. Dahm. "Effects of heat release on turbulent shear flows. Part 1. A general equivalence principle for nonbuoyant flows and its application to turbulent jet flames." *J. Fluid Mech.* 415 (2000): 23-44.

Tavoularis, S. "Course Notes on Theory of Turbulence." 2007.

Vreman, B., B. Geurts, and H. Kuerten. "Large-Eddy Simulation of the Turbulent Mixing Layer." *Journal of Fluid Mechanics* 339 (1997): 357-390.

Wallace, A. K. "Experimental investigation on the effect of chemical heat release in the reacting turbulent plane shear layer." PhD Thesis, University of Adelaide, Adelaide, Australia, 1981.

Wang, C., and B. C. Khoo. "An indirect boundary element method for three-dimensional explosion bubbles." *J. Comput. Phys.* 194 (2004): 451-480.

Wang, J.K., and R.E. Milane. "Large Eddy simulation (2D) of a spatially developping Mixing Layer using Vortex-In-Cell for flow field and probability density function for scalar field." *International Journal For Numerical Methods in Fluids* 50 (2006): 27-61.

Yanenko, N.N. *The method of Fractional Steps.* Springer Verlag, 1971.

Zhang, X., and A.F. Ghoneim. "Transport element method for axisymmetric variable-density flow and its application to the spreaf and dispersion of a dense cloud." *ESAIM Proc. 1*, 1996: 77-94.

Zhou, Ming, and I. Wygnanski. "The response of a mixing layer formed between parallel streams to a concomitant excitation at two frequencies." *Journal of Fluid Mechanics* 441 (2001): 139-168.

Zhou, X.Y., and J.C.F. Pereira. "Large Eddy Simulation (2D) of a Reacting Plane Mixing Layer using Filtered Density Function." *Flow, Turbulence and Combustion* 64 (2000): 279-300.

APPENDIX A - FLOWCHARTS

The LES code was written using Fortran and comprises more than 4000 lines. Therefore, representative flowcharts are used to illustrate the code, and the subroutines' interactions. The simulations use one main program and two post-processing programs. The post-processing programs are the same for the reacting mixing layer and for the thermal mixing layer described as follows:

VICPP.f90: A post-processing program for the flow field. It is run after the main program finishes. It reads the flow field output data files of the main program, computes the similarity variable, vorticity thickness, velocity spread, and normalizes the flow field statistics. Then, it generates the data files ready to be plotted using Tecplot. The output is written to files named: EddyC.dat, VorThickness.dat, MeanVel.dat, Stats.dat, StatA.dat and StatB.dat

SCALAR.f90: A post-processing of the Monte-Carlo simulation for scalar field after running VICPP.f90. The program reads output data files generated from the main program and from the VICPP.f90. it computes the similarity variable for the scalar field, concentration or temperature spread and normalizes and writes scalar statistics for plotting. The output is written to files named: MeanConc.dat, RMSConc.dat, Mixfrequency.dat and ScalarPdf.dat

The main programs used to simulate the reacting mixing layer (Passive_Vic_PDF.f) and the thermal mixing layer (Active_VIC_PDF.f) are illustrated as Flowcharts in Sections A.1 and A.2 respectively.

A.1 Isothermal Chemically Reacting Mixing Layer

Passive_VIC_PDF.f:

The main program is a numerical simulation of flow field and scalar field for the isothermal reacting mixing layer. (Setting for Base Run)

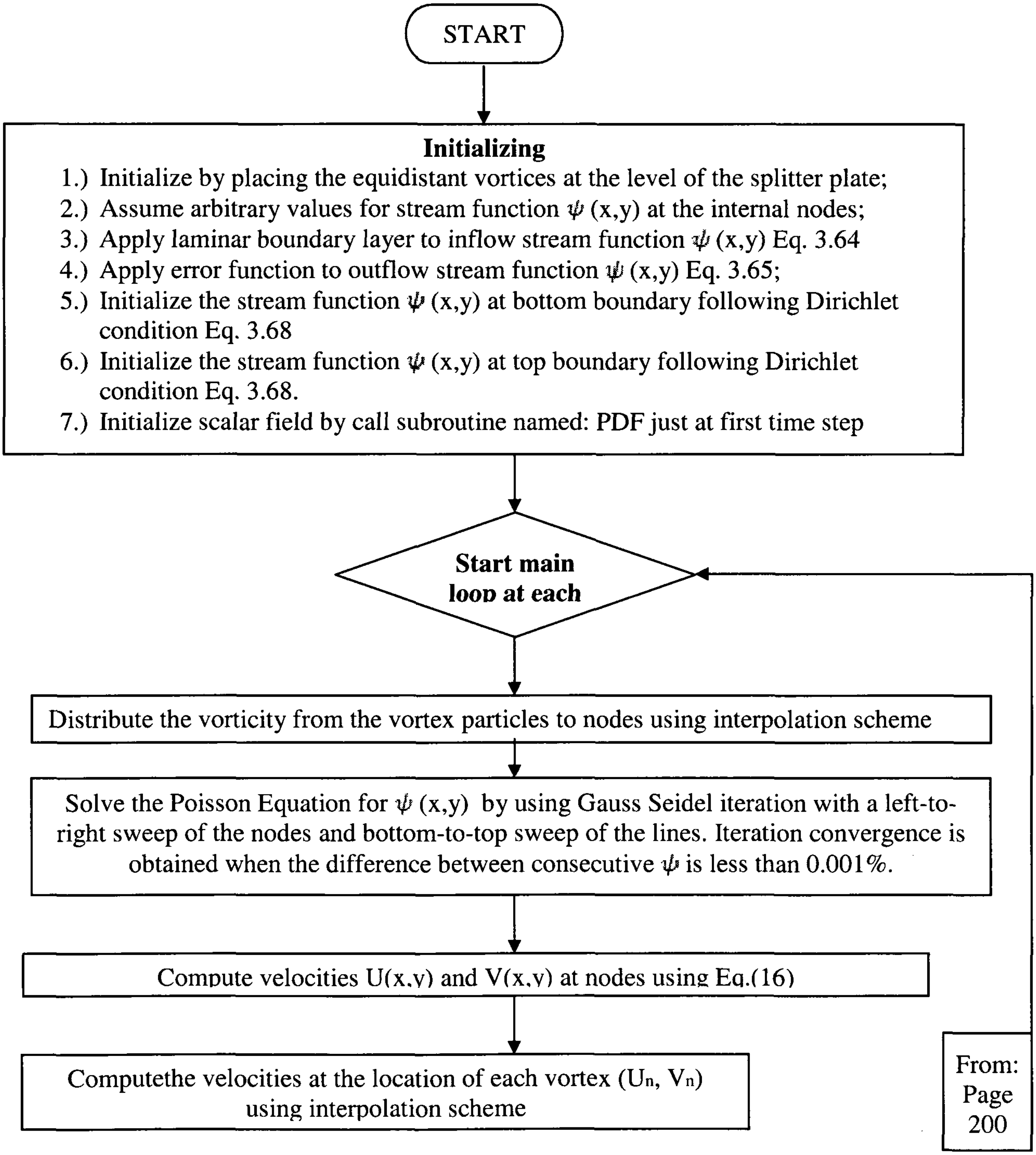

Initializing

1.) Initialize by placing the equidistant vortices at the level of the splitter plate;
2.) Assume arbitrary values for stream function ψ (x,y) at the internal nodes;
3.) Apply laminar boundary layer to inflow stream function ψ (x,y) Eq. 3.64
4.) Apply error function to outflow stream function ψ (x,y) Eq. 3.65;
5.) Initialize the stream function ψ (x,y) at bottom boundary following Dirichlet condition Eq. 3.68
6.) Initialize the stream function ψ (x,y) at top boundary following Dirichlet condition Eq. 3.68.
7.) Initialize scalar field by call subroutine named: PDF just at first time step

Distribute the vorticity from the vortex particles to nodes using interpolation scheme

Solve the Poisson Equation for ψ (x,y) by using Gauss Seidel iteration with a left-to-right sweep of the nodes and bottom-to-top sweep of the lines. Iteration convergence is obtained when the difference between consecutive ψ is less than 0.001%.

Compute velocities U(x,y) and V(x,y) at nodes using Eq.(16)

Computethe velocities at the location of each vortex (U_n, V_n) using interpolation scheme

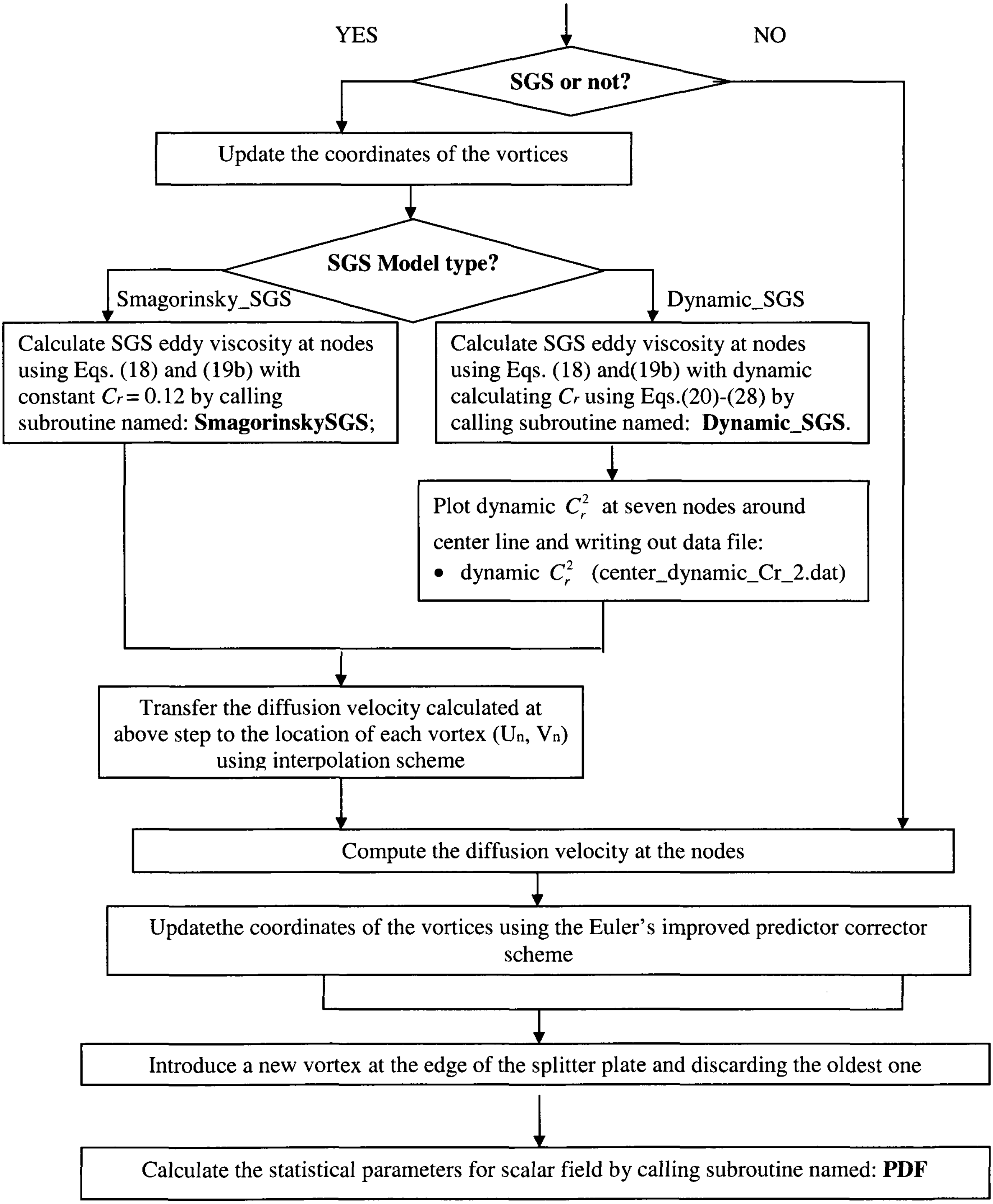
YES
NO
SGS or not?
Update the coordinates of the vortices
SGS Model type?
Smagorinsky_SGS
Dynamic_SGS
Calculate SGS eddy viscosity at nodes using Eqs. (18) and (19b) with constant C_r = 0.12 by calling subroutine named: SmagorinskySGS;
Calculate SGS eddy viscosity at nodes using Eqs. (18) and(19b) with dynamic calculating C_r using Eqs.(20)-(28) by calling subroutine named: Dynamic_SGS.
Plot dynamic C_r^2 at seven nodes around center line and writing out data file:
• dynamic C_r^2 (center_dynamic_Cr_2.dat)
Transfer the diffusion velocity calculated at above step to the location of each vortex (U_n, V_n) using interpolation scheme
Compute the diffusion velocity at the nodes
Updatethe coordinates of the vortices using the Euler's improved predictor corrector scheme
Introduce a new vortex at the edge of the splitter plate and discarding the oldest one
Calculate the statistical parameters for scalar field by calling subroutine named: PDF

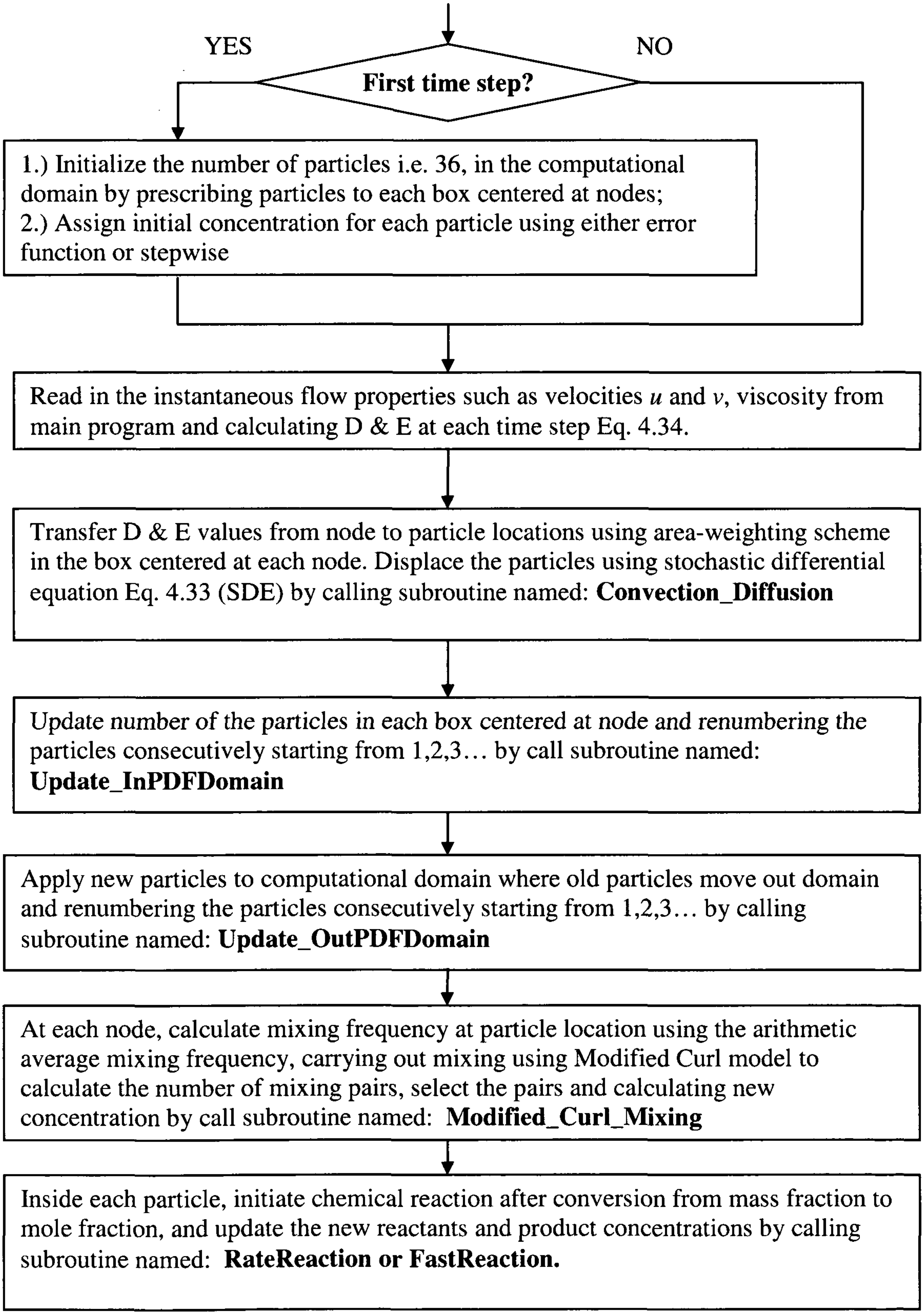
YES
First time step?
NO
1.) Initialize the number of particles i.e. 36, in the computational domain by prescribing particles to each box centered at nodes;
2.) Assign initial concentration for each particle using either error function or stepwise
Read in the instantaneous flow properties such as velocities *u* and *v*, viscosity from main program and calculating D & E at each time step Eq. 4.34.
Transfer D & E values from node to particle locations using area-weighting scheme in the box centered at each node. Displace the particles using stochastic differential equation Eq. 4.33 (SDE) by calling subroutine named: **Convection_Diffusion**
Update number of the particles in each box centered at node and renumbering the particles consecutively starting from 1,2,3… by call subroutine named: **Update_InPDFDomain**
Apply new particles to computational domain where old particles move out domain and renumbering the particles consecutively starting from 1,2,3… by calling subroutine named: **Update_OutPDFDomain**
At each node, calculate mixing frequency at particle location using the arithmetic average mixing frequency, carrying out mixing using Modified Curl model to calculate the number of mixing pairs, select the pairs and calculating new concentration by call subroutine named: **Modified_Curl_Mixing**
Inside each particle, initiate chemical reaction after conversion from mass fraction to mole fraction, and update the new reactants and product concentrations by calling subroutine named: **RateReaction or FastReaction.**

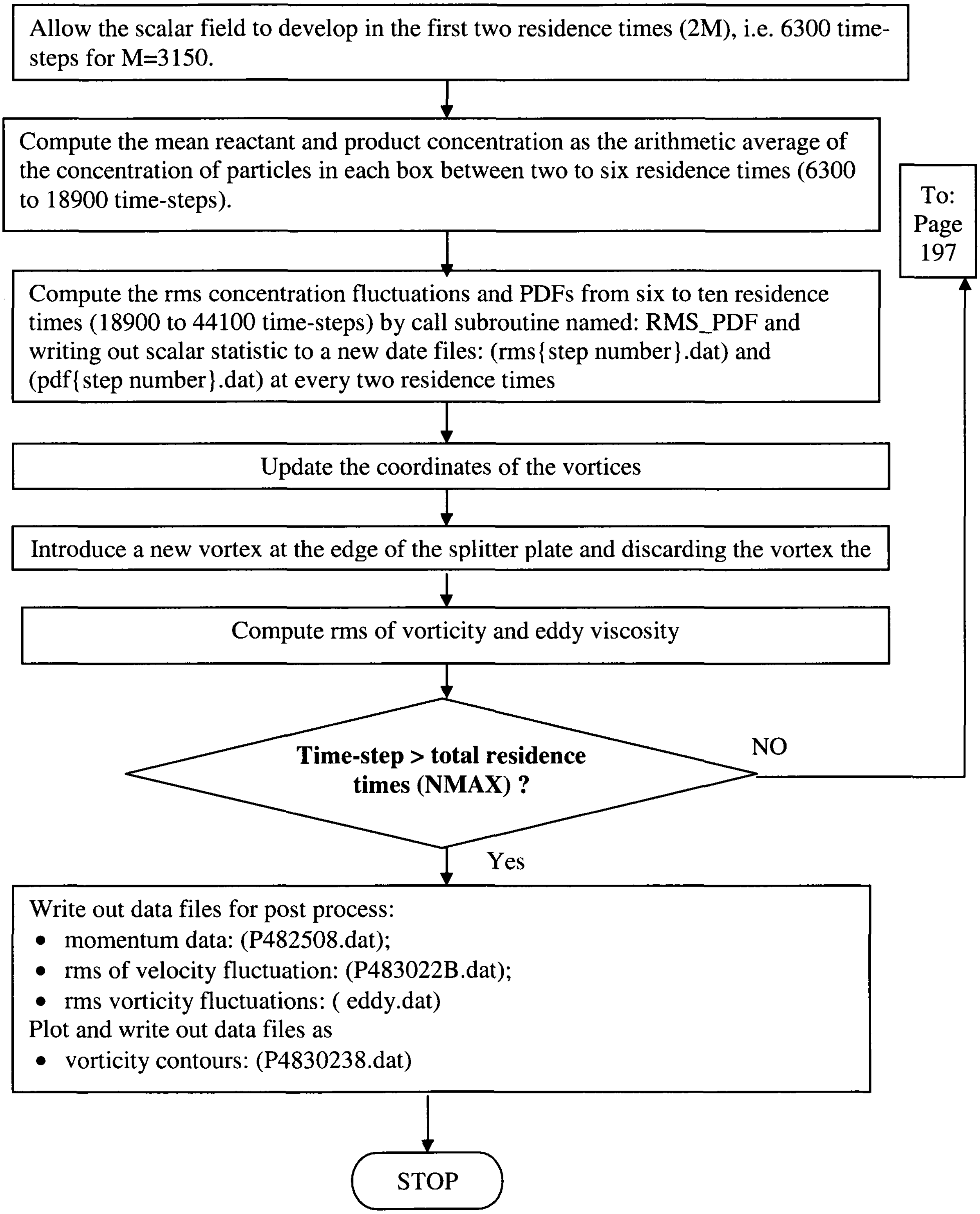

Allow the scalar field to develop in the first two residence times (2M), i.e. 6300 time-steps for M=3150.

Compute the mean reactant and product concentration as the arithmetic average of the concentration of particles in each box between two to six residence times (6300 to 18900 time-steps).

Compute the rms concentration fluctuations and PDFs from six to ten residence times (18900 to 44100 time-steps) by call subroutine named: RMS_PDF and writing out scalar statistic to a new date files: (rms{step number}.dat) and (pdf{step number}.dat) at every two residence times

Update the coordinates of the vortices

Introduce a new vortex at the edge of the splitter plate and discarding the vortex the

Compute rms of vorticity and eddy viscosity

Time-step > total residence times (NMAX) ?

Write out data files for post process:
- momentum data: (P482508.dat);
- rms of velocity fluctuation: (P483022B.dat);
- rms vorticity fluctuations: (eddy.dat)

Plot and write out data files as
- vorticity contours: (P4830238.dat)

A.2 Thermal Mixing Layer

Active_VIC_PDF.f:

The main program is a numerical simulation of flow field and scalar field for the isothermal reacting mixing layer. (Setting for Base Run)

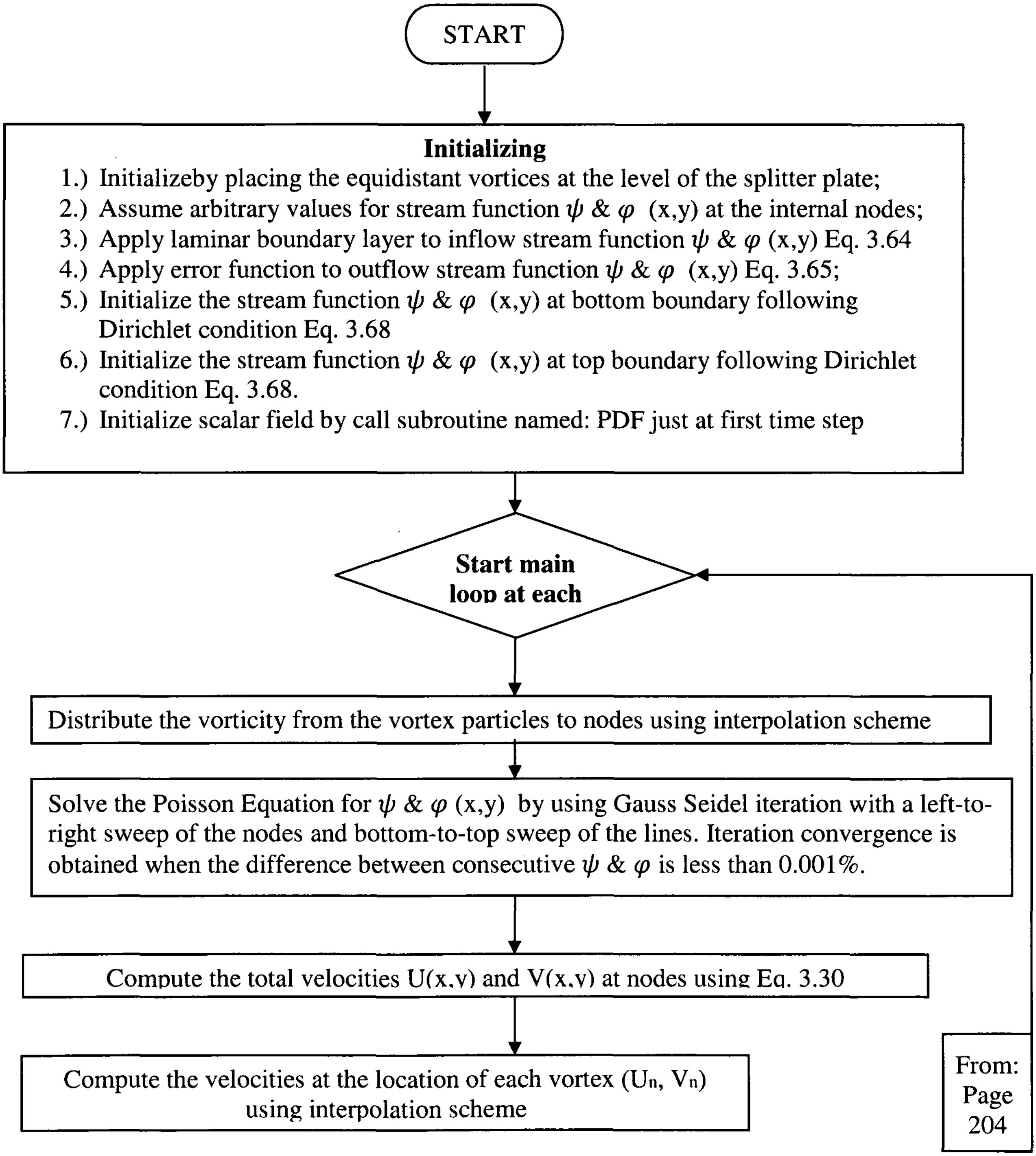

START

Initializing

1.) Initializeby placing the equidistant vortices at the level of the splitter plate;
2.) Assume arbitrary values for stream function ψ & φ (x,y) at the internal nodes;
3.) Apply laminar boundary layer to inflow stream function ψ & φ (x,y) Eq. 3.64
4.) Apply error function to outflow stream function ψ & φ (x,y) Eq. 3.65;
5.) Initialize the stream function ψ & φ (x,y) at bottom boundary following Dirichlet condition Eq. 3.68
6.) Initialize the stream function ψ & φ (x,y) at top boundary following Dirichlet condition Eq. 3.68.
7.) Initialize scalar field by call subroutine named: PDF just at first time step

Start main loop at each

Distribute the vorticity from the vortex particles to nodes using interpolation scheme

Solve the Poisson Equation for ψ & φ (x,y) by using Gauss Seidel iteration with a left-to-right sweep of the nodes and bottom-to-top sweep of the lines. Iteration convergence is obtained when the difference between consecutive ψ & φ is less than 0.001%.

Compute the total velocities U(x,y) and V(x,y) at nodes using Eq. 3.30

Compute the velocities at the location of each vortex (U_n, V_n) using interpolation scheme

From: Page 204

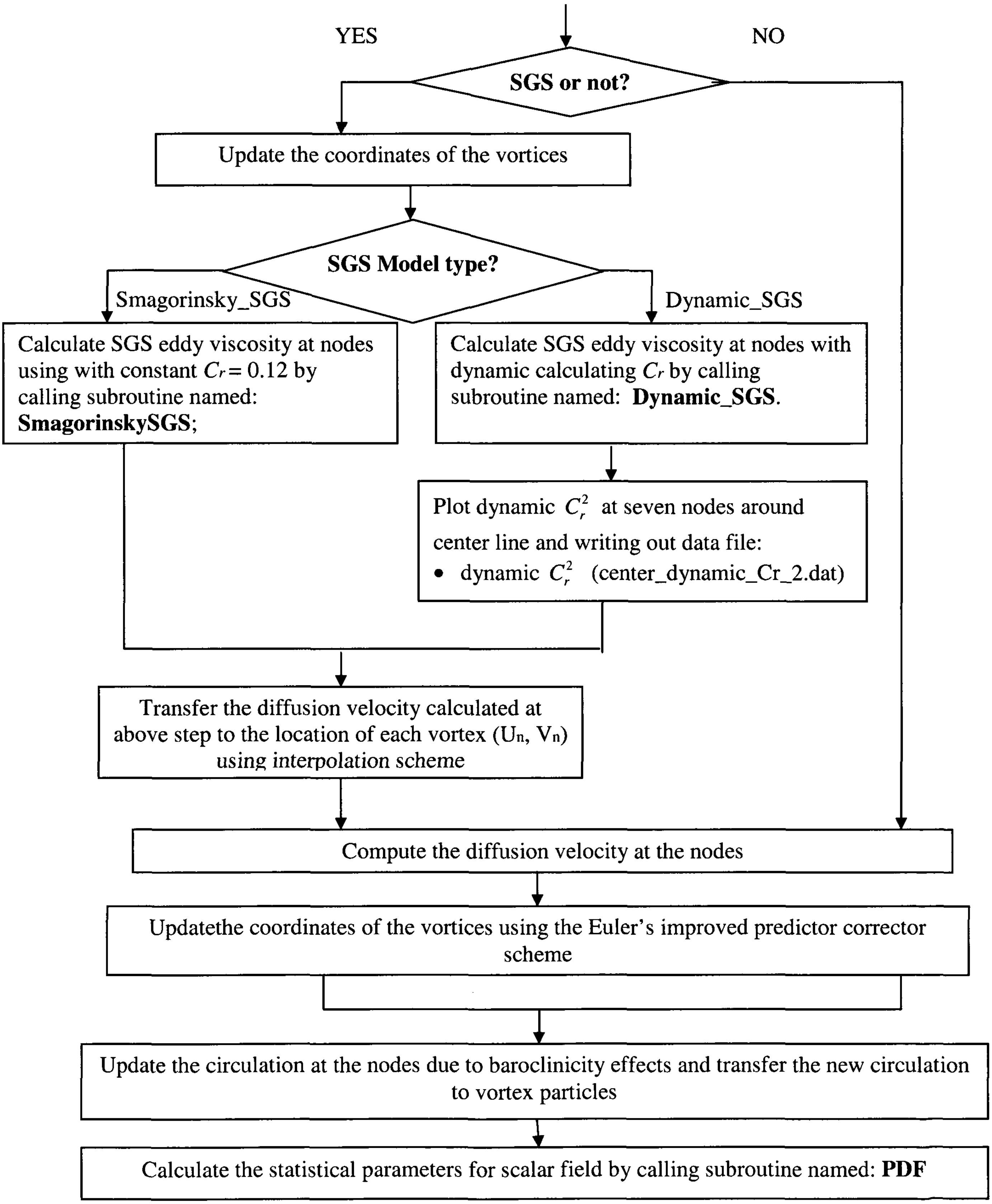
YES
SGS or not?
NO
Update the coordinates of the vortices
SGS Model type?
Smagorinsky_SGS
Dynamic_SGS
Calculate SGS eddy viscosity at nodes using with constant $C_r = 0.12$ by calling subroutine named: **SmagorinskySGS**;
Calculate SGS eddy viscosity at nodes with dynamic calculating C_r by calling subroutine named: **Dynamic_SGS**.
Plot dynamic C_r^2 at seven nodes around center line and writing out data file:
- dynamic C_r^2 (center_dynamic_Cr_2.dat)
Transfer the diffusion velocity calculated at above step to the location of each vortex (U_n, V_n) using interpolation scheme
Compute the diffusion velocity at the nodes
Updatethe coordinates of the vortices using the Euler's improved predictor corrector scheme
Update the circulation at the nodes due to baroclinicity effects and transfer the new circulation to vortex particles
Calculate the statistical parameters for scalar field by calling subroutine named: **PDF**

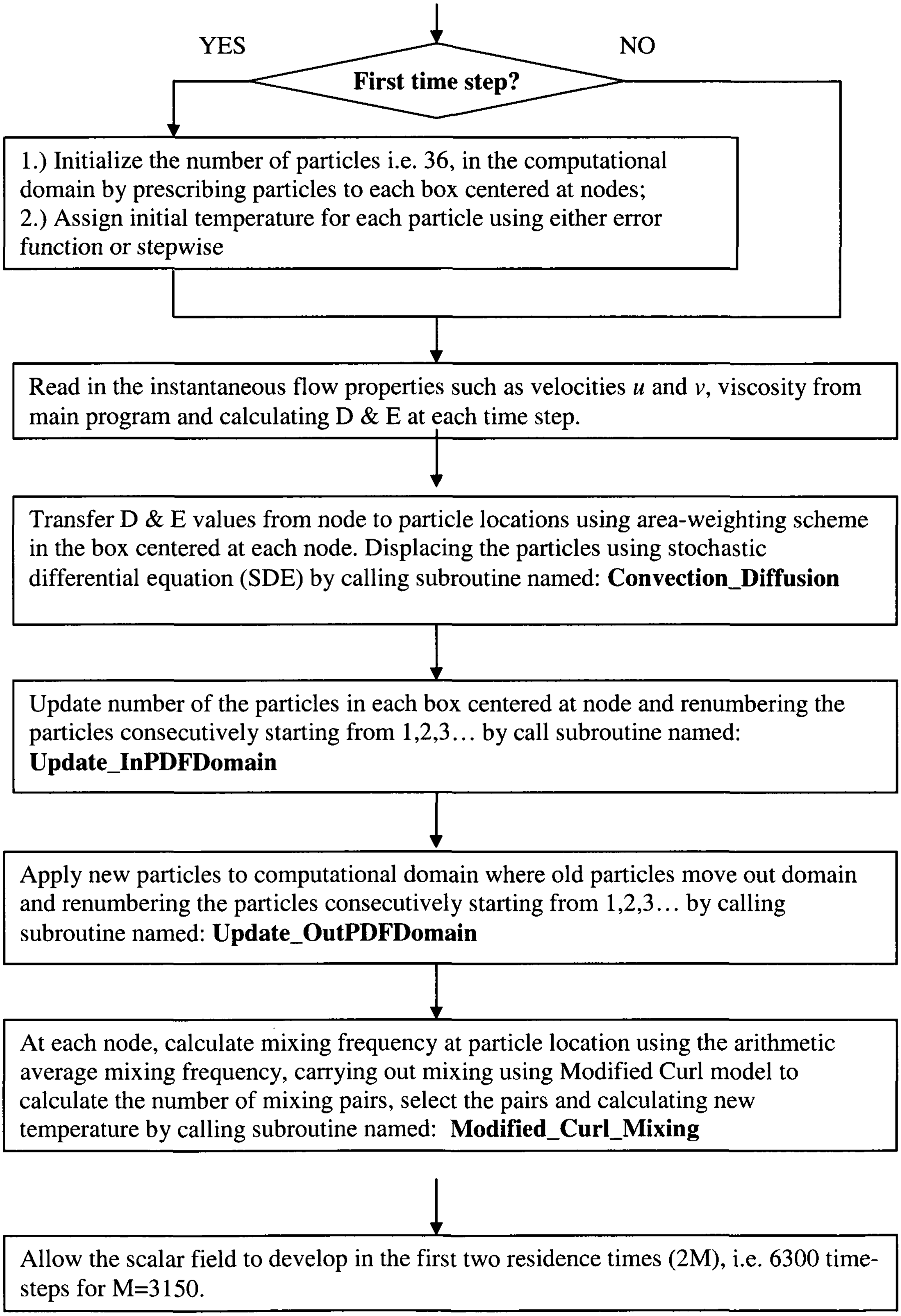

1.) Initialize the number of particles i.e. 36, in the computational domain by prescribing particles to each box centered at nodes;
2.) Assign initial temperature for each particle using either error function or stepwise

Read in the instantaneous flow properties such as velocities *u* and *v*, viscosity from main program and calculating D & E at each time step.

Transfer D & E values from node to particle locations using area-weighting scheme in the box centered at each node. Displacing the particles using stochastic differential equation (SDE) by calling subroutine named: **Convection_Diffusion**

Update number of the particles in each box centered at node and renumbering the particles consecutively starting from 1,2,3… by call subroutine named: **Update_InPDFDomain**

Apply new particles to computational domain where old particles move out domain and renumbering the particles consecutively starting from 1,2,3… by calling subroutine named: **Update_OutPDFDomain**

At each node, calculate mixing frequency at particle location using the arithmetic average mixing frequency, carrying out mixing using Modified Curl model to calculate the number of mixing pairs, select the pairs and calculating new temperature by calling subroutine named: **Modified_Curl_Mixing**

Allow the scalar field to develop in the first two residence times (2M), i.e. 6300 time-steps for M=3150.

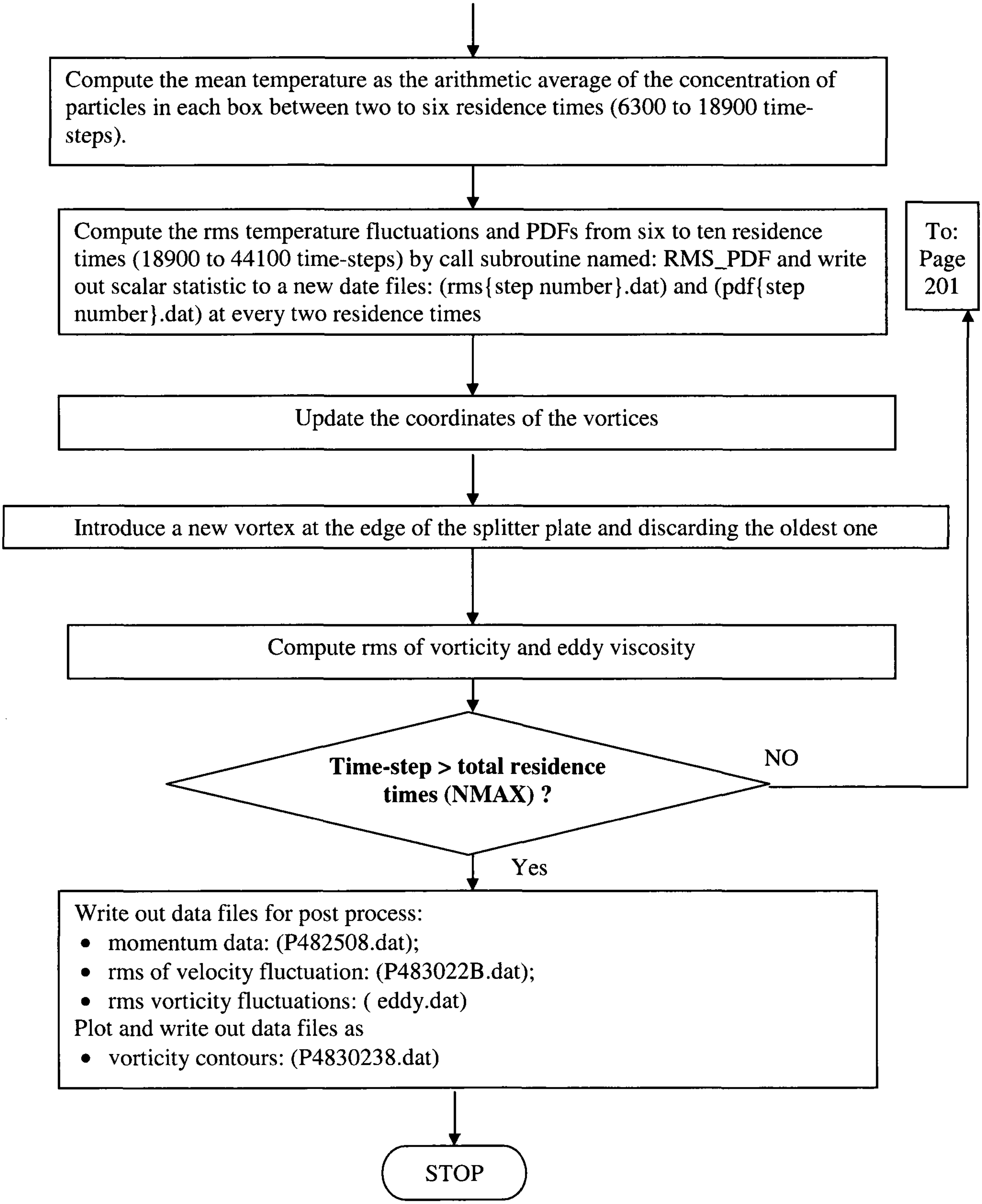

Compute the mean temperature as the arithmetic average of the concentration of particles in each box between two to six residence times (6300 to 18900 time-steps).

Compute the rms temperature fluctuations and PDFs from six to ten residence times (18900 to 44100 time-steps) by call subroutine named: RMS_PDF and write out scalar statistic to a new date files: (rms{step number}.dat) and (pdf{step number}.dat) at every two residence times

Update the coordinates of the vortices

Introduce a new vortex at the edge of the splitter plate and discarding the oldest one

Compute rms of vorticity and eddy viscosity

Time-step > total residence times (NMAX) ?

Write out data files for post process:
- momentum data: (P482508.dat);
- rms of velocity fluctuation: (P483022B.dat);
- rms vorticity fluctuations: (eddy.dat)

Plot and write out data files as
- vorticity contours: (P4830238.dat)